AD-A047 526 VISIDYNE INC BURLINGTON MASS F/G 4/1
COMPARISON OF ICECAP AND EXCEDE ROCKET MEASUREMENTS WITH COMPUT--ETC(U)
FEB 77 A G HURD, J W CARPENTER, T C DEGGES F19628-74-C-0177
UNCLASSIFIED VI-381 AFGL-TR-77-0060 NL

1 OF 3
ADA047 526

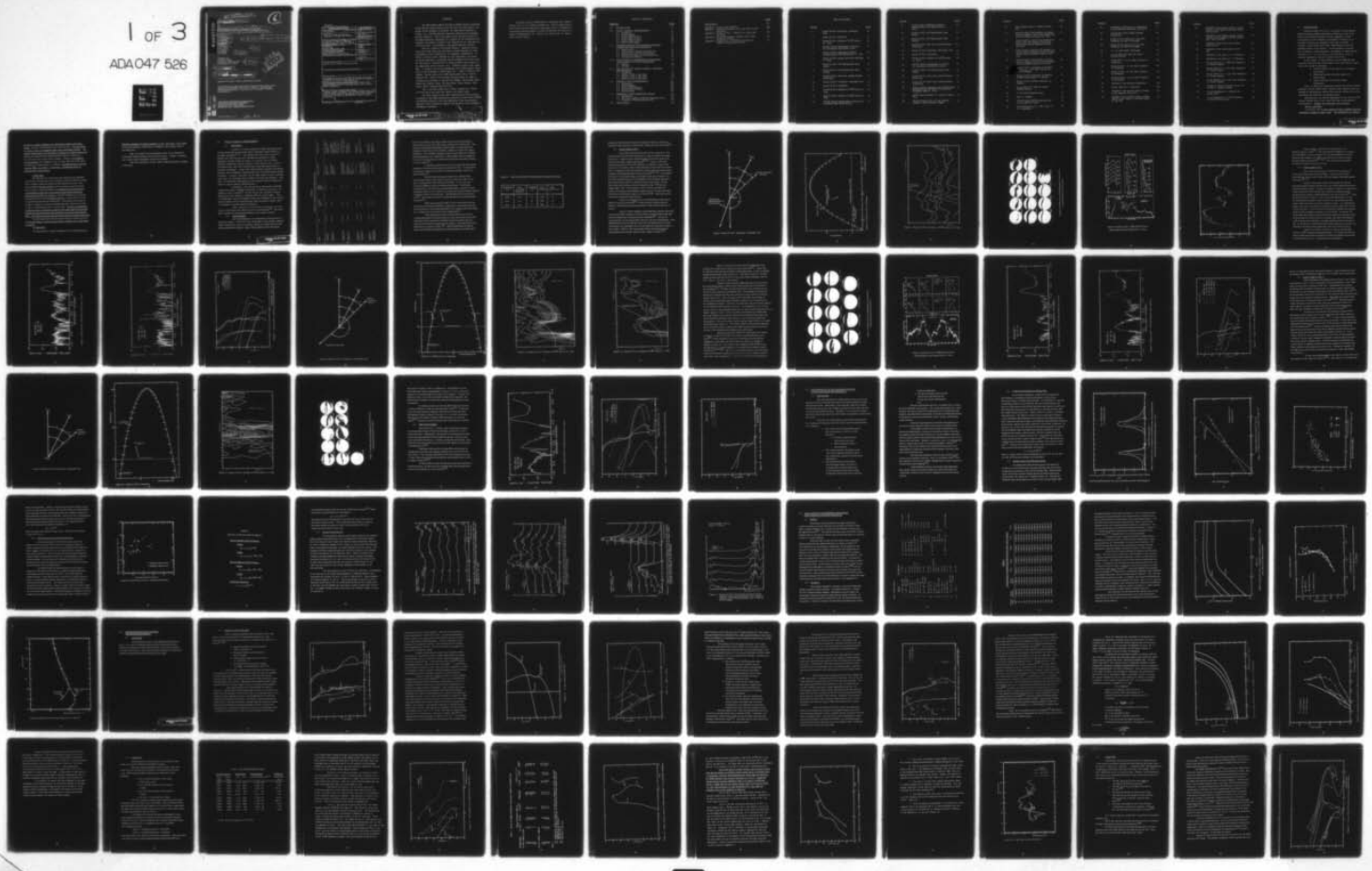

(19) (18) AFGL, DNA

AFGL-TR-77-0060, HAES-61
HAES Report DNA 61

(6) B.S.

COMPARISON OF ICECAP AND EXCEDE ROCKET MEASUREMENTS WITH COMPUTER CODE PREDICTIONS.

(10) A. G. Hurd,
J. W. Carpenter,
T. C. Degges,
W. F. Grieder
W. P. Reidy
O. Shepherd
A. T. Stair, Jr.
R. R. O'Neil
J. C. Ulwick
D. J. Baker
K. D. Baker

Visidyne, Inc.
19 Third Avenue
Northwest Industrial Park
Burlington, MA 01803

(14) VI-381

(15) F19628-74-C-0177

(17) 64

(16) 2310

(12) 222p.

(11) 15 Feb 77

(9) Final Report,
9 Oct 74 - 30 Dec 76

61102F

This research was sponsored by the Defense Nuclear Agency under Subtask L25AAXYX966, Work Unit 16, entitled: "Analysis and Feasibility Assessment," and Work Unit 19, entitled: "ICECAP Data Analysis."

AIR FORCE GEOPHYSICS LABORATORY
AIR FORCE SYSTEMS COMMAND
UNITED STATES AIR FORCE
HANSCOM AFB, MASSACHUSETTS 01731

AIR FORCE (1) NOVEMBER 10, 1977--310

390 862

UNCLASSIFIED

SECURITY CLASSIFICATION OF THIS PAGE (When Data Entered)

REPORT DOCUMENTATION PAGE		READ INSTRUCTIONS BEFORE COMPLETING FORM
1. REPORT NUMBER AFGL-TR-77-0060	2. GOVT ACCESSION NO.	3. RECIPIENT'S CATALOG NUMBER VI-381
4. TITLE (and Subtitle) Comparison of ICECAP and EXCEDE Rocket Measurements with Computer Code Predictions		5. TYPE OF REPORT & PERIOD COVERED FINAL REPORT 9 OCT 74 - 30 DEC 76 6. PERFORMING ORG. REPORT NUMBER HAES Report No. 61
7. AUTHOR(s) A.G. Hurd, J.W. Carpenter, T.C. Degges, W.F. Grieder, W.P. Reidy & O. Shepherd of Visidyne, Inc; A.T. Stair, Jr., R.R. O'Neil, & J.C. Ulwick of AFGL; D.J. Baker & K.D. Baker of UTAH State University		8. CONTRACT OR GRANT NUMBER(s) F19628-74-C-0177
9. PERFORMING ORGANIZATION NAME AND ADDRESS Visidyne, Inc. 19 Third Avenue Burlington, Massachusetts 01803		10. PROGRAM ELEMENT, PROJECT, TASK AREA & WORK UNIT NUMBERS 2310G402 2310G404
11. CONTROLLING OFFICE NAME AND ADDRESS Air Force Geophysics Laboratory Hanscom AFB, Massachusetts 01731 Contract Monitor: A.T. Stair, Jr./OPR		12. REPORT DATE 15 FEBRUARY 1977 13. NUMBER OF PAGES 264
14. MONITORING AGENCY NAME & ADDRESS(if different from Controlling Office)		15. SECURITY CLASS. (of this report) Unclassified 15a. DECLASSIFICATION/DOWNGRADING SCHEDULE

16. DISTRIBUTION STATEMENT (of this Report)

Approved for public release; distribution unlimited.

17. DISTRIBUTION STATEMENT (of the abstract entered in Block 20, if different from Report)

18. SUPPLEMENTARY NOTES

This research was sponsored by the Defense Nuclear Agency under Subtask L25AAXYX966, Work Unit 16, entitled: "Analysis and Feasibility Assessment", and Work Unit 19, entitled: "ICECAP Data Analysis".

19. KEY WORDS (Continue on reverse side if necessary and identify by block number)

Aurora; Atmospheric Visible and IR Emissions; ICECAP; EXCEDE II Test; Atmospheric Modelling Codes; Electron Energy Spectra; Auroral Simulation; Rocket Instrumentation.

20. ABSTRACT (Continue on reverse side if necessary and identify by block number)

An analysis is made of rocketborne HAES experiments performed as part of the ICECAP and EXCEDE II Test Programs. The results are compared to atmospheric emissions from code modelling. Relationships between auroral electron spectra and visible aurora have been determined. Sources of auroral IR are explained.

DD FORM 1 JAN 73 1473 EDITION OF 1 NOV 65 IS OBSOLETE

UNCLASSIFIED

PREFACE

The High Altitude Effects Simulation (HAES) Program sponsored by the Defense Nuclear Agency since the early 1970 time period, comprises several groupings of separate, but interrelated technical activities, e.g., ICECAP (Infrared Chemistry Experiments-Coordinated Auroral Program). Each of the latter has the common objective of providing information ascertained as essential for the development and validation of predictive computer codes designed for use with high priority DoD radar, communications, and optical defensive systems.

Since the inception of the HAES Program, significant achievements and results have been described in reports published by DNA, participating service laboratories, and supportive organizations. In order to provide greater visibility for such information and enhance its timely applications, significant reports published since early calendar 1974 shall be identified with an assigned HAES serial number and the appropriate activity acronym (e.g., ICECAP) as part of the report title. A complete and current bibliography of all HAES reports issued prior to and subsequent to HAES Report No. 1, dated 5 February 1974 entitled, "Rocket Launch of an SWIR Spectrometer into an Aurora (ICECAP 72)", AFCRL Environmental Research Paper No. 466, is maintained and available on request from DASIAC, DoD Nuclear Information and Analysis Center, 816 State Street, Santa Barbara, California, 93102, Telephone [805] 965-0551.

This is the final report under AFCRL Contract No. F19628-74-C-0177 and is the sixty first report in the HAES series.

The main purpose of the work reported herein was to provide an analysis of the HAES Experiments performed as part of the ICECAP and EXCEDE Programs and of the application of the measurements obtained in these programs to physics and chemistry code modelling of atmospheric emissions.

The authors wish to acknowledge the contributions and continued interest of Dr. H. J. P. Smith of Visidyne, Inc. Sincere appreciation is hereby expressed for the generous cooperation of Dr. R. Hegblom and Carol Foley of Boston College; G. Allred of Utah State University; Dr. I. Kofsky of PhotoMetrics, Inc.; and Dr. R. S. Narcisi, Dr. W. Swider and P. Doyle of AFGL.

TABLE OF CONTENTS

LIST OF FIGURES

1.0 INTRODUCTION

Contract F19628-74-C-0177 is an analysis of High Altitude Effects Simulation (HAES) experiments performed as part of the ICECAP and EXCEDE Programs and the application of these measurements to the modelling of atmospheric emissions as determined by physics and chemistry codes such as OPTIR. A scientific report (AFGL-TR-76-0039, HAES Report No. 40) was published earlier in the contract. It was primarily concerned with modelling of energy deposition, calculations of zenith spectral radiances at 4.3, 9.6, and 15 μm, and calculations of the vibrational population of the first excited level of CO_2.

In this report, we first consider at some length the data associated primarily with rocket probes of the more intense aurora. These data include the following:

1) Temporal history of the auroral arc brightness and position.
2) Differential electron intensity spectra and energy fluxes.
3) Optical data from the forward-looking instruments.

Next, we determine relationships between the auroral electron deposition and the visible aurora along the same magnetic field line. Methods of calculating the effects of the auroral electron flux on the atmosphere are discussed and examples given.

Following this, we provide explanations for the sources of the several infrared bands in the aurora and make some qualitative determinations. Briefly, our conclusions are as follows:

The 5.3 μm Band

In all cases, the 5.3 μm emission is due to radiation from the fundamental vibration of nitric oxide. The mechanisms for exciting

the NO are usually earthshine and collisional excitation with atomic oxygen, the latter predominating above about 120 km. The NO density is about an order of magnitude higher than mid-latitude models. The density enhancement is not localized to regions of a visible auroral arc, although the apparent NO density probably requires a prior low level electron flux of many hours duration. However, in an intense auroral breakup, the brightness of the 5.3 μm band due to the above mechanisms in enhanced and, in addition, chemiluminescence from the reaction $N(^2D) + O_2 \rightarrow NO' + O$ becomes a significant source of radiation below about 100 km.

2.7 μm Band

The field data at 2.7 μm due to the relatively weak excitation in normally occurring auroras are generally comparable with the system noise, making it extremely difficult to determine their source. One major exception (Rocket 10.205-2) occurrs during an auroral breakup when 2.7 μm is readily detectable and identified as the first overtone of vibrationally excited NO, the mechanism again being chemiluminescent from the $N(^2D) + O_2$ reaction. Another exception occurs during descent when the wake of the Rocket (18.219-1) is in the field of view of the forward-looking infrared instruments. The spectral band center at 2.7 μm is shifted to a shorter wavelength than that measured on Rocket 10.205-2, indicating the signal is not due to NO. We have concluded this emission must be considered an artifact of the experiment and associated with the fact that the vertical instrumentation was looking in the payload wake. This enhancement was not measured by the side looking instruments.

We have determined from the measurements on Rocket 10.205-2 that the percentage of auroral energy which is emitted in the 2.7 μm band is about 1%.

4.3 μm Band

We show that the 4.3 μm band appears to be in good agreement

with the mechanism of energy transfer, N_2 (V) + $CO_2 \rightarrow N_2 + CO_2$ (001). We present examples of theoretical calculations and compare them to the actual data.

Next, we consider the measurements taken by the EXCEDE II Test Rocket and the geometry of its electron beams. Finally, emissions due to high electron deposition levels are predicted.

Five of the appendices to this report contain information relating to the above.

2.0 ICECAP AURORAL MEASUREMENTS

2.1 Introduction

A number of rockets launched as HAES experiments have carried instruments for measuring short wavelength infrared (SWIR) in the upper atmosphere[1,2]. The infrared data may be the result of relatively slow chemical processes following the deposition of either naturally occurring auroral electrons, or, as in the case of Project EXCEDE, artificially injected electrons. In the former case, at least, the infrared data come from measurements along long optical paths in the upper atmosphere. Many of the rocket payloads included electrostatic analyzers and scintillators which provided data on electron energy spectra and fluxes. However, these data are for single points in space and time, and aurora are notoriously time variable in location and intensity. How, then, can theoretical determination of the expected infrared radiation be made to compare with the experiment data?

Fortunately, some ground-based instruments essentially monitor the auroral conditions continuously in both space and time. In addition to radar scanning[3], all-sky cameras and meridian-scanning photometers were utilized in conjunction with the rocket flights. Thus, if relationships could be established between the brightness of the auroras and the character of the electron fluxes, then, theoretical models could be formulated to predict infrared radiations.

Table 1 lists some of the rockets for which data are available and which have made infrared auroral measurements[4]. Several of these rockets are discussed individually in the sections to follow.

2.2 Instrumentation

The measurements of the differential energy spectra of electrons between 1 and 30 keV were made with an electrostatic analyzer (ESA) consisting of a pair of concentric spherical octants with the outer plate grounded and a positive sweep voltage applied to the inner plate.

TABLE 1

Summary of Infrared Auroral Measurements

ROCKET	DATE	ALT. RANGE OF MEAS. (KM)	SPECTRAL RANGE OF IR MEAS. (μm)	AURORAL CONDITION	PRIMARY RESULTS
Black Brant (17.110-3)	16 Mar 72	60-144	1.3-5.4	Possible IBC II near descent only	Low level signals from side-looking radiometers.
Black Brant VA (18.006-2)	22 Mar 73	40-185	7-23	Rocket penetrated post-breakup auroral glow IBC II	First longwave infrared spectral measurements in aurora. Altitude profiles of 9.6 μm (O_3) and 15 μm (CO_2) emissions.
Paiute-Tomahawk (10.205-2)	24 Mar 73	70-211	1.6-5.3	Rocket penetrated very bright auroral breakup. IBC II$^+$	Aurorally enhanced 4.3 μm (CO_2), 2.8 and 5.3 μm (NO) emissions
Black Brant VA (18.205-1)	27 Mar 73	68-181	1.6-5.3	Rocket ascent penetrated bright auroral arc. IBC II$^+$ Descent into quiet region	Measurements of SWIR emissions from auroral arc.
Black Brant VA (18.006-4)	13 Feb 74	65-199	7-23	Aurorally quiet	Background for auroral case.
Black Brant VA (18.219-1)	25 Feb 74	80-195	1.6-5.6	Rocket penetrated IBC II aurora in region previously occupied by IBC II$^+$ auroral arc.	Auroral IR emission profiles.
Nike-Javelin (NJ74-1)	11 Apr 74	56-118	1.6-5.3	Aurorally quiet	Background for auroral case.
Sergeant-Hydac (IC519.07-1B)	12 Mar 75	58-184	1.8-5.5	Aurorally quiet	Background for auroral case.

Every 0.52 seconds, this sweep voltage was decreased exponentially from a peak of about 3 keV with a time constant of 90 milliseconds. The electrons transmitted through the analyzer plates were detected by an aluminum coated CaF_2 (Eu) scintillator coupled to an EMR 541-D photomultiplier. The aluminum coating prevents auroral light from reaching the photomultiplier and, additionally, a high voltage (~3kv) is applied to it to accelerate the electrons and thereby extend the instrument response to lower energies[5].

A scintillator detector was used to measure the total energy deposition of electrons with energies greater than 4 keV. It consisted of an aluminum-coated pilot B plastic scintillation phosphor viewed by a photomultiplier[5].

The SWIR spectral measurements were obtained with spectrometers whose entire optical train was housed in a high vacuum dewar cryogenically cooled with liquid nitrogen. A cold cover was removed in flight just prior to taking measurements. Wavelength scanning from 1.6 to 5.3μm was accomplished with a circular-variable interference filter (CVF) rotated at two scans per second and with a spectral resolution of three to four percent. The InSb detector was operated at 77°K[4]. Procedures used in processing the data have been documented elsewhere[6].

SWIR measurements of the 4.3 and 5.3μm bands were also made with dual channel radiometers, which were constructed much like the spectrometers except that fixed filters were used in front of the optics, and a chopper was used instead of the rotating filter[7].

The ground-based auroral measurements were made by scanning photometers mounted inside an acrylic dome on the roof of the Utah State mobile observatory (ARGUS) located near the launch site. The scan was along the expected rocket azimuth. Characteristics of the photometers are given in Table 2[8]. Similar photometers located at other ground stations approximately along the magnetic meridian were

TABLE 2: SPATIAL SCANNING PHOTOMETER CHARACTERISTICS

Wavelength (A)	FOV Full Angle (Degrees)	Bandwidth (A)	Scan Direction	Scan Time (sec.)
6300	4.5	14	N→S	14
5577	4.5	18	N→S	14
3914	4.5	15	N→S	14

operated by the University of Alaska Geophysical Institute, which also operated all-sky cameras at Ester Dome, Poker Flat, and Fort Yukon[9].

2.3 Rocket Flight 18.205-1

This rocket was launched at 0937:45 UT on March 27, 1973 from the Poker Flat Research Range into a relatively intense and stable auroral arc. Figures 1 and 2 show horizontal and vertical views of the trajectory and other angular information[10, 11]. Figure 3 shows the ground range position and 5577Å intensity in isoradiance values of the auroral arc in the plane of the rocket trajectory versus time from launch and is a composite of the data presently available from the ground-based meridian scanning photometers at three locations[12, 13, 14]. Also plotted in Figure 3 is the ground range in the plane of the rocket trajectory to the 100 km altitude intercept of the magnetic field line which intersects the position of the rocket as a function of time from launch. Shortly after launch, the maximum observed intensity in the 5577Å line was greater than 75 kR. From Figures 2 and 3 it can be seen that the rocket on ascent passed through this region about 20 seconds later when the aurora was still quite intense (~35 kR at 5577Å). Minimum auroral activity was observed on the downleg.

Figure 4 is composed of all-sky photographs of the aurora taken by University of Alaska[15]. These pictures verify the data in Figure 3, which shows the long time history of the relative stability of the arc.

Figure 5 shows examples of the differential spectra measured by the electrostatic analyzer at various times during the flight along with the total energy flux as measured by the scintillator[5]. Because of arcing at turn on of the electrostatic analyzer, the first measurement of the differential flux was not until the rocket was well within the auroral arc. At this point, the scintillator was also saturated and remained so until T + 123 seconds. However, the total energy flux has been determined by integrating the electrostatic analyzer data, shown in Figure 6[16].

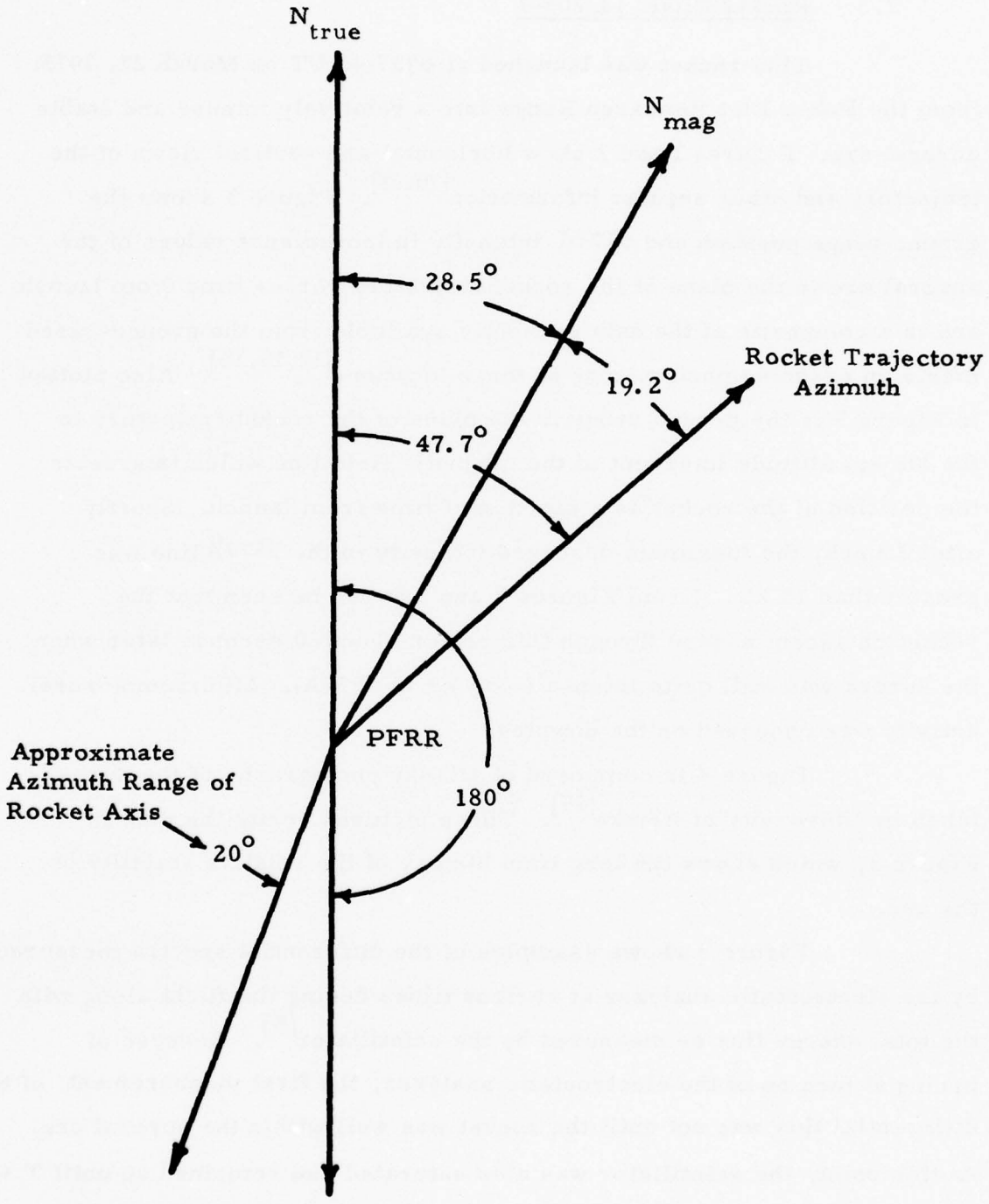

Figure 1 Rocket 18.205-1 Trajectory, Horizontal View

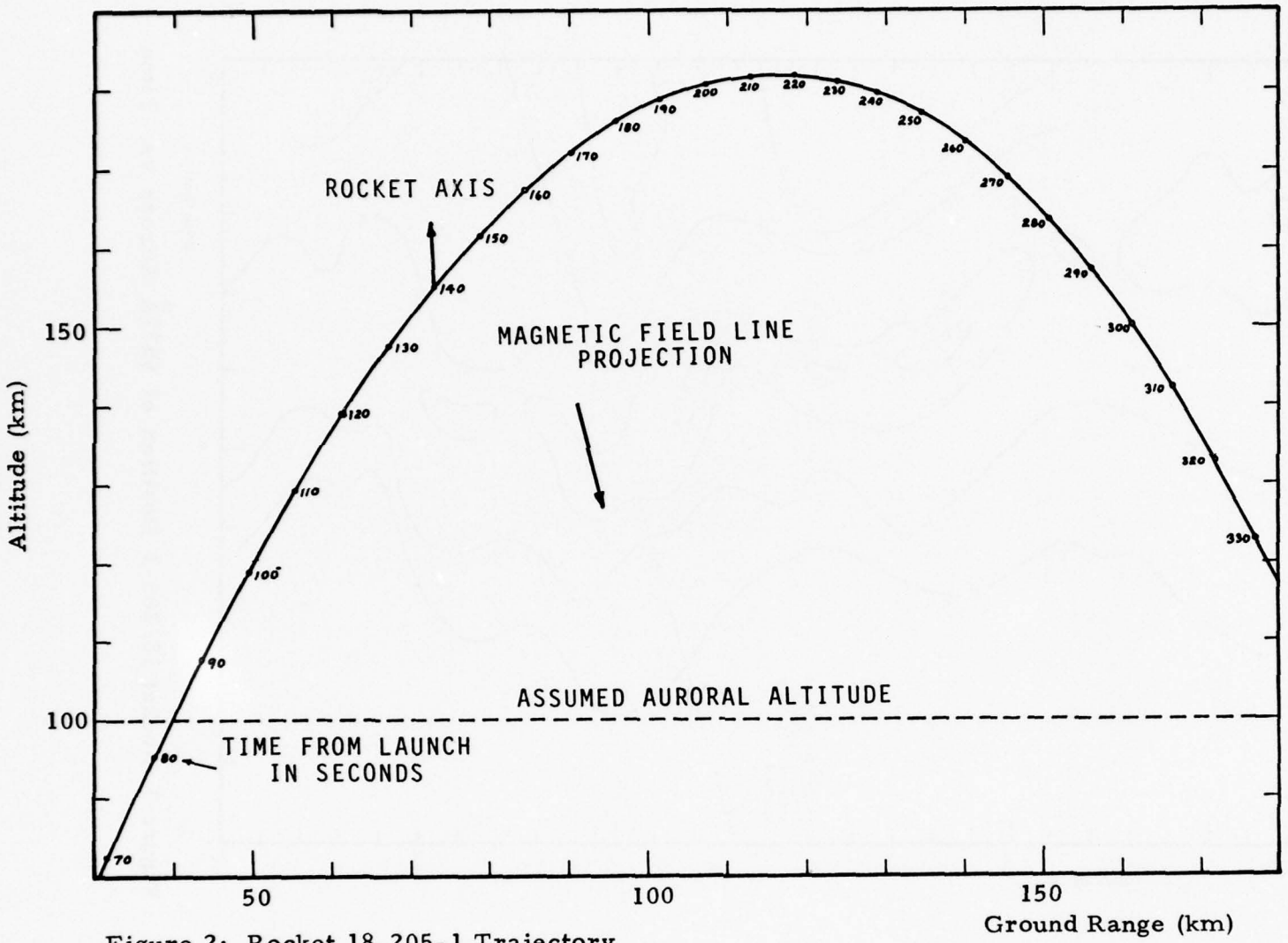

Figure 2: Rocket 18.205-1 Trajectory

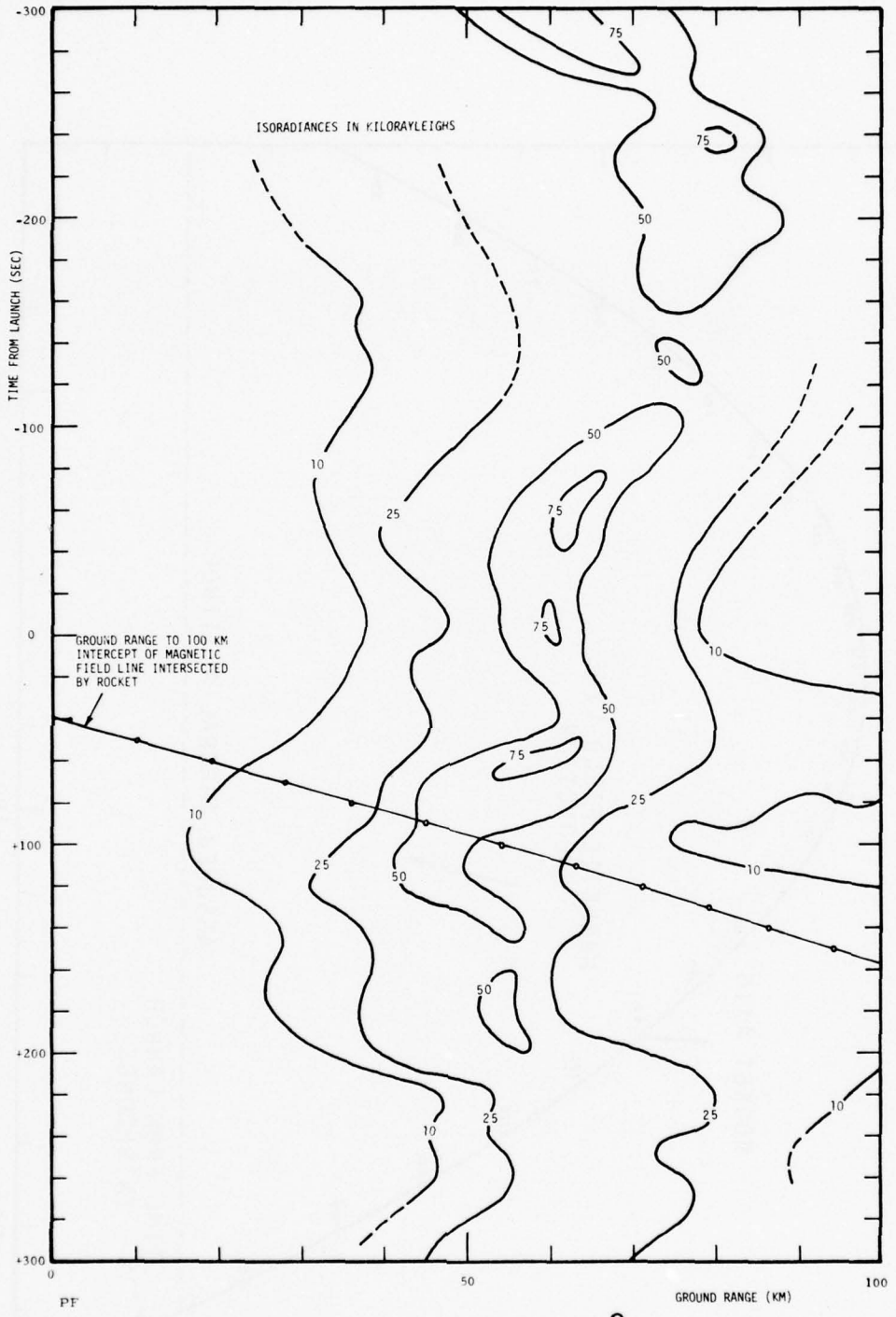

Figure 3 Rocket 18.205-1 Position of 5577Å Aurora vs. Time

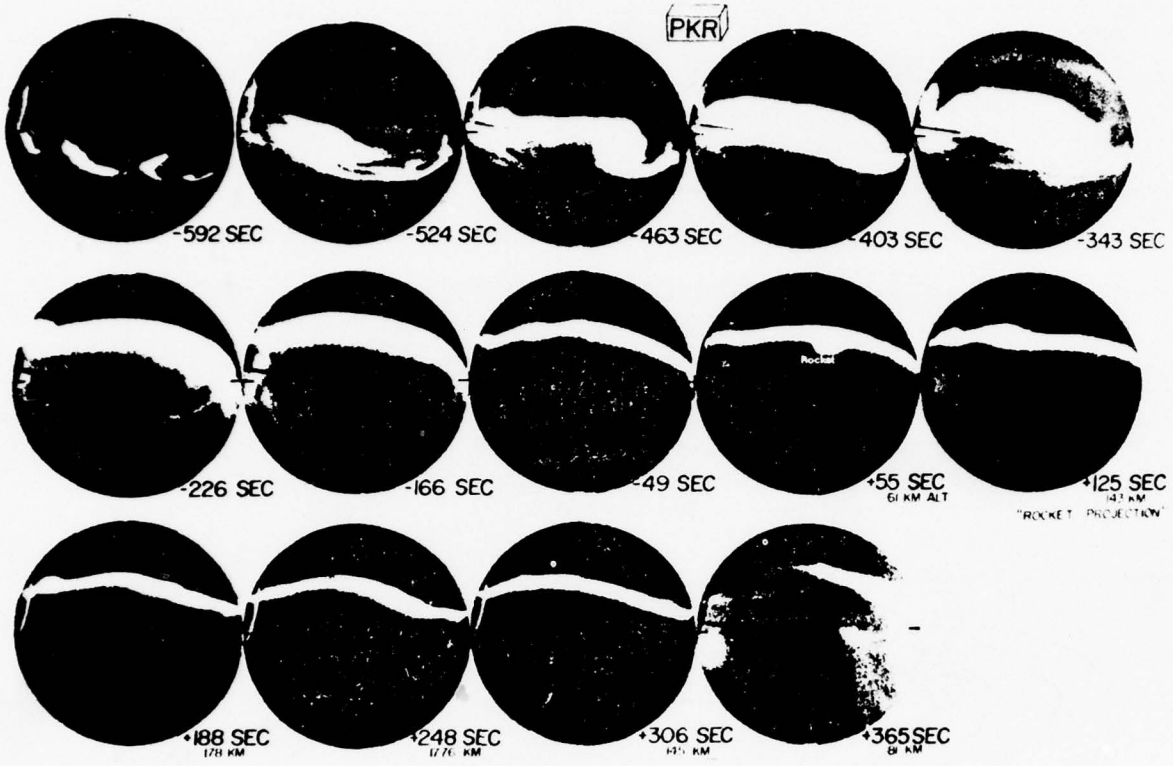

Figure 4 All-Sky Camera Photographs of Auroral Arc Associated With Rocket 18.205-1

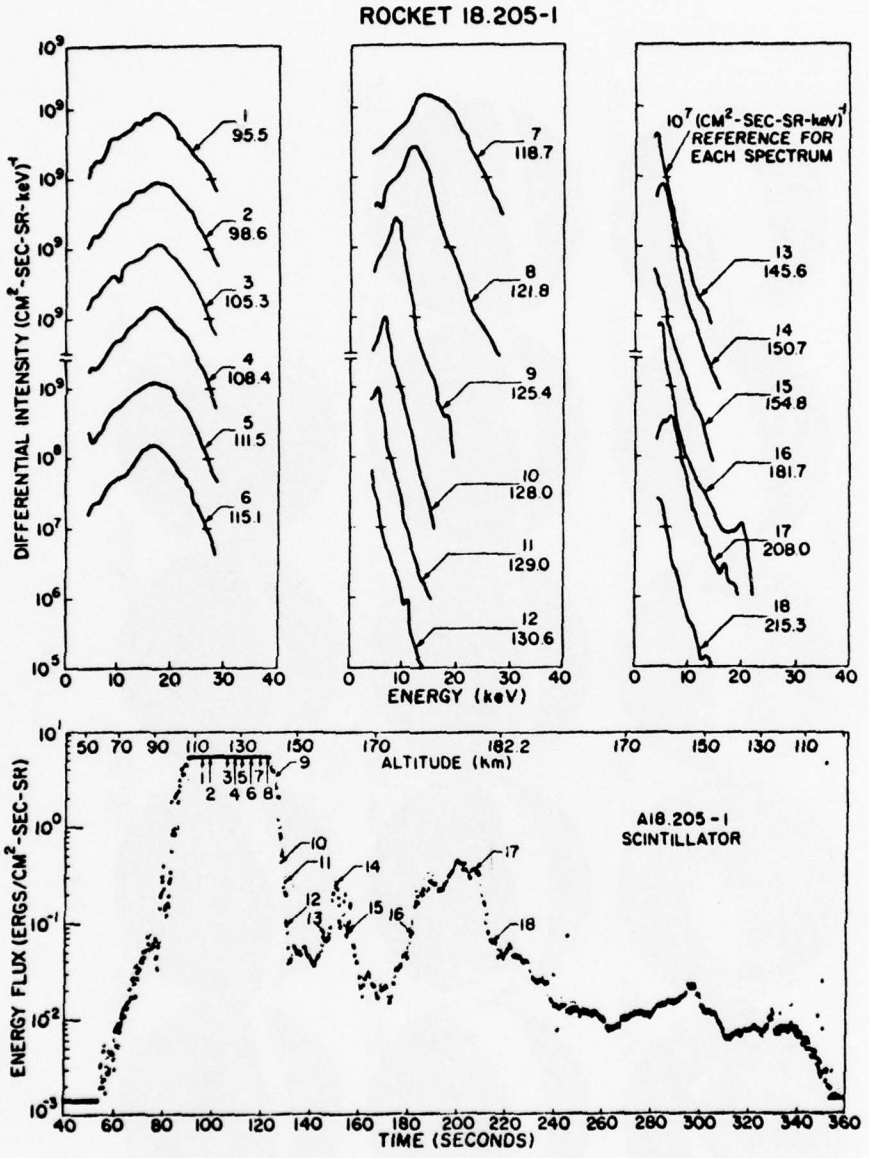

Figure 5 Rocket 18.205-1 Differential Electron Intensity Spectra and Energy Flux vs. Time

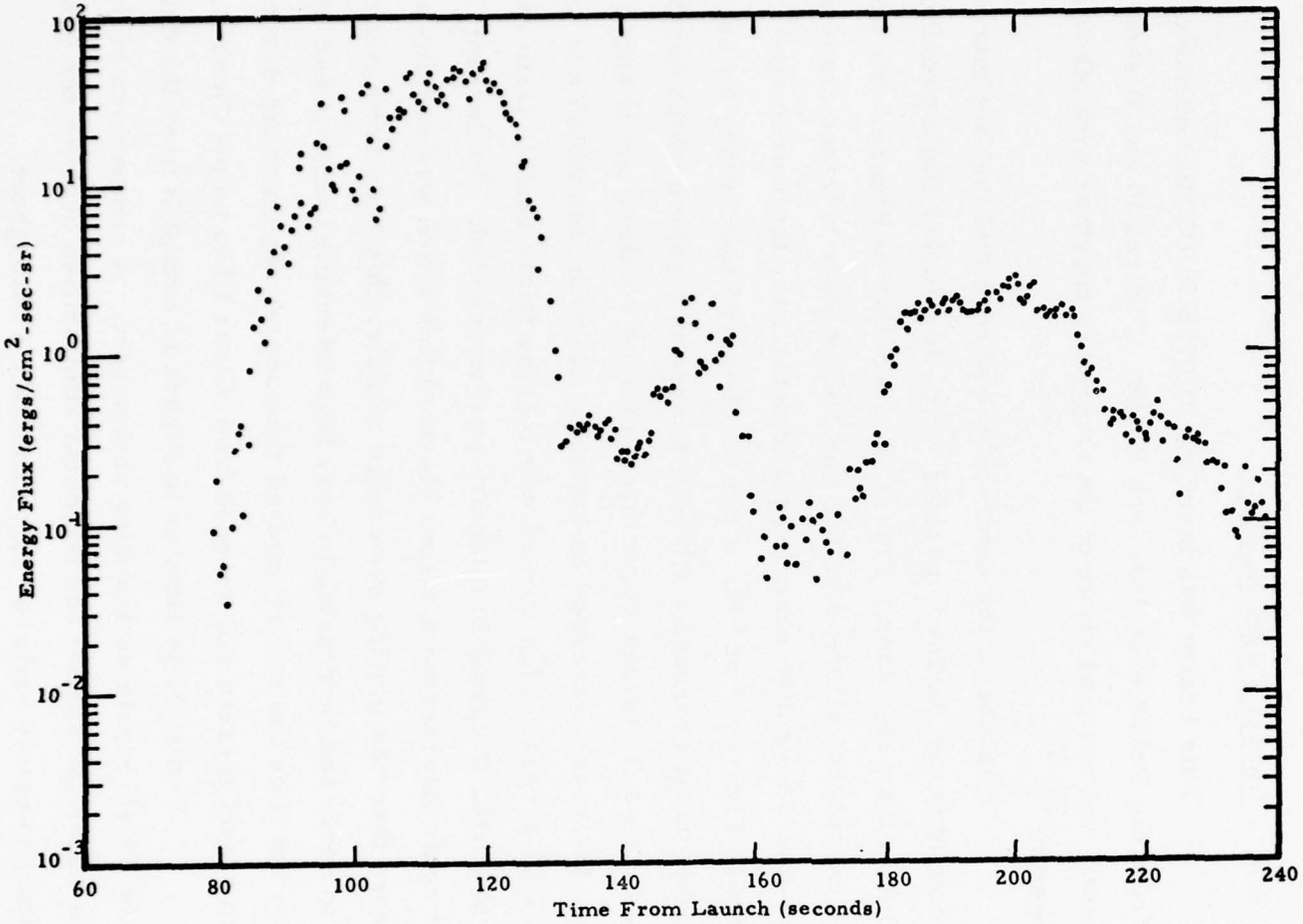

Figure 6 Rocket 18.205-1 Energy Flux from ESA Data vs. Time

Typical spectra of the SWIR CVF spectrometer are shown in Figures 7 and 8[17]. The peak spectral brightness as a function of rocket altitude is given in Figure 9 for the peak brightness of the IR bands and the brightness of 3914Å as measured by the various axially-mounted payload instruments[17, 18, 19]. The arrows indicate whether the data were taken on ascent or descent.

2.4 Rocket Flight 18.219-1

This rocket was launched at 0738:30 UT on February 25, 1974 from the Poker Flat Research Range. Figures 10 and 11 show horizontal and vertical views of the trajectory together with other angular information[20, 21].

Because of the nature of the aurora and the fact that the fully instrumented payload operated well, this rocket flight provided more useful data than any other. Figure 12 is similar to Figure 3 for the 18.205-1 rocket except that all the data for this rocket were obtained from the ground-based meridian scanning photometer near the launch site[8]. From the data in Figures 11 and 12, it can be observed that during its ascent, the rocket passed through a Class II aurora in a region which had been nearly a Class III aurora about three minutes earlier. As it approached apogee, the rocket recorded an incoming electron flux which was causing a Class III aurora. This aurora was moving fairly rapidly from magnetic north to south, dropping in intensity as it proceeded. On descent, the rocket again intercepted a strong electron flux which was causing a Class III aurora that was moving even more rapidly, this time from magnetic south to north and increasing to very high intensities after it had moved off. By the time the rocket entered the auroral region on its descent, the intensity level therein had dropped from Class III to below Class II.

Figure 13 is similar to Figure 12 except it uses the data from the 3914Å meridian scanning photometer. A comparison of the two figures shows the spatial and temporal similarities between the two with a constant intensity ratio of approximately 2 throughout.

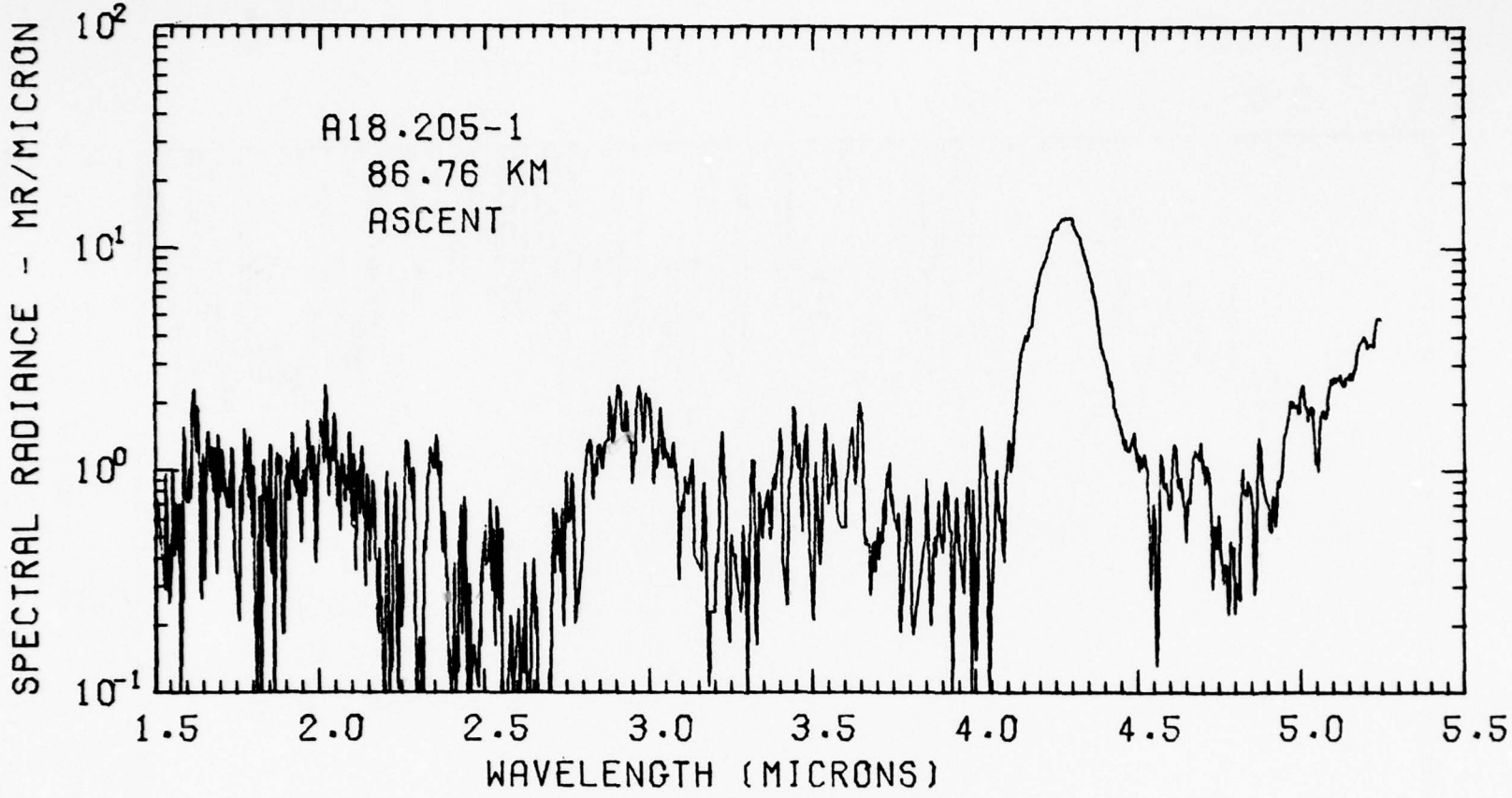

Figure 7 Rocket 18.205-1 CVF Spectrometer Scan, Ascent

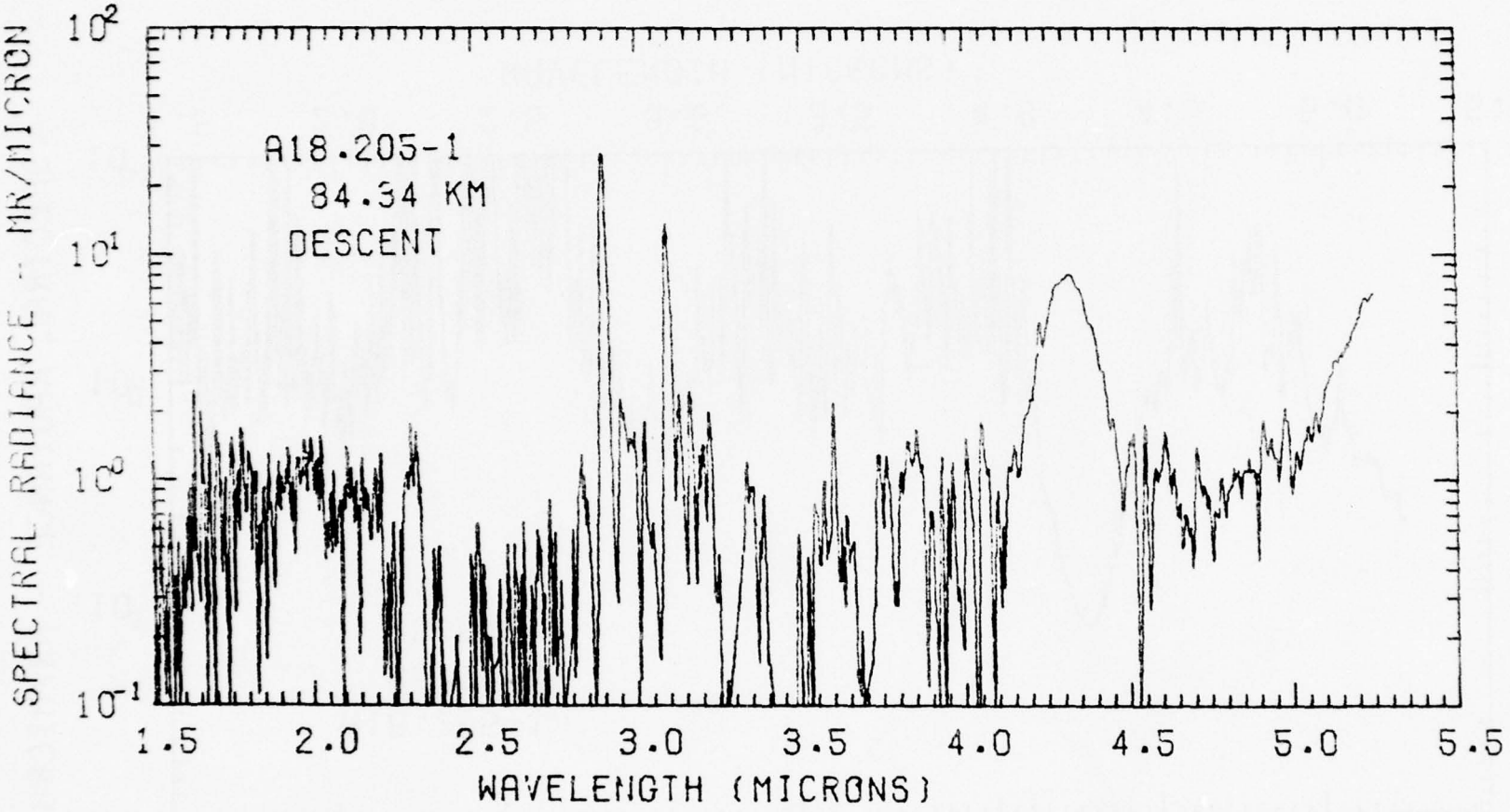

Figure 8 Rocket 18.205-1 CVF Spectrometer Scan, Descent

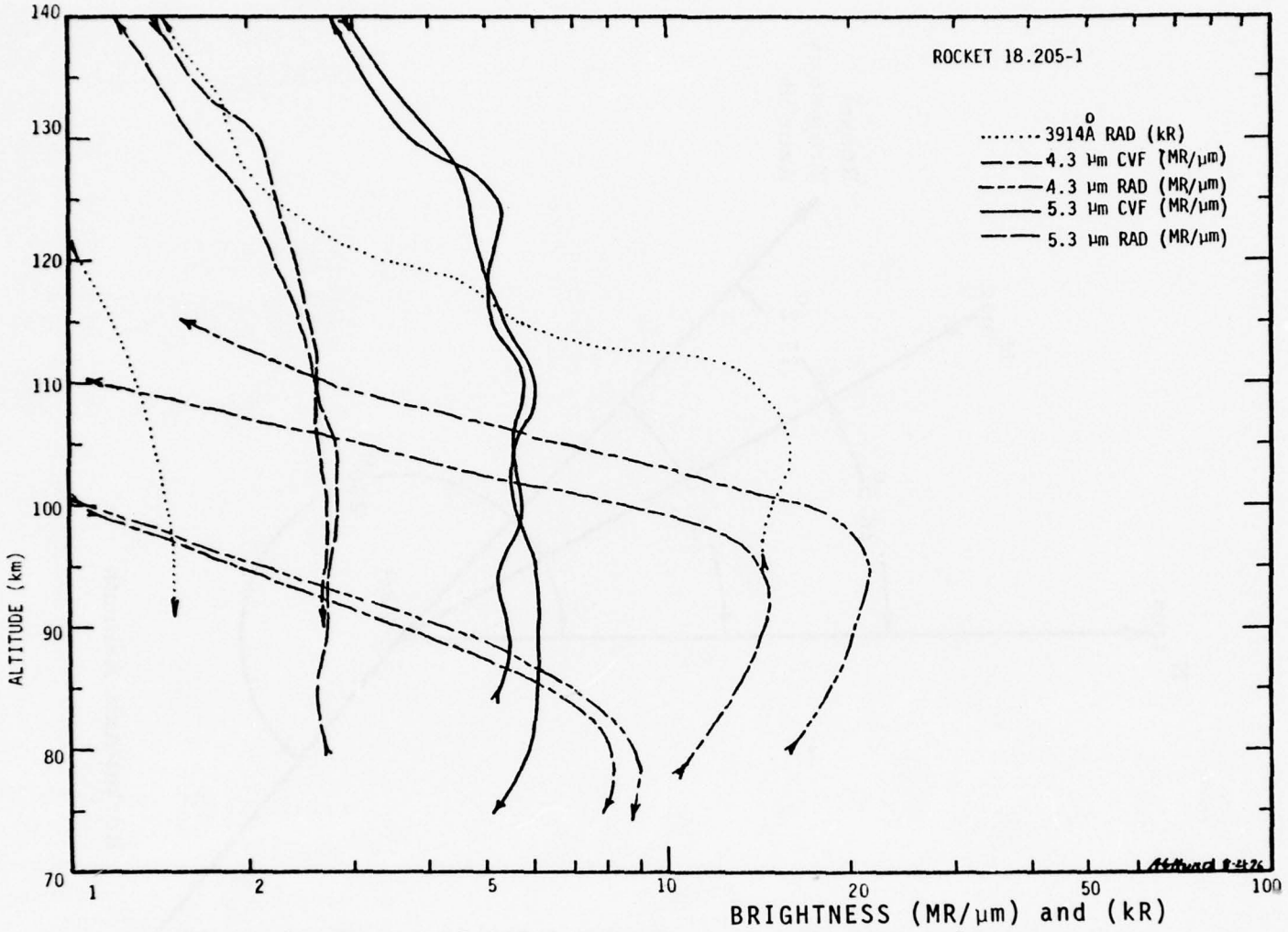

Figure 9 Rocket 18.205-1 Data From Axially-Mounted Instruments

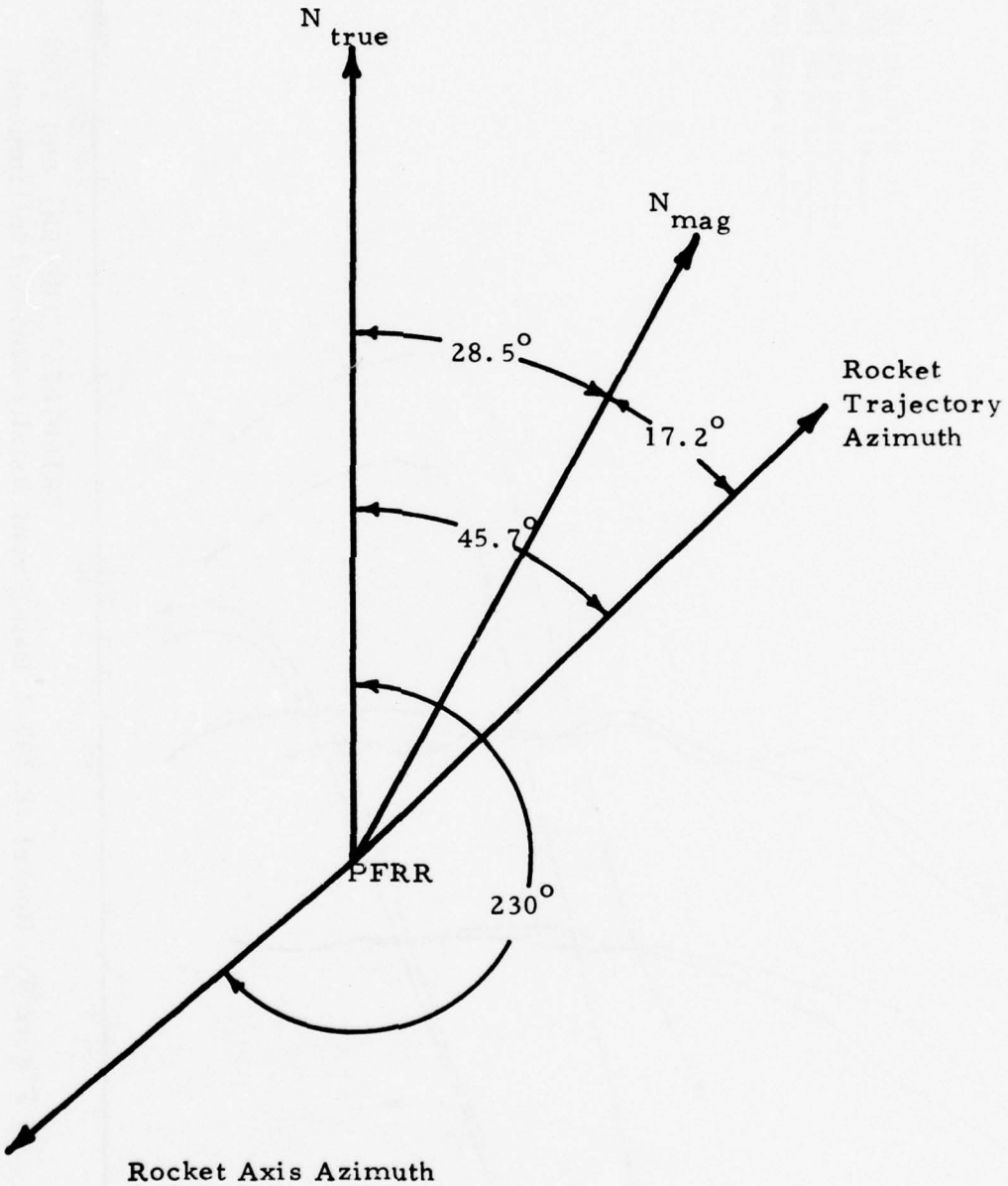

Figure 10 Rocket 18.219-1 Trajectory, Horizontal View

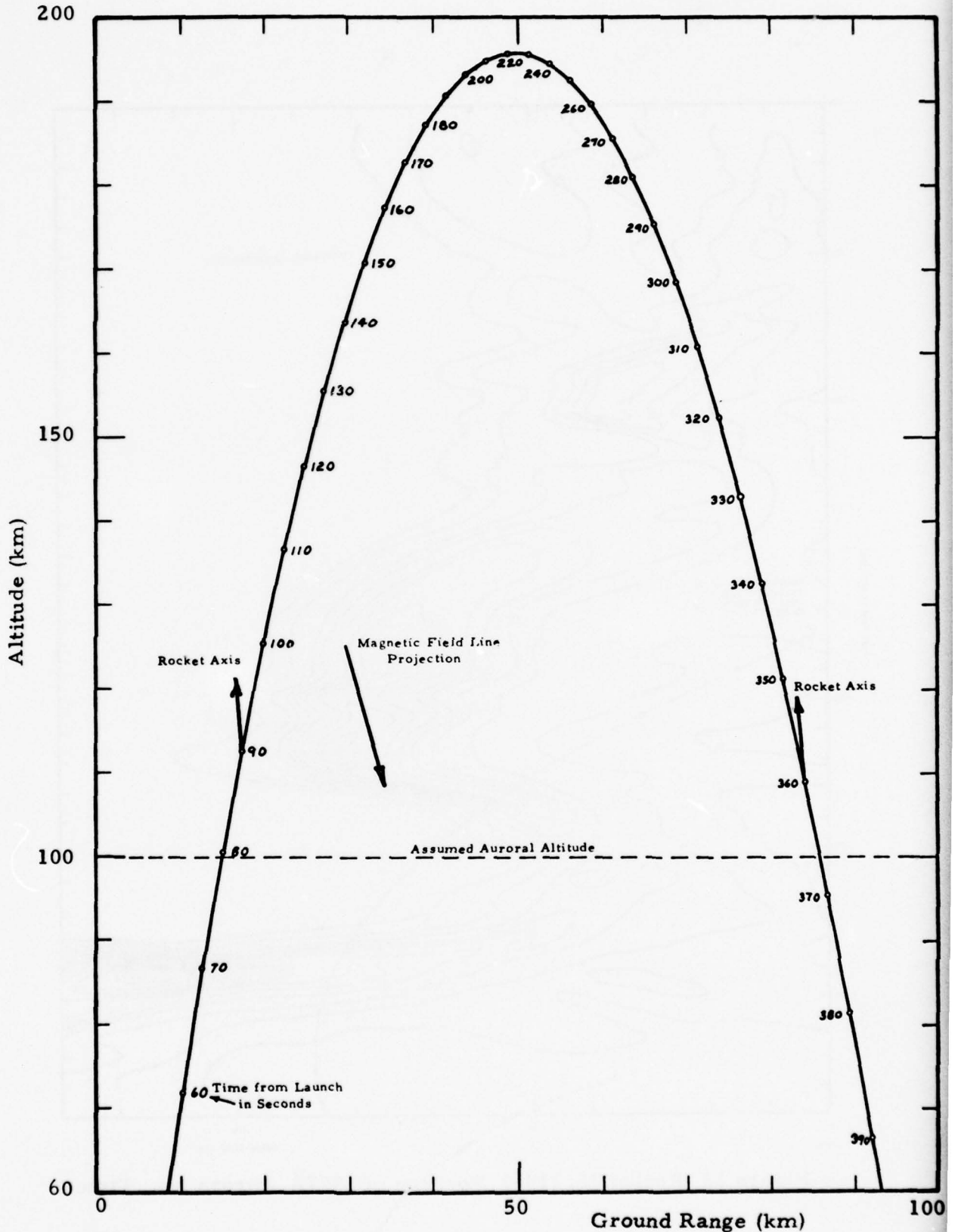

Figure 11: Rockét 18.219-1 Trajectory

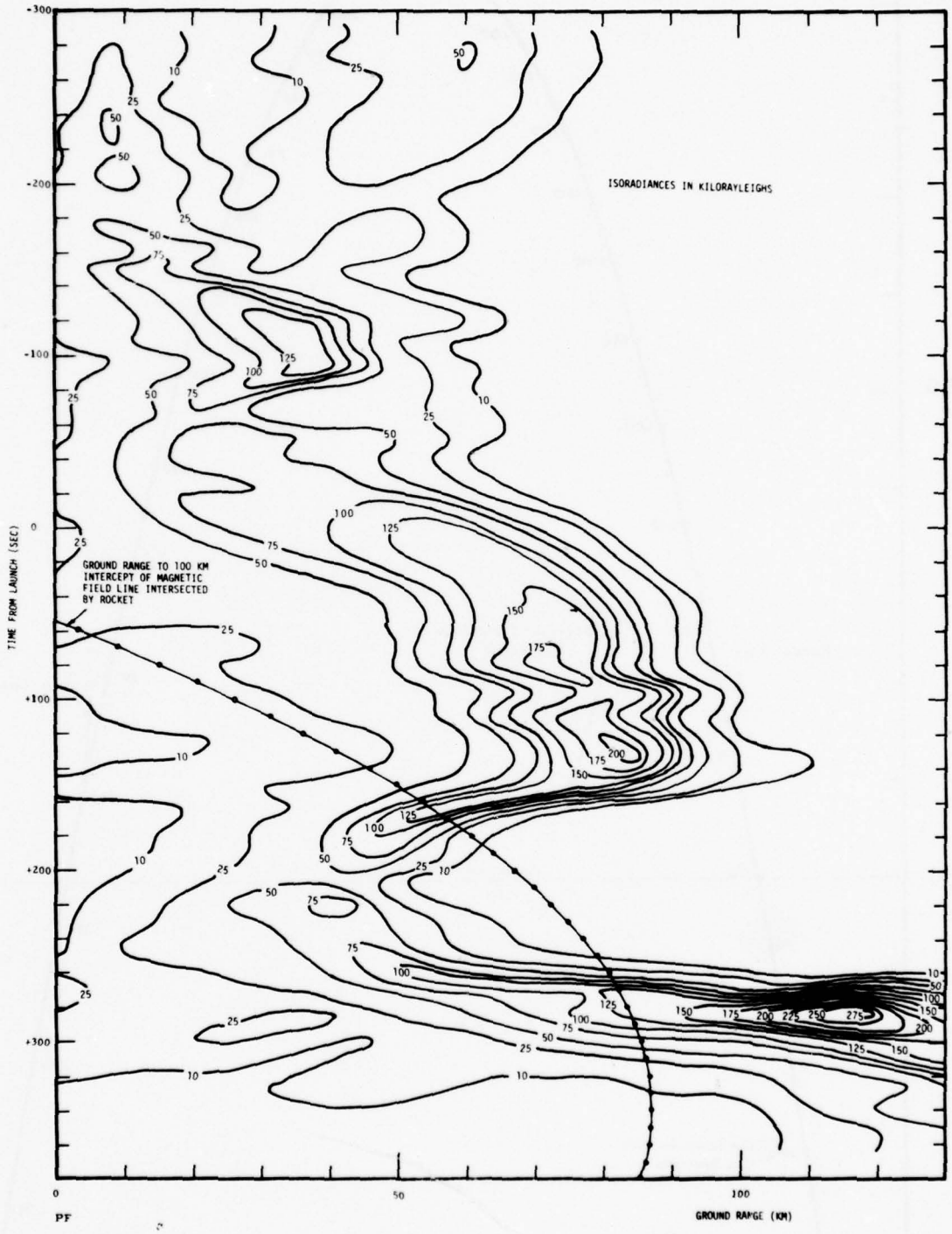

Figure 12 Rocket 18.219-1 Position of 5577Å Aurora vs. Time

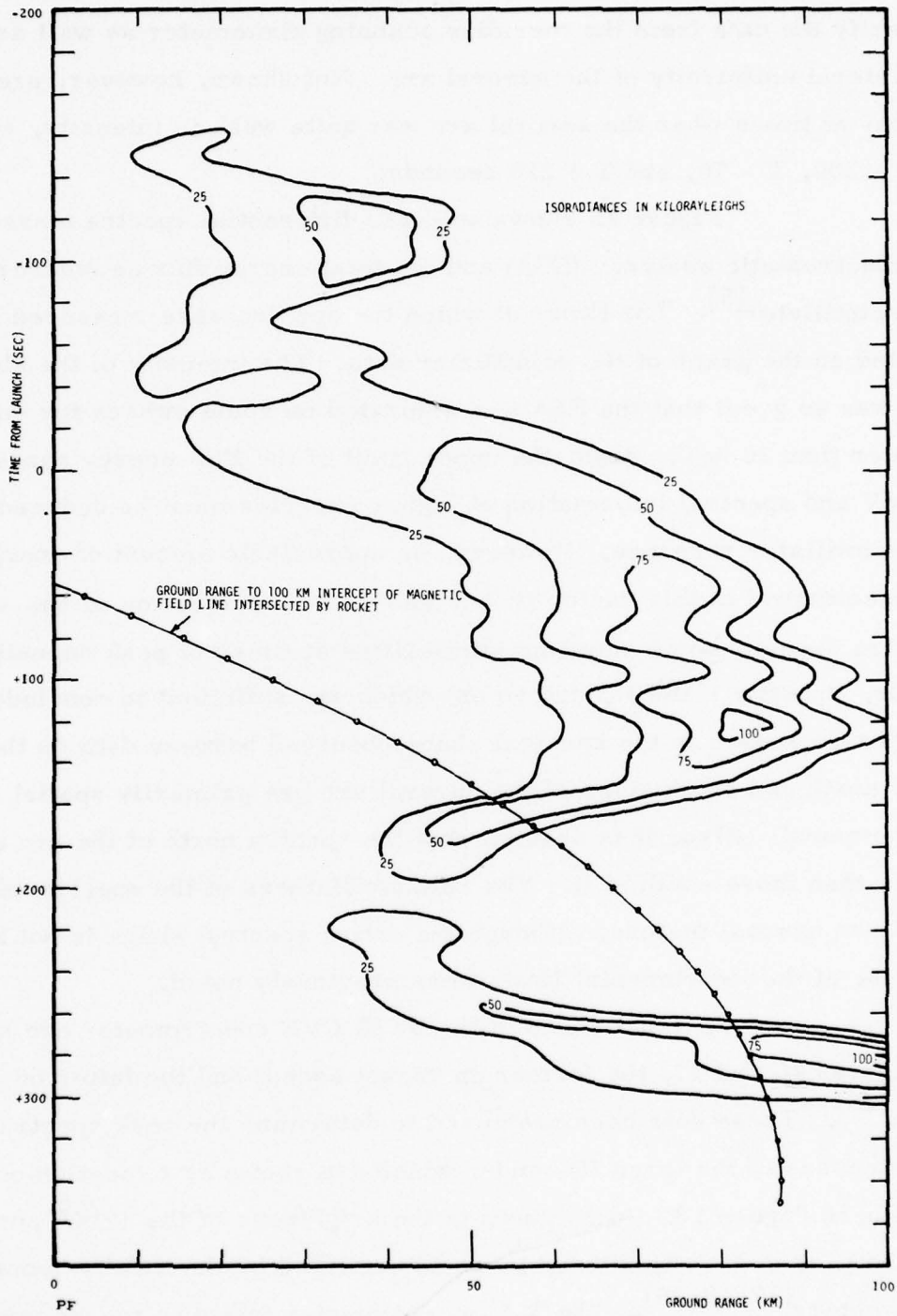

Figure 13 Rocket 18.219-1 Position of 3914Å Aurora vs. Time

Figure 14 shows some of the all-sky photographs of the auroral arc as taken by the camera near the launch site[22]. These tend to verify the data from the meridian scanning photometer as well as showing the lateral uniformity of the auroral arc. Not shown, however, are photographs at times when the auroral arc was quite weak in intensity, such as at T - 200, T - 70, and T + 210 seconds.

Figure 15 shows selected differential spectra measured by the electrostatic analyzer (ESA) and the total energy flux as measured by the scintillator[5]. The times at which the spectra were measured are indicated on the graph of the scintillator data. The intensity of the electron flux was so great that the ESA was saturated on some sweeps for energies greater than 20 keV. Also, the upper limit of the ESA energy range is 30 keV and spectral information at higher energies must be deduced from the scintillator response. However, an appreciable amount of energy appears to be contained in this region ($E > 30$ keV). An examination of the various spectra reveals some startling similarities at times of peak deposition (for example, spectra 1 and 1', and so on) which are sufficient to conclude that the gross changes in the spectral shape observed between data on the magnetic north and south sides of the auroral arc are primarily spatial and not temporal. Also, it is obvious that the spectra north of the arc are much softer than those south of it. The relative flatness of the spectra within the arc is an unusual feature, although the entire spectral shape is not known because of the instrumental limitations previously noted.

Spectral scans of the SWIR CVF spectrometer are shown in Figures 16 and 17, the former on rocket ascent and the latter on descent[23]. These data have been used to determine the peak spectral brightnesses of the three IR bands, which are shown as a function of altitude in Figure 18. Also shown is the brightness of the 3914Å aurora and the peak 4.3 m band brightness as recorded by the axially-mounted radiometers[17, 19, 24]. The 5.3 m radiometer failed to record any data. Above 115 kilometers onupleg, the rocket motor moved within the field of view of the vertical looking CVF. Much of the CVF data on the upleg tra-

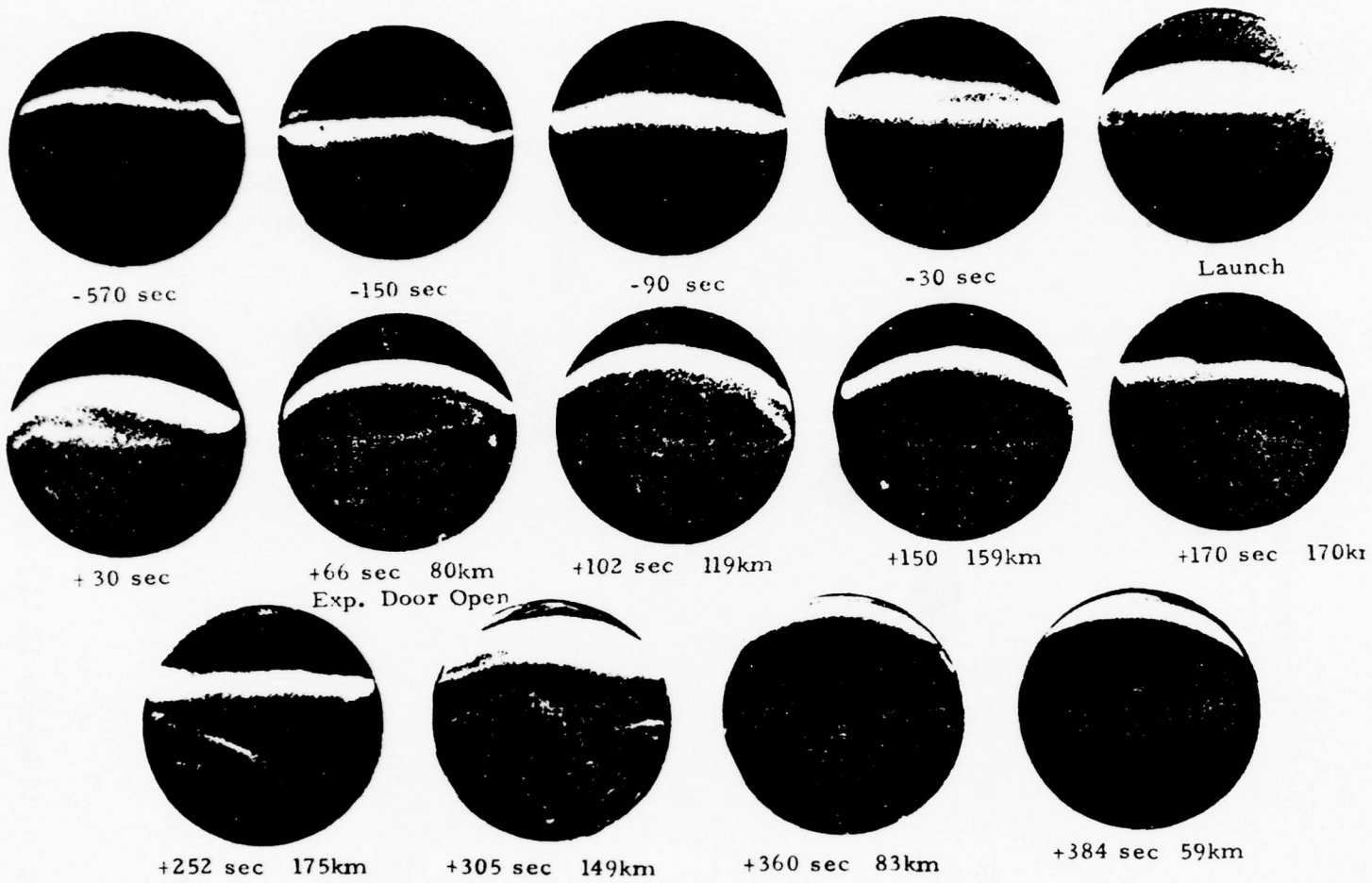

Figure 14 All-Sky Camera Photographs of Auroral Arc Associated With Rocket 18.219-1

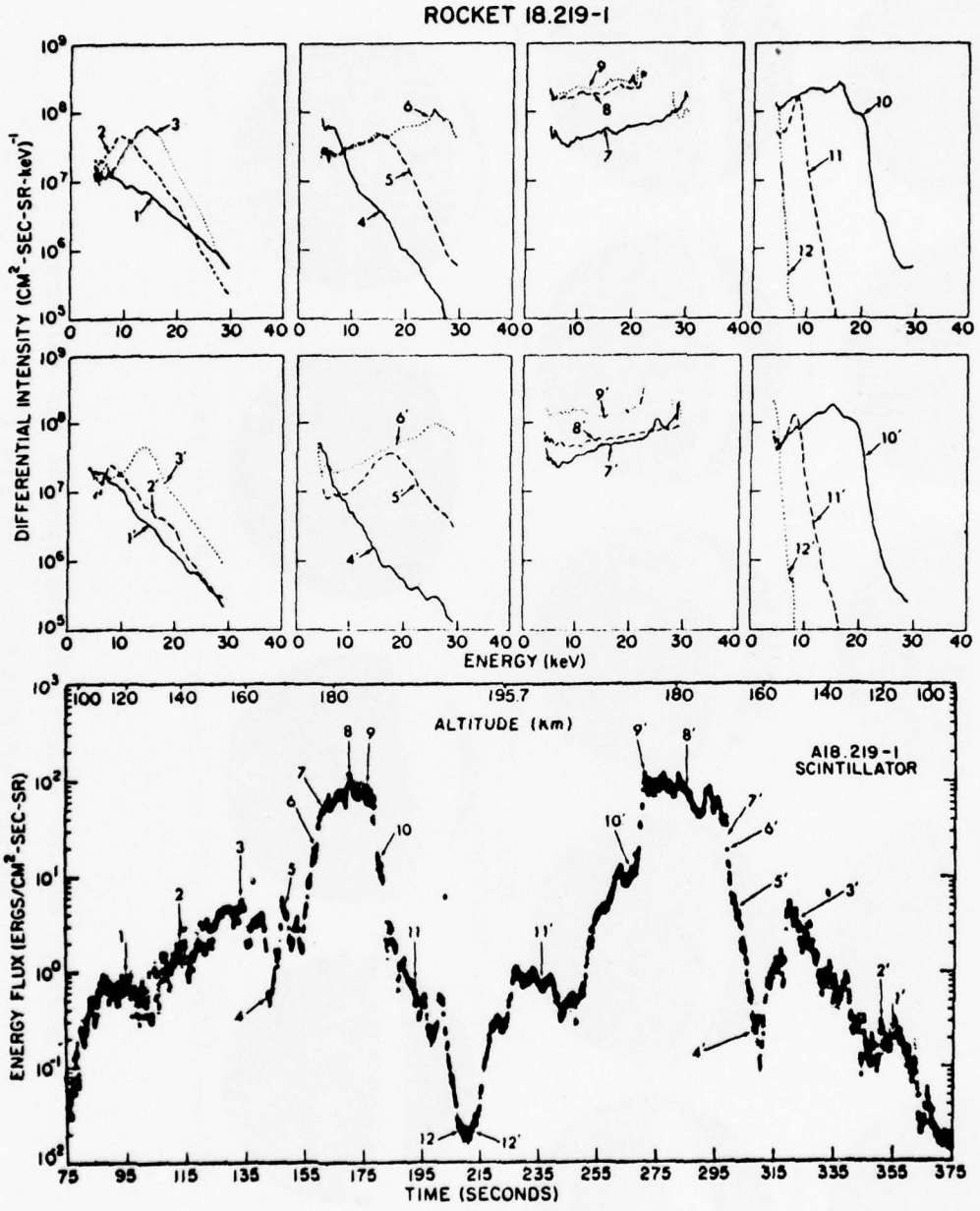

Figure 15 Rocket 18.219-1 Differential Electron Intensity Spectra and Energy Flux vs. Time

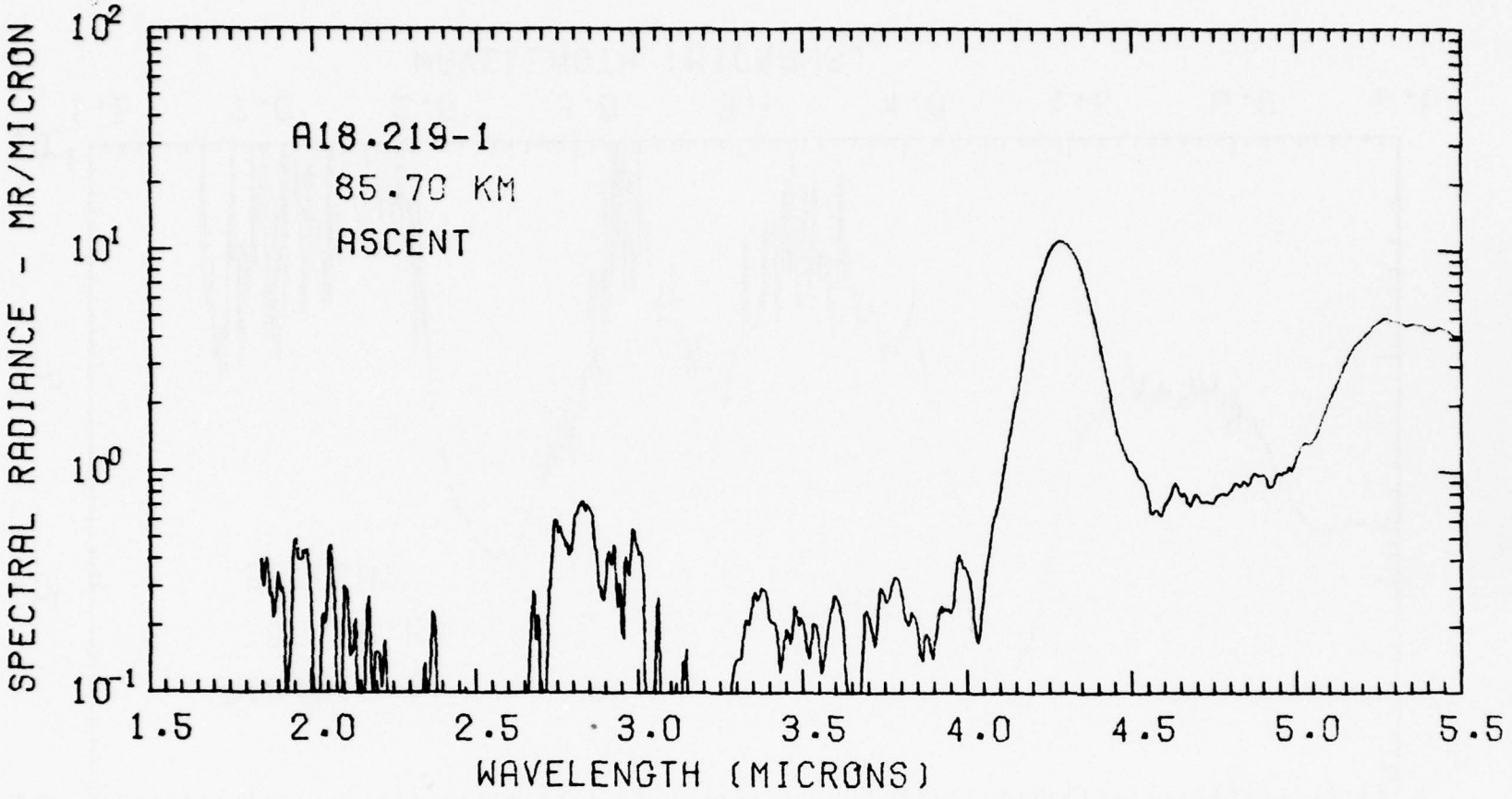

Figure 16 Rocket 18.219-1 CVF Spectrometer Scan, Ascent

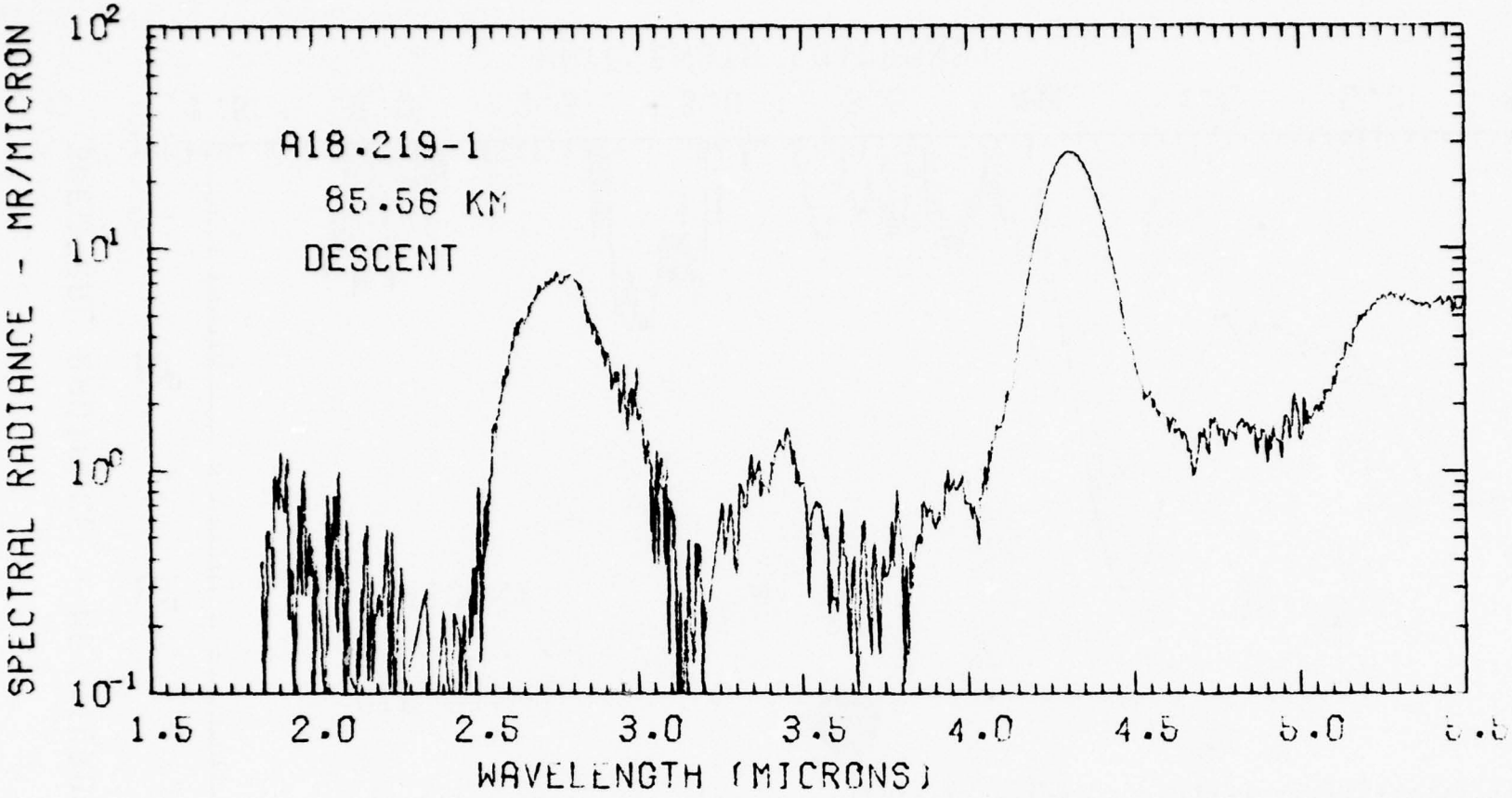

Figure 17 Rocket 18.219-1 CVF Spectrometer Scan, Descent

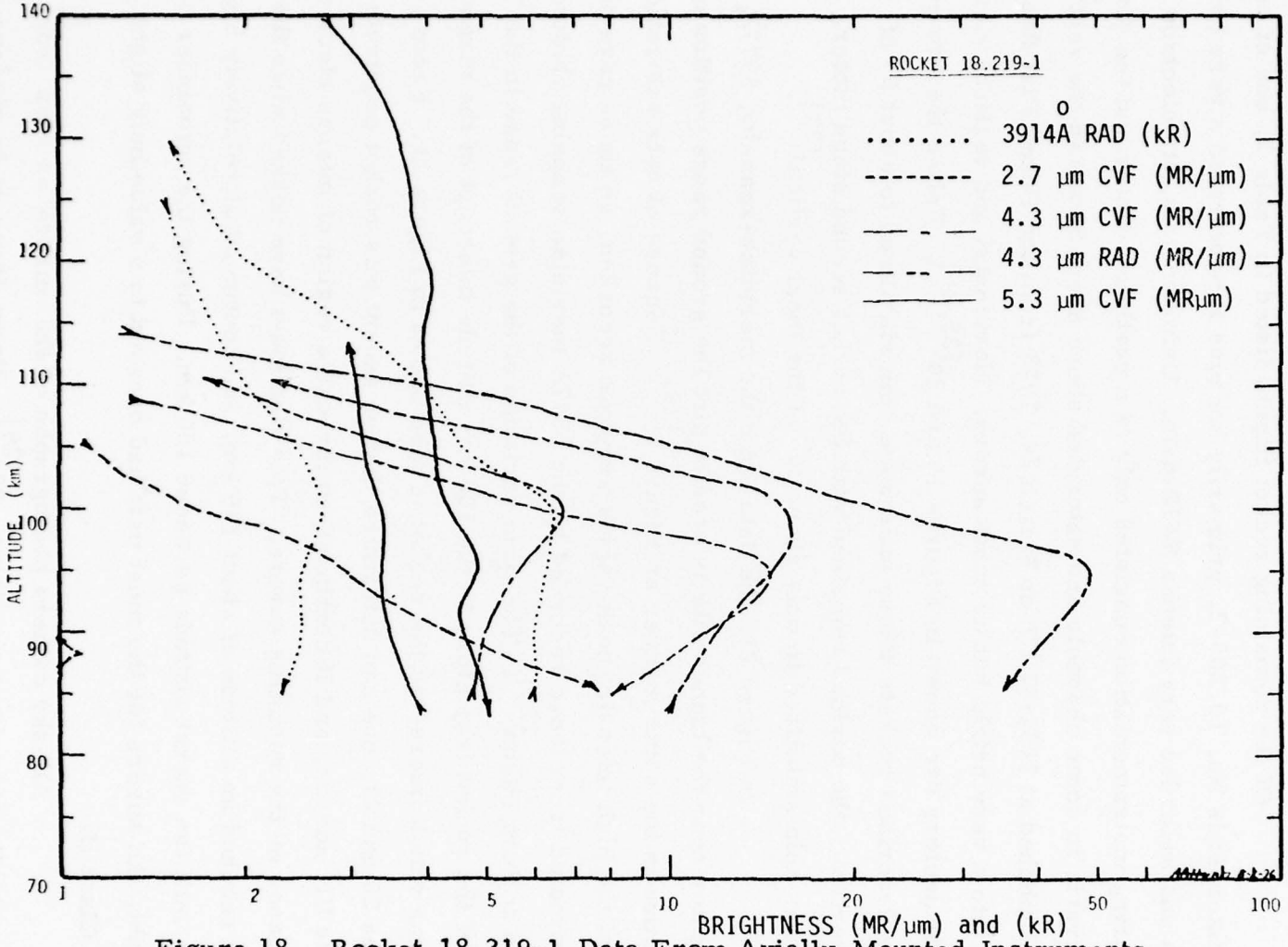

Figure 18 Rocket 18.219-1 Data From Axially-Mounted Instruments

jectory was degraded and the anomalously intense 2.7 μm emission observed on downleg below 105 kilometers appears to be an artifact of the experiment.

2.5 Rocket Flight 10.205-2

Of the remaining rocket flights listed in Table 1, one of particular interest is No. 10.205-2, primarily because it penetrated a very bright aurora and recorded very intense SWIR data. Unfortunately, its electron monitoring instrumentation consisted only of a particle counter and the data was erratic in some channels and saturated above about 80 km in the rest[16]. It was launched at 1031:42 UT on March 24, 1973 from the Poker Flat Research Range into a very bright but unstable aurora. Horizontal and vertical views of the trajectory are shown in Figures 19 and 20[25, 26]. Unlike the two previously described rockets whose axes were spin stabilized to about 5° of local vertical, the payload remained with the rocket second stage motor, which was spin stabilized to only about 30° of the local vertical[27].

In Figure 21, the data from the meridian-scanning 5577Å photometer near the launch site is used to plot the ground range position of the aurora in the same manner as Figure 3[28]. Because of data saturation, many of the high intensity peak values were not recorded, so these have been approximated from those recorded by the 5577Å meridian scanning photometer located at Fort Yukon[29]. The time variation of the ground range in the plane of the rocket trajectory to the 100 km altitude intercept of the magnetic field line which intersects the rocket is also shown in Figure 21. From Figures 20 and 21, one can determine that on ascent this rocket penetrated a Class III$^+$ aurora, and it continued on through a region of intense electron flux, based on the resulting aurora. This flux must have peaked when the rocket reached an altitude of about 130 km, and continued at relatively high values until the rocket altitude exceeded 150 km. During the remainder of its flight, the aurora for the most part had decayed to a value only slightly above Class II.

All-sky camera photographs of the aurora as seen from near the launch site are shown in Figure 22[29]. From these it is obvious that

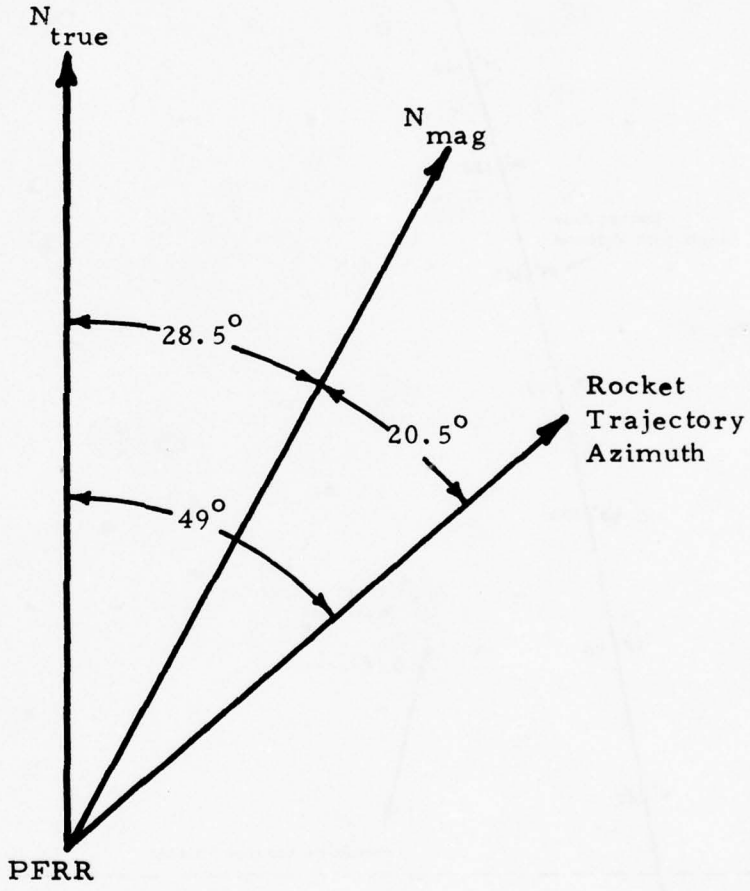

Figure 19 Rocket 10.205-2 Trajectory, Horizontal View

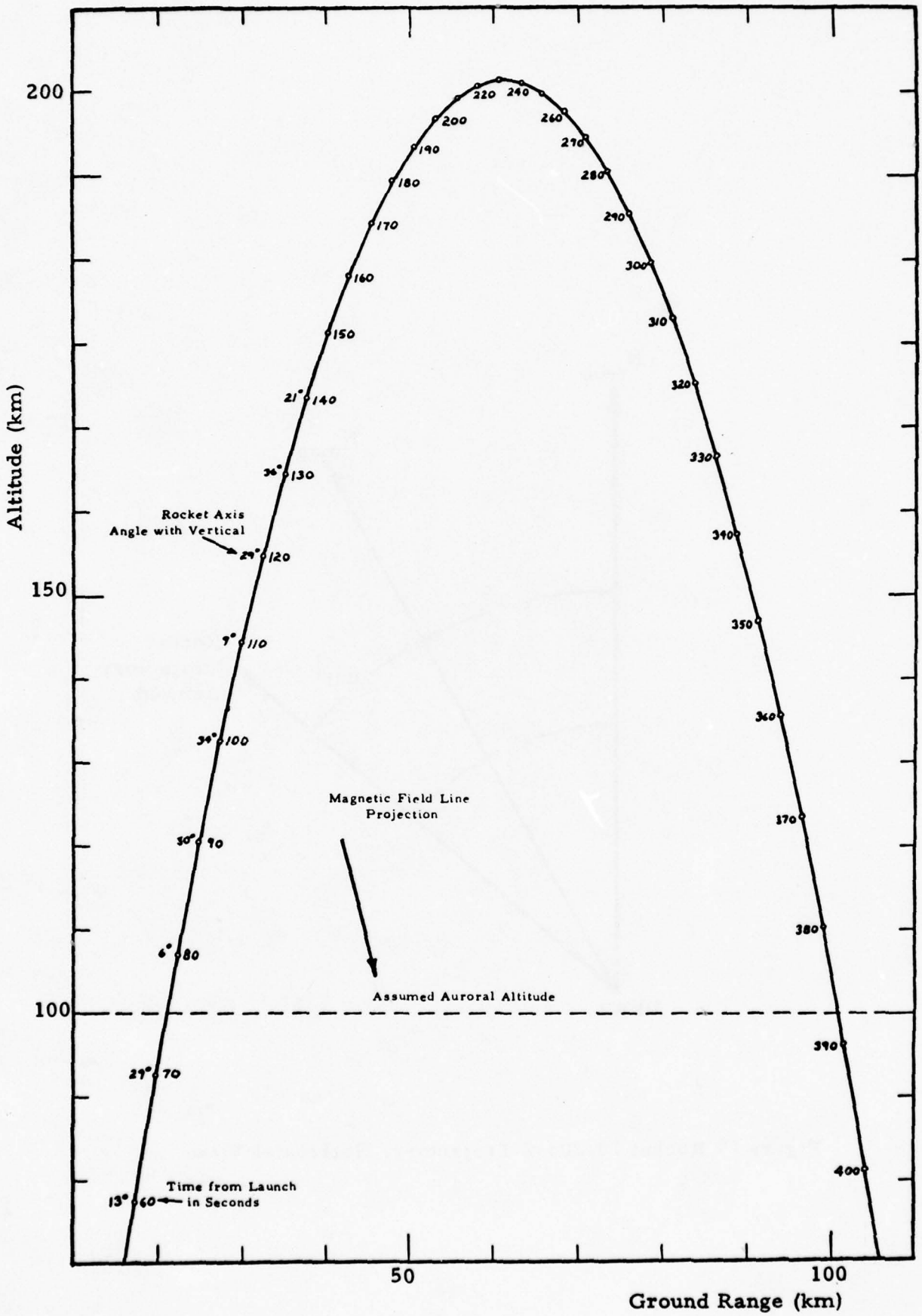

Figure 20: Rocket 10.205-2 Trajectory

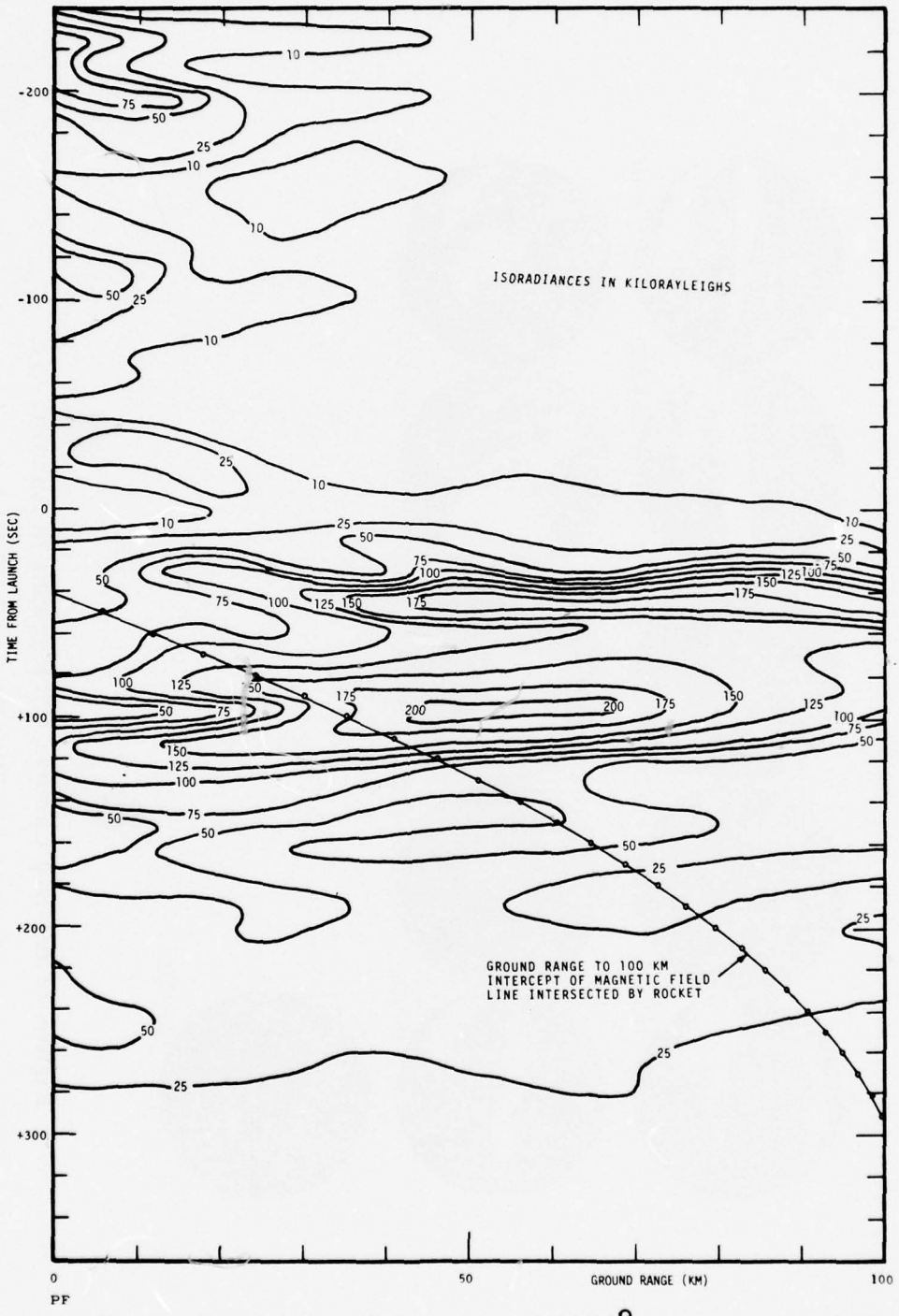

Figure 21 Rocket 10.205-2 Position of 5577Å Aurora vs. Time

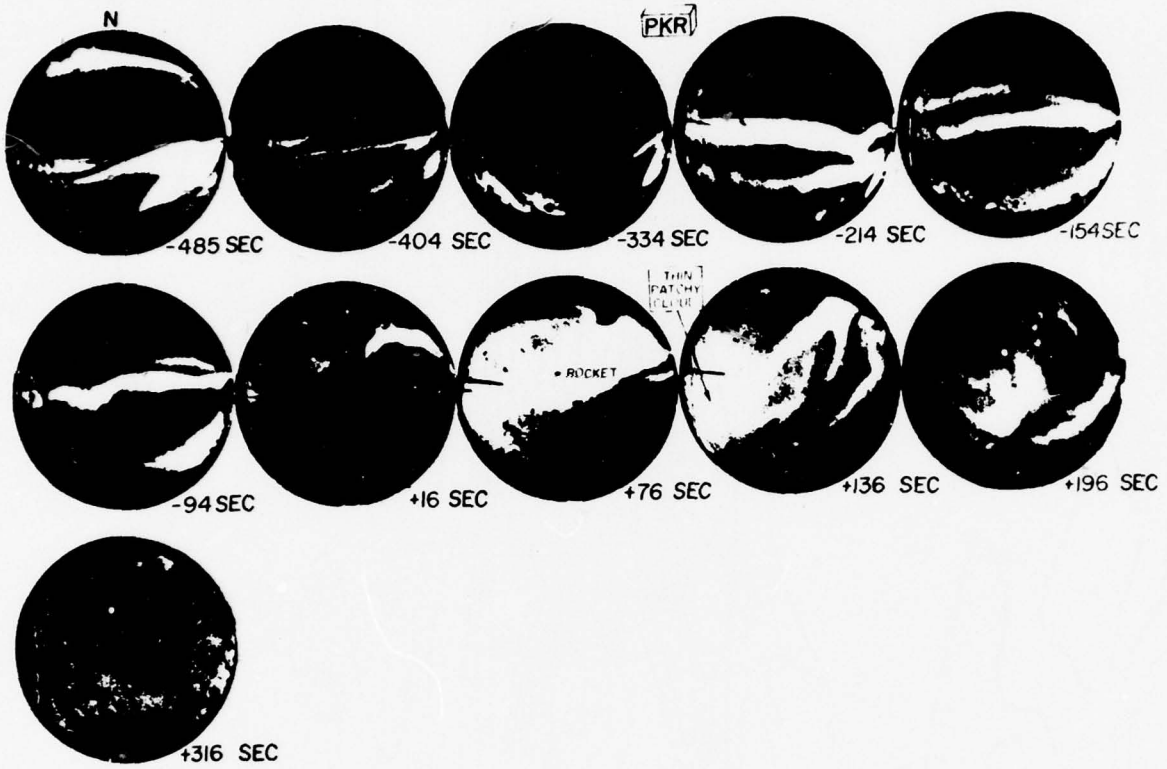

Figure 22 All-Sky Camera Photographs of Auroral Arc Associated With Rocket 10.205-2

the aurora is rarely, if ever, a uniform arc. Nevertheless, for the times when the rocket is penetrating it, say at T + 76 sec., the aurora appears to be broadly dispersed as well as very intense. It would seem plausible, then, to use the auroral data in Figure 21 to calculate the theoretical IR radiance once the other required relationships have been determined.

A sample spectral scan from the SWIR CVF spectrometer is shown in Figure 23, taken during the rocket ascent[30]. From such scans, the peak spectral brightness of the three IR bands have been determined as shown in Figure 24 for the 2.7, 4.3, and 5.3μm bands. The data from the axially-mounted 3914Å radiometer arc are also shown[23]. Saturation occurred during ascent from about 80 to 100 km.

2.6 Other Rocket Flights

Rocket A17.110-3, carrying a fully instrumented payload, was launched from Poker Flat Research Range on March 16, 1972 at about 17:00 MLT. Unfortunately, the auroral arc remained north of the rocket until approximately 100 km altitude on descent, and the rocket never penetrated the main arc. However, during the entire flight, some good low-level electron data were recorded in the diffuse auroral region surrounding the arc[31].

Additional rocket probes carrying SWIR instrumentation launched into aurorally quiet regions included NJ74-1 and IC519.07-1B (see Table 1). The variation with altitude of the peak brightnesses of the 4.3 and 5.3μm bands as determined from the spectrometer data of NJ74-1 is shown in Figure 25[24].

A large number of other rockets have made measurements of auroral electrons, but these have not included SWIR instrumentation and were involved with IBC II or less auroras[32].

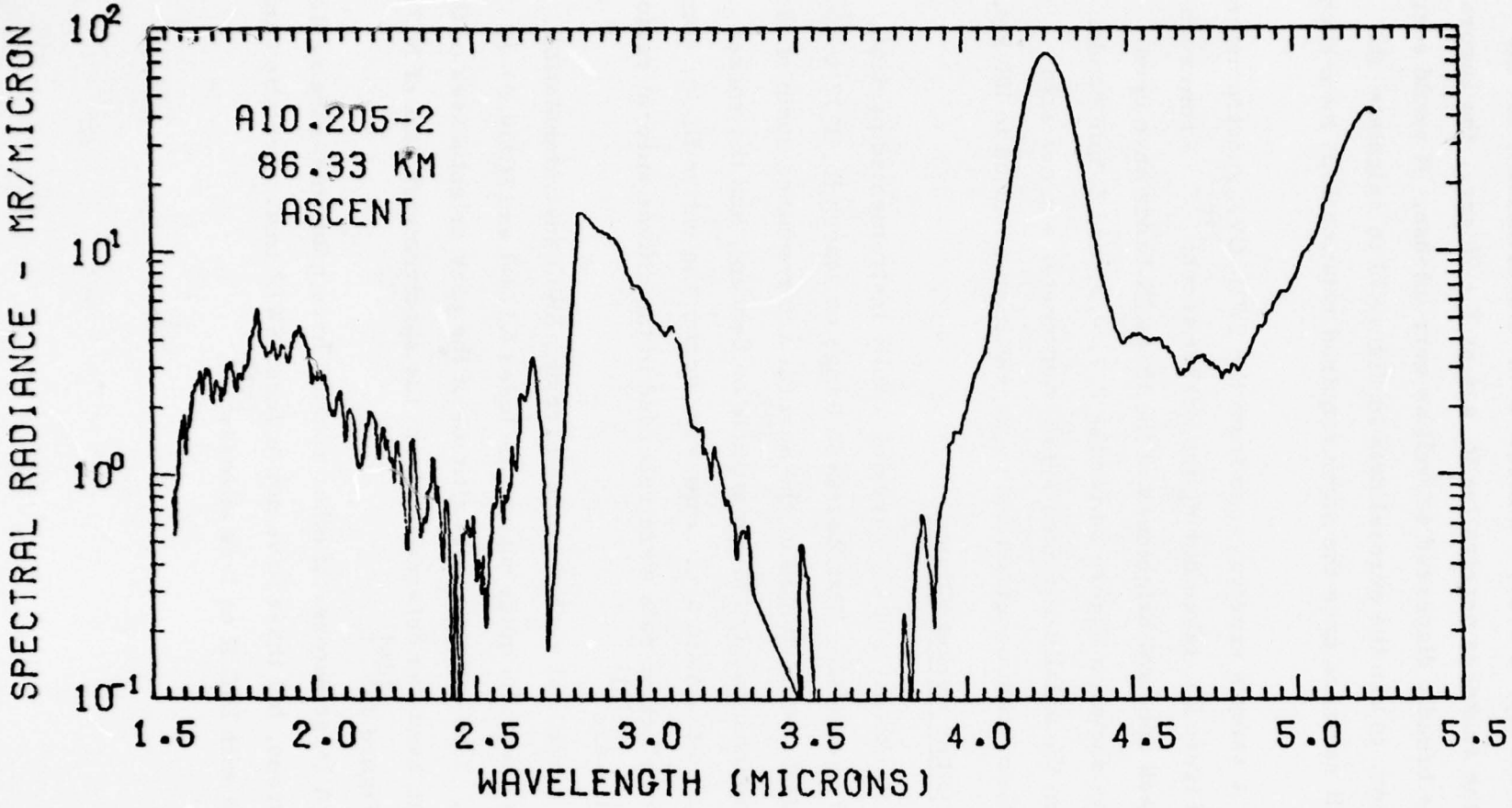

Figure 23 Rocket 10.205-2 CVF Spectrometer Scan, Ascent

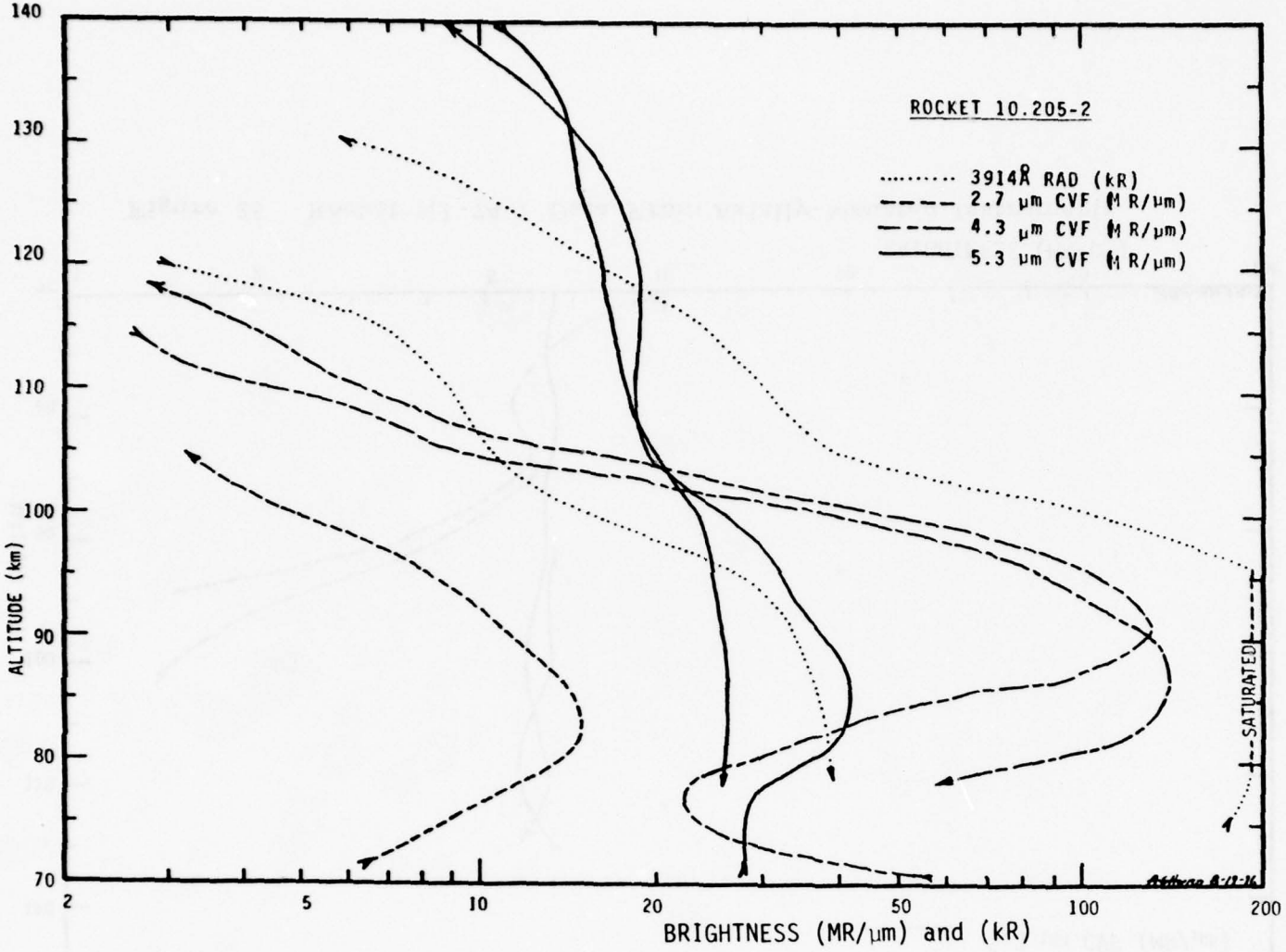

Figure 24 Rocket 10.205-2 Data From Axially-Mounted Instruments

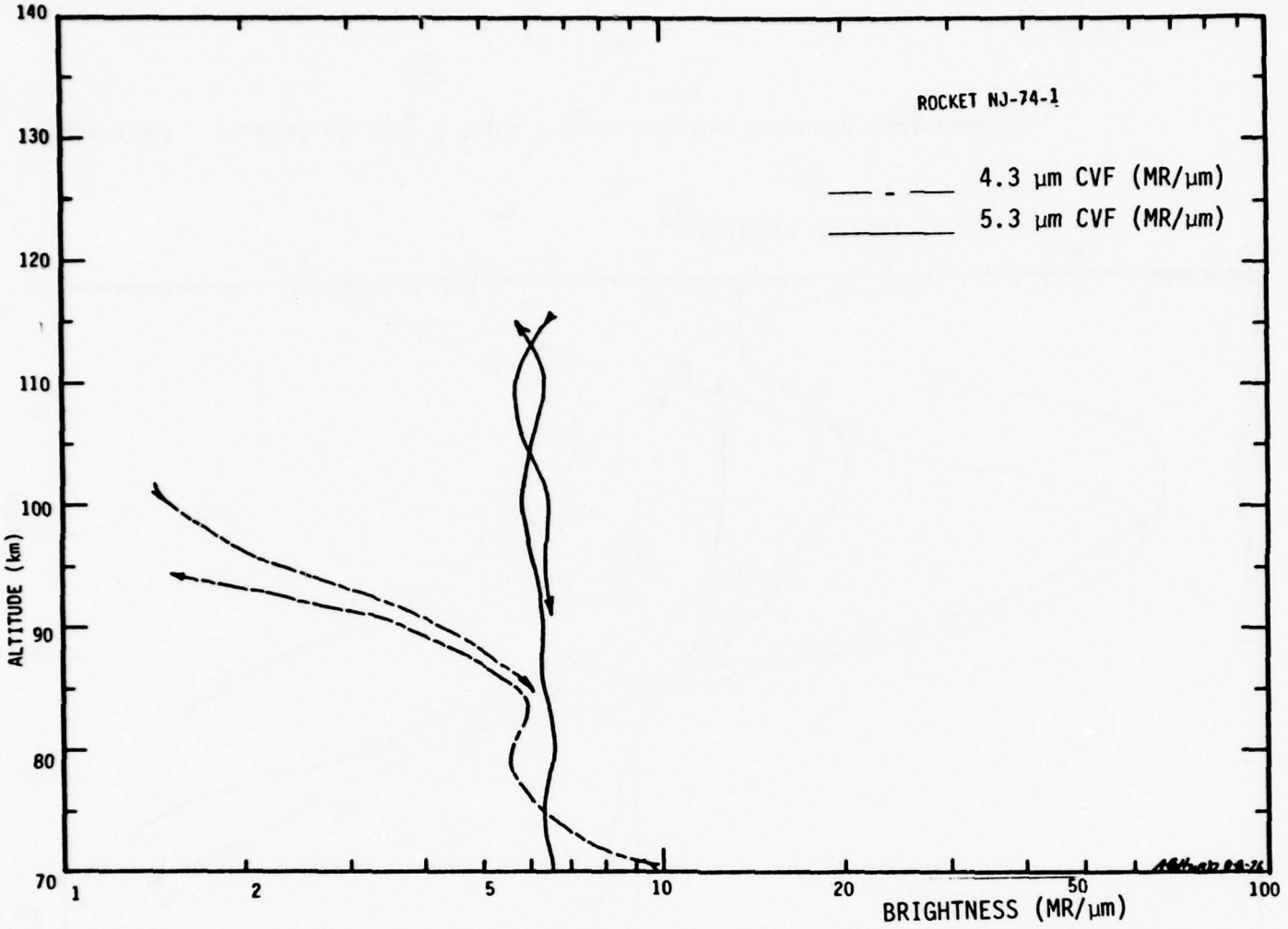

Figure 25 Rocket NJ-74-1 Data From Axially-Mounted Instruments

3.0 DETERMINATION OF RELATIONSHIPS BETWEEN AURORA AND ELECTRON DEPOSITION

3.1 Requirements

The usual procedure in rocket probes of aurora is to time the launch of the instrumented payload so that it will penetrate a bright, stable auroral form. Quite often, by the time the rocket has reached the altitude of the aurora, the brightest auroral form has either decayed or moved off to another position. Therefore, it is necessary to utilize data from both ground-based and rocket-borne instruments to characterize the aurora.

Basically, the requirements of the ICECAP experiments for relating auroral infrared emission to the auroral energy deposition are as follows:

1. The rocket probe instrumentation should have included most, if not all, of the following:
    a. Energetic particle probes, both spectral and total.
    b. SWIR photometers and/or spectrometers.
2. The rocket trajectory should have been close to the magnetic meridian, which was continuously scanned by ground-based photometers.
3. The rocket trajectory should have passed through regions of recent or existing intense electron fluxes and its IR instruments should have viewed through the regions where these electron

fluxes are deposited.

4. The all-sky ground-based cameras should have confirmed that the aurora was a fairly homogeneous arc.

The first requirement was met, or partially met, in only a few of the ICECAP rocket probes. The second requirement was usually fulfilled, the rocket trajectories being within 20° of azimuth from the magnetic meridian with an assortment of meridian scanning photometers in operation at several ground stations before, during, and after the rocket launches.

The third requirement was met with varying degrees of success due to the vagarious nature of the aurora as already noted.

Confirmation of the aurora's being a homogeneous arc (the fourth requirement) is necessary because the rocket's trajectory, the magnetic field lines which intersect it, and the magnetic meridian which is being scanned by the ground-based photometer are only close to being in the same plane. However, auroral arcs are, to a first approximation, aligned along circles of constant geomagnetic latitude[33]. Therefore, the aurora related to the measured electron flux can be approximated by using the projection of the magnetic field line in the plane of the meridian scan.

One final approximation is that the peak intensity of the aurora is at an altitude of 100 km. This is a reasonable value[34] for the brightest visible aurora (5577Å) although there is some variation in altitude with auroral intensity[35].

In the following sections, the ground-based photometer data and the rocket-borne electron data are used to find empirical relationships between visible auroral brightness and electron energy spectra.

3.2 Visible Aurora Intensity to Energy Flux

As previously mentioned, rocket 18.219-1 provides the most extensive combination of data pertaining to visible aurora, auroral electrons, and SWIR measurements. In searching for a possible relationship between auroral intensity and auroral electron flux, the data for visible aurora at the 100 km intercept from Figures 12 and 13 and the energy flux from Figure 15 were plotted as a function of time, with the results shown in Figure 26. Clearly, there is a positive correlation between the two. The spread in values is due in large part to the previously mentioned approximations concerning auroral height and uniformity, trajectory and aspect angles, the relatively rapid temporal variations in the aurora, and the low energy cutoff ($E < 4$ keV) of the scintillator. If, however, one or two of the obviously inconsistent data points are deleted and an arithmetic mean calculated from both the scintillator and the integrated electrostatic analyzer fluxes, then the resulting values for 5577Å aurora are as plotted in Figure 27. Also shown are some peak values of data from four earlier rocket probes[36] and a theoretical calculation based on measurements of the ionization cross section of nitrogen[37]. The two sets of data points seem to fall very close to a curve whose formula has been graphically calculated as

$$\Psi = 3.8 \times 10^{-2} N^{1.55}$$

where Ψ is the auroral electron energy flux in ergs/cm^2-sec-sr, and N is the 5577Å auroral radiance in kilorayleighs.

3.3 Energy Flux to Peak Electron Energy

An examination of the electron spectra and energy fl[illegible] in Figures 5 and 15 leads to the conclusion that the peak value of the energy spectra increases with increased energy flux. When the peak values from these and other energy spectra are plotted against the energy fluxes, the results are as shown in Figure 28. Note that the integrated ESA energy fluxes are a factor of two or three higher than

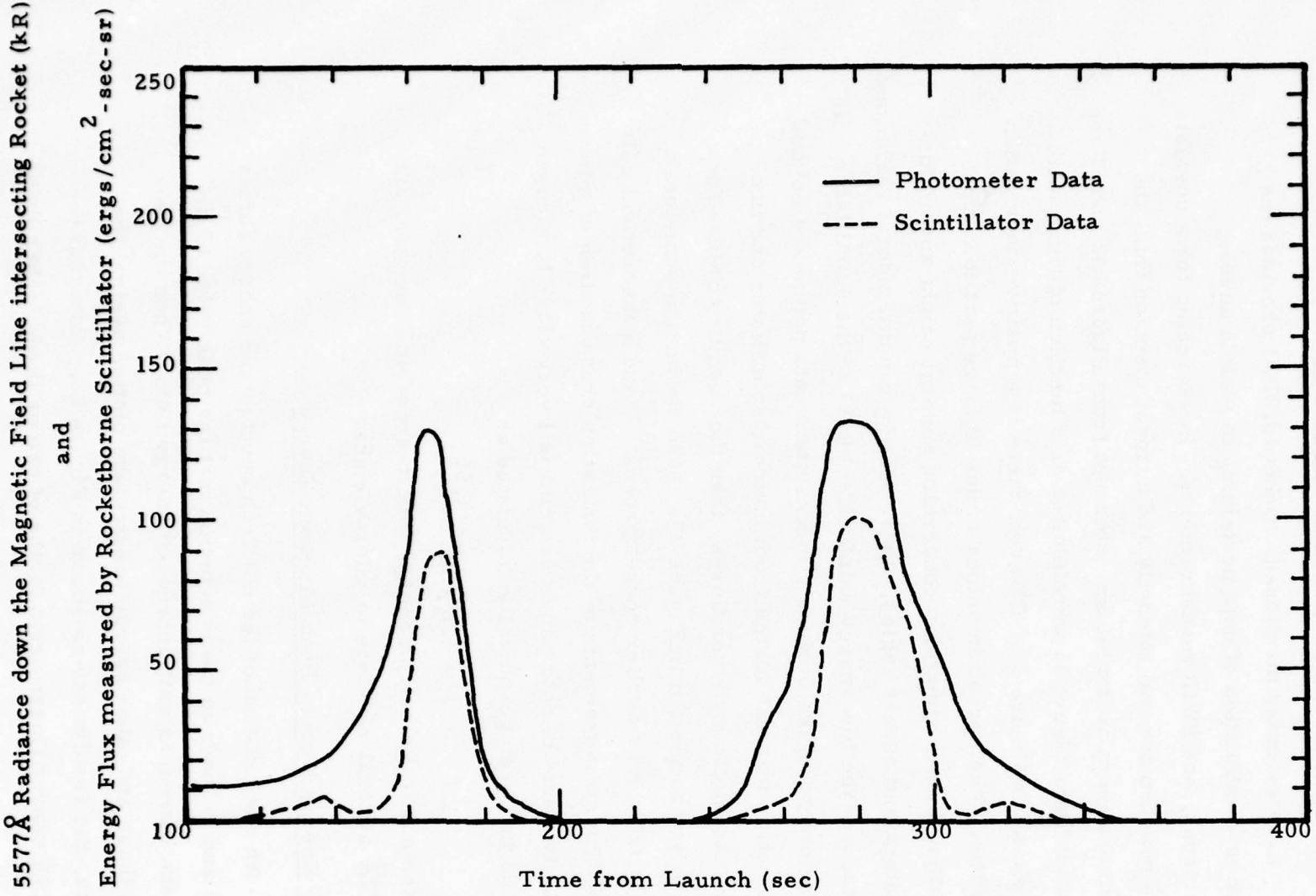

Figure 26 Rocket 18.219-1 Comparison of 5577Å Meridian Scanning Photometer Data and Rocketborne Scintillator Data vs. Time

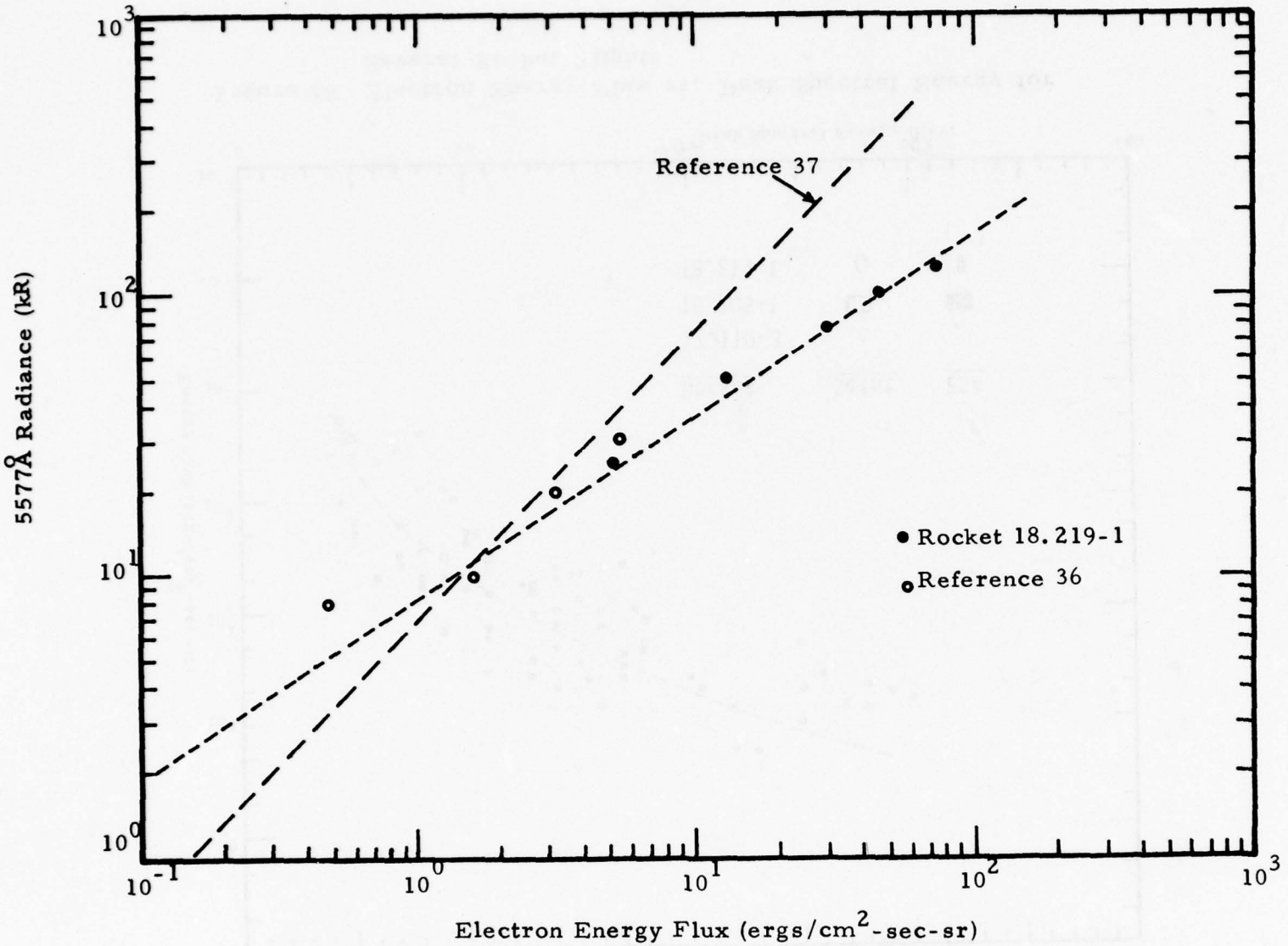

Figure 27 5577Å Auroral Radiance vs. Electron Energy Flux

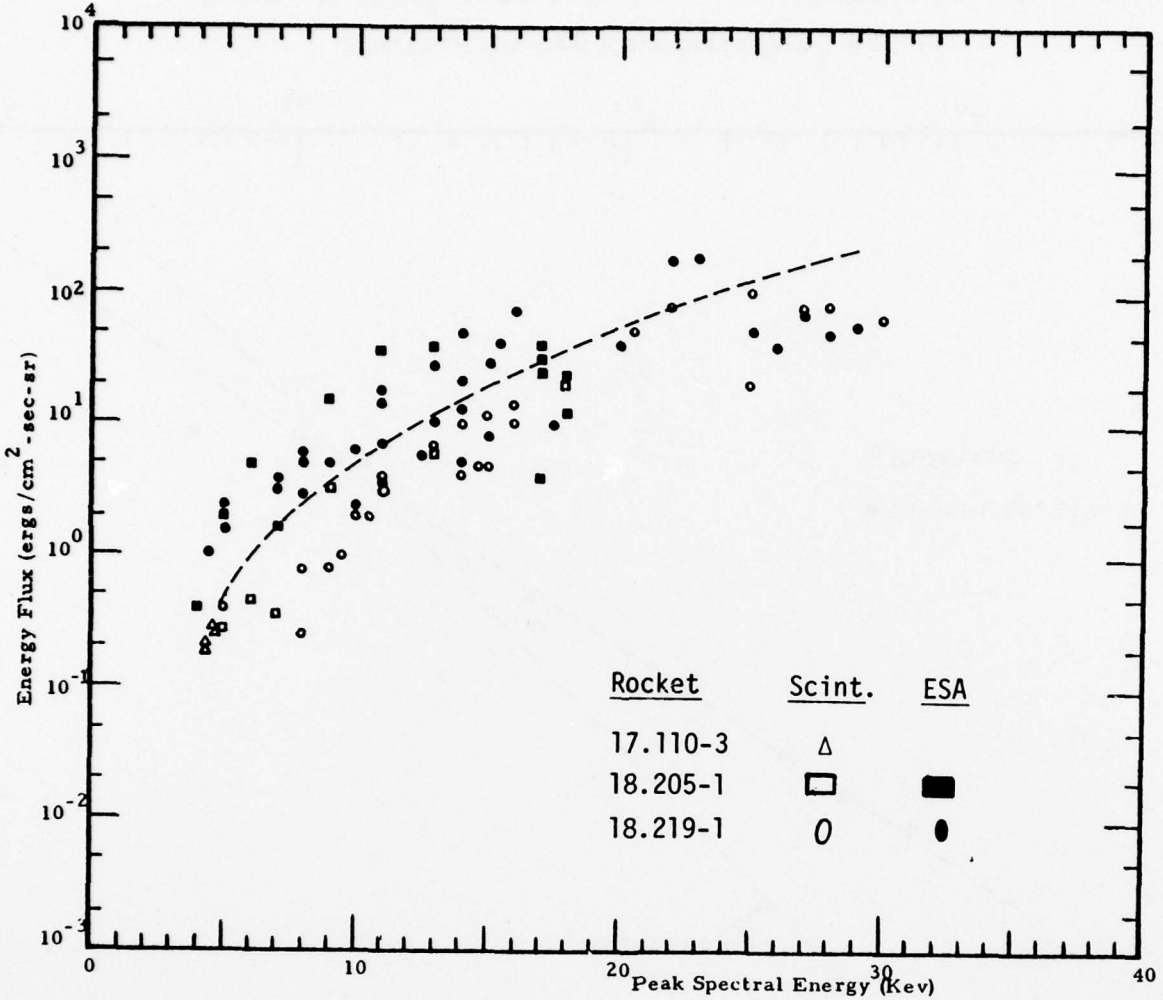

Figure 28 Electron Energy Flux vs. Peak Spectral Energy for Several Rocket Flights

that of the scintillator. However, when the peak spectral energy exceeds 25 keV as it did on Rocket 18.219-1, the two sets of data are approximately equal indicating that there was an appreciable flux of higher energy electrons which was not measured by the ESA. Hence, the curve shown (Fig 28) which approximates the average values is above all the data points for the peak spectral energy greater than 25 keV. The equation for this curve was determined by graphical methods to be

$$Ep = 6.5\Psi^{.27}$$

where Ep is the peak spectral energy in keV, and Ψ is the energy flux in ergs/cm^2-sec-sr.

3.4 Peak Electron Energy to Energy Spectrum

Further examination of the electron energy spectra in Figure 15 and the position of the auroral arc as shown in Figure 12 makes it apparent that the energy spectra recorded when the rocket was on the magnetic south side of the arc are relatively hard compared to those on the north side. These soft and hard spectral shapes appear to remain roughly constant and just shift in position depending on the peak electron energy. A plot in Figure 29 of the peak electron flux as a function of the electron energy at the peak flux clearly shows the separation between the north and south spectra.

By using straight line approximations for the slopes on either side of the peak spectral fluxes as plotted semilogarithmically, the equations for the spectra given in Table 3 were determined by graphical means. When spectra were recorded in the region of the arc, there is evidence that the spectral shape may be considerably different from those determined above. The slope below the spectral peak is almost flat in some instances. However, further data is necessary before the entire spectral shape and the spatial extent in the auroral arc in which it occurs can be approximated. Generally speaking, in addition to electron energy spectra characterized by an energy peak, there is always present

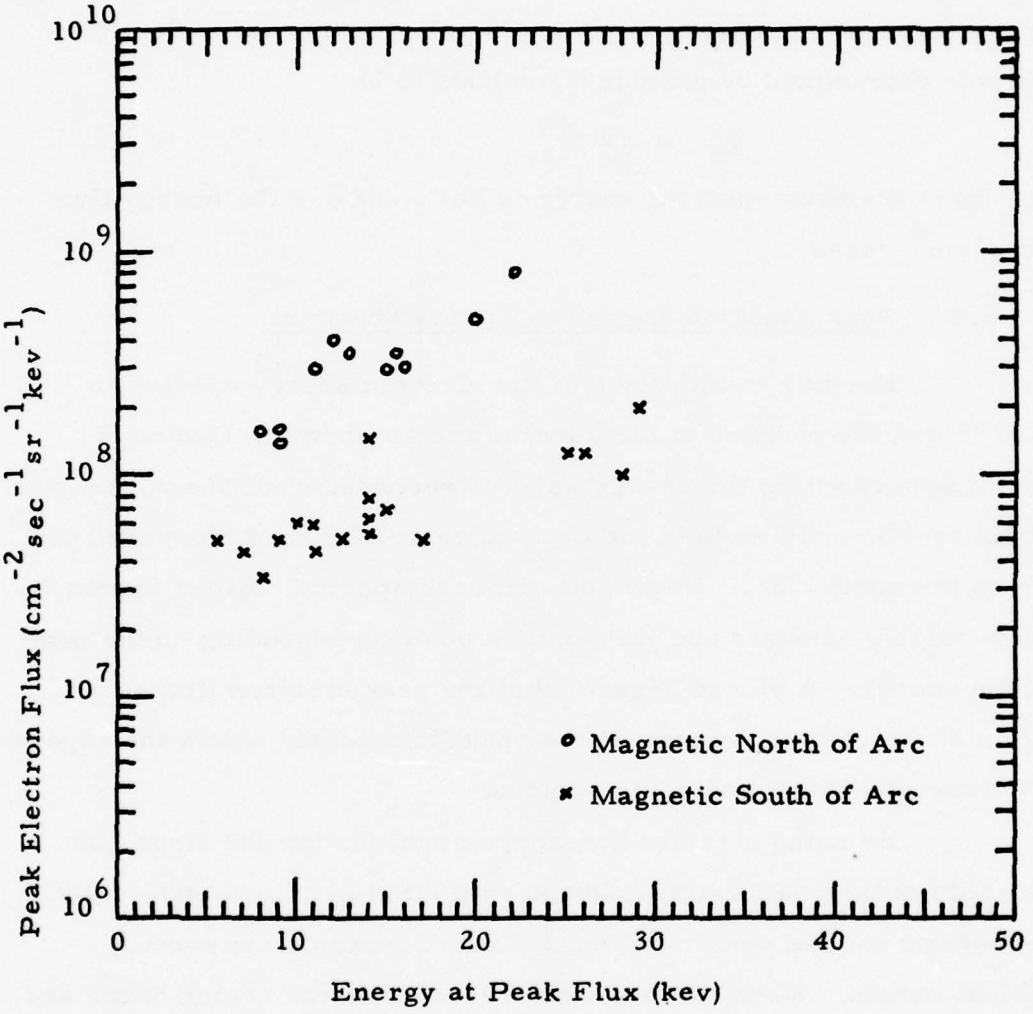

Figure 29 Peak Electron Flux vs. Energy at Peak Flux

TABLE 3

Equations for Electron Intensity Spectra

Spectra Magnetic South of Aurora

$E < Ep$

$$\phi = 5.0 \times 10^{7} e^{\cdot 06E}$$

$E > Ep$

$$\phi = 5.0 \times 10^{7} e^{\cdot 35Ep - .29E}$$

Spectra Magnetic North of Aurora

$E < Ep$

$$\phi = 1.2 \times 10^{8} e^{\cdot 13E - .07Ep}$$

$E > Ep$

$$\phi = 1.2 \times 10^{8} e^{\cdot 94Ep - .88E}$$

Background Spectrum

$$\phi = 2.5 \times 10^{8} E^{-2.0}$$

an essentially monotonically decreasing "background" spectrum[32], which herein has been approximated by the equation

$$\emptyset = 2.5 \times 10^{8} E^{-2.0}$$

where $\emptyset$ is the electron intensity in electrons/cm^2-sec-sr-keV and E is the electron energy in keV. This component should always be added to the peaked energy spectrum to obtain an approximation of the total energy spectrum down to below 1 keV.

3.5 Auroral Time Histories

The auroral time history of the region viewed by the forward looking optical instruments have been calculated in the following manner. For each rocket we have divided the trajectory into 10 kilometer intervals. At each 10 kilometer position of the rocket, we have derived the intercept point of the optical instruments at various altitudes above the rocket. The magnetic field line passing through each intercept point has been extended to find its location at the 100 kilometer level. Using the ground based meridian-scanning photometer time history and the empirical technique presented in Section 3.2, 3.3 and 3.4 we have derived the electron flux at prior times along that field line and used the derived fluxes to calculate the time history of the energy deposition at the altitude of the intercept point.

The time histories of the 5577Å on the field lines corresponding to the intercept of the optical instrumentation at different altitudes were determined for Rockets 18.205-1, 18.219-1, and 10.205-2. Some examples are shown in Figures 30 and 33. These and similar curves were used to determine mean values over 20 second intervals for the 200 seconds prior to the data, and also whether the data point is north or south of the auroral arc. A complete listing of these mean values for all three rockets is given in Appendix A.

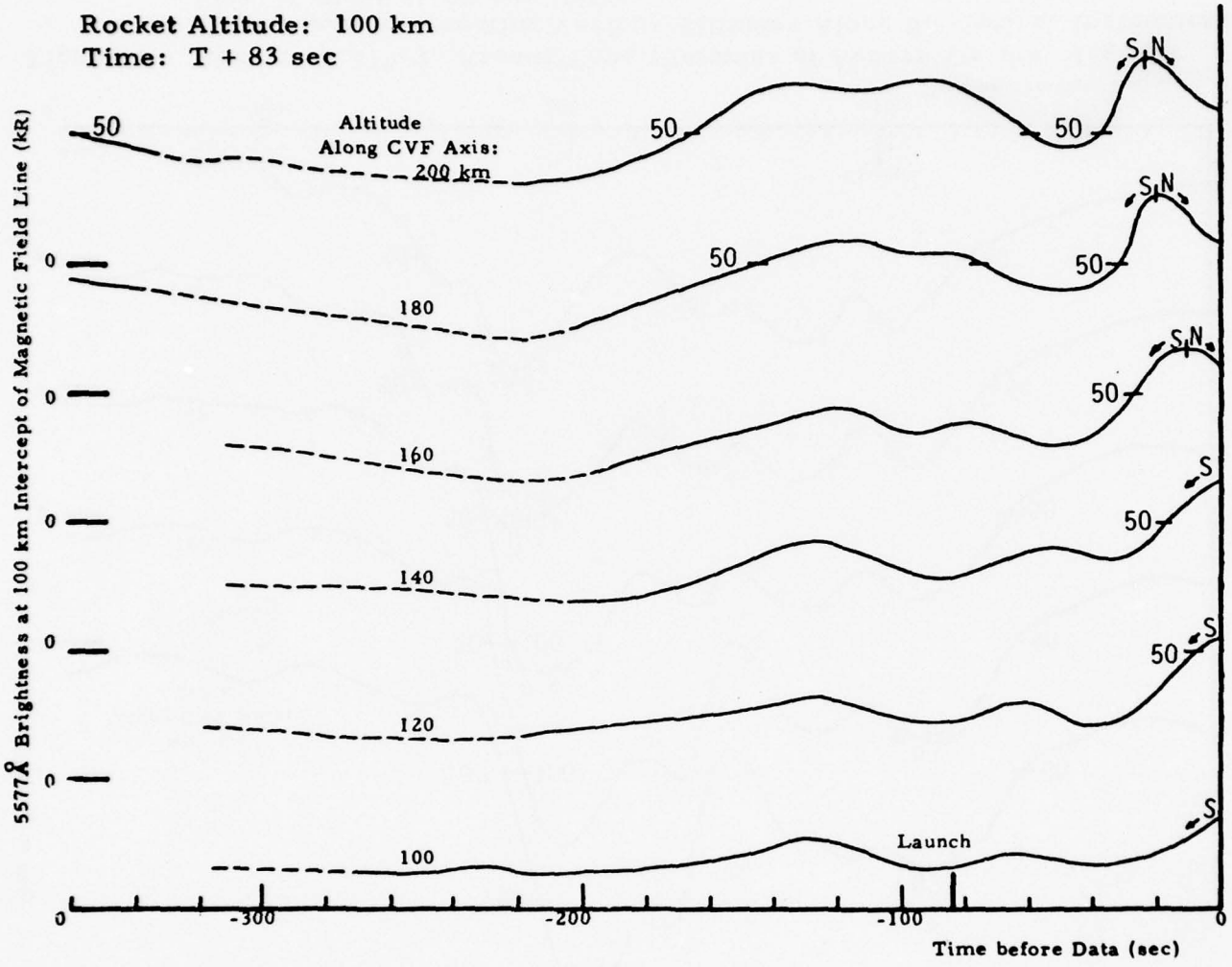

Figure 30: Rocket 18.205-1 Time Histories of Aurora On the Magnetic Field Lines Intersecting Various Altitudes Along the Optical Instrumentation Line of Sight at 100 km Upleg.

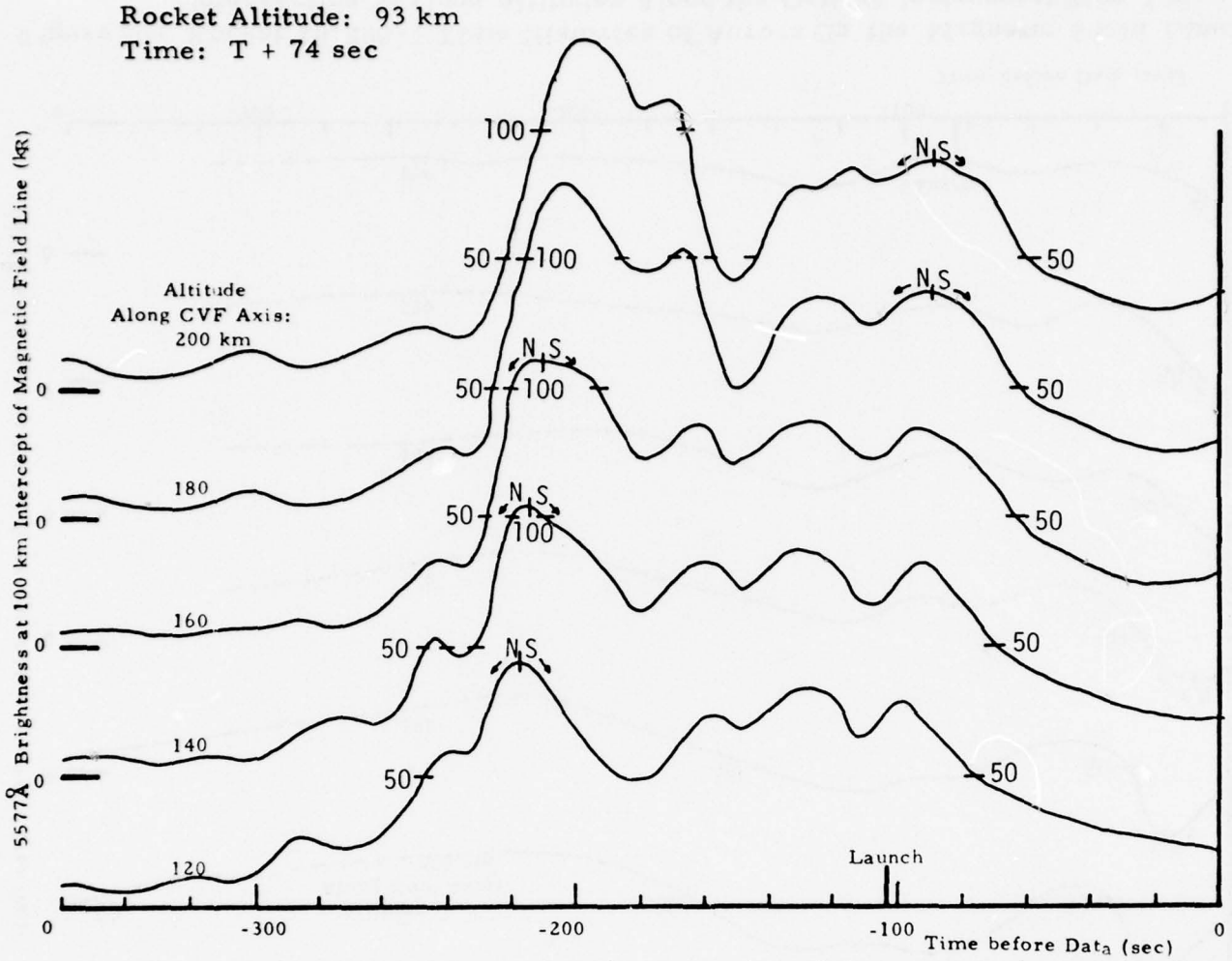

Figure 31: Rocket 18.219-1, Ascent Time Histories of Aurora On the Magnetic Field Lines Intersecting Various Altitudes Along the Optical Instrumentation Line of Sight at 93 km Upleg.

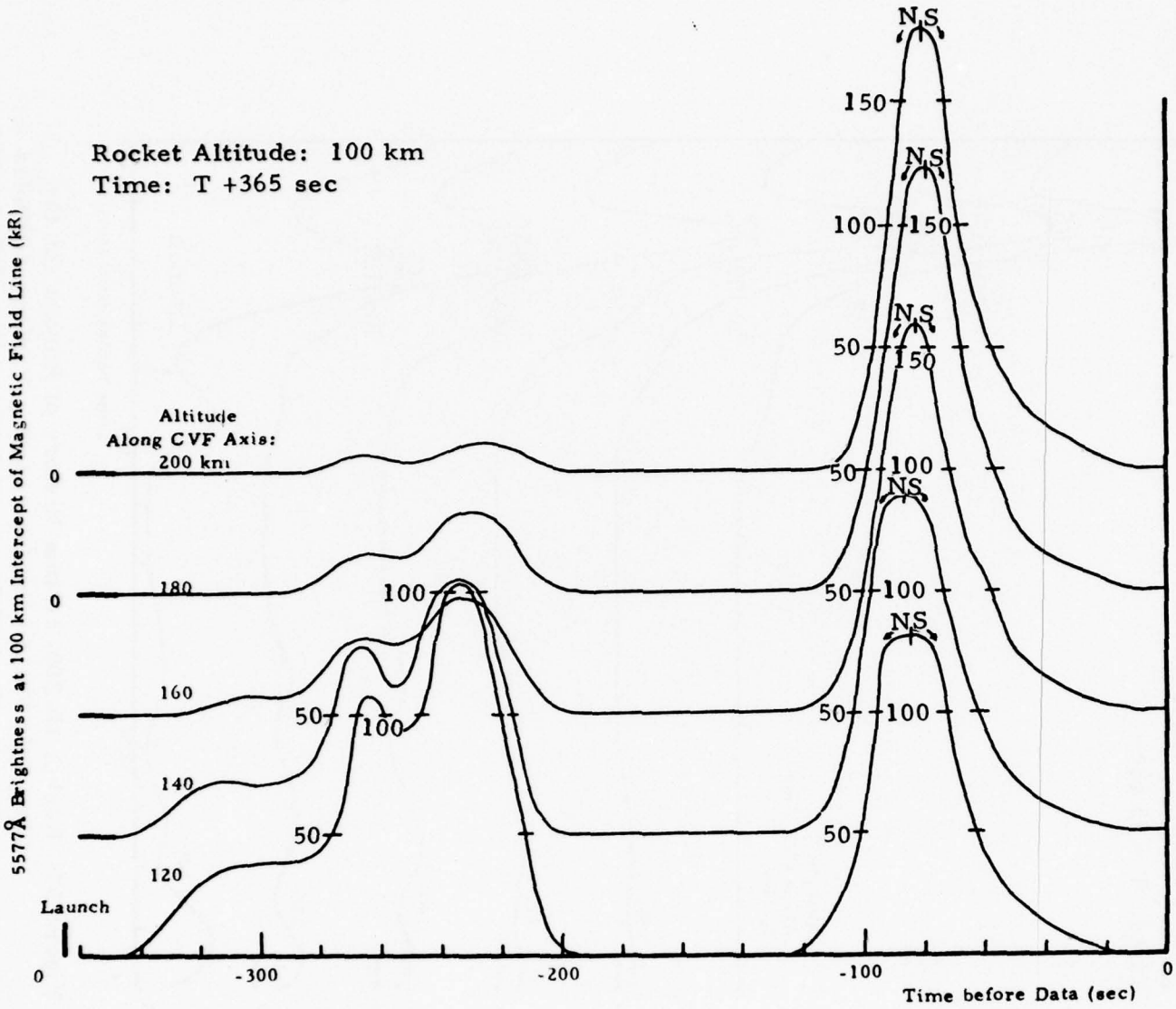

Figure 32: Rocket 18.219-1 Descent Time Histories of Aurora On the Magnetic Field Line Intersecting Various Altitudes Along the Optical Instrumentation Line of Sight at 100 km Downleg.

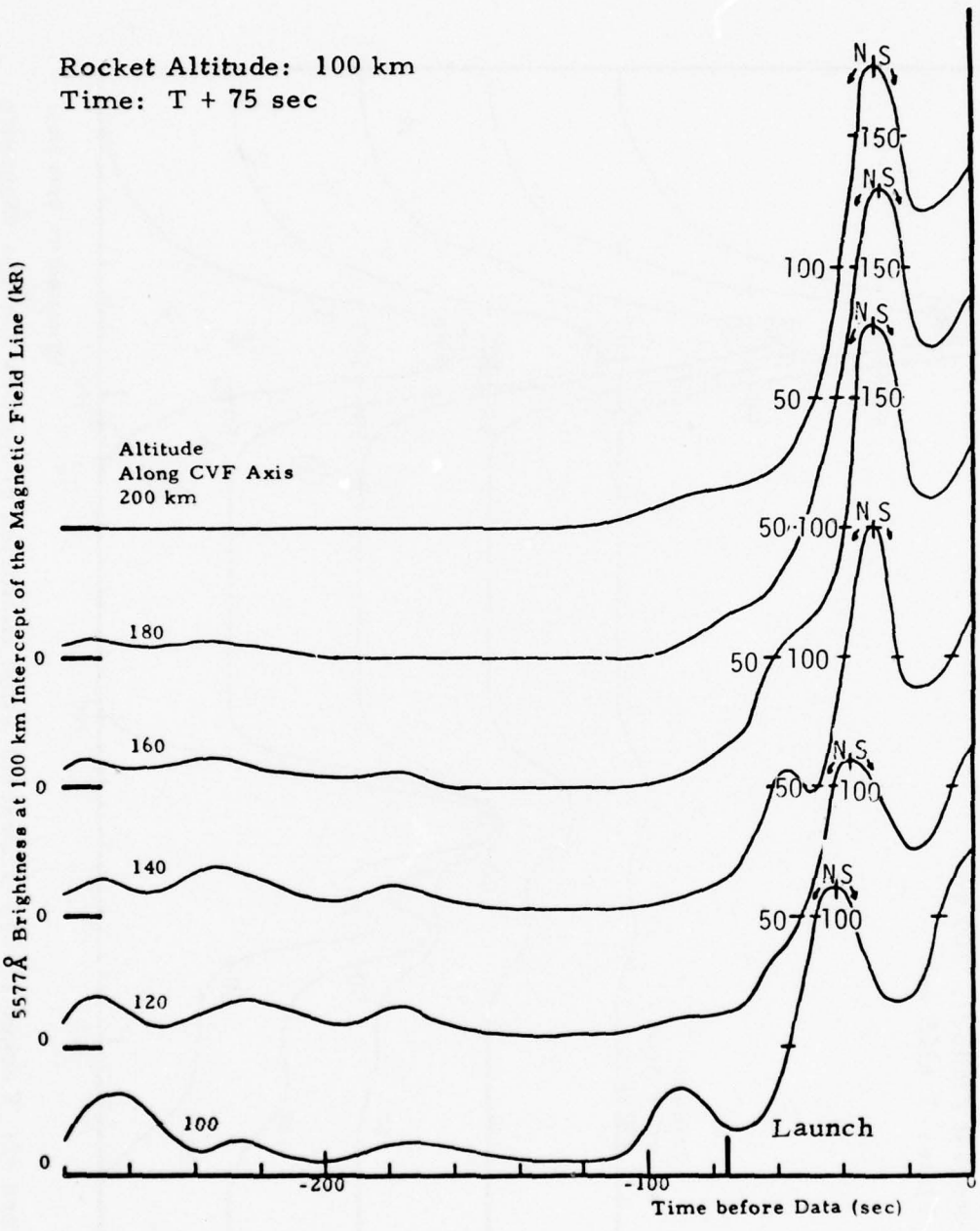

Figure 33: Rocket 10.205-2 Time History of Aurora On the Magnetic Field Line Intersecting Various Altitudes Along the Optical Instrumentation Line of Sight at 100 km Upleg.

4.0 CALCULATION OF ATMOSPHERIC PARAMETERS FROM AURORAL ELECTRON DEPOSITION

4.1 Methods

Predictions of the ionization in the upper atmosphere caused by the flux of auroral electrons are provided by portions of the AFGL/Visidyne OPTIR Code, in particular the SOURCE subroutine and the QEAUR function[38]. The ionization is then used in the AFGL/Visidyne QCHEM Code to calculate the various infrared band emissions as a function of time for various altitudes.

Reactions and reaction rates pertinent to the study of NO infrared emissions and related chemistry are shown in Table 4[39]. This chemistry, the atmospheric composition, and the deposition rate are used to calculate time profiles of the neutral and charged species. Radiance levels can be calculated using known excited-state excitation rates for given reactions, and the radiative and quenching lifetimes, and these calculated levels compared to the measured data. Alternatively, rocket measurements can be used to determine these data where no other measurement exists. In this analysis we have used as our model auroral atmosphere the atmospheric composition shown in Table 5[40] and have assumed that the electron flux is turned on 200 seconds before the time of observation. Mean ground-based measurements of the 5577Å auroral intensities averaged over 20 second intervals are used to compute the input electron spectra and deposition rates (Section 3.5 and Appendix A).

4.2 Examples

The simplest example to consider is an auroral deposition which is uniform in space and time. As noted in Section 2.6, Rocket A17.110-3 passed through a diffuse, homogeneous auroral region and measured a relatively constant incident electron energy spectrum. By using this electron spectrum in the OPTIR code, the electron densities for several altitudes as a function of time from an assumed turn-on were

TABLE 4: CHEMISTRY MODELLED

	REACTION	RATE COEFFICIENT
1.	$O^+ + N_2^{\ddagger} \rightarrow NO^+ + N(^2D)$	3.0 (-10)
2.	$E + NO^+ \rightarrow N\begin{pmatrix}^4S\ (1/4)\\ ^2D\ (3/4)\end{pmatrix} + O$	4.0 (-7)
3.	$N(^2D) + O_2 \rightarrow NO + O$	5.0 (-12)
4.	$N(^2D) + NO \rightarrow N_2^{\ddagger} + O$	7.0 (-11)
5.	$O + O + M \rightarrow O_2 + M$	2.5 (-29) $T^{-3/2}$
6.	$N(^4S) + O + M \rightarrow NO + M$	1.8 (-31) $T^{-1/2}$
7.	$NO + O_2^+ \rightarrow O_2 + NO^+$	4.4 (-10)
8.	$N_2^+ + O \rightarrow NO^+ + N\begin{pmatrix}^4S\ (1/2)\\ ^2D\ (1/2)\end{pmatrix}$	1.4 (-10)
9.	$N_2^+ + O_2 \rightarrow N_2 + O_2^+$	6.0 (-11)
10.	$N_2 + O^+ \rightarrow NO^+ + N$	1.2 (-12)
11.	$O + N_2^{\ddagger} \rightarrow O + N_2$	1.07 Exp ($-69.9T^{-1/3}$)
12.	$O_2^+ + E \rightarrow O + O$	2.0 (-7)
13.	$N_2^+ + E \rightarrow N(^4S) + N(^2D)$	3.0 (-7)
14.	$O^+ + NO \rightarrow NO^+ + O$	2.0 (-11)
15.	$O^+ + O_2 \rightarrow O_2^+ + O$	2.0 (-11)
16.	$O_2^+ + N(^4S) \rightarrow NO^+ + O$	1.8 (-10)
17.	$N^+ + O_2 \rightarrow O_2^+ + N\begin{pmatrix}^2D\ (1/2)\\ ^4S\ (1/2)\end{pmatrix}$	4.0 (-10)
18.	$\rightarrow NO^+ + O$	2.0 (-10)
19.	$N + N + M \rightarrow N_2 + M$	8.3 (-34) Exp (+500/T)
20.	$N_2^+ + NO \rightarrow NO^+ N_2$	3.3 (-10)
21.	$N(^4S) + O_2 \rightarrow NO + O$	1.1(-14)T Exp (-3150/T)
22.	$N(^4S) + NO \rightarrow N_2^{\ddagger} + O$	$1.5(-12)T^{\frac{1}{2}}$
23.	$O(hot) + N_2 \rightarrow NO + N(^4S)$	5.0 (-11)
24.	$O(hot) + M \rightarrow O + M$	5.0 (-10)
25.	$O + N_2\ (A^3\Sigma) \rightarrow NO + N(^4S)$	2.0 (-11)
	$\rightarrow NO + N(^2D)$	4.0 (-11)
	$\rightarrow O(^1D) + N_2$	1.0 (-11)
	$\rightarrow O(^1S) + N_2$	3.0 (-11)
26.	$O_2 + N_2\ (A^3\Sigma) \rightarrow N_2 + O_2$	4.0 (-12)
	$\rightarrow N_2 + 2O$	
	$\rightarrow N_2O + O$	
	$\rightarrow N_2O + O(^1D)$	
	$\rightarrow 2\ NO$	
27.	$N(^2D) + O \rightarrow N + O(^3P, ^1D)$	4.0 (-12) Exp (-250/T)

Table 5

ATMOSPHERIC PARAMETERS FOR STUDY OF IBC TYPE I AURORA

Altitude (km)	Temp. (neutral)	Temp. (elect)	$[N_2]$	$[O_2]$	[NO]	[N]	[O]
85	1.80E+02	1.80E+02	9.20E+13	2.60E+13	9.70E+07	2.20E+03	1.00E+11
90	1.80E+02	1.80E+02	3.40E+13	1.10E+13	8.40E+07	1.00E+04	2.50E+11
95	1.90E+02	1.90E+02	1.20E+13	4.10E+12	7.00E+07	4.80E+04	2.50E+11
100	2.10E+02	2.10E+02	4.70E+12	1.50E+12	5.90E+07	2.20E+05	2.20E+11
105	2.35E+02	2.35E+02	2.10E+12	6.20E+11	5.00E+07	1.00E+06	1.80E+11
110	2.65E+02	2.65E+02	9.90E+11	2.60E+11	4.00E+07	1.20E+06	1.40E+11
115	3.10E+02	3.10E+02	4.90E+11	1.20E+11	3.30E+07	1.40E+06	9.80E+10
120	3.55E+02	3.55E+02	2.60E+11	6.00E+10	2.70E+07	1.60E+06	6.80E+10
125	3.90E+02	3.90E+02	1.50E+11	3.30E+10	2.20E+07	1.90E+06	4.80E+10
130	4.20E+02	4.30E+02	9.70E+10	2.00E+10	1.80E+07	2.30E+06	3.50E+10
135	4.50E+02	4.80E+02	6.30E+10	1.20E+10	1.45E+07	2.70E+06	2.70E+10
140	4.80E+02	5.45E+02	4.30E+10	7.70E+09	1.15E+07	3.20E+06	2.10E+10
150	5.30E+02	7.05E+02	2.10E+10	3.40E+09	7.60E+06	4.40E+06	1.30E+10
160	5.75E+02	9.15E+02	1.10E+10	1.70E+09	5.00E+06	6.00E+06	8.70E+09

calculated with the results shown in Figure 34. For a comparison with the measured electron densities, the electron flux is assumed to have been on for at least 100 seconds prior to the rocket measurements. The electron and ion density were measured with a rocket-borne plasma frequency probe and a retarding potential analyzer, respectively. The electron density was also measured by ground-based radar. Figure 35 is a comparison of these measurements with the calculated electron density profile[35], showing them to be in good agreement.

Probably the most complicated auroral condition we have attempted to analyze involved an intense auroral breakup and a rocket probe which was not instrumented for particle measurements. The particle flux was derived from the ground-based meridian scanning photometers using the method presented in Section 3 of this report.

Rocket 10.205-2 passed through an intense auroral breakup region. The mean values of the aurora from Appendix A were fed into a computer program which used the equations in Table 3 to determine the electron fluxes. The chemistry code was then employed with these flux inputs. An example of the resulting electron density along the CVF axis is shown in Figure 36 with a comparison of the electron density as determined from radar measurements[16]. It has been pointed out previously here and elsewhere[41] that because of geometric limitations, only qualitative correlation between the two sets of data should be expected. Also, the data times differ by about 10 seconds. In addition, the ground-based photometer data was degraded because of saturation and clouds. Since, in the empirical relations we have developed, peak energy increases with auroral brightness, a decrease in photometer brightness would be modelled as a softer electron spectrum which deposits at higher altitudes than the real case.

The chemistry code has been run for specific cases associated with the ascent and descent of Rocket 18.219-1 and the ascent of Rocket 10.205-2 since these have the most prominent or well-documented infrared auroral features.

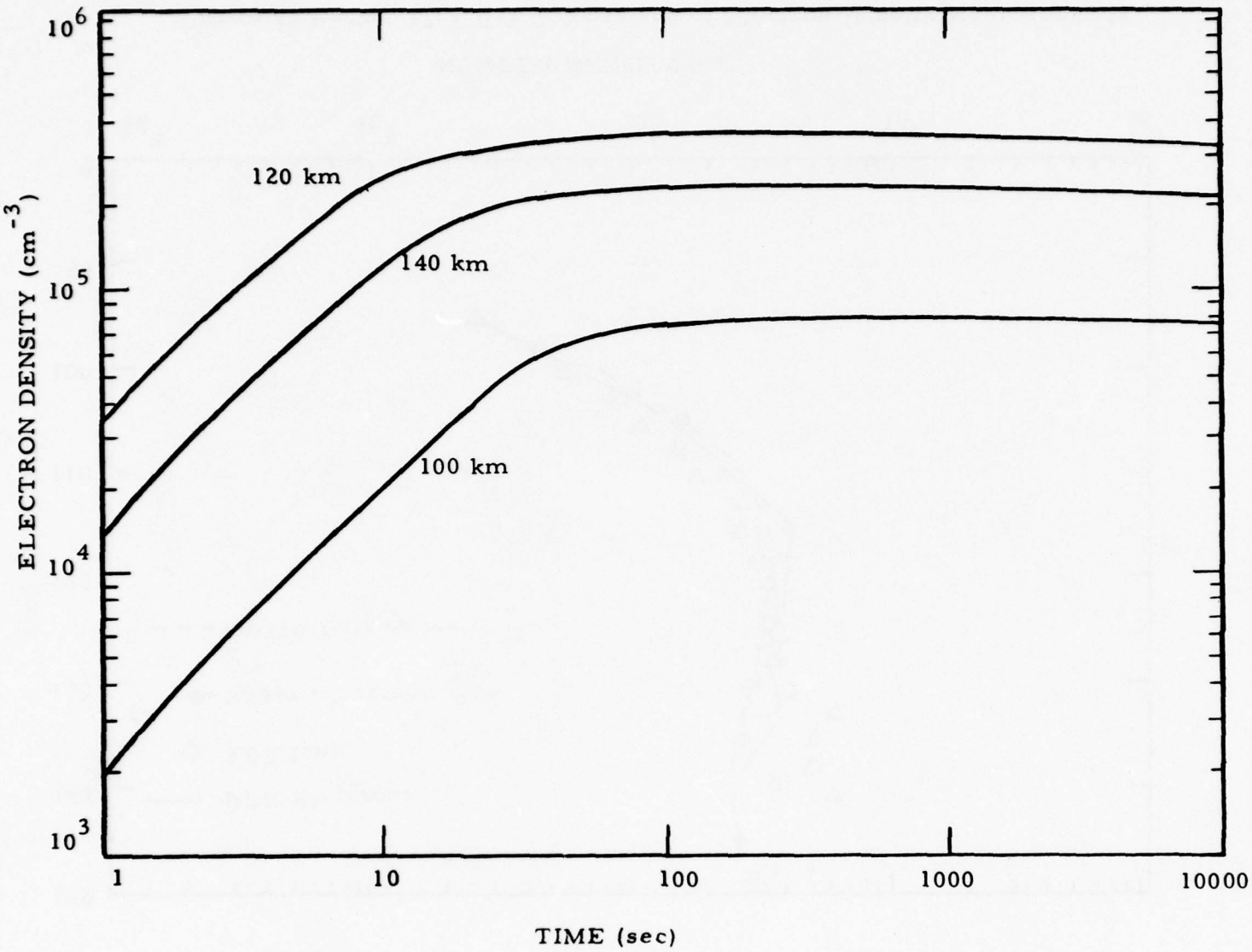

Figure 34 Rocket 17.110-3, Calculation of Electron Densities vs. Time from Turn-on for Several Altitudes

ICECAP 72 IONIZATION

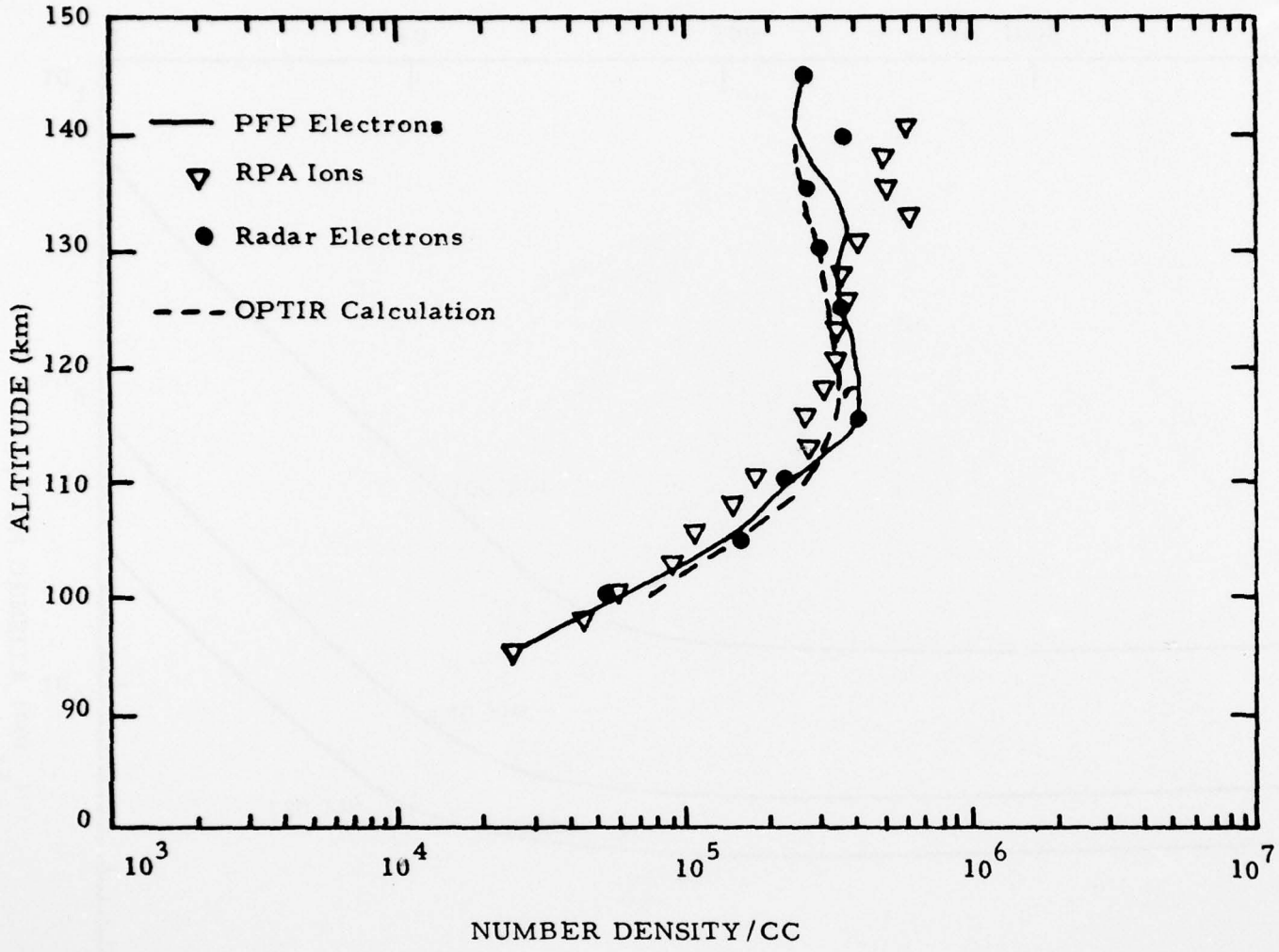

Figure 35 Rocket 17.110-3 Comparison of Electron Density Measurements vs. Altitude

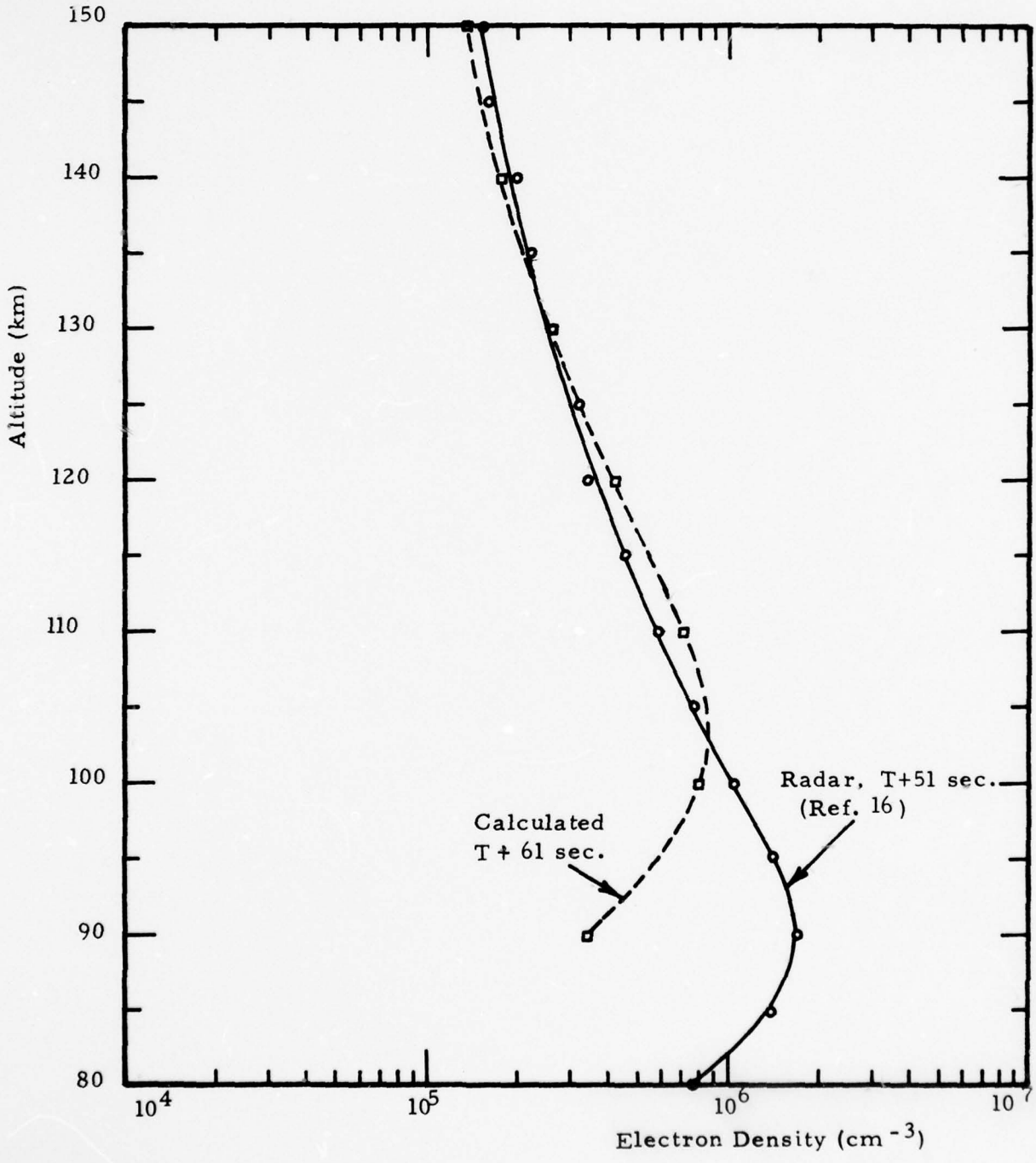

Figure 36 Rocket 10.205-2 Electron Densities vs. Altitude

5.0 EXPLANATION OF ICECAP AURORAL INFRARED MEASUREMENTS

5.1 Introduction

In the following sections, the ICECAP measurements of the 2.7, 4.3, and 5.3 infrared auroral bands are examined in detail, proposed mechanisms for each band discussed, and conclusions drawn as to the actual sources. Also, where possible, qualitative comparisons between the data and theoretical calculations are made.

5.2 Radiance in the 5.3μm Band

There is general agreement that the signals in the 5.3μm band are from the fundamental of vibrationally excited nitric oxide. Several mechanisms have been proposed for exciting the NO molecule, as follows[42, 43]:

1) Chemiluminescence from the reaction
   $N(^2D) + O_2 \rightarrow NO' + O$
2) Resonant scattering of earthshine by
   $NO + h\nu \rightarrow NO'$
3) Collisional excitation from the reaction
   $O' + NO \rightarrow NO' + O$
4) Chemiluminescence from the reaction
   $N_2 (A^3\Sigma) + O(^3P) \rightarrow NO(x^2\pi) + N(^4S, {}^2D)$

The various 5.3 band spectra from these mechanisms can be quite different, extending to beyond 6μm in the first case, for example. The CVF spectrometers used InSb detectors whose sensitivity drops sharply beyond 5.3μm, thus making identification of the mechanisms from the spectral data inconclusive. Although the data sometimes show a peak spectral signal at less than 5.3μm, it may be an artifact of the analysis.

The 5.3μm data from four rocket probes are shown in Figure 37. Although these rockets penetrated a variety of auroral activity levels, with the exception of the 10.205-2 data, the brightness levels versus altitude are approximately the same, and the differences are within the limits of the instrument calibrations. In addition, the measured altitude profile of the 5.3μm emission differs strongly from the auroral arc energy deposition profile determined experimentally for 18.205-1 and 18.219-1. The conclusion is that there is little or no auroral arc enhancement of the 5.3μm band, except during or after an auroral breakup of the intensity

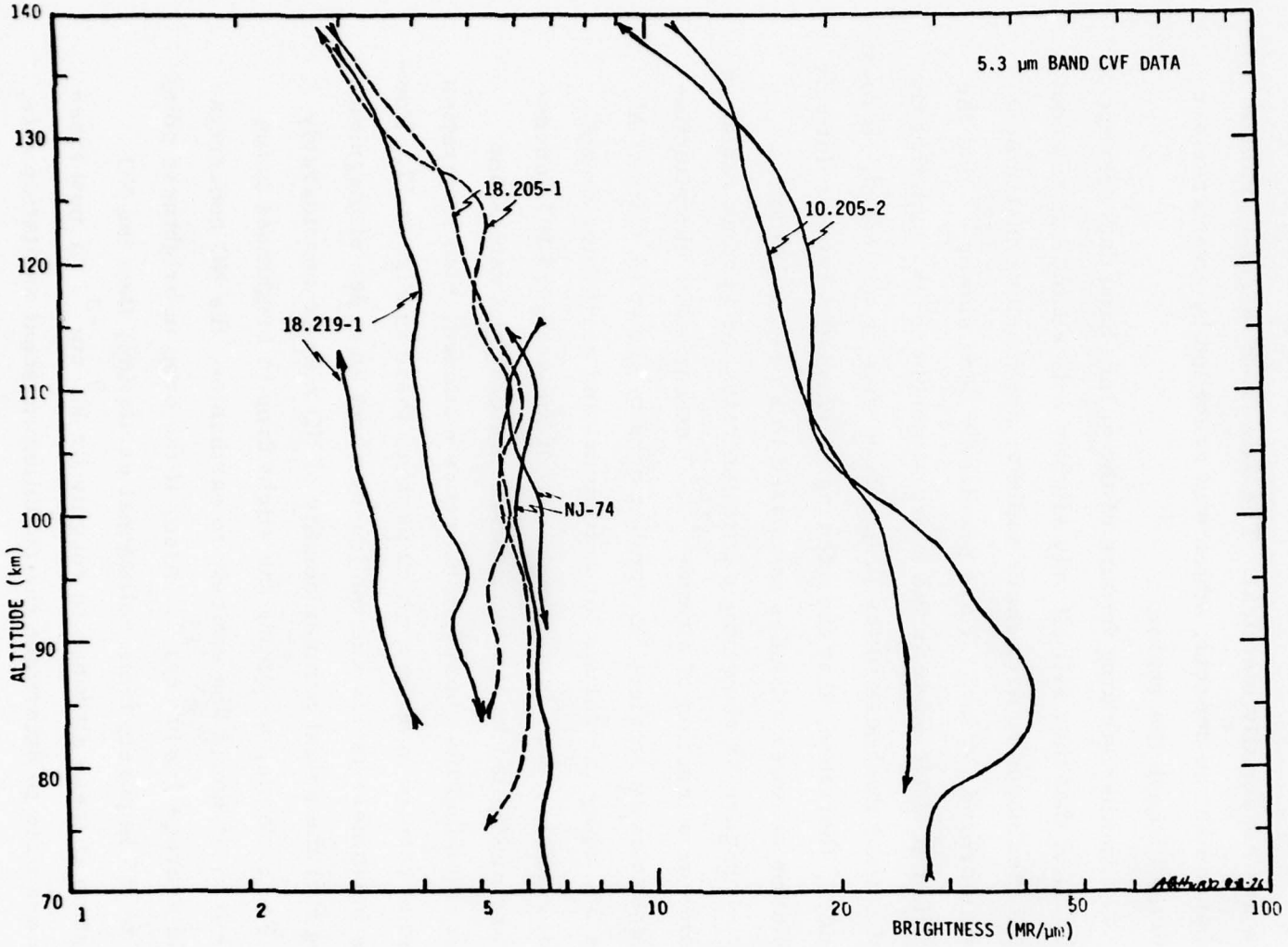

Figure 37 5.3 μm Band CVF Data for Various ICECAP Rockets

viewed by the 10.205-2 rocket payload. This lack of enhancement is particularly apparent in the 18.205-1 data. The payload penetrated a bright, stable arc on ascent and an aurorally quiet region on descent, as is verified by the 3914Å radiometer. Yet the 5.3μm data in both instances are essentially identical. The data from 18.219-1 indicate some enhancement on descent, which was preceded by an intense arc moving twice through the region.

Another striking feature of the 5.3μm band data (except for 10.205-2) is that they fell off only slightly with altitude up to about 120 km and then began to drop more rapidly, approaching instrument noise levels around 150 km. It has previously been shown[42] that the concentration of nitric oxide in the upper atmosphere is such that the effects of optical thickness in the 5.3μm band may be neglected. It must be concluded, therefore, that the exciting mechanisms cause relatively little radiation at lower altitudes compared to a peak at 120 km.

Figure 38 shows the excitation rates for various radiative mechanisms as a function of altitude[42]. The curve for chemiluminescence assumes an ambient NO number density shown as Curve "A" in Figure 39, while the curves for collisional and earthshine do not require any number density assumptions. If the assumed NO concentrations are multiplied by the combined collisional and earthshine excitation rates and the chemiluminescence excluded, then integration with altitude results in curves which parallel those in Figure 37. However, the brightness levels are too low by about an order of magnitude indicating that the actual number density of NO may be considerably higher. For example, assuming the slight drop in brightness going from 70 km to 115 km is due entirely to earthshine, the NO concentration would average 7×10^{8} cm^{-3}. Also, if the drop in brightness going from 125 to 135 is purely from collisional excitation, then the NO concentration at these altitudes is roughly 1×10^{9} cm^{-3}. If now these densities are used to determine the chemiluminescent excitation rate,

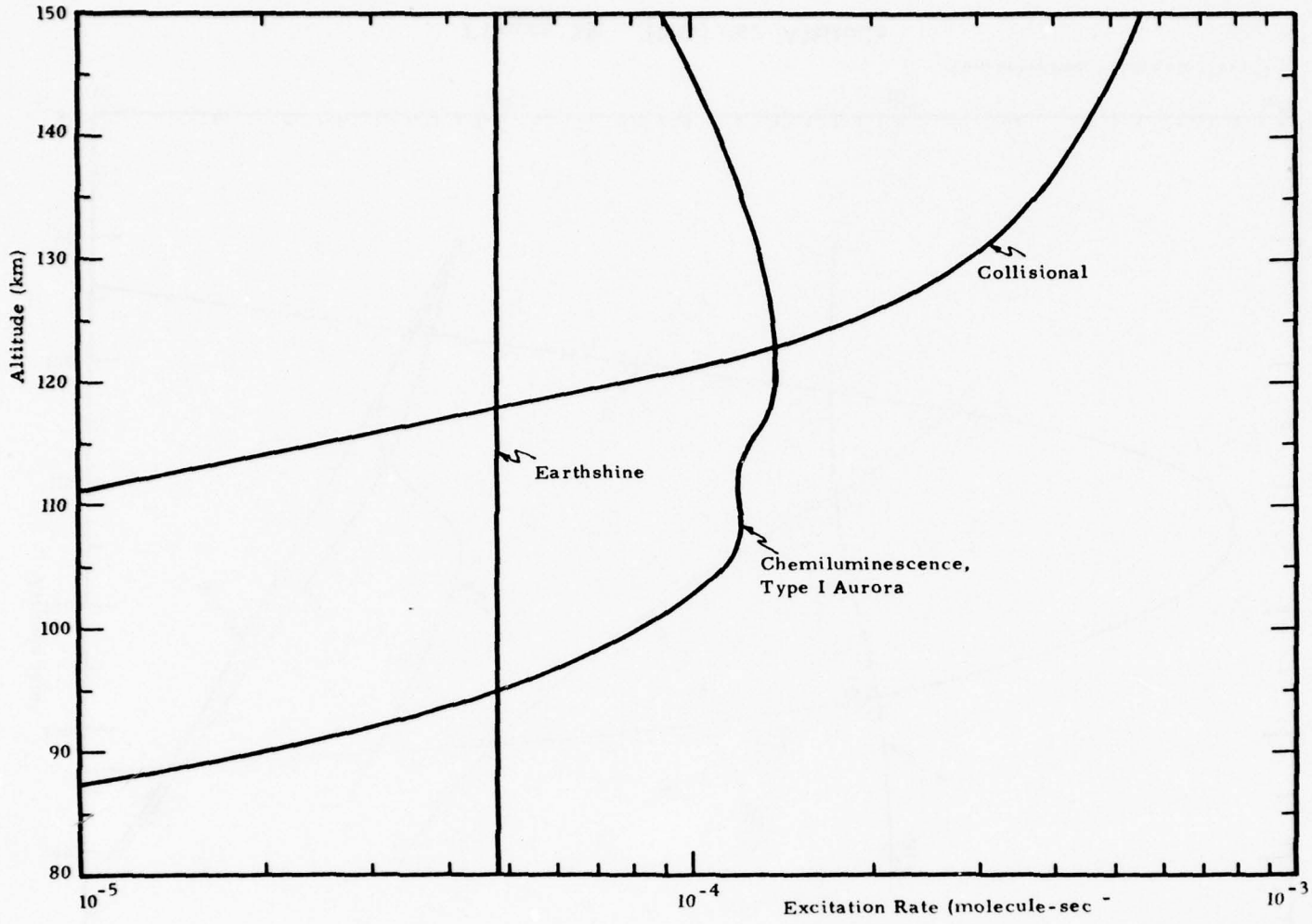

Figure 38 5.3 μm Band Excitation Rates

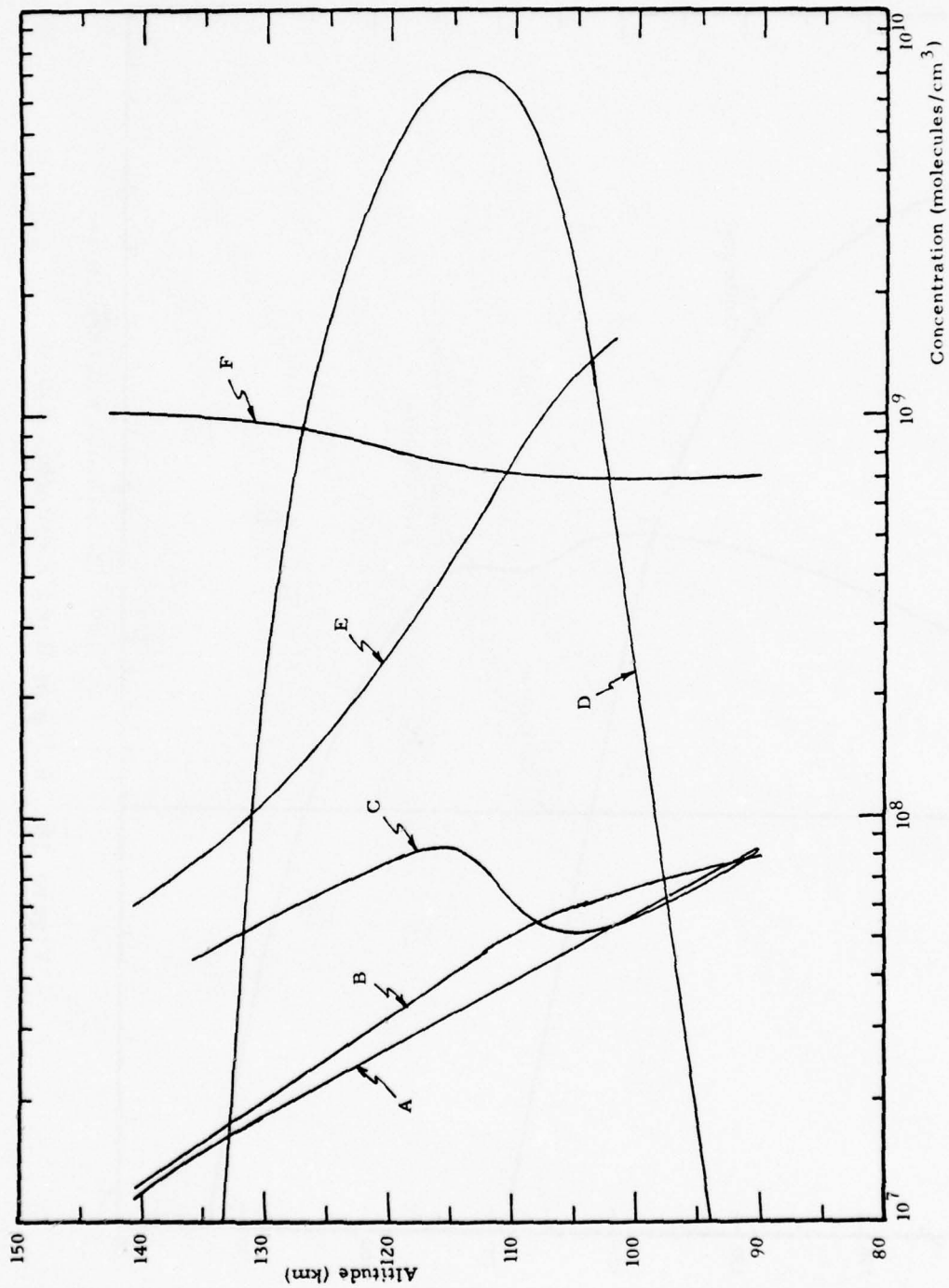

Figure 39 [NO] vs. Altitude

then it would be more of the order of 10^{-5} peak in Figure 38. This means that chemiluminescent radiation in the 5.3μm passband of these rocket instruments is of little or no consequence even in relatively bright aurora, and this is verified by the data.

The exception to the foregoing discussion is the 5.3μm data associated with Rocket 10.205-2 which, as can be seen in Figure 37, show enhancement at all altitudes both on ascent and descent. However, as mentioned in Section 2.5, the aurora associated with this rocket is not a homogeneous arc; it is a rapid auroral breakup. And there are other complications, as follows:

1) The rocket-borne 3914Å radiometer data show that the auroral intensity was far greater during the rocket ascent than that estimated from the ground-based meridian scanning photometers at Fort Yukon. (The photometers at Poker Flat were saturated during this time.)
2) Similarly, on descent the rocket-borne 3914Å radiometer detects a bright aurora while the ground-based instruments are recording auroras much lower in intensity (increased cloudiness).
3) No electron energy spectrum instruments were carried in the payload, and the actual energy spectra associated with an auroral breakup may be far different from the extrapolations used based on lower intensity aurora.

The peak signal of the 5.3μm band during ascent occurs at about 85 km and then drops with increasing altitude. From this, it is apparent that a large fraction of the auroral electrons must have had energies in the 40 keV range[44]. The bulge shape is due in part to the increasing auroral activity as the rocket ascends.

Above 110 km, the 5.3μm band signals for the 10.205-2 rocket on both ascent and descent are very similar to those of the other rockets but increased by a factor of about three. Presumably, the signals are due to the same mechanism, collisional excitation from the reaction $O' + NO \rightarrow NO' + O$, with a combination of increased O and NO concentration and/or reaction rate (which has a strong temperature dependence).

Below 110 km on descent, the 5.3μm band data is rather meager because of telemetry dropout, but it appears that the enhanced signal peak recorded during ascent at 85 km is present but much weaker on descent. The enhanced 5.3μm band radiance from Rocket 10.205-2 data below 110 km is presumably due to chemiluminescence, and this is confirmed by the signal in the 2.7μm band as will be discussed further on.

Figure 40 presents the data from the various rocketborne 3914Å radiometers in comparison with the 5.3μm data. For clarity, the 5.3μm data from rockets other than 10.205-2 have been averaged. The data suggest that NO chemiluminescence at 5.3μm is significant only with the brightest of auroras, perhaps approaching Class III. It is interesting to note from Figure 40 that chemiluminescent NO radiation might well have been recorded with 18.205-1 had the payload penetrated the auroral arc at a slightly lower altitude. Similarly, the auroral arc associated with 18.219-1 was certainly bright enough at times, but the payload was far above the region of NO chemiluminescence on these occasions.

It must be emphasized that the rocket instrumentation sensitivity decreases very sharply at wavelengths longer than 5.3μm. The instrument response is heavily weighted towards transitions from the lower vibrational states. Because of this, the instrumentation is less sensitive to emissions associated with $N(^2D) + O_2$ chemiluminescence than to emissions from reactions such as earthshine or NO + O that only excite the first vibrational level of NO.

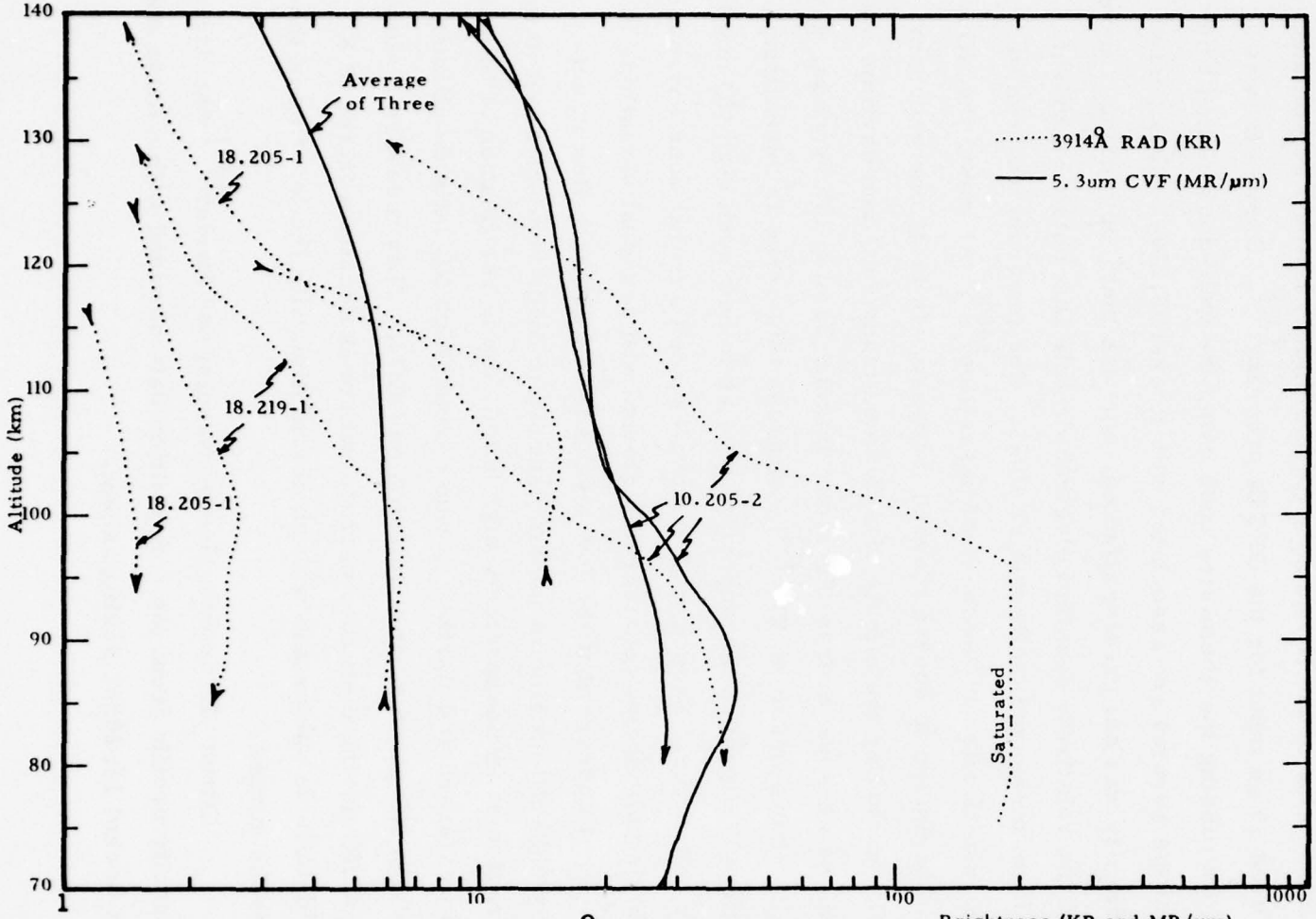

Figure 40 ICECAP Rocket 3914Å Radiometer and 5.3 μm Band CVF Data

Finally, there is the persistent problem of the ambient nitric oxide concentrations in the auroral region as a function of altitude. Several appropriate curves are presented in Figure 39. Curve "A" is the assumed value of the NO density for the middle latitude region and the one used as an input for the OPTIR program[45]. Curve "B" was obtained by running the chemistry code using the well-documented time history of the auroral arc associated with Rocket 18.219-1. Obviously, the NO density was not greatly affected, nor was the 5.3μm data. Curve "C" used the relatively constant electron drizzle flux outside a bright auroral form measured on Rocket 17.110-3. The program was run to show the results after 10^4 seconds of deposition[46]. At least, the NO density is beginning to show a marked increase. In fact, one program (ARCTIC), excluding the effects of diffusion, transport, and daytime solar radiation, using a low energy electron "drizzle" lasting 10^6 seconds, gave the results shown in Curve "D"[47]. Although this curve is unrealistic, it and Curve "C" provide an important clue as to how such high NO number densities can occur. Even though the oval-shaped auroral zone surrounding the magnetic pole shows considerable diurnal and seasonal variations in latitude[48], it appears that the low level auroral electron flux is sufficiently constant to maintain the ambient nitric oxide concentration in the auroral region at an unexpectedly high level. Some verification of this is provided by Gerard and Barth[49], who derived high NO latitude altitude profiles from NO gamma band emission on OGO4. They measure a slow build-up of NO during disturbed periods with peak density a factor of 8 above mid-latitude values and with no correlation with the location of the instantaneous aurora.

Curve "E" is provided by Narcisi and Swider[50] who derived the NO density profile from ion composition data obtained with a mass spectrometer on Rocket 18.205-1 during ascent.

Curve "F" represents the calculation of NO density from earthshine and collisional excitation using the values given in Table 5 for [NO], [O], and T. While the NO number density below 110 km (earthshine) in Curve "F" is the same order of magnitude as Curve "E", at higher altitudes (collisional excitation), the NO number density in Curve "F" is too high by about an order of magnitude.

Assuming the Narcisi/Swider profile is correct, then the two curves can be brought into agreement either by increasing the atomic oxygen number density and/or the collisional excitation rate. Between 200° K and 600° K, the reaction rate for collisional excitation is quite temperature dependent, changing by approximately four orders of magnitude. Several determinations are given in Figure 41. Even with the uncertainties in NO and O densities, the atmospheric temperature for temperatures below 600°K can be determined within a reasonable accuracy by using the drop in brightness of the 5.3 μm signals over specific increments of altitude. If the number of photons per cm^3 - sec created through collisional excitation is defined as "P", then

$$P = k\,[NO]\,[O]$$

where k is the reaction rate (cm^3-sec^{-1})

[NO] is the nitric oxide concentration (cm^{-3})

and [O] is the atomic oxygen concentration (cm^{-3})

In addition,

$$P = \frac{(\Delta I)(\Delta \lambda)}{\Delta H} \times 10^{12}$$

where ΔI is the drop in brightness over the altitude increment (MR/μm)

$\Delta \lambda$ is the bandwidth (0.3μm)

ΔH is the altitude increment used (5 km)

10^{12} is the conversion from MR to photons/sec

Combining the above equations, substituting, and solving for k yields

$$k = \frac{6 \times 10^5 (\Delta I)}{[NO][O]}$$

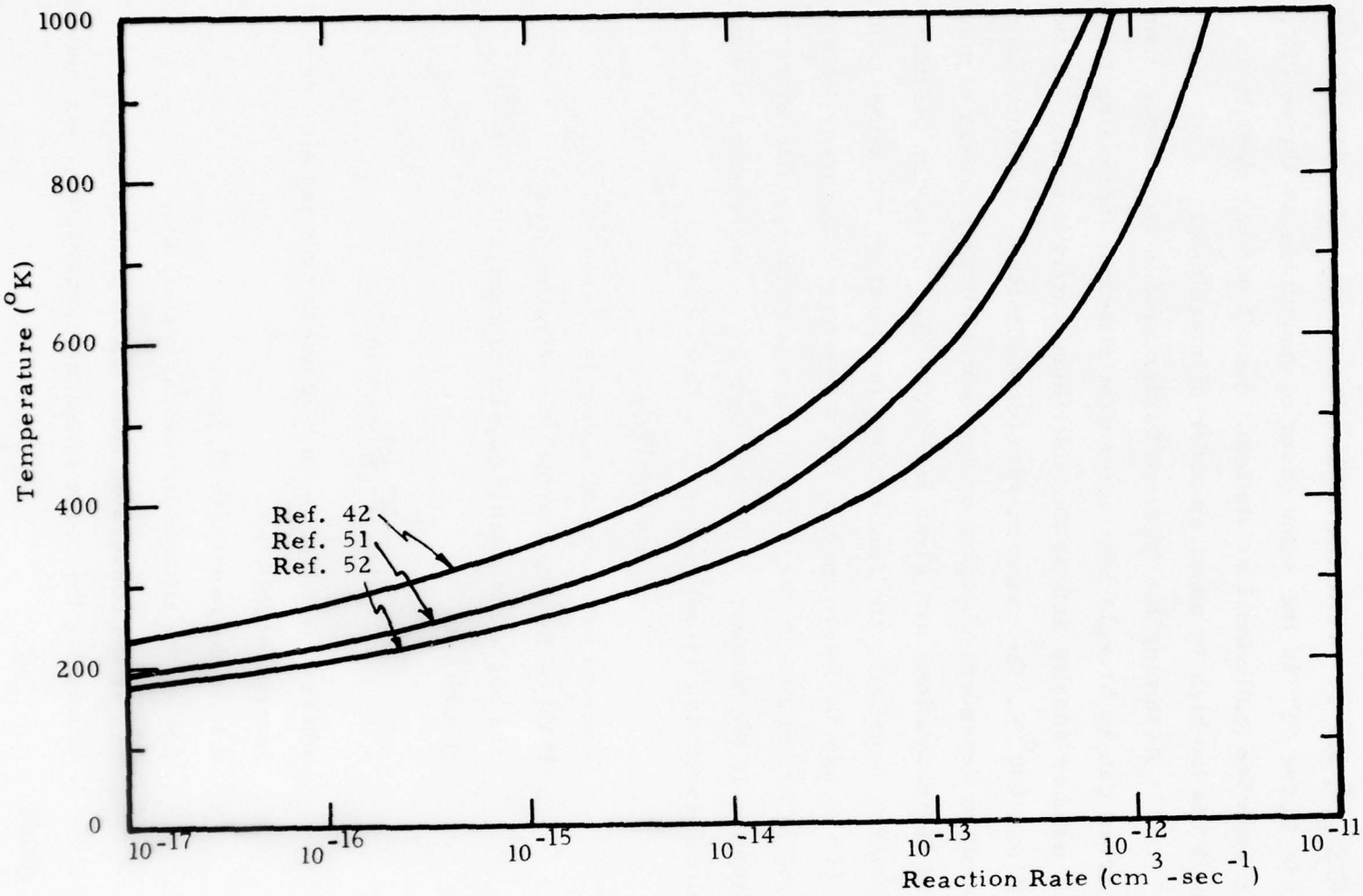

Figure 41 Rate Coefficient For O' + NO → NO' + O vs Temperature

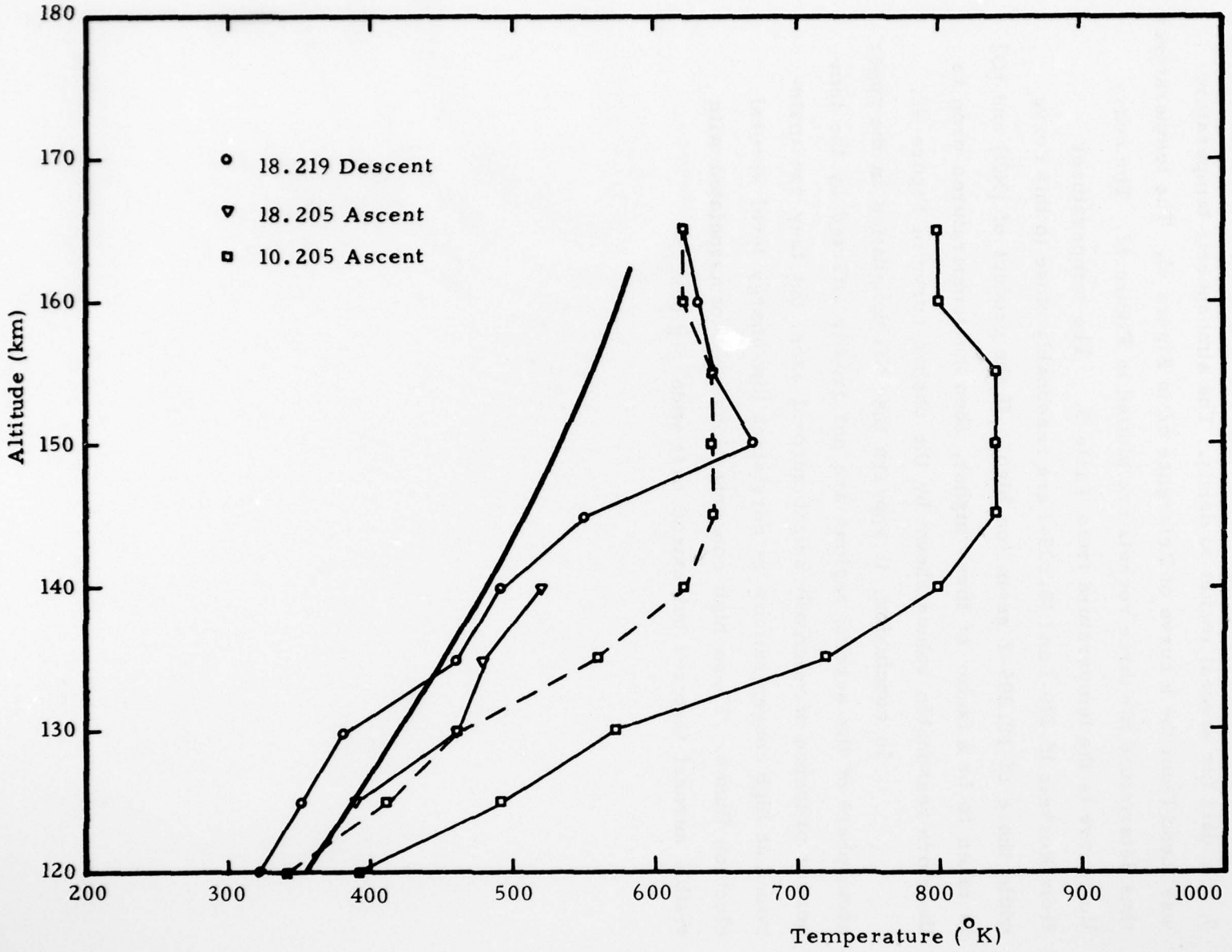

Figure 42 Atmospheric Temperature as Determined by the Collisional Excitation of NO by O

Values for [NO] and [O] were obtained from Reference 50 and Table 5 respectively. The k was determined using the ΔI's of the 5.3μm data for several rocket payloads. The atmospheric temperature was found from the k curve of Reference 52 in Figure 41. The temperatures thus determined for three rockets are plotted in Figure 42. The heavy line curve is the temperature from Table 5. The temperatures from Rockets 18.219-1 and 18.205-1 are reasonably close to this curve while those of 10.205-2 seem too high. If the product of [NO] and [O] is taken to be a factor of three higher, then the temperatures drop to the more reasonable values shown by the dashed curve in Figure 42.

In conclusion, it appears that NO densitities in the upper atmosphere of the auroral regions are not greatly affected by the temporary presence of relatively bright auroral arcs, but they are maintained at high concentrations by persistent low energy level auroral electron fluxes. These high concentrations are not associated with visible auroral features but extend over wide regions.

5.3 2.7μm Band

Measurements of emission in the 2.7μm band have been made as part of the ICECAP and EXCEDE programs.

The most common explanation of the auroral 2.7μm band is that it arises from the first overtone of vibrationally excited nitric oxide. Other emissions which might lead to 2.7μm data are the following:

1) CO_2, 101-000 transitions, band origins at 2.69 and 2.77μm
2) H_2O, 100-000 transition, band origin at 2.74μm
3) H_2O, 001-000 transition, band origin at 2.66μm
4) OH, $\Delta V = 1$, band origin at 2.80μm

Two CO_2 vibration-rotation bands originating on the ground vibrational state occur near 2.7μm wavelength. They are the 10011-00001 and 10012-00001 bands with band centers at 2.69 and 2.77μm, respectively. The upper level of each of these bands also gives rise to four other bands at longer wavelengths as shown in Table 6.

The enhanced vibrational excitation of atmospheric molecular nitrogen resulting from auroral electron bombardment enhances emission by CO_2 at 4.3μm, through the near resonant vibrational energy exchange process $N_2(V=1) + CO_2(00001) \rightarrow N_2(V=0) + CO_2(00011)$. The exchange processes

$$N_2(V=1) + CO_2(10001) \rightarrow N_2(V=0) + CO_2(10011)$$
$$N_2(V=1) + CO_2(10002) \rightarrow N_2(V=0) + CO_2(10012)$$

excite the upper levels that give rise to the 2.7μm bands. These processes are closer to exact resonance than that which excites the 00011 level.

Table 6 CO_2 Vibration-Rotation Bands

Band Designation		Band Center		Band Strength	Einstein A
Upper State	Lower State	μm	cm^{-1}	$cm^{-1}(molecule\ cm^{-2})^{-1}$	Coefficient sec^{-1}
10011	00001	2.64	3715	1.500 - 18*	15.60
10011	10002	4.12	2429	1.059 - 22	0.24
10011	10001	4.30	2327	1.183 - 19	411.1
10011	20001	10.90	918	8.7 - 25	0.44
10011	01111	14.07	711	2.02 - 24	6.75
10012	00001	2.77	3613	1.035 - 18	10.18
10012	10002	4.30	2327	1.934 - 19	408.1
10012	10001	4.50	2225	1.272 - 22	0.40
10012	20002	10.62	942	1.146 - 24	0.33
10012	01111	16.43	604	1.75 - 24	4.29

*1.500 - 18 is to be read as 1.500×10^{-18}.

If we assume equal reaction rates then the excited states will be produced in the ratio of the populations of the (00001) (10001) and (10002) states. Even if there is significant production of the 10011 and 10012 state, the branching ratio is such that only 2.5 to 4.0 percent of the resultant radiation is emitted at 2.7 μm; this may result in a detectable increase in CO_2 2.7 μm radiation during intense auroras.

The filter in the CVF spectrometer is a composite of short and long wavelength portions. In the instruments flown in rockets 18.205-1 and 10.205-2, the dividing wavelength is at 2.75μm, which tends to obscure some of the 2.7μm band data. However, on the 18.219-1 instrument, the short wavelength filter does not cut off until 3.2 μm.

Examination of Figures 9, 18, 24, and 25 reveals that 2.7μm band signals are readily detected only with rockets 10.205-2 and 18.219-1. In other cases, it is either buried in the noise or just detectable with a brightness approaching 1 MR/μm. The upleg data of rocket 18.219-1 show a systematic variation in signal strength indicating an instrumental problem. This is discussed in some detail in Appendix (B).

The 2.7 μm data for 10.205-2 and 18.219-1 are shown together with the 3914Å data in Figure 43. The 10.205-2 rocket data show 2.7 μm band signals well above the noise level. The brightnesses of various auroral features as functions of altitude are listed in Table 7, which also gives ratios of these to the 2.7 μm band. These ratios are plotted in Figure 44. The signal for the 5.3 μm band has been modified so that only the portion possibly due to chemiluminescence remains, as explained in Table 7. The ratios show that the 3914Å, 2.7 μm, and 5.3 μm brightnesses vary similarly with altitude. This is important if the 2.7 μm and 5.3 μm are both due to chemiluminescent NO, because the emission following the formation of NO is relatively fast (~0.1 sec) and the mechanism for the 3914Å radiation is prompt. The gross altitude variation of the

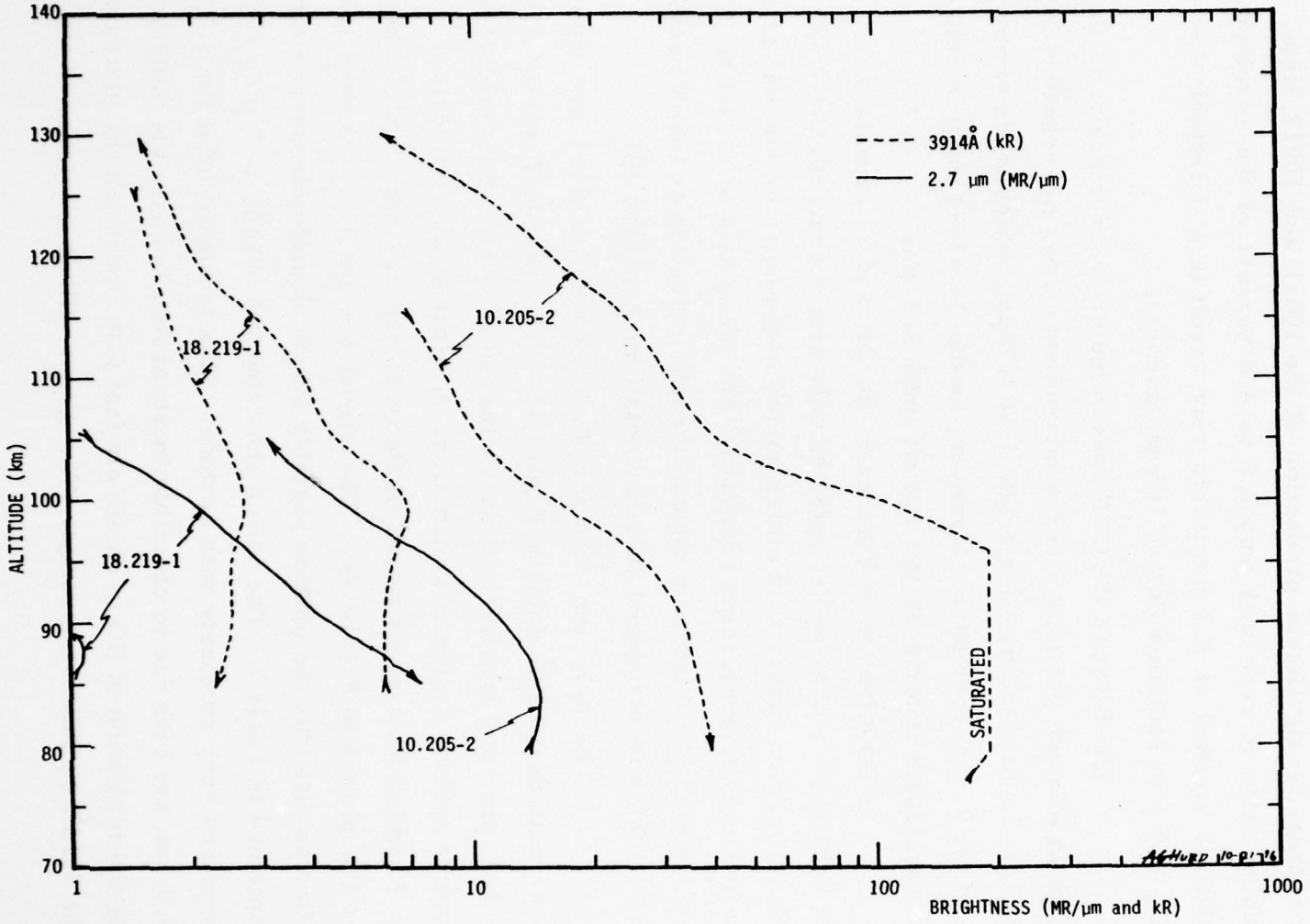

Figure 43 Auroral Data from Axially-Mounted Instruments

TABLE 7: RATIOS OF AURORAL BRIGHTNESS FROM AXIALLY-MOUNTED INSTRUMENT DATA

Altitude (km)	Auroral Brightness (MR/μm) 2.7 μm[1]	4.3 μm	5.3 μm[2]	3914A (kR)	Ratios to 2.7 μm 4.3 μm	5.3 μm	3914Å
10.205-2 ROCKET, UPLEG							
80	12	(3)	18	~200	(3)	1.5	~15
85	13	(3)	24	(4)	(3)	1.8	(4)
90	11	125	21	(4)	11	1.9	(4)
95	7	110	14	~200	16	2.0	~29
100	4	50	7	110	13	1.8	27
105	1	15	~2	40	16	~2	40
18.219-1 ROCKET, DOWNLEG							
105	.9	9	0.9	2.5	10	1	2.8
100	1.4	22	0.9	2.7	16	0.6	1.9
95	2.8	50	1.4	2.5	18	0.5	0.9
90	4.5	(3)	1.1	2.5	(3)	0.2	0.6
85	7.5	(3)	1.1	2.3	(3)	0.1	0.3

NOTES:

(1) System noise levels of 2 MR/μm for 10.205-2 and .25 MR/μm for 18.219-1 subtracted
(2) Background of 18 MR/μm subtracted for 10.205-2 and difference between upleg and downleg used for 18.219-1.
(3) Optically thick
(4) Photometer saturated

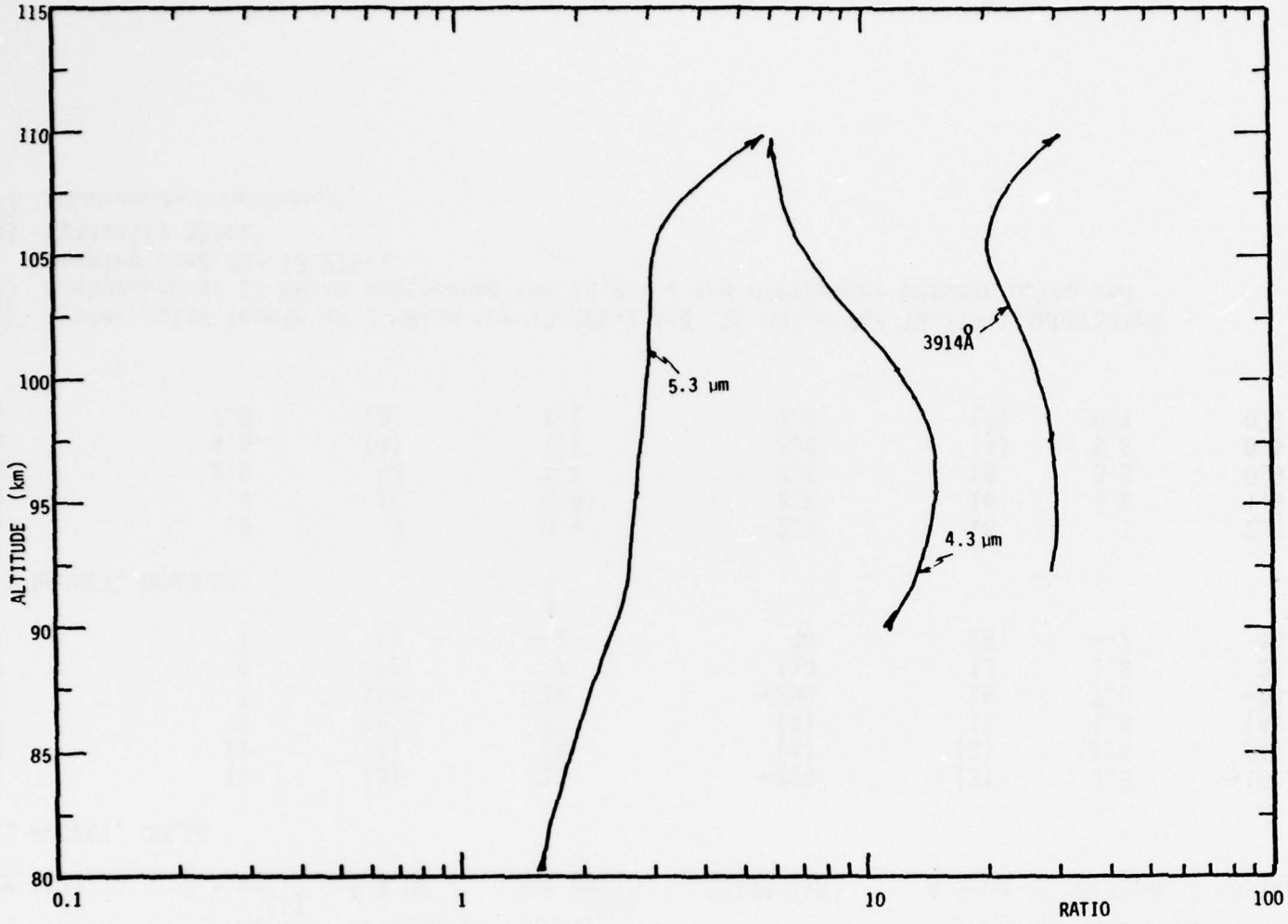

Figure 44 Rocket 10.205-2 Ratio of Various Wavelengths to 2.7 μm Peak Brightness

4.3 μm radiation on upleg is opposite to that of the 3914Å and 5.3 μ. However, no data can be compared below 90 km because the 4.3 μm band is optically thick. The upleg data are consistent with the assumption that the 2.7 μ emission is the NO overtone from chemiluminescence.

The ascent data of rocket 10.205-2 can be used to determine the percentage of incident auroral energy which is emitted in the 2.7 μm band. Previous determinations have shown that the efficiency of 3914Å radiation from auroral electrons is 4×10^{-3}. Using this number and an average brightness ratio of 2.7 μm to 3914Å from Table 7, noting that the per photon energy ratio of 2.7 μm to 3914Å is .145, and assuming a 2.7 μm bandwidth of 0.3 μm, then the efficiency for 2.7 μm radiation is about 1%.

The 10.205-2 rocket data taken during descent show possible enhancement of the 2.7 μm band below 100 km. Qualitatively, the data are poor because of telemetry dropout. Below 80 km, the rocket began to tip over.

The 2.7 μm data associated with Rocket 18.219-1 is quite another story. During ascent, the 2.7 μm signal is barely detectable below 115 km at which point the motor moves into the field-of-view (Appendix B); but during descent, it is detectable at 105 km, and by the time the payload begins to tip over at about 85 km, it has increased to the point that it even exceeds that of the 5.3 μm band. The values of the various brightnesses are listed in Table 7 together with ratios to the 2.7 μm band radiance, which are also plotted in Figure 45. Obviously, the 2.7 emission is not tracking the prompt emission at 3914Å and the behavior appears qualitatively different from the upleg of Rocket 10.205-2. We consider this increase below 105 km on downleg to be an artifact of the measurement associated with the rocket wake and not an emission from the aurorally perturbed atmosphere. This is based on the following observations which are discussed in detail in Appendix B.

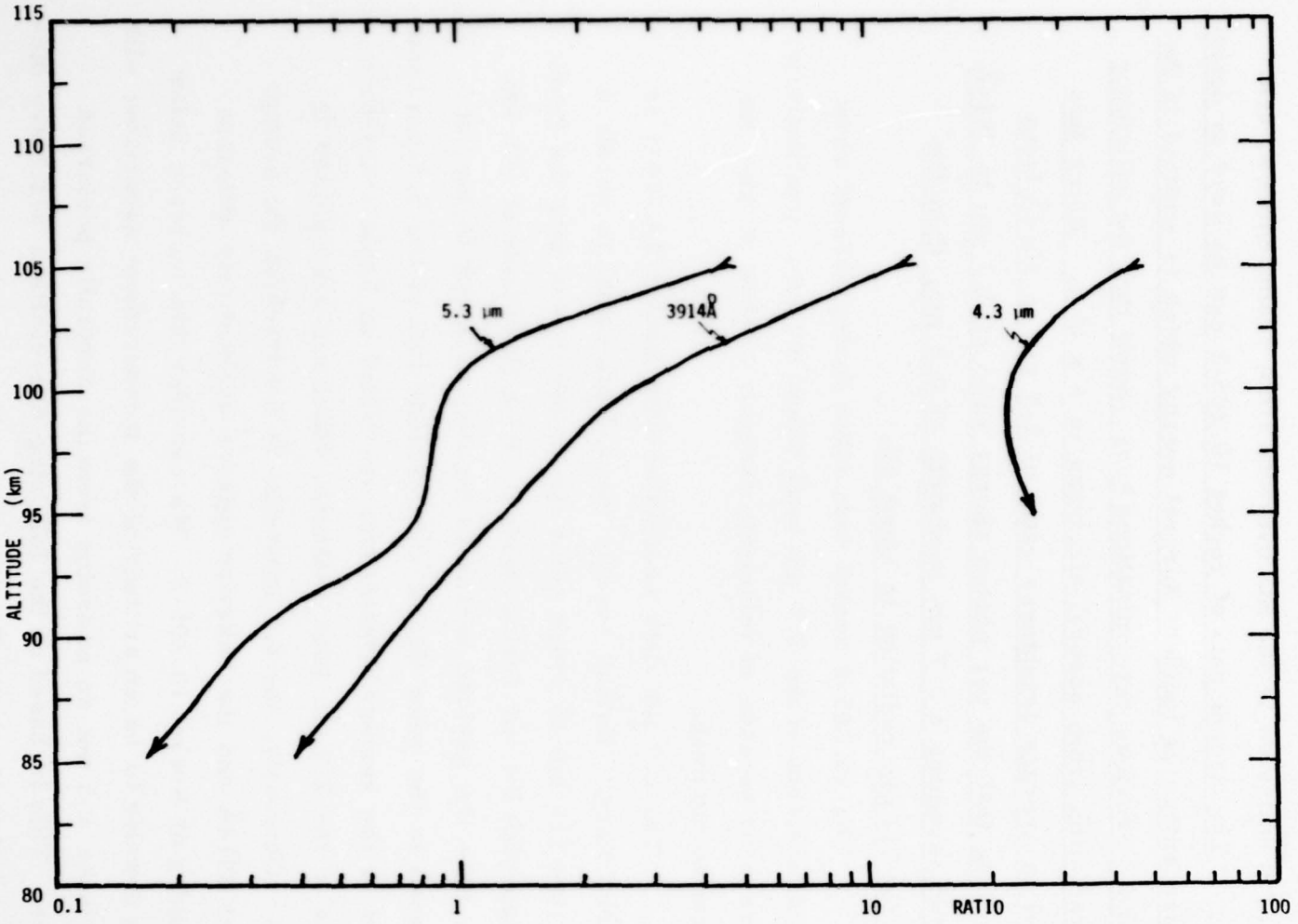

Figure 45 Rocket 18.219-1 Ratio of Other Wavelengths to 2.7 μm Peak Brightness

1. The rocket on downleg is tilted slightly to the south. The vertical looking instrumentation is looking through the rocket wake.

2. The 2.7 μ emission increases monitonically until rocket starts to tip over. The dependence of intensity with elevation angle is not consistent with that which would be observed either from an optically thick or an optically thin emitter. Rather, the behavior is indicative of emission from a small region (e.g., the rocket wake).

3. The ratio of 2.7 μm side looking (radiometer) signal to vertical looking CVF is different on upleg and downleg. The side looking radiometer clearly does not show the enhancement on downleg shown by the vertical looking CVF.

4. The behavior of the band center is qualitatively different on 18.219 downleg from 10.205 upleg and from that measured on 519.07. Figure 46.

5. If the mechanism producing the 2.7 μ emission is closely coupled to the 4.3 μ emission, the 2.7 μ emission should have been seen on upleg of 18.219 when the 4.3 emission exceeds 10 MR/μm at 100 kilometers. It was not. (Figure 18)

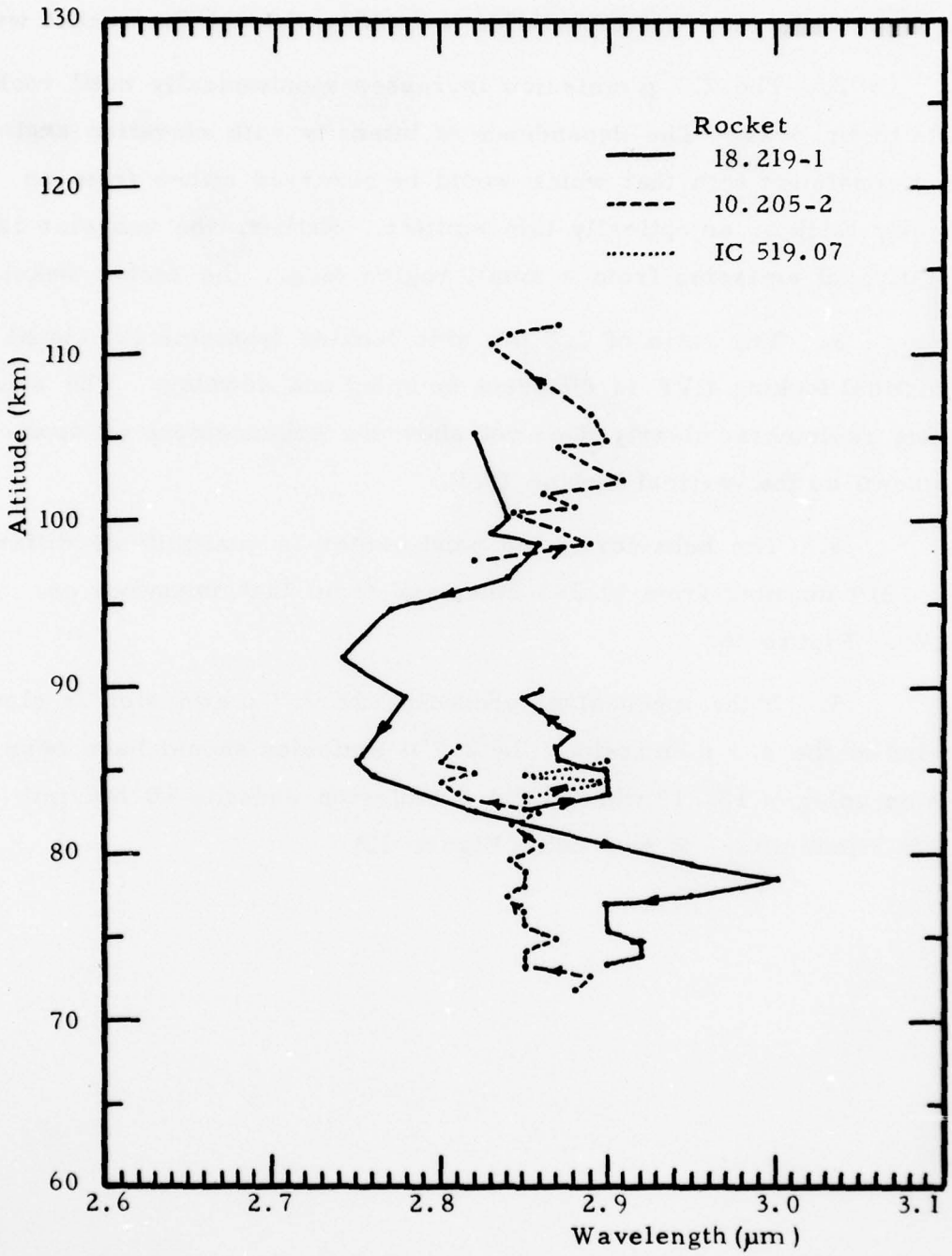

Figure 46 2.7μm Band Center Wavelength

5.4 4.3μm Band

The present conclusion is that the source of radiation in the 4.3μm band is vibrationally excited CO_2 resulting from the energy transfer $N_2(V) + CO_2 \rightarrow N_2 + CO_2(001)$. In addition, NO^+ chemiluminescence resulting from reactions such as $O_2^+ + NO \rightarrow O_2 + NO^+$ and $N_2^+ + O(^3P) \rightarrow NO^+ + N(^4S)$ also occurs in a band at 4.3μm. However, this has generally been ruled out as an appreciable fraction of the 4.3μm auroral signal for the following reasons:

1. The NO^+ spectrum is much wider than that recorded by the CVF spectrometer[53].
2. The NO^+ spectrum shape differs from that of the data[53].
3. The time and altitude variations of the 4.3μm band data are poorly matched to those resulting from an analysis of the NO^+ radiation mechanism[54].
4. The center wavelength of the 4.3μm band data is essentially constant at all altitudes, indicating only one mechanism predominates throughout[17].

It is believed that the excited NO^+ is quenched by vibrational transfer to N_2.

The 4.3μm emission resulting from CO_2 excited by earthshine has been calculated as being of little significance [56].

The CVF spectrometers and infrared radiometers provided good data since their InSb detectors have peak sensitivity near 4.3μm, and there is no spectral break in the filter near 4.3μm.

Figure 47 shows the 4.3μm CVF spectrometer data from four rocket probes. There is a wide range of brightness levels, as is to be expected if the excitation mechanism is directly related to the auroral arc energy deposition profile.

The NIKE-JAVELIN (NJ-74)[24] is the only rocket flight shown which may require an additional mechanism for excitation at 4.3μm. This rocket was intended to provide background measurements during a quiet period with little auroral activity. Figure 48 compares the results of this flight with predicted night levels of 4.3μm brightness. At 90 km and above, the measured radiance level is about four times that predicted by calculation. A possible explanation for the difference is that winds have transported air subjected to auroral bombardment from farther North. This is plausible, as shown by a computed brightness that corresponds to the decay of radiance from a strong arc at a time 3.16×10^3 seconds after the excitation is turned off. Another mechanism is vibrational excitation of molecular nitrogen by quenching of vibrationally excited OH, suggested by Kumer, et. al.[57]. Using the recent measurements of Streit and Johnston[58], we have found that significant enhancement of N_2 vibrational levels can occur during nights of strong hydroxyl emission. If the upleg signal increase between 75 and 85 km is correct, the hydroxyl mechanism may be the main contribution to the signal.

A similar explanation may be required for the downleg portion of the 18.205-1 rocket measurements. In this case there was sufficient nearby auroral activity to make wind transported excited air an attractive explanation. Figure 49 compares upleg and downleg brightness values with a calculation of auroral brightness corresponding to 10^3 seconds of excitation by a strong arc, of about IBC II intensity.

Figure 50 compares observations and calculations for the Black Brant 18.219-1 rocket. The analytic techniques used to process the raw

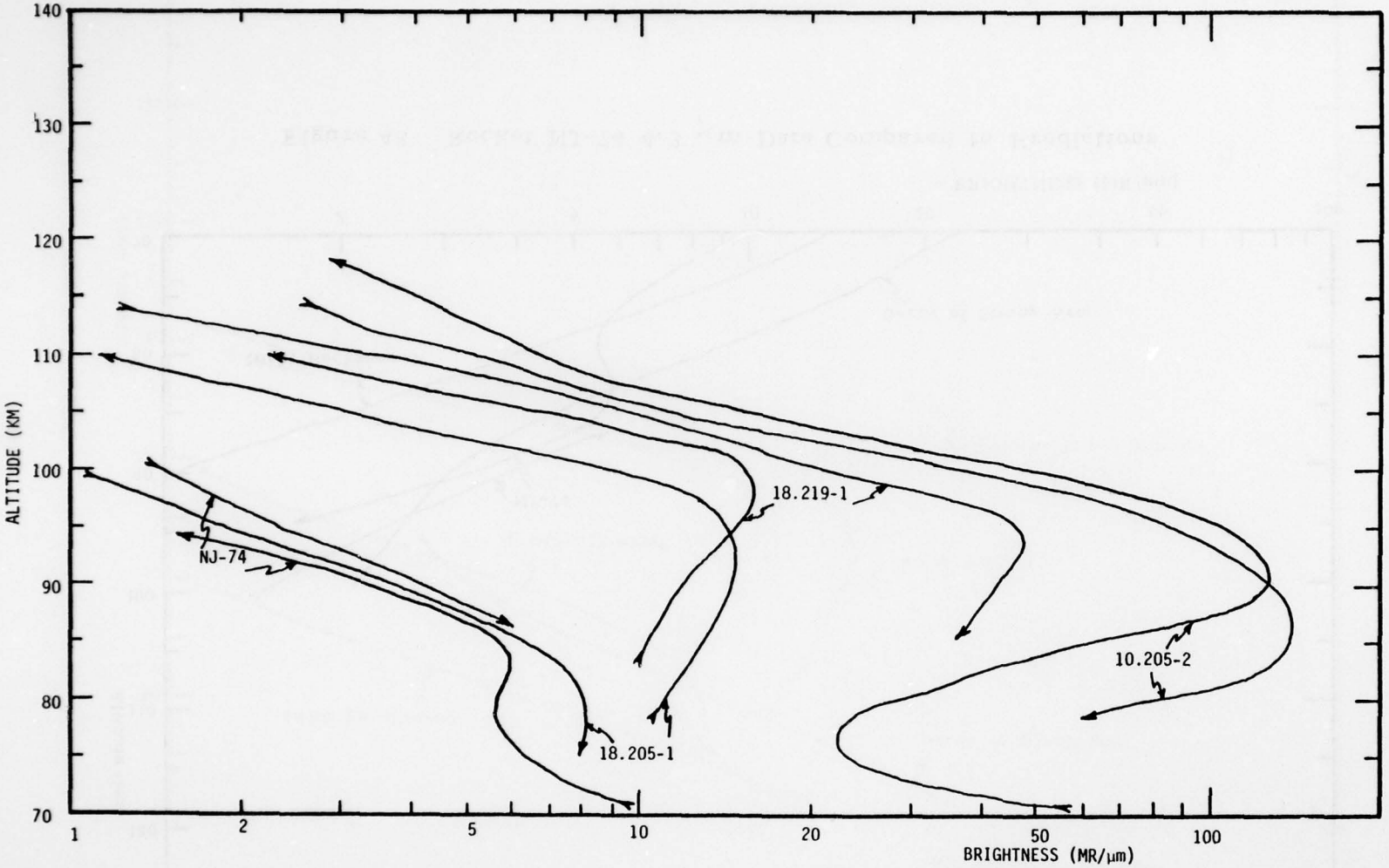

Figure 47 4.3 μm Band CVF Data for Various ICECAP Rockets

AD-A047 526 VISIDYNE INC BURLINGTON MASS F/G 4/1
COMPARISON OF ICECAP AND EXCEDE ROCKET MEASUREMENTS WITH COMPUT--ETC(U)
FEB 77 A G HURD, J W CARPENTER, T C DEGGES F19628-74-C-0177
UNCLASSIFIED VI-381 AFGL-TR-77-0060 NL

2 OF 3
ADA047 526

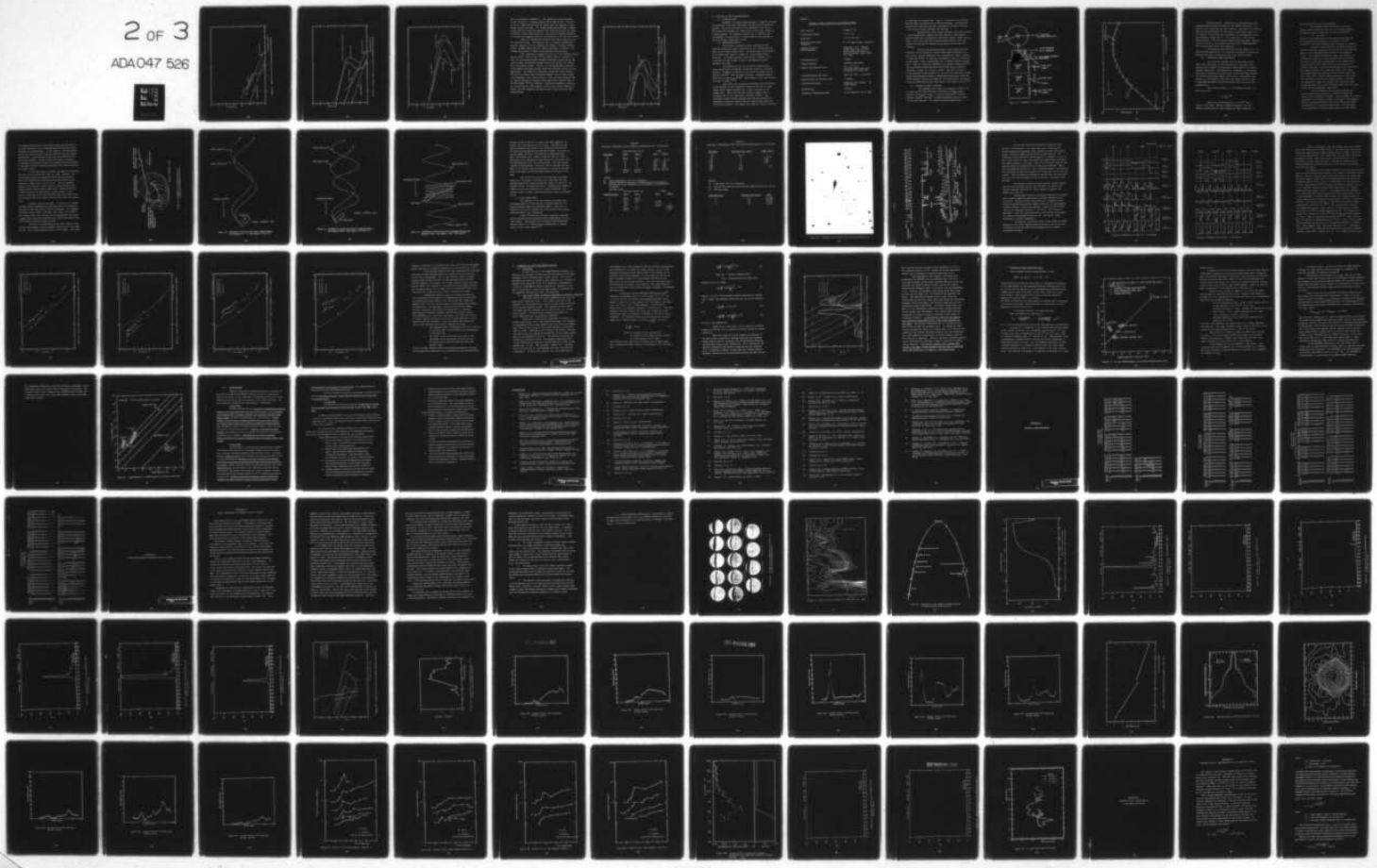

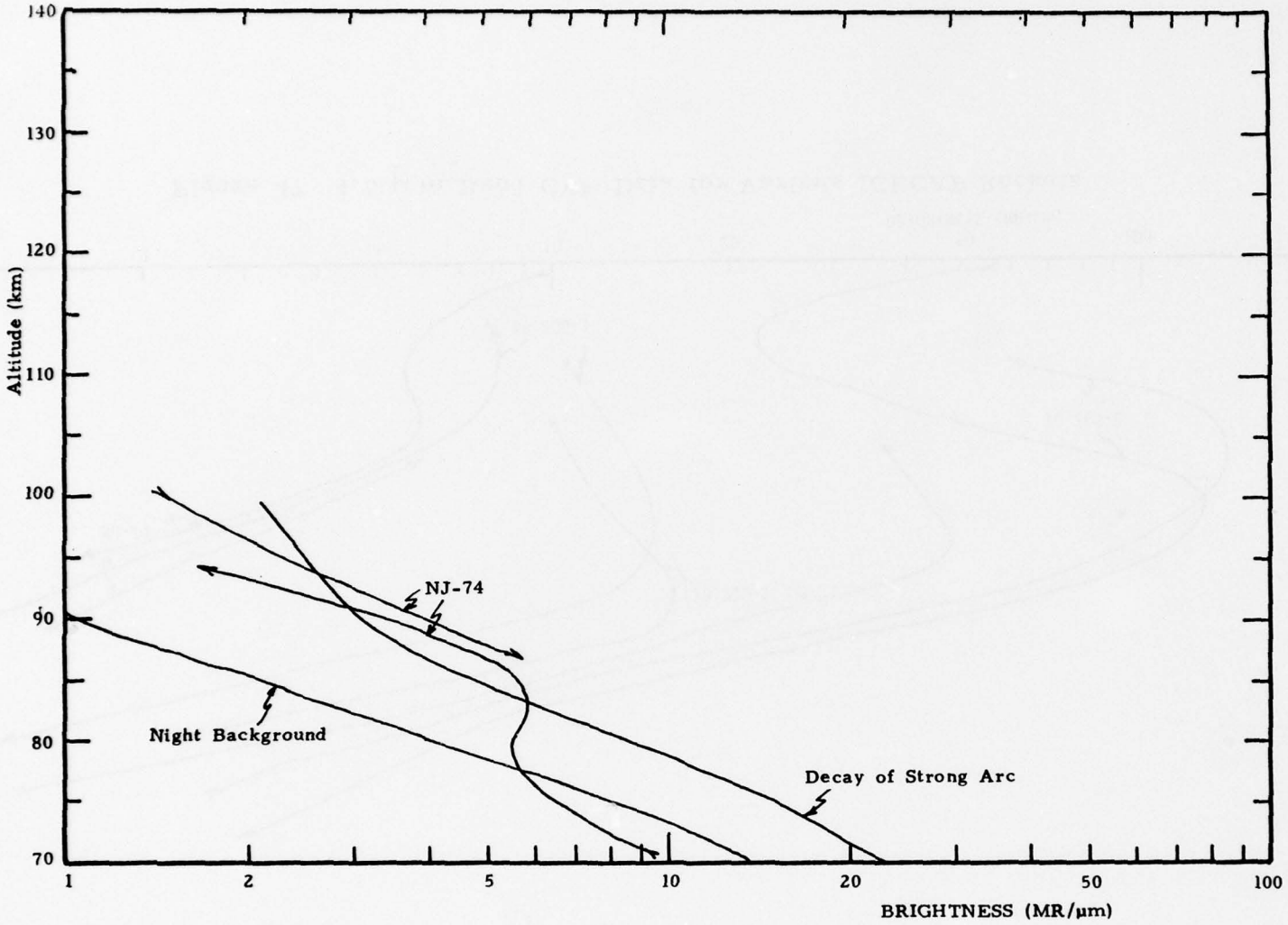

Figure 48 Rocket NJ-74 4.3 μm Data Compared to Predictions

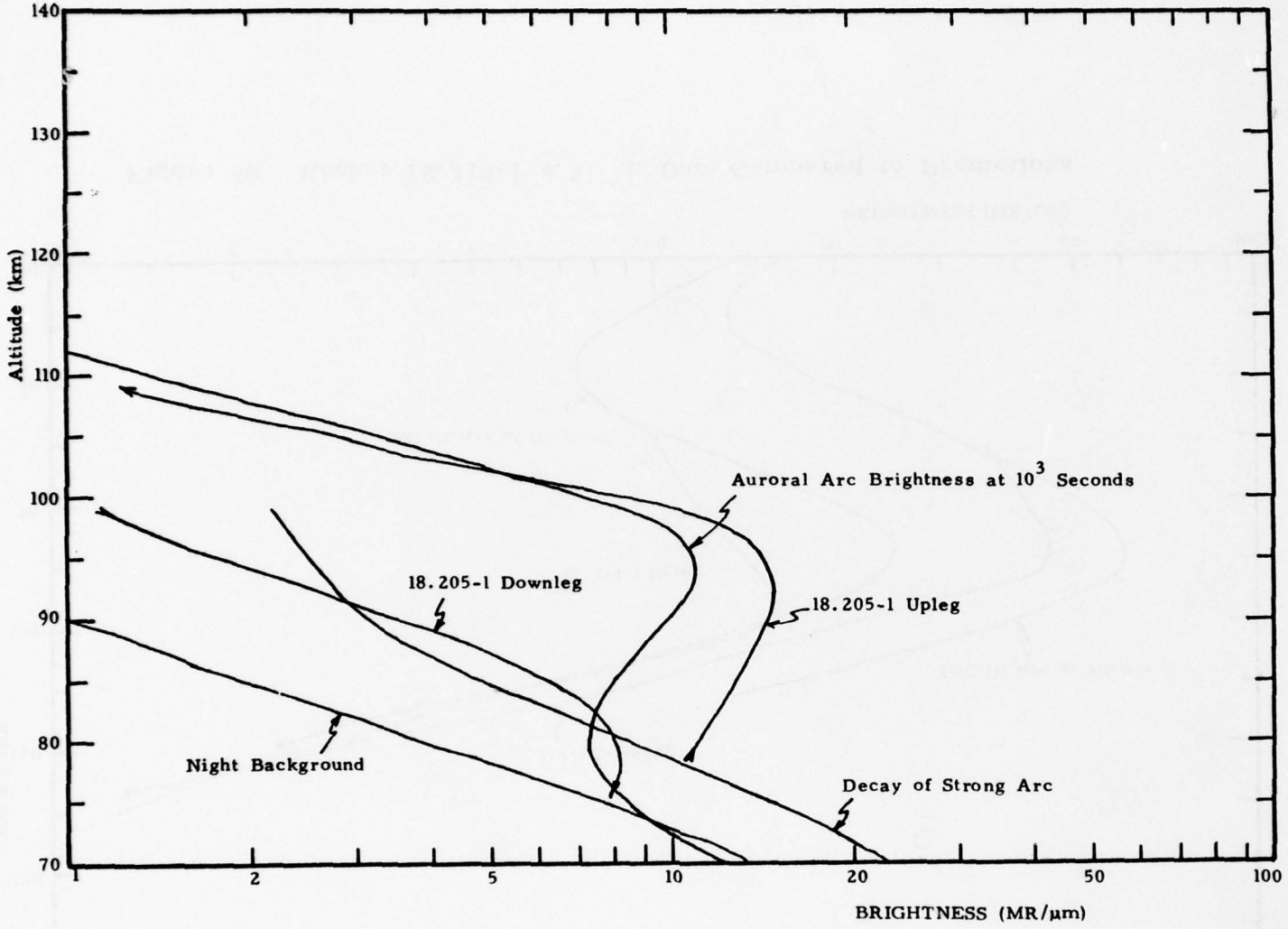

Figure 49 Rocket 18.205-1 4.3 μm Data Compared to Predictions

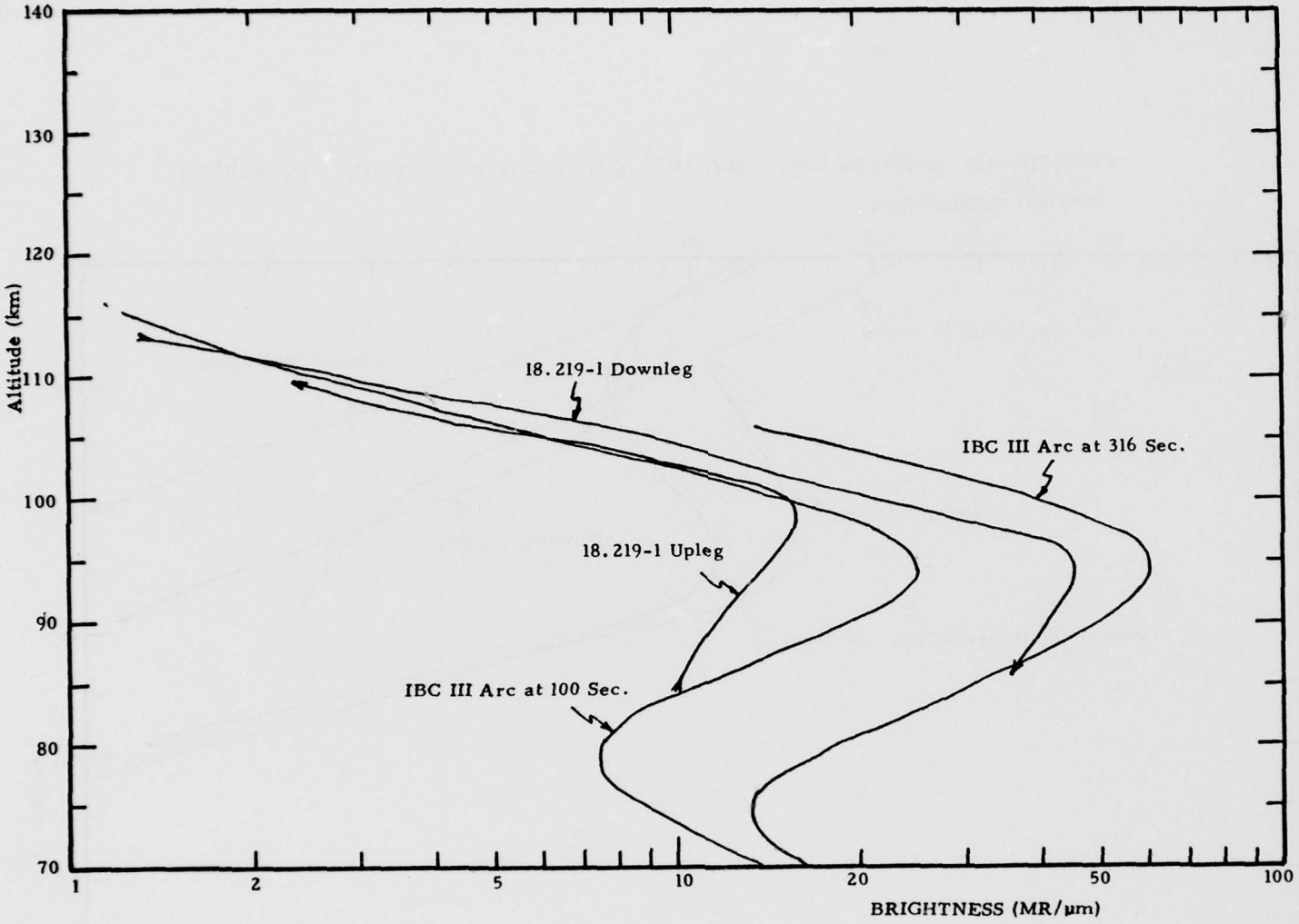

Figure 50 Rocket 18.219-1 4.3 m Data Compared to Predictions

data are presented in Appendix C. The upleg was a passage through an IBC II aurora in a region predosed with an IBC III flux. The peak occurs at a higher altitude than the downleg peak and suggests a lower energy electron spectrum. The downleg flight passed through a rapidly moving IBC III arc which had passed to the North by the time the rocket entered the auroral region on descent. The measured downleg brightness is bracketed by computed values for an IBC III arc at 100 and 316 seconds.

Figure 51 compares the 10.205-2 data with an IBC III arc at 316 and 1000 seconds. The spectrum used to compare deposition has electron energies too low to reproduce the altitude of the peak radiance values. A higher energy and more intense deposition is required. The downleg data requires a higher energy spectrum than the upleg.

The calculations we have made for the 4.3 μm radiance include only the 00011 - 00001 of the $^{12}C^{16}O_2$ isotopic species. Inclusion of other 4.3 μm transitions which exchange vibrational energy with N_2 will act to increase the computed radiance values and decrease the storage time of vibrational energy. The use of a one-dimensional formulation of the radiative transport problem means that calculated results are only approximate. The build-up of vibrational excitation at lower altitudes will not be as rapid as the calculations indicate, and the power profile of the brightness curves will be steeper. This increased steepness will be offset by inclusion of radiances from bands not as optically thick as the 00011-00001 $^{12}C^{16}O_2$ transition. Within these limitations, however, we conclude that the main features of the 4.3 μm auroral radiation is known, and time dependent calculations yield results that agree with measurements.

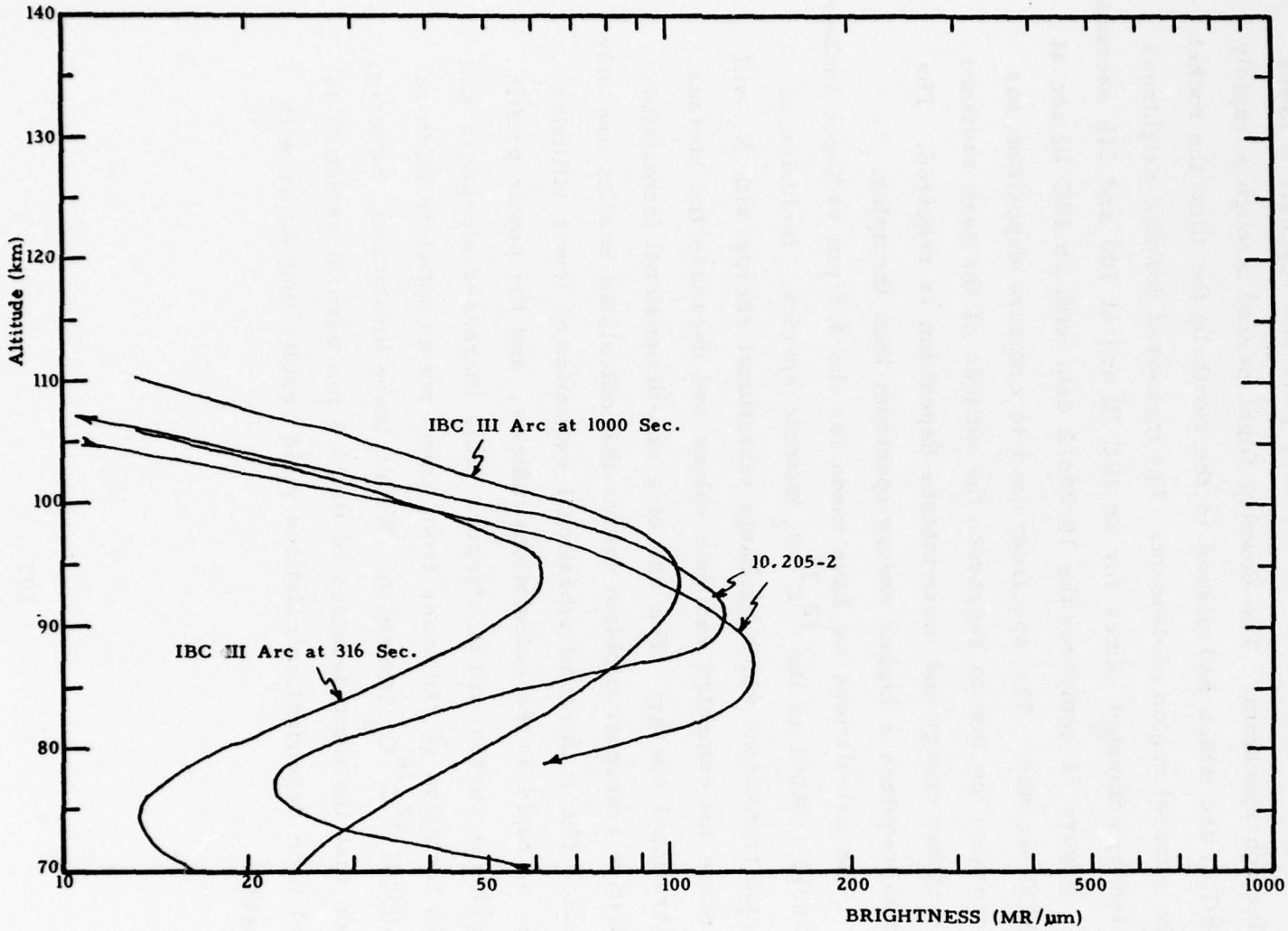

Figure 51 Rocket 10.205-2 4.3 μm Data Compared to Predictions

6.0 EXCEDE II TEST MEASUREMENTS

6.1 INTRODUCTION

EXCEDE is an experimental program to study the emission and chemistry of the upper atmosphere at high levels of energy deposition. The primary objective of the EXCEDE II Test was to demonstrate the operation of a high power (30 kw) E-gun system on a rocket payload. An additional objective was to determine the compatability of various types of instrumentation when operated in close proximity to high power E-guns.

6.2 INSTRUMENTATION

The electron accelerator module consisted of three separate electron gun units, each having its own electron gun and high and low voltage battery banks. An electron gun unit consisted of an electron gun chamber mounted on a high voltage battery enclosure. The battery enclosure had pressure integrity so as to maintain all high voltage circuits at atmospheric pressure throughout the flight.

The electron gun for the accelerator module uses a strip cathode made of lanthanum hexaboride, heated by a tungsten filament. Lanthanum hexaboride is not readily poisonable and can operate at 1700°K. For equivalent emission, a tungsten filament would have to operate at 2600°K. Specifications of the electron gun are given in Table 8 [59].

One of the most significant technology advances achieved in the EXCEDE II Test accelerator design was the use of a high voltage power supply comprised of a series connection of low voltage cells. The use of this type of power supply made unnecessary the use of a high power converter-rectifier. The elimination of this circuitry improved the inherent reliability of high power accelerator systems and also reduced both weight and cost of such systems. The battery was made of a series connection

TABLE 8

EXCEDE II TEST ELECTRON GUN SPECIFICATION

Beam Current:	5 amps at 3 kv
Accelerating Voltage:	1 kv to 5 kv
Beam Size:	1 cm x 10 cm typ.
Maximum Beam Angular Divergence:	5^{o}, 1/2 angle (design parameter)
Maximum Filament Power Required:	Operating, 1 kw. Filament voltage will be 10 volts DC. Beam current will not be reduced if filament voltage drops to 9 volts.
Filament Material:	Tungsten
Cathode Material:	Lanthanum Hexaboride
Range of Operating Pressure:	$\leq 1 \times 10^{-4}$ torr All performance testing will be done at $< 5 \times 10^{-6}$ torr
Typical Operation Duty Cycle:	50% (1 sec ON - 1 sec OFF)
Operating Time at 50% Duty Cycle:	5 minutes
Cooling Requirements:	Conductive and radiative. No liquid cooling
Filament Life:	20 hours
Mechanical Package Size (max):	10 cm diameter x 40 cm long

of 1,824 high rate lithium cells. Thus, a 3 kv electron accelerating potential with 5 amp beam current could be obtained. By splitting the payload 30 kw requirement into two independent 15 kw power sources, a much greater system reliability was achieved.

Measurements of the energy spectrum of the beam electrons as they returned to the payload skin were made by an Electrostatic Analyzer (ESA) which measured the differential electron energy spectra below 5 keV, and a Retarding Potential Analyzer (RPA), which was capable of measuring the integral energy spectra of both ions and electrons.

Optical instrumentation included a dual-channel infrared radiometer for measuring the electron beam induced emission at 2.7 and 4.3 um, and two photometers for measuring the visible irradiance at 3914Å and 5577Å. To determine the magnetic aspect of the payload during flight, a single magnetometer was co-aligned with the electron guns. Figure 52 shows the EXCEDE II Test payload configuration[59]. The implemented experiment plan did not include booster-payload separation, an ACS, or a recovery system. The spin rate was to be fin controlled to approximately 2.7 rps (1.85 rps achieved). Ground-based instrumentation included a telephotometer measuring 3914Å and 5577Å emission, and four low light level television systems situated at selected geophysical positions with respect to the rocket trajectory[60].

6.3 ROCKET FLIGHT SUMMARY

The EXCEDE II test rocket was launched at 0946.00 UT on April 13, 1975 from the Poker Flat Research Range during a period of low auroral activity. From the Trajectory[61] and Preliminary Aspect[62] Reports, the flight information shown in Figure 53 has been extracted. The vehicle performed satisfactorily.

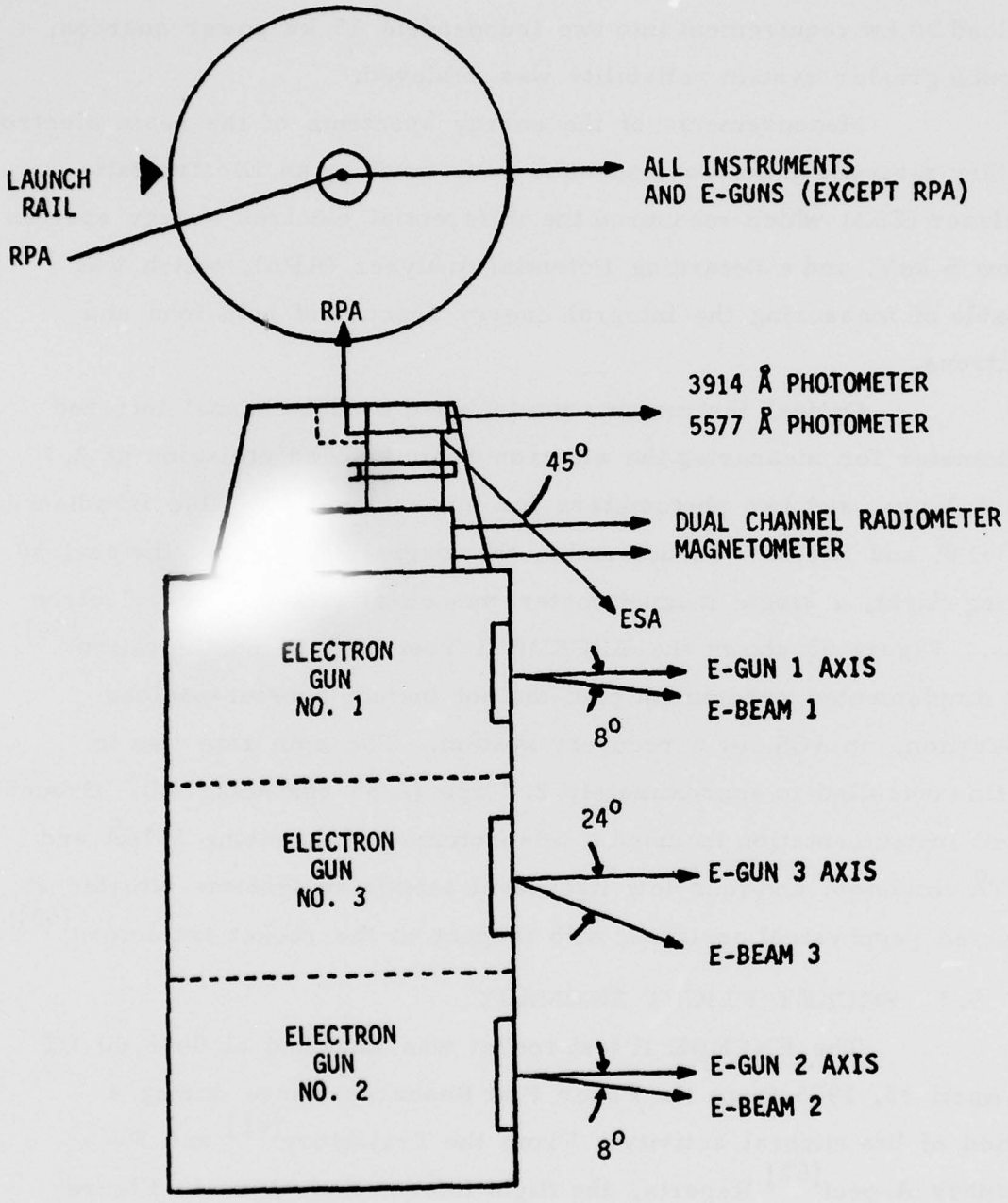

Figure 52. EXCEDE II Test Payload Configuration

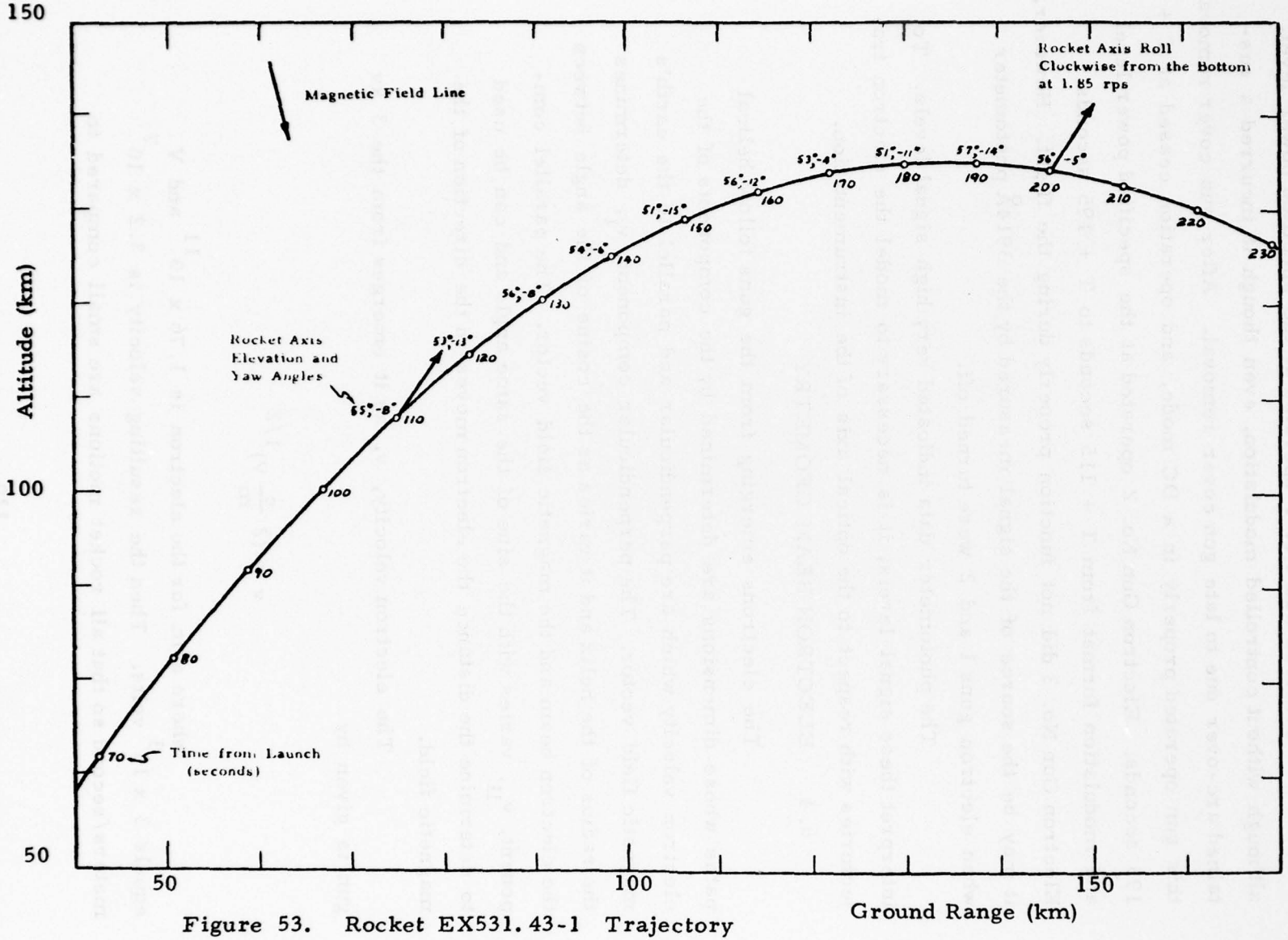

Figure 53. Rocket EX531.43-1 Trajectory

Electron Gun No. 1 operated at the specified power level, although without controlled modulation, even though it incurred a sustained arc-over due to late gun cover removal. After gun cover removal, this gun operated properly in a DC mode, and operation ceased at T + 195 seconds. Electron Gun No. 2 operated at the specified power level and modulation format from T + 115 seconds to T + 195 seconds. Electron Gun No. 3 did not function properly during the flight. However, it may be the source of the signal measured by the 3914Å photometer when electron guns 1 and 2 were turned off.

The photometer data indicated very high signal levels. To interpret these signal levels, it is necessary to model the electron trajectories with respect to the optical axis of the instrumentation.

6.4 ELECTRON BEAM GEOMETRY

The electrons emerging from the guns follow helical paths whose dimensions are determined by the components of the electron velocity which are perpendicular and parallel to the earth's magnetic field vector. The perpendicular component, v_1, determines the radius of the helix and it varies as the cosine of the angle between the electron beam and the magnetic field vector. The parallel component, v_{11}, varies with the sine of the same angle and can be used to determine the distance the electron moves in the direction of the magnetic field.

The electron velocity, v, as it emerges from the 3 kv gun is given by

$$v = (2 \frac{e}{m} V)^{1/2}$$

where e/m for the electron is 1.76×10^{11} and V equals 3×10^{3} volts. Then the resulting velocity is 3.2×10^{7} meters/second so that all rocket motions are small compared to

the electron motions and can be neglected.

The maximum radius of the helix is when the electron beam emerges from the gun in a direction normal to the magnetic field, in which case the radius of the helix is

$$r = v\,(B\ e/m)^{-1}$$

where B is the magnetic field in the region of the trajectory and whose value from Reference 62 is about 5.3×10^{-5} webers/m^2. Then the maximum radius is equal to 3.4 meters.

It became obvious that the most logical approach to finding any possible intersection of the electron beams with the fields-of-view of the photometers would be to use graphical means. Two mutually perpendicular planes were chosen, one containing the rocket axis and the magnetic field lines which intersect it and the other perpendicular to the magnetic field. This permits the helical paths of the electron beams to be drawn as sine waves in the former plane and circles in the latter. Spin angles about the rocket axis were chosen in 15° steps. The supplementary angle between the field and the rocket axis was chosen as 50°, which is within four degrees of the actual value throughout the entire data taking portions of the flight. The photometers looked out normal to the rocket axis while the electron beams were pointed 8° below normal but in the plane of the rocket and photometer optical axes.

A scale drawing of 10.1 was made assuming one electron gun and two photometer positions to simplify the number of helical paths to be plotted. The horizontal and vertical components of the electron velocity with respect to the magnetic field were determined and the portions near the rocket of the helical paths for various spin angles drawn. The look angles of the photometers for the same spin angles were then drawn.

The apparent intersections of the electron beams and the fields-of-view were determined in the horizontal plane and then the location checked in the vertical plane. In this manner, it was determined that the two did not intersect near the rocket for any spin angle. Consequently, a scale drawing of 100:1 was made and the electron beam paths replotted. Figure 54 shows the circular projection of the helices in the plane normal to the magnetic field and Figures 55 through 57 show the sinusoidal projections in the plane parallel to the magnetic field.

For the spins angles not shown, the apparent intersection does not occur in at least one of the two views. Moreover, for the spin angles shown, the graphical solution demonstrated that there is no intersection of the primary electron beams and the photometer fields-of-view, not even close. The one exception appears to be when the velocity vector is nearly normal to the magnetic field so that the helix closes into a cylindrical surface. It should be pointed out that when the velocity vector is very close to being normal, the electron beams make one circular orbit and strike the body of the rocket on the side away from the electron guns.

Failing to find any intercept, or at least one to explain the high intensity photometer data, the next step was to determine the effect of the rocket velocity along its trajectory. For although the lifetime of the 3914$\mathring{A}$ is extremely short, that of the 5577$\mathring{A}$ is long enough so that if the field-of-view of the photometer intersects a region where the electron path had been a short time before, then 5577$\mathring{A}$ radiation would be readily detected.

The first case chosen was for the rocket velocity vector normal to the magnetic field and with the rocket axis at a yaw angle of -10^{o}. This is approximately true at T+ 160 seconds. The rocket

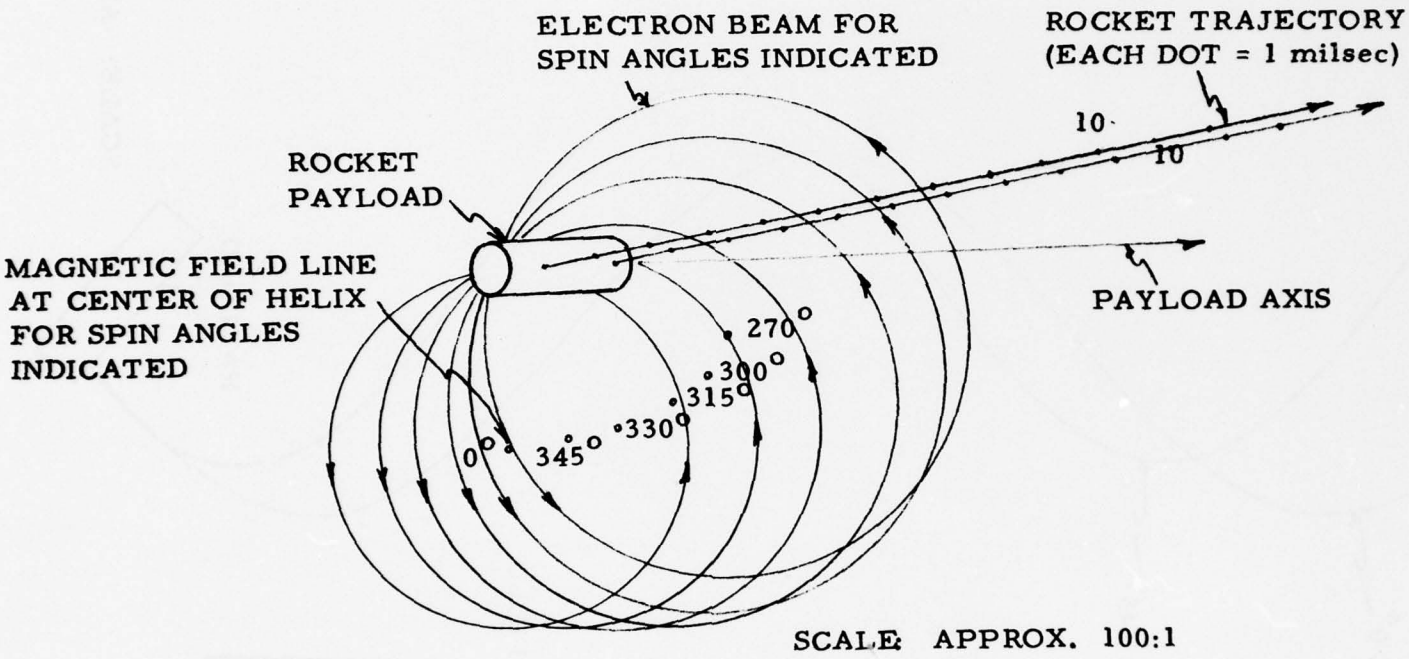

Figure 54. EXCEDE II Test Electron Beams
Looking up the Magnetic Field Lines

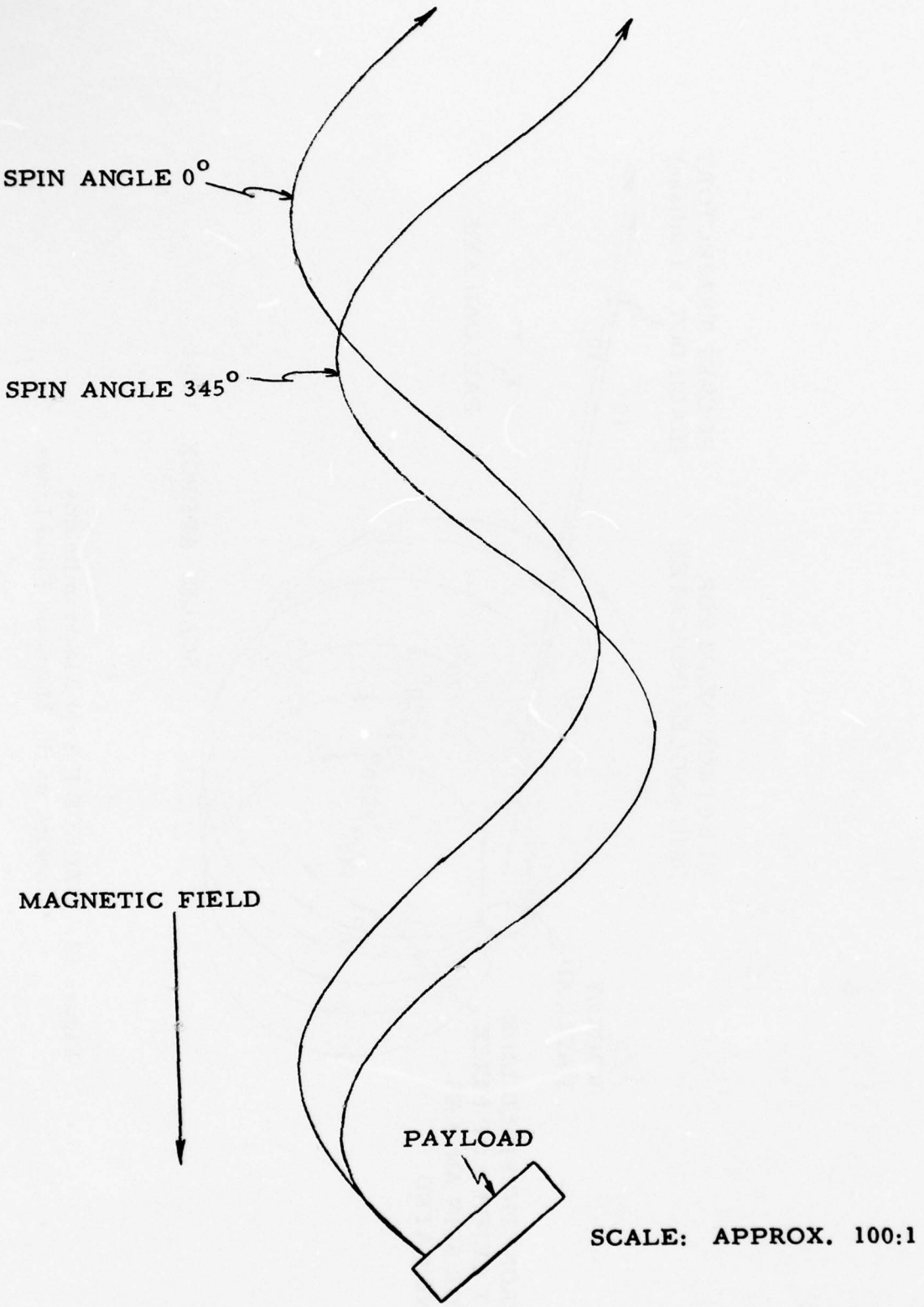

Figure 55. EXCEDE II Test Electron Beams Looking Normal to the Magnetic Field. Spin Angles: 0° and 345°

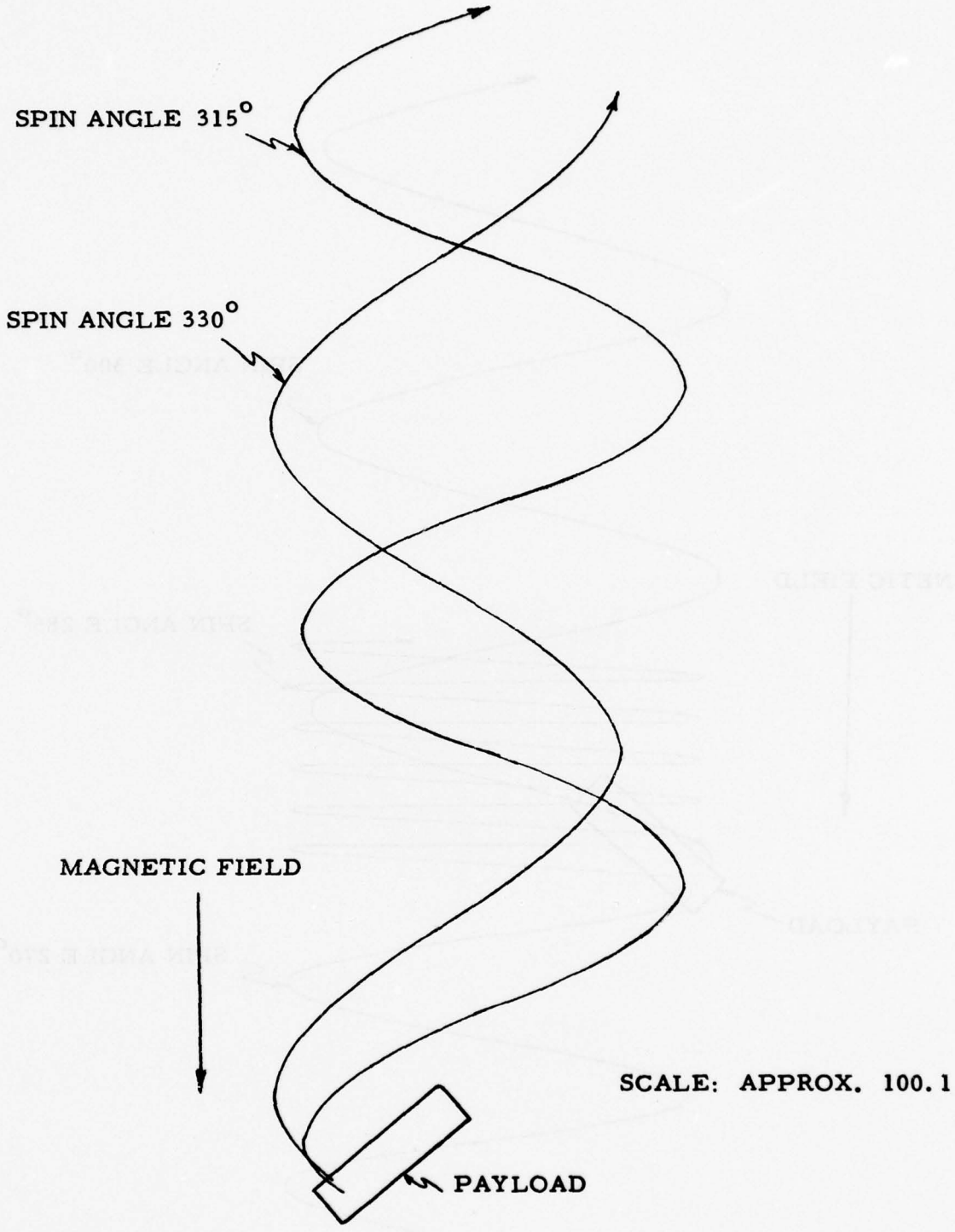

Figure 56. EXCEDE II Test Electron Beams Looking Normal to the Magnetic Field. Spin Angles: 330° and 315°

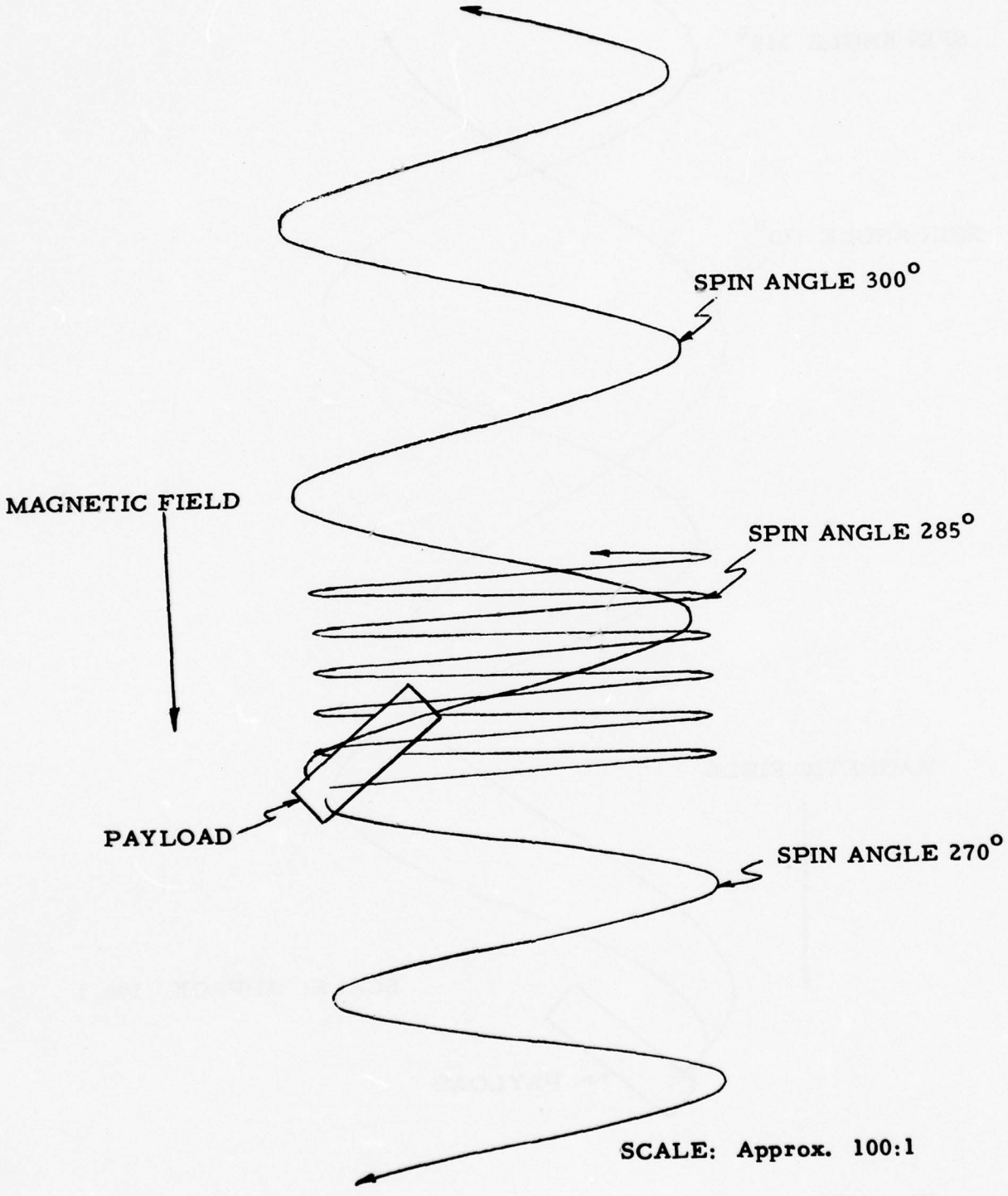

Figure 57. EXCEDE II Test Electron Beams Looking Normal to the Magnetic Field. Spin Angles: 300°, 285°, and 270°

velocity is about 0.8 km/sec, so that in the 100:1 graphical reduction, the rocket body moves 0.8 cm/sec. The fields-of-view of the photometers were drawn at one millisecond intervals and the intersections graphically searched for as before. For some of the spin angles, the FOV's did intercept the deposition region after a few milliseconds, and the results are shown in Table 9. Also shown is the approximate angle between the optical axis and the deposition path at the time of interception. The most significant piece of information to come out of this is that when the spin angle is 0°, which is when the photometer is looking in the plane of the rocket wake, the deposition path length in the field is very long.

The second case was near the time when data taking began at T+ 110 seconds. Here the yaw is still about -10° but the angle between the rocket axis and the velocity is only 13.3°. In addition, the No. 1 electron gun was off. Using the same graphical method as above, the results are as in Table 10 which are very similar to those in Table 9 except the intercept times are somewhat earlier.

6.5 DATA REDUCTION

The operation of the two electron accelerators was determined from the rocket telemetry data and analysis of the ground-based low light level television images. Figure 58 is a frame from the LLLTV showing the aurora caused by the electron deposition against a star background.

Figure 59 shows the accelerator operating conditions and the estimated energy deposition based on integrations over the video images. These values were normalized to measurements obtained with a $1^{\circ} \times 2^{\circ}$ field-of-view telephotometer co-aligned with one of the video systems [60].

TABLE 9

Intercepts of Photometer FOV's and Electron Depositions at T + 160 seconds

	Intercept Time (m sec)		Angle	
Spin Angle	Gun 1	Gun 2	Gun 1	Gun 2
15°	Never	Never	-	-
0	14	12	~0° (1)	0° (1)
345	13	11	~40°	~40°
330	10	8	~40°	~40°
315	8	7	~60°	~60°
300	8	7	~40°	~40°
285 (2)	Several	Several	Several	Several
270	Never	Never	-	-

NOTES:

(1) Looks along approx. 300 cm of deposition

(2) Vertical velocity of electrons is small compared to horizontal so that several orbits of deposition are intersected by the photometers, as follows:

285° Spin Angle

	Intercept Time (m sec)		Angle	
Deposition Orbit	Gun 1	Gun 2	Gun 1	Gun 2
1	Never	Never		
2	Never	Never		
3	0-2	0-2	~30-50°	
	and 8		~ 60°	
4	4-6	0	~90-60°	~ 60°
5	Never	2-4		~90-70°
6	Never	6		~ 60°

TABLE 10

Intercepts of Photometer FOV's and Electron Depositions at T + 110 seconds

Spin Angle	Intercept Time, Gun 2	Angle, Gun 2
15°	Never	
0°	9	~ 0° (1)
345	9	~ 60°
330	8	~60°
315	7	~60°
300	(2)	
285	(3)	(3)
270	Never	

NOTES:

(1) Looks along 250 cm of deposition

(2) Does not intercept but closely parallels deposition from 0 to 8m sec.

(3) 285° Spin Angle:

Deposition Orbit	Intercept Time (m sec)	Angle
3	0-1	~40-80°
4	2-3	~70-90°
5	4-5	~90-70°
6	6-7	~50-30°

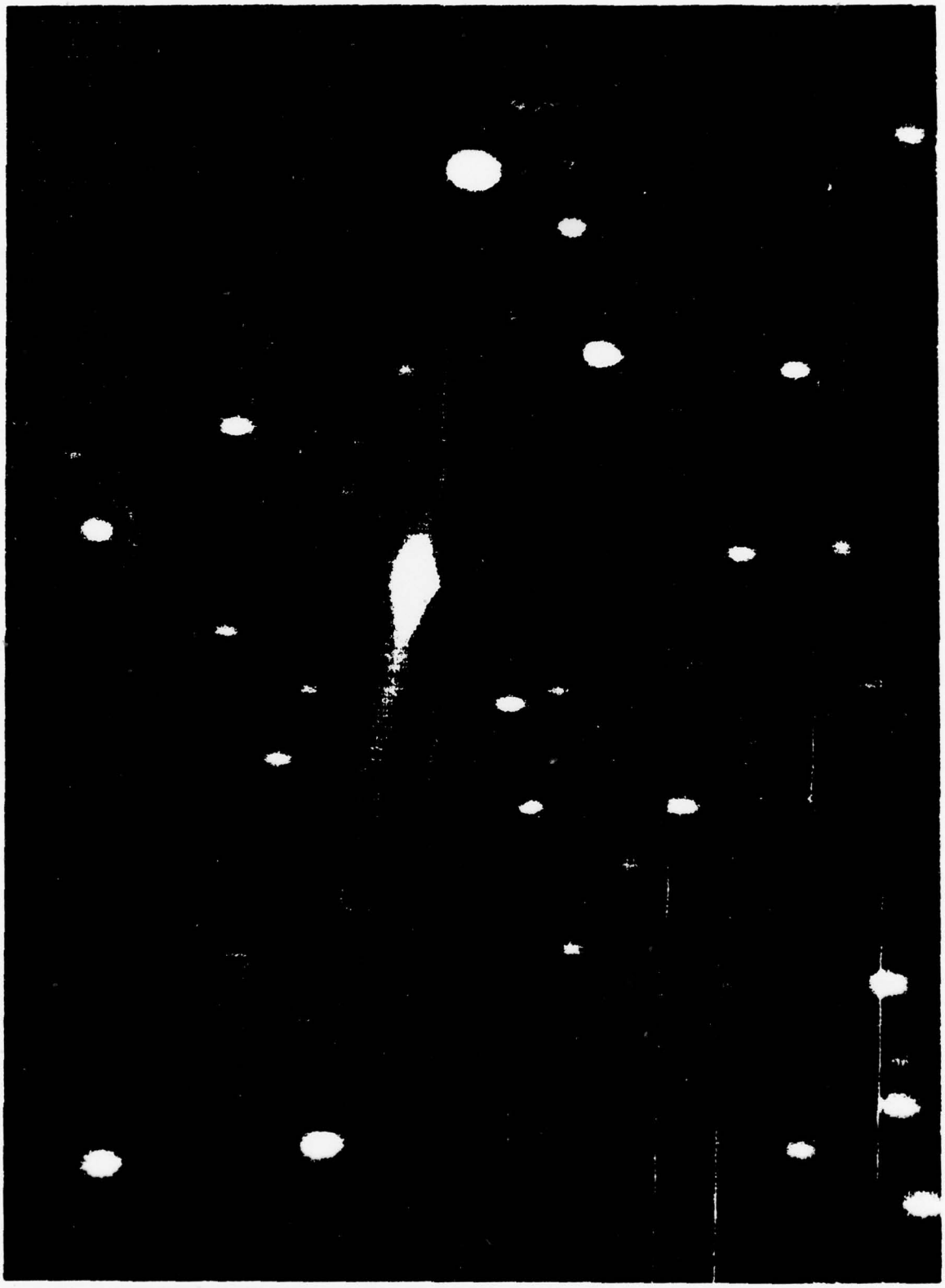

Figure 58. EXCEDE II Test Aurora from Ground Based LLLTV

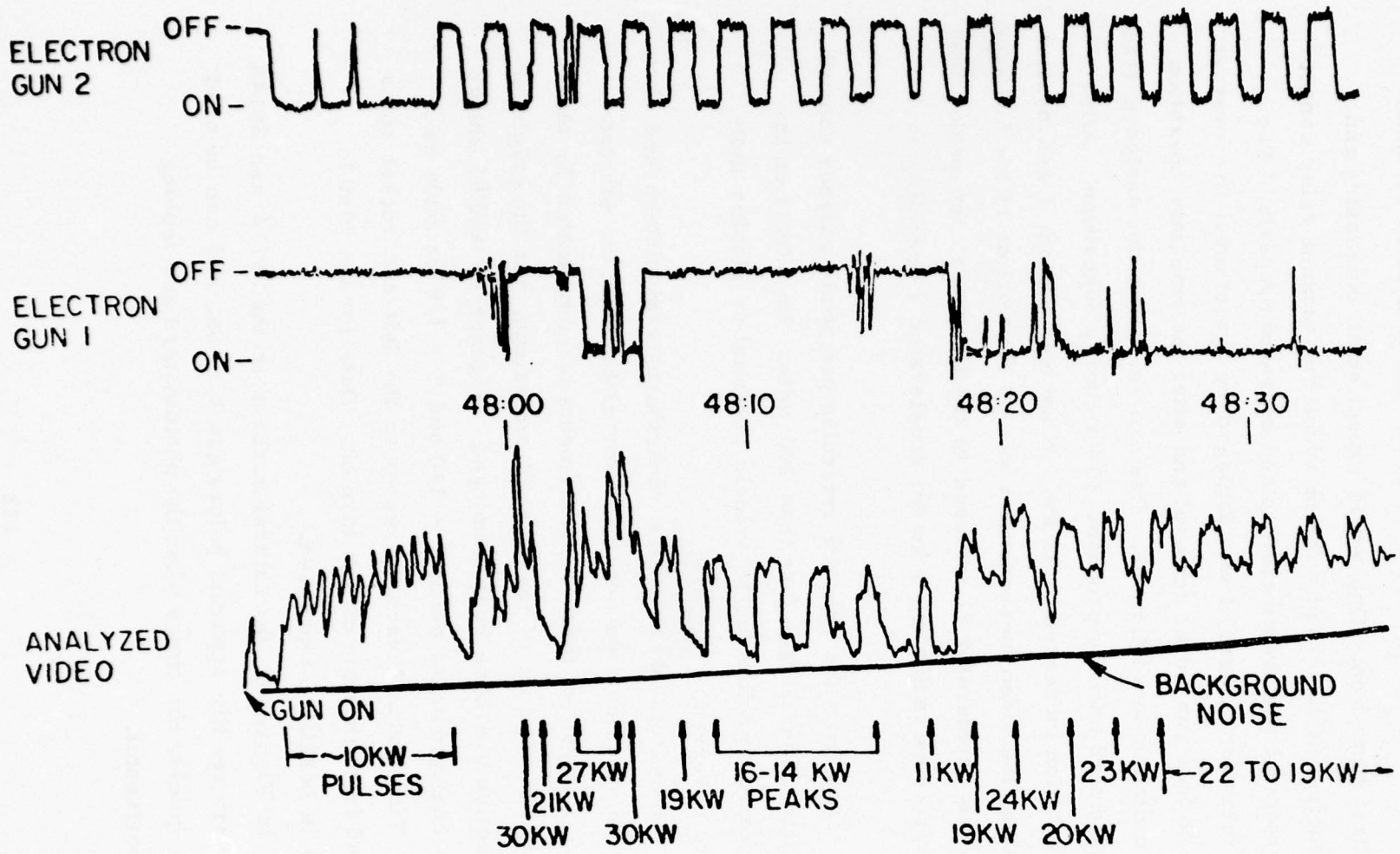

Figure 59. EXCEDE II Test Ground Based LLLTV Data

The top trace shows the operation of System #2 when the unit is first turned on. One would expect some outgassing and arcing producing an increased current which the vacuum relay cannot quench. System #2 rapidly cleaned up and operated properly. The modulation relay for System #1 was damaged by a sustained arc over at turn on due to late gun cover removal and after intermediate operation, the system switches to a DC mode. One can see from the analyzed video data that System #2 initially produced 10 kw energy deposition. After clean up, deposition increased to 15 kw. When both System 1 and System 2 were operating, the video measurement was 30 kw total or 15 kw for each module. When accelerator #1 switched to the DC mode, the peak power measured was 24 kw indicating 9 kw for accelerator 1 operating in the DC mode.

Data from the onboard retarding potential analyzer showed that the vehicle potential was less than 200 volts. No effects on the electron deposition profile due to vehicle potential or plasma instabilities were observed.

Measurements from the rocketborne radiometers and photometers showed significant enhancement correlated with the electron accelerator. Analysis of these measurements is complicated by the geometry and time history of the delayed emissions, but the graphical results of Section 6.4 have been employed. Figures 60 and 61 show some of the analog data at about T + 110 and T + 160 seconds respectively. Time from launch increases to the left and rocket spins are numbered from the time of gun turn on. Data for the visible photometers is heavily compressed.

In Figure 60, the natural auroras in the 5577Å and 3914Å photometers are readily apparent before gun turn on, and can be used to determine quickly the times when the photometers are looking essentially horizontal.

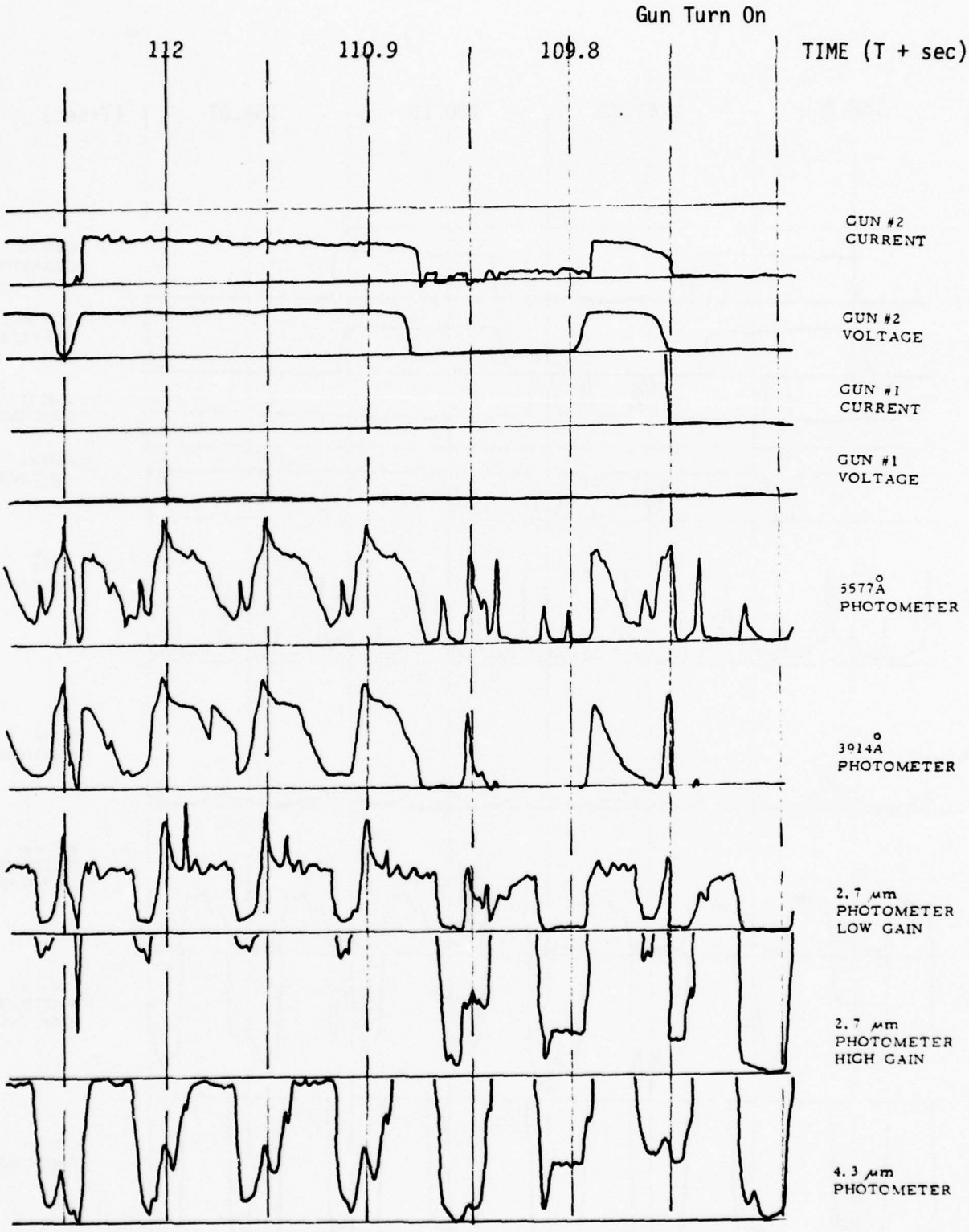

Figure 60 EXCEDE II Test Data at T + 110 Seconds

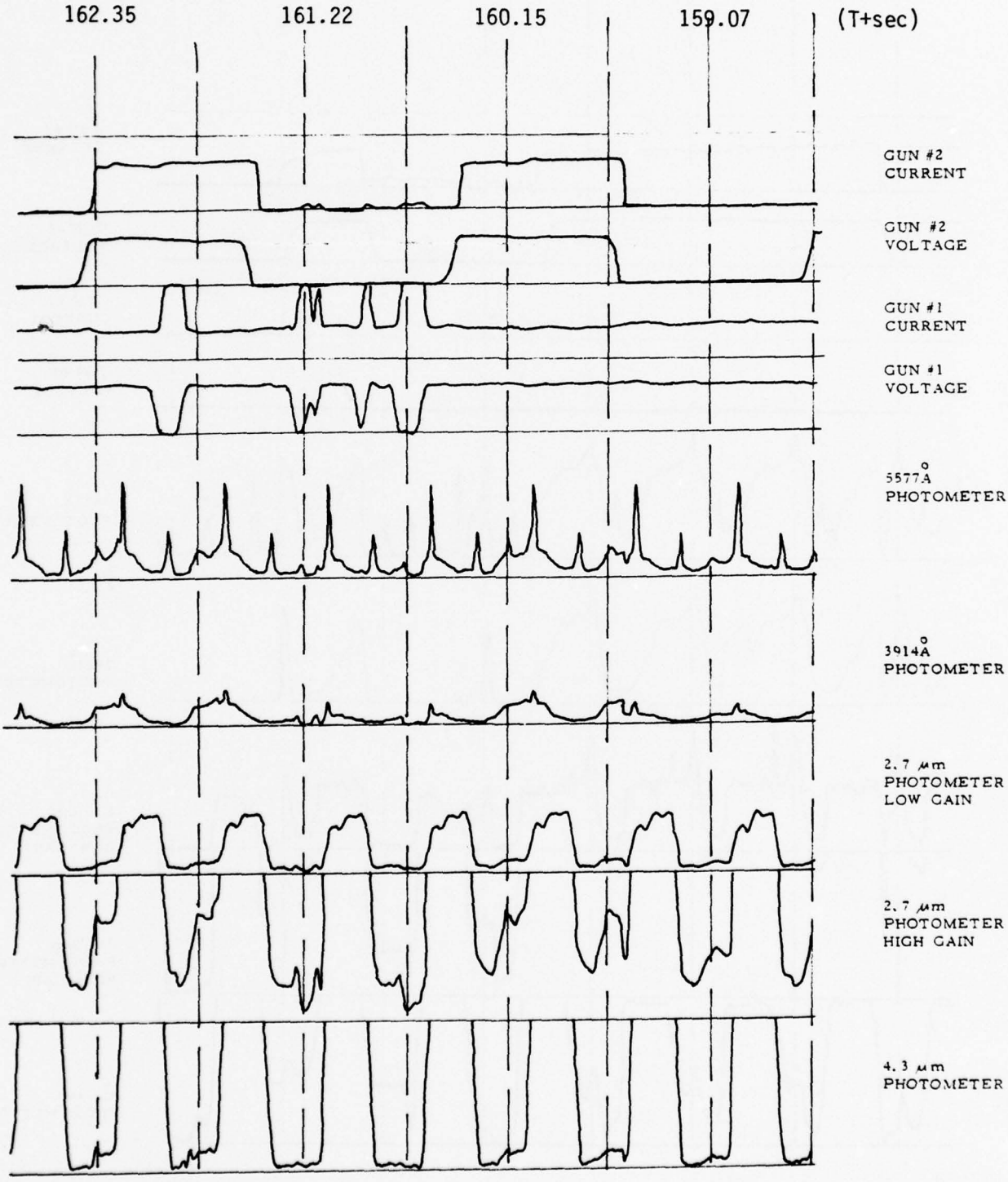

Figure 61 EXCEDE II Test Data at T + 160 Seconds

Figures 62 through 65 show the variation with rocket altitude of the peak brightnesses of 3914Å, 5577Å, 2.7 μm and 4.3 μm respectively. Also shown in these figures is the atmospheric density profile. The model used is from Reference 40. The 3914Å profile does not follow exactly the atmospheric profile. Either the density profile is incorrect, or it is necessary to consider other effects (e.g., the altitude dependence of the vehicle potential and its effect on the return beam) which may contribute to the measured signal.

A significant result of the EXCEDE II Test is the first measurement of 4.3 μm emission not attributed to CO_2 excited by vibrational transfer with N_2. Because of the high down range rocket velocity, the dosing time for a given region is on the order of 10 milliseconds while the lifetime for vibrational transfer from N_2 to CO_2 is on the order of 4×10^3 seconds at 110 Km. Approximately 6% of the energy deposit will be emitted by CO_2 at 4.3 μ. Since the deposition time is only 10 milliseconds, the apparent emission efficiency will be 1.5×10^{-7}. (The apparent emission efficiency is the ratio of the rate of energy emission in a given feature to the rate of energy deposition.) The peak 3914Å emission was 45 MR; then the peak 4.3 μm emission due to vibrational transfer from N_2 to CO_2 is on the order of 20 kR. The measured value was 3.4 MR and was corrected for filter transmission R by O'Neil, et. al.[63]. The corrected value is 10 MR. The implication is that the 4.3 μm emission is a relatively fast radiator such as NO^+ or $N^{14}N^{15}$ or prompt CO_2 fluorescence. The lifetime for the NO^+ (1-0) transition is 74 msec[64] while the CO_2 (001-000) transition is 3 msec. There is insufficient information of $N^{14}N^{15}$. If the emitter is NO^+, we estimate an energy efficiency of 7×10^{-4}. This is a lower limit for the efficiency since we have not considered the finite time to produce NO^+. If the emitter is CO_2, the energy efficiency is 10^{-4}. Laboratory measurements[65] have shown that 20% of the energy deposited by kilovolt electrons in CO_2 will be radiated at 4.3 μ. If we assume that the energy

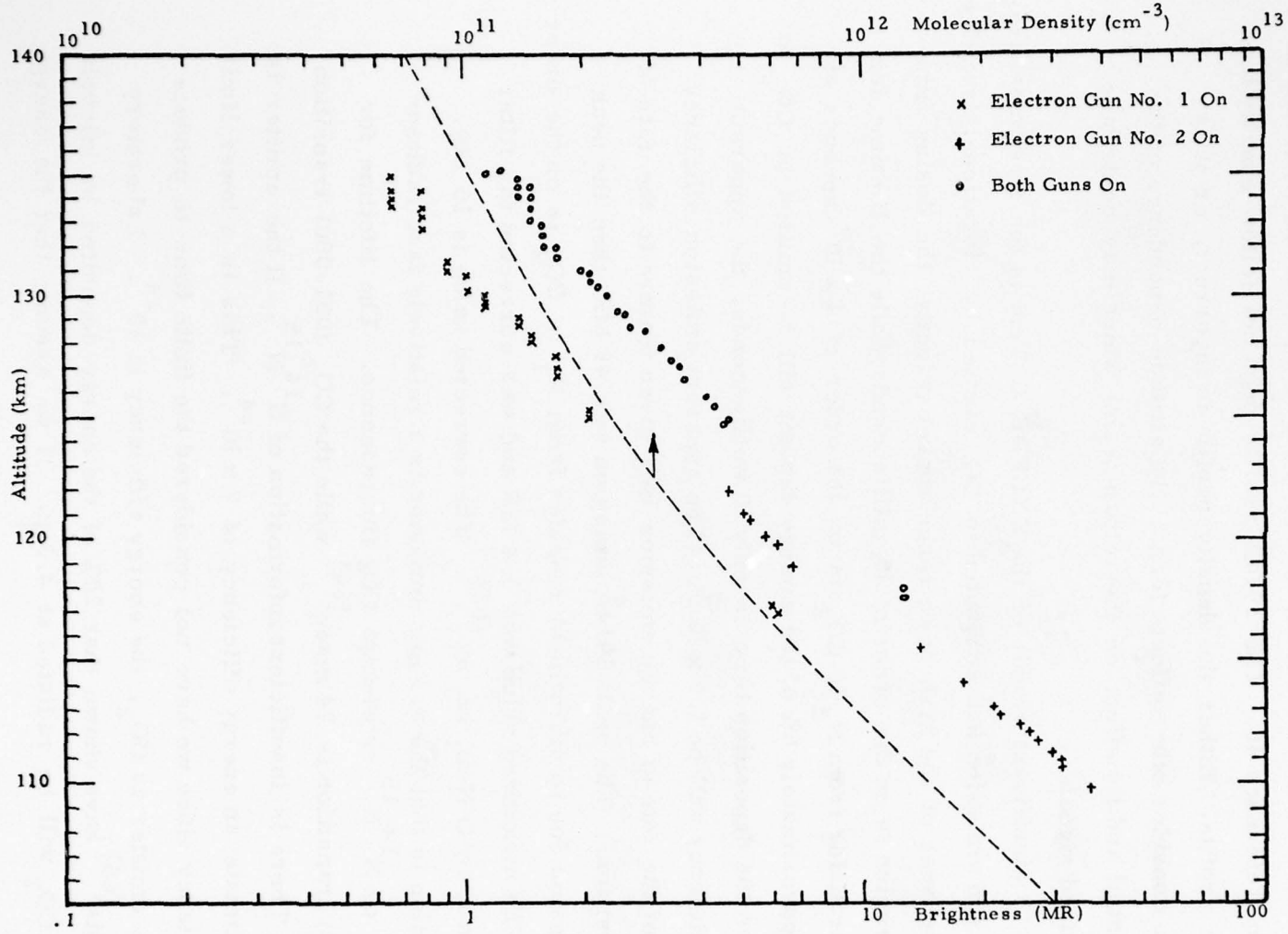

Figure 62. Rocket EX531.43-1 3914Å Peak Brightness vs. Rocket Altitude

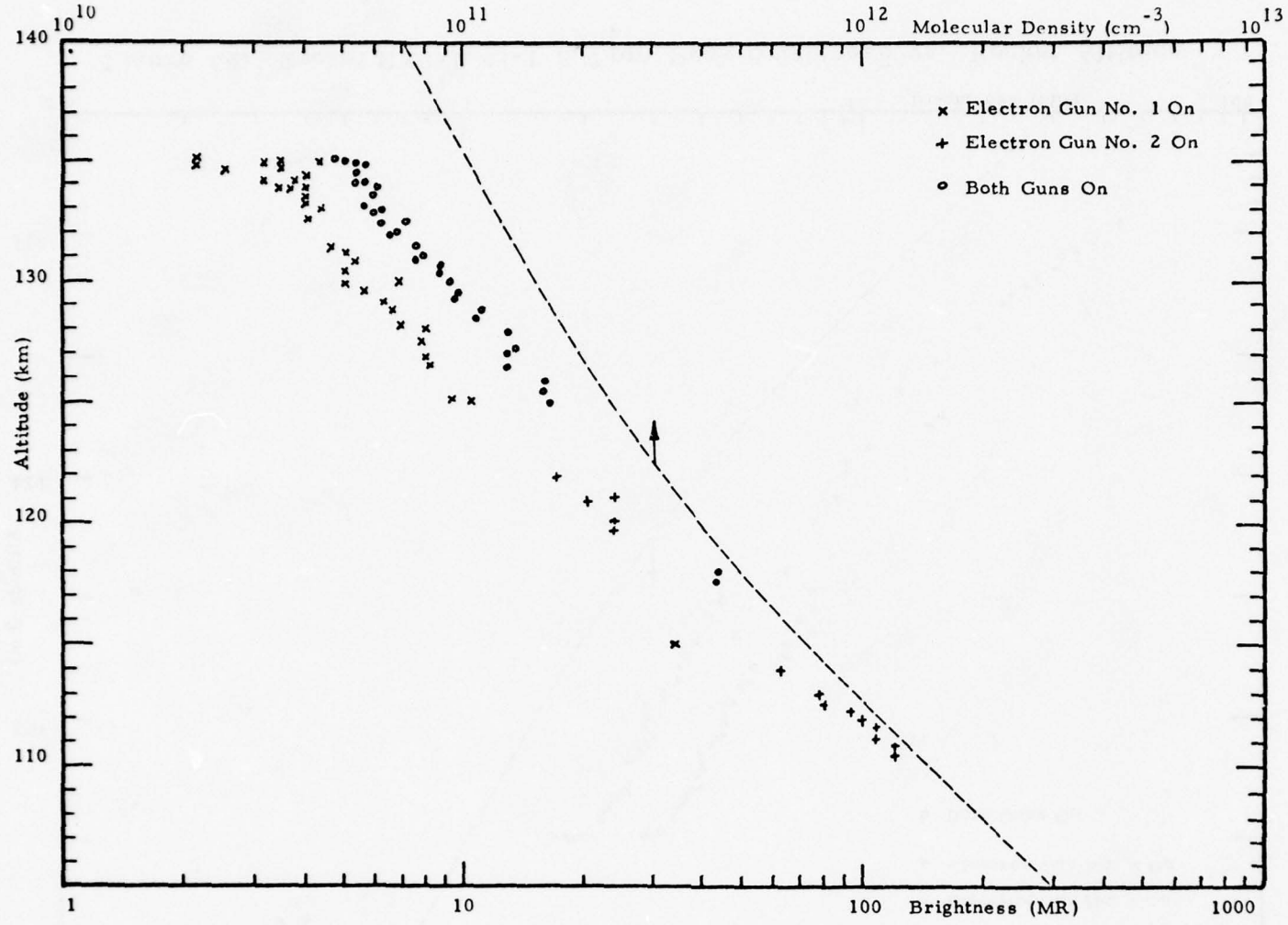

Figure 63. Rocket EX531.43-1 5577Å Peak Brightness vs. Rocket Altitude

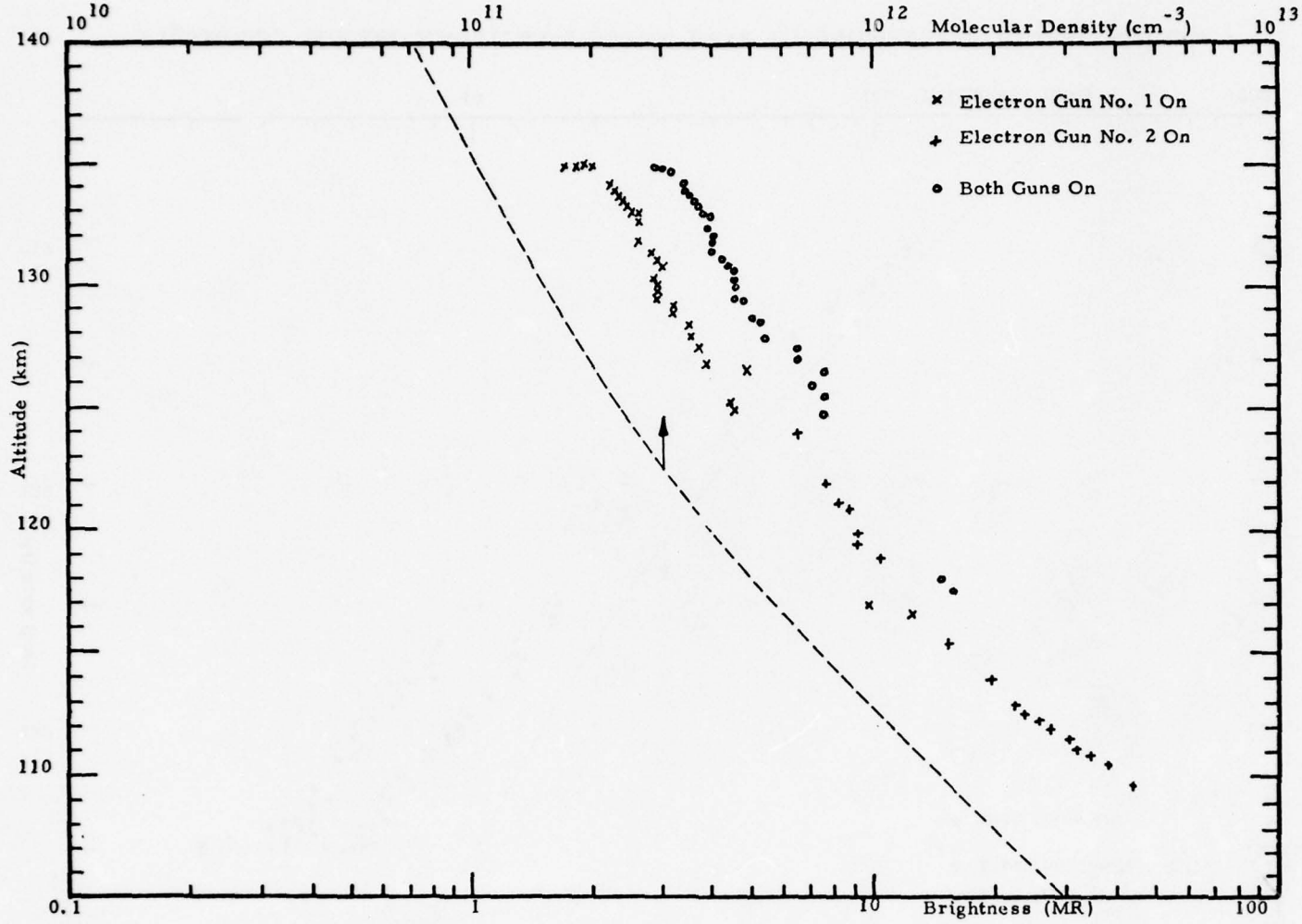

Figure 64. Rocket EX531.43-1 2.7 μm Peak Brightness vs. Rocket Altitude

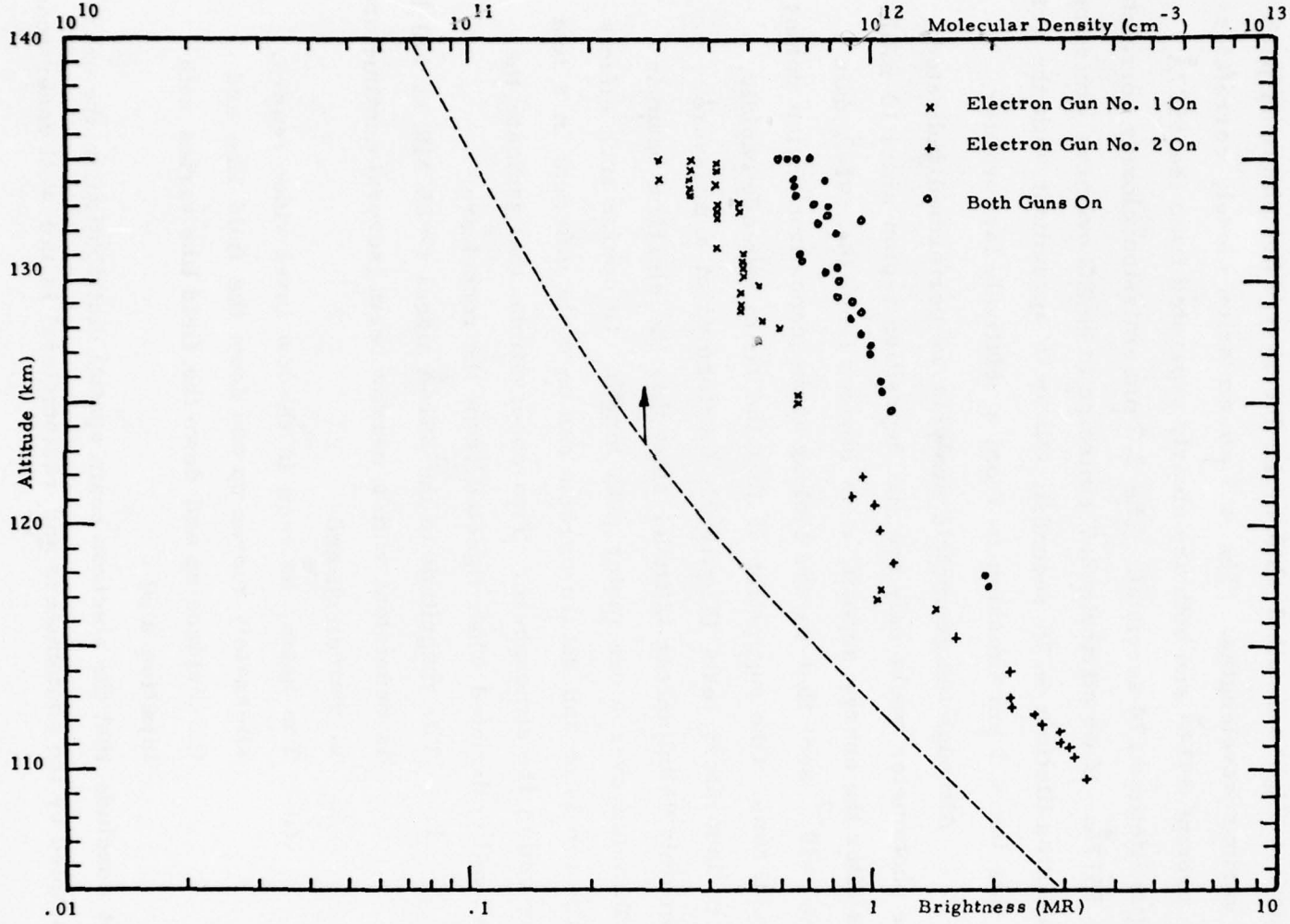

Figure 65. Rocket EX531.43-1 4.3 μm Peak Brightness vs. Rocket Altitude

partition is on the order of the mixing ratio ($\leq 3 \times 10^{-4}$) then the anticipated energy efficiency for prompt CO_2 fluorescence is on the order of 6×10^{-5}.

A more detailed analysis of the spin dependence of the emission peak shows a slight azimuthal shift in the location of the emission peak for the various wavelengths. The 4.3 μm emission closely correlates with the prompt 3914Å and both are clearly separated from the 5577Å peak [0('s) lifetime .74 seconds]. The 2.7 μm emission clcsely correlates with the 5577Å. If we attribute 2.7 emission to be NO overtone emission (2-0 transition lifetime ~.76 seconds), this is in agreement with the conclusion that the 4.3 μm emission is from a relatively fast emitter.

Although the geometric analysis we performed indicated that the photometer would only see the deposition region about 10 milliseconds after the energy deposit, it is obvious from the 3914Å data (lifetime $\sim 10^{-7}$ sec) that we are looking at the deposition region during the deposit time. One suggestion is that the beam spreads rapidly. However, laboratory tests (Figure 62) (performed at a pressure approximately 95 kilometer altitude) show that the electron beam is well collimated over a one meter path length. Of course such effects as charge repulsion and return current can be quite different in a test chamber and in the atmosphere. Two observations that indicate the beam is well collimated when injected from the rocket are:

1. The magnitude of the 3914Å signal (~25 MR at 110 km) is consistent with a narrow beam (several centimeters in diameter); and
2. The beam, as seen in the low level video record, alternately moves up and down the field line and the distance up and down the field line varies with injection angle.

We must conclude that the electron beam spatial distribution in the near field (sampled by the photometers and radiometers) is not well understood.

7.0 EMISSIONS AT HIGH DEPOSITION LEVELS

7.1 Introduction

A major objective of the HAES/EXCEDE program is to determine the chemistry set that describes the behavior of the upper atmosphere after irradiation with a nuclear device. The level of irradiation will depend on altitude, yield, distance, etc. Section 7.2 presents some comments by Dr. R.E. Meyerott, a consultant to Visidyne, on atmospheric dosing at high levels. Section 7.3 compares measurement at high and low dosing levels to determine how the applicable chemistry set varies with deposition.

7.2 Non-Linear Effects of Electron Deposition in Air (R.E. Meyerott)

Non-linear effects of electron deposition in air occur at high electron deposition levels. These effects arise due to the excitation of, and energy loss to, atomic or ionic species produced by the electron deposition itself. The magnitude of these effects will depend upon the ionization rate as well as dose, i.e. current times duration. The present note analyzes the possible non-linear effects that may be important to EXCEDE.

When air is excited by the deposition of electrons of energy greater than ~1 kev, the prompt fluorescence and ionization is proportional to the energy deposition per unit volume and independent of the electron energy or the energy deposition, provided the latter is small. Under these circumstances, the primary electrons lose their energy by ionizing and exciting the air and finally slowing down to the temperature of the air. The number and energy distribution of secondary electrons is essentially independent of the energy of the primary electrons, provided they have initial energy greater than ~1 kev. The secondary, tertiary, etc., electrons ionize and excite the air and eventually slow down to ambient air temperature. As long as the electron, ion, and excited species

concentrations are small compared to the air molecule concentrations, the concentrations of excited and ionized species, as well as the fluorescence produced by the slowing down of the electrons is proportional to the energy deposition. If one excites low density air that is initially un-ionized or weakly ionized with high electron doses, the long life species (electrons, ions, and metastable atoms and molecules) can build up concentrations to the extent that they must be considered in the electron ionization, excitation, and slowing down processes.

According to Project EXCEDE: SWIR Experiment[63] which had an ionization rate of 5×10^{8} ion pairs cm^{-3} sec^{-1} for 0.1 sec at 105 km, the electron concentration/molecular concentration, f, starts at a value equal to $\sim 10^{-9}$ at ambient, and builds up to $\sim 10^{-5}$ at 0.1 sec. If the ionization is increased by a factor of 100, the fractional ionization, f, would be 10^{-3}. When the fractional ionization becomes this large, the energy loss to the electron gas must be considered, in addition to that due to the air molecules. The fractional energy loss of electrons per cm path length due to collisions with air molecules, $\frac{1}{E}\frac{dE}{dx}$, is given by

$$-\frac{1}{E}\frac{dE}{dx} = N \lambda \sigma \qquad (1)$$

where N = number of air molecules/cm^3

λ = fraction of the energy lost per collision

σ = total collision cross-section

The fraction of the energy loss of electrons per cm path length due to collision with other electrons at temperature kT_e, less than E is

$$-\frac{1}{E}\frac{dE}{dx} = \frac{3.2 \times 10^{-12}}{E_{ev}^2} N_e \qquad (2)$$

where N_e = number of electrons/cm^3

E_{ev} = electron energy in electron volts

Equation (2) can be written

$$-\frac{1}{E}\frac{dE}{dx} = \frac{3.2 \times 10^{-12}}{E_{ev}^2} fN \qquad (3)$$

where $f = N_e / N$ is the fractional ionization (assuming no negative ions!) Hence, the fractional energy loss per cm per air molecule is

$$-\frac{1}{NE}\frac{de}{dx} = \lambda \sigma \text{ cm}^2 \qquad (4)$$

and

$$-\frac{1}{NE}\frac{dE}{dx} = \frac{3.2 \times 15^{12} f}{E_{ev}^2} \text{ cm}^2 \qquad (5)$$

for loss to an electron gas.

Figure 66 is a plot of Eq. (4) as a function of electron energy, E, and Eq. (5) as a function of electron energy for various values of f.

When the energy loss to the electron gas becomes of the same order as that lost to exciting vibrational and rotational energy states of the air molecules, the non-thermalized electrons will give their energy to the electron gas. As a consequence, the electron temperature will increase during the time the excitation is on. Inspection of Figure 66 shows that near ambient electron densities, energy loss to the thermalized electron gas does not take

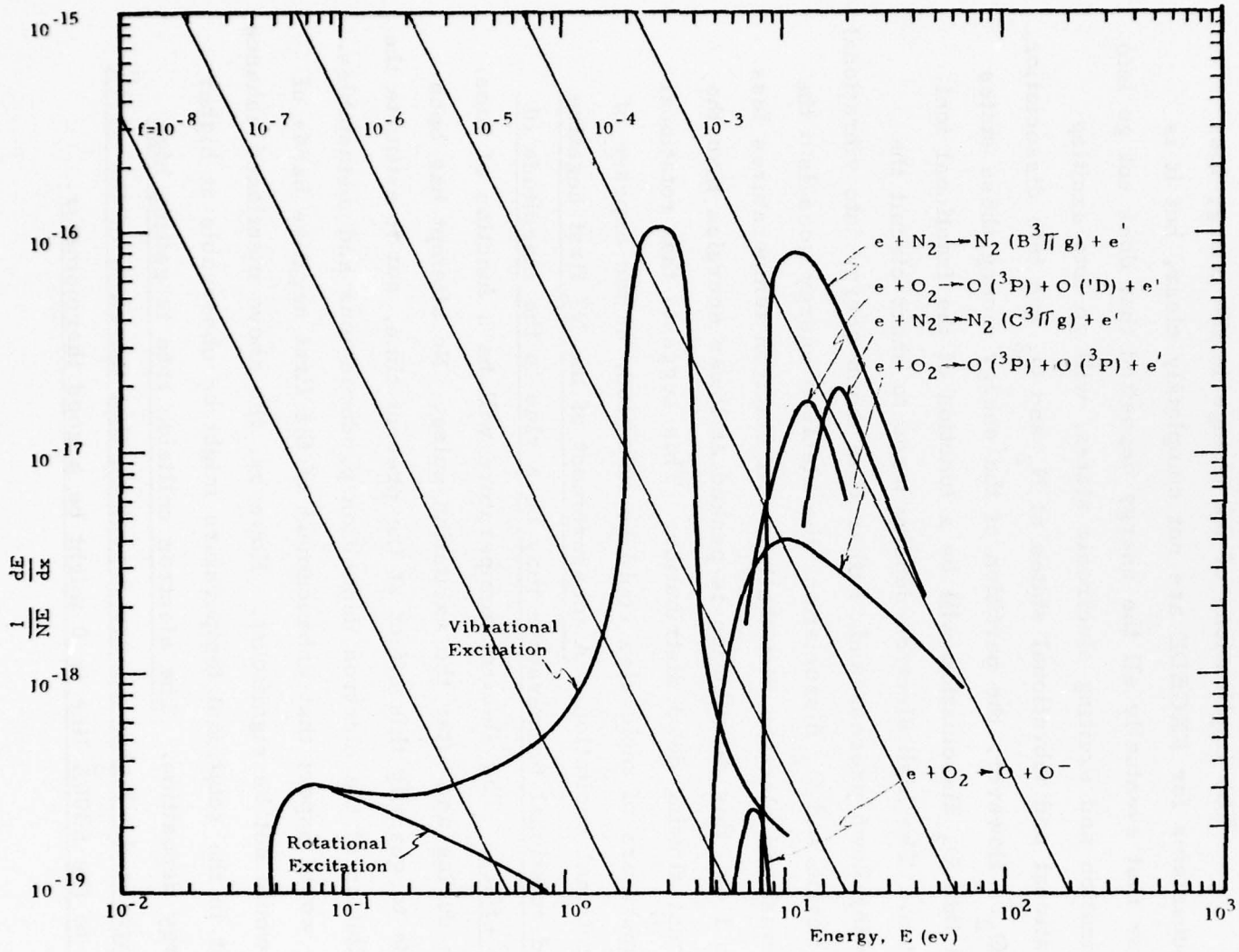

Figure 66 Fraction of Electron Energy Loss per cm of Path vs. Electron Energy

place until the electron energy has been degraded to a 10^{-1} ev. For ionization fractions of 10^{-4}, energy loss to the thermalized electron gas is important at energies greater than 10 ev!

The implications of the change in the energy loss mechanisms for EXCEDE are not completely clear, but it is clear that eventually all the energy deposited that does not go into ionization and exciting electronic states, will go into exciting rotational and vibrational states of N_2 and O_2 and into dissociation of O_2. However, the partition of the energy among these states and into O_2 dissociation will be a function of the fractional ionization. The high electron density tends to short circuit the slowing down process and, rather than dump energy into vibrational excitation and O_2 dissociation, the electron energy goes into the thermalized electron distribution. At electron temperatures less than 1 ev, this distribution is peaked at lower energies than the normal slowing down distribution. This suggests that rotational temperature of molecules could be enhanced, at the expense of vibrational excitation. A measurement of the N_2^+ first negative band rotational temperature may be a clue to the magnitude of this effect. The electron temperature will be a function of time, both during and after the excitation pulse. No attempt has been made to quantify this effect at the present time, nor to estimate the excitation of the electron deposition produced ions and metastables. One would expect that enhancement of the first negative bands of N_2^+ would not be significant. However, the above mentioned enhancement in the rotational temperature might be observable at higher energy deposition. The electron collision rate is getting high enough at the higher energy deposition that the ratio of the 5577Å line to the 6300Å line in 0 might be a good thermometer.

7.3 Emissions at High Deposition Levels

The pre-ICECAP predicted photoefficiency for the

$$N(^2D) + O_2 \rightarrow NO^{\ddagger} + O \rightarrow NO + h\nu$$

chemiluminescent reaction was based either on a hypothetical distribution of the exothermicity over the energetically allowed vibrational levels up to $v \approx 18$ of the NO molecule or by extrapolation from laboratory (LABCEDE) measurements of the $N(^4S)$ reaction where levels up to $v \approx 6$ were allowed. The measured value for the overtone was about 0.02 photons at 2.7 μm per $N(^4S) + O_2$ reaction.
one $N(^2D)$ is produced per ion pair produced and further that in proportion to the number of possible excited levels there are three times as many photons per reaction, then we have

0.06 photons/reaction = 0.06 photons/ion pair

This corresponds to an efficiency of

$$\eta = \frac{0.06 \text{ photons}}{\text{ion pair}} \times \frac{0.5 \text{ ev/photon}}{30 \text{ ev/ion pair}} \approx 10^{-3}$$

or 0.1% as an extrapolation from the ground state laboratory measurements.

In Figure 67, we show the 2.7 μm radiation measured (or bounds on the amount) versus the rate of production of electrons per cm^3 -sec. For this scale, the correspondence of about 10^4 elec/cm^3 -sec is with an aurora of brightness IBCI, 10^5 with IBC II, etc. The production levels corresponding to EXCEDE SWIR II Test (15 Kw) and the forthcoming II Experiment (120 Kw) are noted. For the EXCEDE experiments, we have considered deposition at an altitude (~100 km) where the beam length along the field line is about 1 km. The diameter of the beam is about 30 m. The solid line corresponds to an efficiency of production of 2.7 μm

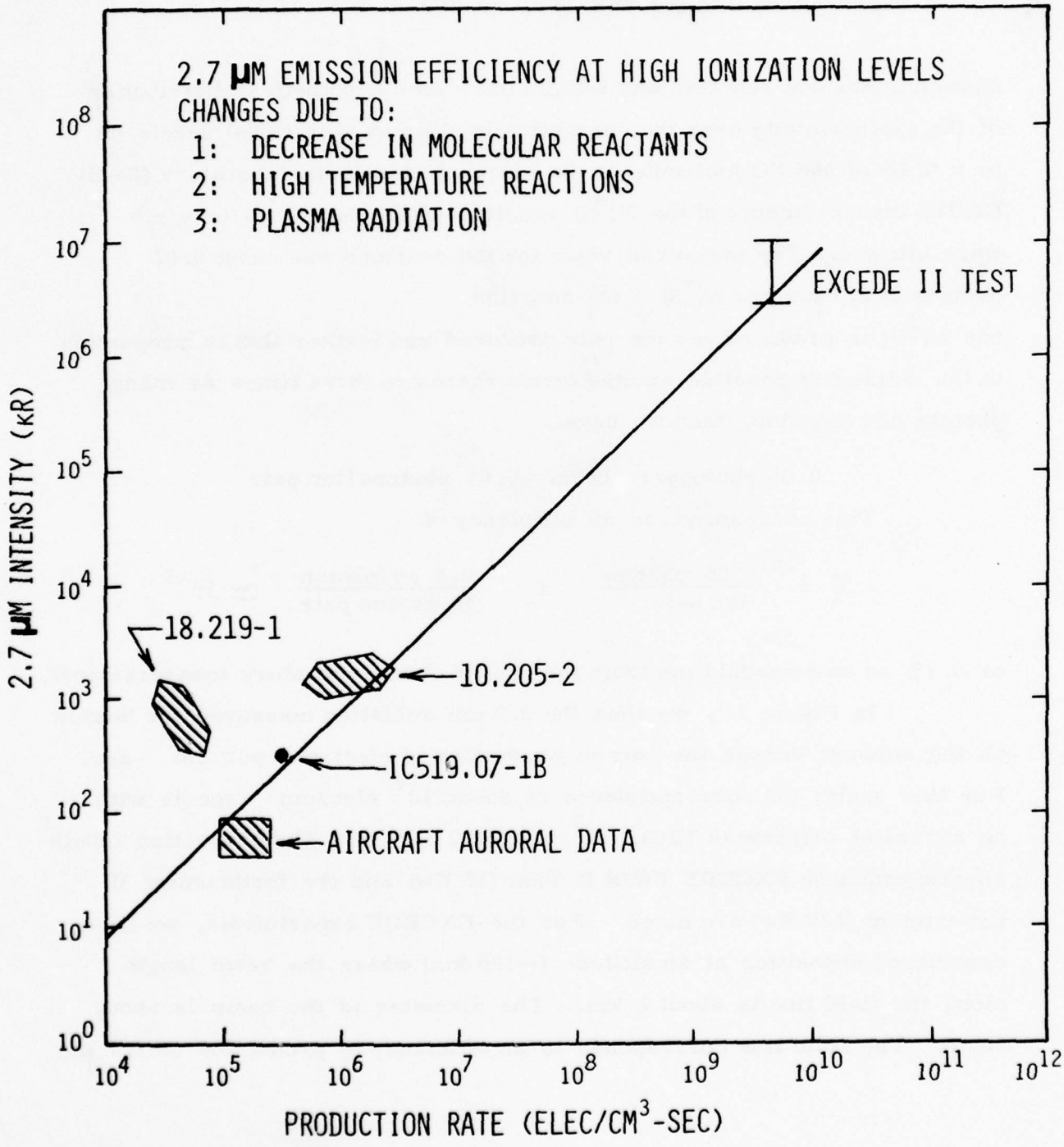

FIGURE 67 2.7 μm BRIGHTNESS vs ELECTRON PRODUCTION RATE

radiation of 1%.

Consider first the aircraft measurement of the correlation between 3914Å visible radiation and 2.7 μm infrared while flying under a bright arc. After correcting for atmospheric extinction on both passbands, the efficiency (energy out to energy in) varies between 0.5 and 1% corresponding to the vertical extent of the plotted box. These are variations during the measurement by about a factor of three in the 3914Å brightness - hence, the measurement uncertainties are represented by the rectangular box.

Rocket 18.205-1 overflew a bright arc. If we take the 3914Å measurement of 15 kR (0.5%) and ask at the 1 MR/μm level minimum detectable level for 2.7 μm (which was not detected), what is the corresponding efficiency, then we find the following:

Measured Intensity @ 3914A = 15 kR = 15×10^{9} photons/cm^2-sec

or (Each photon ~ 3 ev) 4.5×10^{10} ev/cm^2-sec

Minimum Intensity @ 2.7 μm = 1MR/μm=10^{12} photon/cm^2-sec-μm

(Each photon - 0.5 ev, and the passband was ~ 0.3 μm)

Hence 1 MR/μm = 1.5×10^{11} ev/cm^2-sec

Minimum Intensity @ 2.7 ≈ 3 x Measured Intensity @ 3914

which has η = 0.5%

Therefore, if the efficiency were higher than 1.5%, a signal would have been discerned. This, then, furnishes an upper bound at this level of production for these flight conditions and is shown on the figure.

Rocket 18.219-1 overflew a moving arc which later overtook the rocket. If we use the upleg 3914Å measurement of 6 kR and the small 2.7 μm signal at 1.1 MR/μm, then scaling from the above, this implies an efficiency of about 4% for the 2.7 μm radiation.

On the downleg, the 2.7 μm radiation is quite bright. Comparing the input column brightness of 2.5 kR for 3914Å and 4.5 MR/μm for 2.7 μm we obtain an apparent efficiency of about 40% and a brightness of 1,400 kR at 2.7 μm.

For Rocket 10.205-2, we have for 200 kR of 3914Å radiation 7 MR/μm of 2.7 μm radiation which corresponds to a brightness of 2,100 kR and implies an efficiency of about 1%.

Considering next the emission at 4.3 μm, since the emission lifetime is of the order of 500 seconds at 100 km (longer at higher altitudes), the brightness observed depends upon the efficiency of conversion and the length of time the region has been dosed if it is less than the emission time. We let t_d represent how long the region has been dosed by the incident electrons.

Since we do not in all cases know how long the region has been dosed before the rocket makes the measurement, in Figure 68 we have shown four curves for the $kR_{4.3\ \mu m}$ emission as a function of the $kR_{3914Å}$ emission which is proportional to the input flux. We assumed that 10% of the incident energy goes into N_2 vibrational and is eventually emitted by CO_2 at 4.3 μm. Hence

$$I(kR_{4.3\ \mu m}) = 0.4\ I(kR_{3914}) \quad [i\text{-}e\ t/500]$$

The curves for a dosing time of 1 and 10 seconds probably are not needed. Also shown on this graph are the measured values of the 4.3 μm emission for Rockets 18.219-1, 18.205-1, and 10.205-2 as a function of the observed 3914Å emission. The fact that the data for the three Rockets lie above the 100 second dosing curve indicates that the region has been dosed for a longer period of time. However, once t_d exceeds ~500 seconds, the inventory of N_2 vibrational does not continue to increase. If the rocket data exceed this curve, it could imply other species (NO^+?) other mechanisms (prompt CO_2 fluorescence?), or longer emission time.

In the EXCEDE II Experiment on the other hand, since a volume of air is being dosed from a moving rocket, in general, very short dosing times will be involved. For EXCEDE II Test, this dosing time as indicated was perhaps as short as 3×10^{-3} sec. The EXCEDE II Test data point is over two orders of magnitude higher than CO_2

(N_2 vibrational) would predict on the 10% conversion assumption. Hence, either higher efficiencies and/or other mechanisms are occurring. The existence of the 2.2 μm radiation seen in EXCEDE SWIR indicates that a portion of this excess at 4.3 μm could probably be due to the fundamental NO^+ emission.

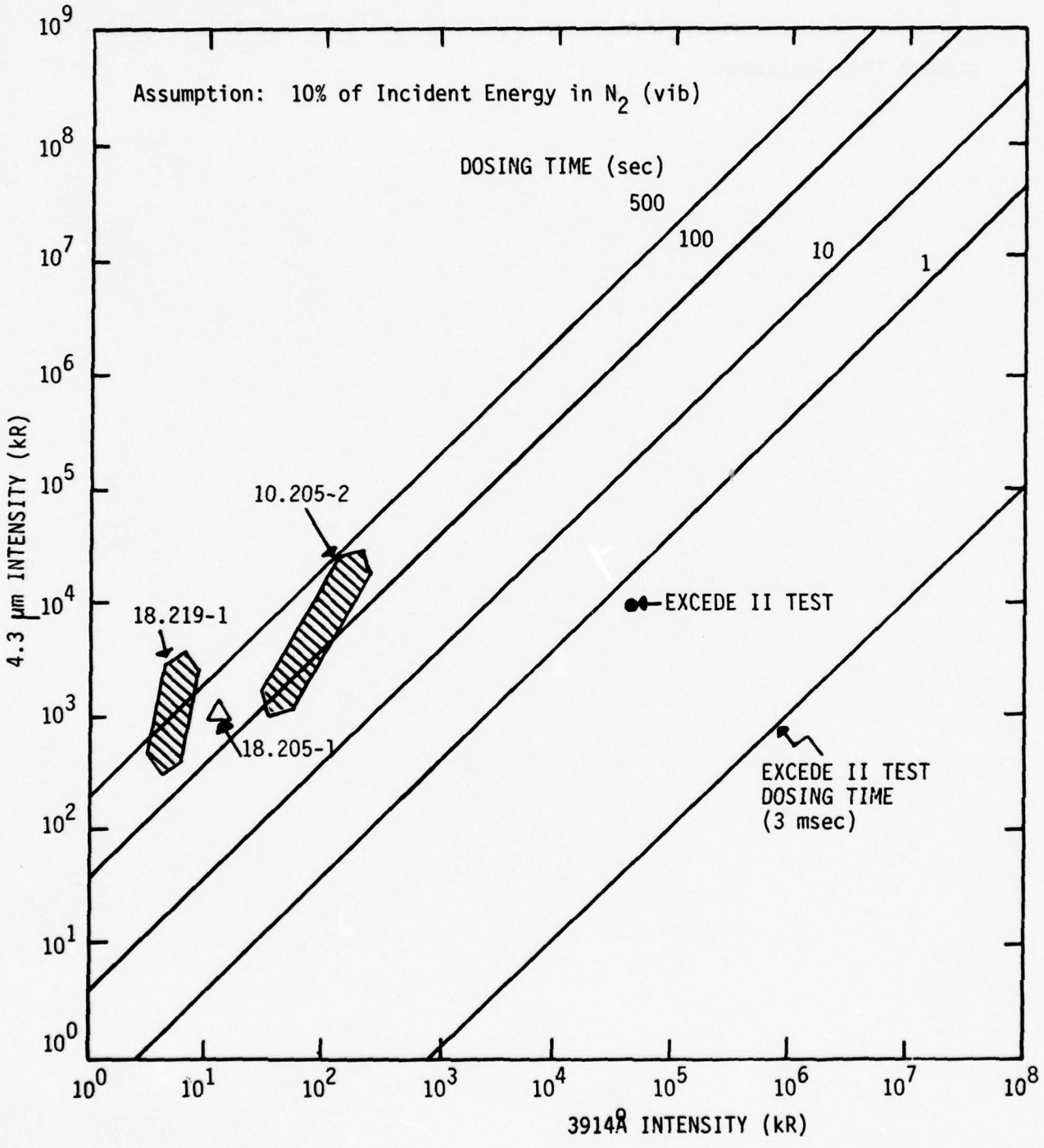

Figure 68. 4.3 μm Brightness vs. 3914Å Brightness for Various Dosing Times

8.0 CONCLUSIONS

Through a study of the temporal positions and intensities of the aurora associated with ICECAP rocket probes and the electron data taken by the probes, we have developed a relationship between the auroral radiance and the energy flux and spectrum of the auroral electrons. We have graphically determined this relationship for 5577Å aurora.

5.3 μm Band

We have concluded that the measured 5.3 μm infrared auroral radiance is from the fundamental vibration of nitric oxide. The mechanism for exciting the NO are usually earthshine and collisional excitation with atomic oxygen, the latter predominating above about 120 km. The NO density is about an order of magnitude higher than mid-latitude models. The density enhancement is not localized to regions of a visible auroral arc, although the apparent NO density probably requires a prior low level electron flux of many hours duration. However, in an intense auroral break up, the brightness of the 5.3 μm band due to the above mechanisms in enhanced and, in addition, chemiluminescence from the reaction $N(^2D) + O_2 \rightarrow NO' + O$ becomes a significant source of radiation below about 100 km.

2.7 μm Band

The field data at 2.7 μm due to the relatively weak excitation of normally occurring auroras are generally comparable with the system noise, making it extremely difficult to determine their source. One major exception (Rocket 10.205-2) occurs during an auroral break up when 2.7 μm is readily detectable and identified as the first overtone of vibrationally excited NO, the mechanism again being chemiluminescent from the $N(^2D) + O_2$ reaction. Another exception occurs during descent when the wake of the Rocket (18.219-1) is in the field-of-view of the forward looking infrared instruments. The spectral band center at 2.7 μm is shifted to a shorter wavelength than that measured on Rocket 10.205-2, indicating the signal is not due to NO. We have concluded this emission must be considered an artifact of the experiment and associated with the fact that the vertical

instrumentation was looking in the payload wake. This enhancement was not measured by the side looking instruments.

We have determined from the measurements on Rocket 10.205-2 that the percentage of auroral energy which is emitted in the 2.7 μm band is approximately 1%.

4.3 μm Band

We show that for auroral emission the 4.3 μm band is in good agreement with the mechanism of energy transfer $N_2(V) + CO_2 \rightarrow N_2 + CO_2(001)$.

In addition for the EXCEDE II Test, we show that the 4.3 μm emission is not due to vibrational transfer from N_2 to CO_2, but probably a rapid emission attributed to NO^+. The 4.3 μ radiation is from a prompt emitter, possibly NO^+ or direct CO_2 excitation.

We recommend that additional experiments be performed to resolve the discrepancies in our understanding of the atmospheric properties and thereby provide additional data to improve the code modelling.

In the ICECAP program, we propose the following experiments:

1. Measure the infrared spectra of an auroral arc to at least 6.5 μm. This would determine the total amount of nitric oxide chemiluminescence.
2. Measure the 2.7 μm band with a high spectral resolution – high sensitivity instrument designed specifically for this purpose. This should give conclusive evidence for source, or sources, of the emissions.
3. Measure the 4.3 μm band at high spectral resolution. This would separate the emissions due to CO_2 from those of other constituents such as NO^+ or $N^{14}N^{15}$.
4. Perform additional aircraft narrow field-of-view zenith looking coaligned photometric and radiometric measurements to determine visible IR spatial correlations.

5. Perform rocket narrow field-of-view nadir looking co-aligned photometric and radiometric spatially scanning measurements to determine visible IR spatial correlations in selected bands.

6. Measure the infrared spectra of the upper atmosphere in a mid-latitude zone. This would determine the infrared background in a non-auroral region and verify our conclusions regarding some of the emission sources.

In the EXCEDE Program, we propose the following:

1. Perform a mother-daughter experiment in which the daughter contains a filtered low light level television (LLLTV) which monitors the electron beam from the gun onboard the mother. This would answer many questions about the spatial, spectra, and temporal nature of the emissions caused by the electron beam.

2. The use of EXCEDE instrumentation to study the development of spatial structure in a uniformly ionized medium.

3. The use of EXCEDE instrumentation to produce controlled ionization irregularities to study the development of instabilities as a function of the degree of inhomogeneity of the deposition.

4. The use of EXCEDE instrumentation to create known charge density inhomogeneities to study the propagation of electromagnetic radiation. A possible experiment is presented in Appendix E.

REFERENCES

1. Baker, K. D., "Studies of Disturbed Ionospheres", AFCRL-TR-75-0342, Final Report Contract No. F19628-72-C-0255, HAES Rprt. No. 25 (June 1975).

2. Baker, D. J., Wyatt, C. L., Pendelton, W. R., Jr., and Ulwick, J. C., "Rocket Launch of a SWIR Spectrometer into an Aurora (ICECAP 72)", AFCRL-TR-74-0077, HAES Report No. 1 (February 1974).

3. Baron, M. and Change, N. J., "ICECAP 73A-Chatanika Rada Results", DNA 3531T, HAES Report No. 15 (April 1975).

4. Stair, A. T., Jr., Ulwick, J. C., Baker, K. D., and Baker, D. J., p. 335 in "Atmospheres of Earth and the Planets", B. M. McCormac, editor, Reidel, Holland (1975).

5. Ulwick, J. C., Reidy, W. P., and Hegblom, E. R., "Rocket Measurements of the Energy Spectra of Auroral Electrons", Paper Presented at the XVI General Assembly of the International Union of Geodesy and Geophysics, Grenoble, France (August 1975).

6. Rogers, J. W., "Instrumentation Analysis and Data Processing for Rocketborne LWIR Spectrometers", AFCRL-TR-75-0535, HAES Report No. 23 (October 1975).

7. Burt, D. A. and Davis, C. S., "Rocket Instrumentation for ICECAP 73A Auroral Measurements Program - Black Brant 18.205-1", AFCRL-TR-74-0195, HAES Report No. 3 (February 1974).

8. Aeronomy Observatory, USU, "Ground Support Data Report in Support of Black Brant 18.219-1 Flight", AFCRL, (September 1974).

9. Kofsky, I. L., "Data Reduction and Auroral Characteristics for ICECAP", HAES Report No. 4, Contract No. DNA001-73-C-0027 Final Report, PhotoMetrics, Inc. (1975), p. 65.

10. "Trajectory Report, Rocket No. A18.205-1", Analysis and Simulation Branch, AFCRL Computation Center (January 1974).

11. "Aspect Report, Rocket No. A18.205-1", Analysis and Simulation Branch, AFCRL Computation Center, Report No. 4531-7.

12. Reference 9, p. 54

13. Romick, G. J., "Report on the Geophysical Description and Available Data Associated with Rocket PF-BB-75", Geophysical Institute, University of Alaska (May 1974).

14. Allred, G., Utah State University, private communication.

15. Reference 9, p. 83

16. Hegblom, E. R., Boston College, private communication.

17. Grieder, W. F., Visidyne, Inc., private communication.

18. Reference 4, p. 339

19. Nadile, R., AFGL, private communication

20. "Trajectory Report, Rocket No. A18.219-1", Analysis and Simulation Branch, AFCRL Computation Center, (March 1975).

21. "Aspect Report, Rocket No. A18.219-1", Analysis and Simulation Branch, AFCRL Computation Center, Report No. 4598.

22. Reference 9, p. 86

23. Grieder, W. F., Stair, A. T., Jr., Condron, T., and Foley, C., "Short Wavelength Infrared Spectral Measurements of Auroral Emission - Rocket A18.219-1", (in publication).

24. Wheeler, N. B., Stair, A. T., Jr., Frodsham, G., and Baker, D. J., "Rocket-Borne Spectral Measurement of Atmospheric Infrared Emission During A Quiet Condition in the Auroral Zone", AFGL-TR-76-0252 (October 1976).

25. "Trajectory Report, Rocket No. A10.205-2", Analysis and Simulation Branch, AFCRL Computation Center (undated).

26. "Aspect Report, Rocket No. A10.205-2", Analysis and Simulation Branch, AFCRL Computation Center, Report No. 4531-8.

27. Reference 4, p. 336

28. "Meridian Scanning Photometer - 5577Å, Paiute-Tomahawk 10.205-2", Center for Research in Aeronomy, Utah State University, (March 1973).

29. Reference 9, p. 82

30. Baker, K.D., Baker, D.J., Ulwick, J.C. and Stair, A.T., Jr., "Rocketborne Measurements of Infrared Enhancements Associated with a Bright Auroral Breakup", HAES Report No. 50 (Report Number not yet assigned).

31. Reidy, W.P., Degges, T.C., Manley, O.P., Smith, H.J., Carpenter, J.W., Stair, A.T., Jr., Ulwick, J.C., and Baker, D.J., "Analysis of HAES Results: ICECAP 72", HAES Report No. 2, *Contract No.* DNA 001-73-C-0020, (April 1974), p.7

32. Boyd, J.S., Reviews of Geophysics and Space Physics, 13, 735, (1975).

33. Chamberlain, J.W., "Physics of the Aurora and Airglow", Academic Press, New York (1961), p. 134.

34. Reference 9, p. 51

35. Harang, L., "The Aurorae", Wiley, New York (1951).

36. Ulwick, J.C., p. 225 in "Aurora and Airglow", B.M. McCormac, editor, Reinhold, New York (1966).

37. Dalgarno, A., Latimer, I.D., and McConkey, J.W., Planetary Space Science, 13, 1008 (1965).

38. Manley, O.P., *Smith*, H.J.P., Treve, Y.M. Carpenter, J.W., Degges, T.C. and Doan, L.R., Major, USAF, "OPTIR III", Special Scientific Report (Vol. 1), Contract No. F19628-71-C-0212, AFCRL-TR-74-0217 (I) (September 1972).

39. Reference 31, p. 46

40. Reference 31, p. 47

41. Tarr, P.W. and Archer, D.H., "Auroral Simulation Studies in Support of ICECAP and EXCEDE", HAES Report No. 24, Contract No. DNA 001-74-C-0143, Final Report DNA 3785F, (Sep 1975).

42. Degges, T.C., Applied Optics, 10, (1971), p. 1856.

43. Swider, W., Geophysical Research Letters, 3, (1976), p. 335.

44. Smith, H.J.P., Visidyne, Inc., private communication.

45. Norton, R.B., and Barth, C.A., Journal of Geophysical Research, 75, (1970), p. 3903.

46. Reference 31, p. 121.

47. Archer, D.H. and Tarr, P.W., "Auroral Simulation Studies", HAES Report No. 6, Contract No. DNA 001-74-C-0143, Topical Report, (April 1975), p. 34.

48. Whalen, J.A., "Auroral Oval Platter and Nomograph", AFCRL-TR-70-0422, Environmental Research Papers, No. 327 (July 1970).

49. Narcisi, R.S. and Swider, W., "Ionic Structure Near an Auroral Arc", to be published in Journal of Geophysical Research (Space Physics).

50. Narcisi, R.S. and Swider, W., AFGL, private communication.

51. Quack, M. and Troe, J., Ber. Bunsenges, Phys. Chem., 70, (1975), p. 170, and Glanzer, K. and Troe, J., J. Chem. Phys., 63, (1975), p. 4352.

52. Gordiets, B.F., Markov, M.N., and Shelepin, L.A., Preprint No. 84 (1976), Lebedev Physical Institute of the USSR Academy of Sciences, Moscow.

53. Reference 41, p. 34

54. Reference 41, p. 44

55. Kumer, J.B., "Analysis of 4.3 μm ICECAP Data", HAES Report No. 19, AFCRL-TR-74-0334, (July 1974).

56. Reference 47, p. 67

57. Kumer, J.B., "Further Analysis of ICECAP Auroral 4.3 μm Zenith Radiance", HAES Report in publication.

58. Streit, G.E. and Johnston, H.S., Jour. of Chem. Physics, 64 (1976), p. 95.

59. Shepherd, O., Carpenter, J.W., Reidy, W.P., Sheehan, W.A., and Zehnpfennig, T.F., "The Design and Flight Test of a 30 kW Rocket-Borne Electron Accelerator Module (EXCEDE II Test)", HAES Report No. 22, Final Report, Contract No. F19628-75-C-0115, Visidyne, Inc. (15 July 1975).

60. Reidy, W.P., Shepherd, O., O'Neil, R.R., Ulwick, J.C., Davis, T.N., and Mitchell, H.J., "EXCEDE II Test Measurements", Paper Presented at the Fall Meeting of the American Geophysical Union, San Francisco, CA, December 1975.

61. "Trajectory Report, Rocket No. EXCEDE - 2", Analysis and Simulation Branch, AFCRL Computation Center, (undated).

62. "Preliminary Attitude Report for EX531.43-1", Analysis and Simulation Branch, AFCRL (15 March 1976).

63. O'Neil, R.R., Lee, E.T.P., Stair, A.T., Jr., and Ulwick, J.C., "EXCEDE II", AFGL-TR-76-0308, Environmental Research Papers No. 586 (December 1976).

64. Billingsley, F.P., II, "Calculation of the Absolute Infrared Intensities for the 0-1, 0-2, and 1-2 Vibration-Rotation Transitions in the Ground State of NO^{+}*", Chem. Phys. letters 23, 160 (1973).

65. Sawada, T., Strickland, D.J., and Green, A.E.S., "Electron Energy Deposition in CO_2", J. Geophysics Res., 77, 4812 (1972).

66. Hushfar, F., Rogers, J.W., and Stair, A.T., Jr., "Infrared Chemiluminescence of the Reaction $N + O_2 \rightarrow NO + O$", Applied Optics, 10, 1843 (1971).

67. Hushfar, F., Rogers, J.W., and Stair, A.T., Jr., "Further Comments on the Chemiluminescent Reaction $N + O_2 \rightarrow NO + O$ and its Overtone Photon Efficiency, Applied Optics, 11, 1656 (1972).

APPENDIX A

AURORAL TIME HISTORIES

A18.219-1 ROCKET ASCENT

5577A BRIGHTNESS (KR)

$L_v = 4.5^o$ THROUGHOUT ASCENT

TIME BEFORE DATA (SEC)	ROCKET AT 83 KM (T + 67 SEC) ALTITUDE ALONG CVF AXIS						ROCKET AT 93 KM (T + 74 SEC) ALTITUDE ALONG CVF AXIS						RKT @ 103 KM(T + 82 SEC) ALTITUDE ALONG CVF AXIS					RKT @ 107 KM(T + 85 SEC) ALTITUDE ALONG CVF AXIS				
	100	120	140	160	180	200	100	120	140	160	180	200	120	140	160	180	200	120	140	160	180	200
0 to -20	S025	S025	S025	S025	S025	S025	S025	S025	S025	S025	S025	S025	S025	S020	S025	S055	S035	S020	S020	S025	S025	S035
-40	30	25	30	30	35	35	25	30	30	30	30	35	30	30	25	30	35	25	25	25	30	35
-60	35	35	40	45	50	55	35	40	40	45	50	50	35	35	35	40	40	35	35	35	40	45
-80	45	45	55	65	80	80	45	50	55	70	75	S075	45	50	60	S065	S070	50	55	60	65	70
-100	55	55	65	75	75	75	55	65	75	80	80	N080	70	80	80	N085	N085	70	80	85	S090	S090
-120	55	55	65	80	85	85	60	65	75	85	80	80	75	75	75	80	85	75	75	80	N080	N085
-140	45	50	70	75	75	75	55	70	75	80	80	75	80	85	85	80	75	80	85	85	85	85
-160	35	40	60	65	80	80	45	65	70	80	80	75	70	75	75	60	50	75	75	70	55	50
-180	40	50	55	60	80	90	40	55	55	75	80	100	60	75	80	95	100	65	80	80	N095	N095
-200	50	60	S065	S080	S100	S110	55	60	S070	S095	S110	120	55	75	90	110	125	60	80	95	S110	S130
-220	S070	S080	N085	N075	N065	N070	S075	S085	N090	N080	N080	80	S085	S100	S110	115	105	S085	S105	S115	N120	N115
-240	N055	N065	60	50	40	30	N080	N070	60	50	35	25	N075	N065	N055	40	35	N070	N075	N060	60	95
-260	45	45	35	25	15	10	50	50	35	20	20	20	45	40	25	20	20	50	40	25	20	20
-280	55	40	35	25	15	10	45	45	25	15	10	05	25	20	10	10	15	20	20	10	10	15
-300	35	35	20	20	05	05	40	40	25	10	05	10	25	15	10	05	10	20	10	10	10	10
-320	25	25	10	10	05	05	30	35	15	05	05	05	10	10	05	05	10	15	05	10	10	15
-340	25	15	15	05	05	05	20	20	05	05	05	05	10	05	05	05	05	10	05	05	05	10
-360	20	15	15	10	05	05	15	15	10	05	05	10	05	05	05	05	10	05	05	05	10	10

TIME BEFORE DATA (SEC)	RKT @ 113 KM(T + 89 SEC) ALTITUDE ALONG CVF AXIS				
	120	140	160	180	200
0 to -20	S025	S025	S025	S035	S040
-40	25	25	25	30	40
-60	35	35	35	40	45
-80	50	55	50	55	65
-100	75	80	85	S080	S085
-120	75	75	80	N075	N085
-140	85	85	S085	70	75
-160	75	75	N070	55	50
-180	80	80	N085	N080	85
-200	75	85	S100	S120	135
-220	S100	S110	S125	N125	125
-240	N070	N070	N070	55	45
-260	40	35	25	15	20
-280	15	10	15	10	15
-300	15	10	05	10	15
-320	10	05	10	10	15
-340	05	05	05	05	10
-360	05	05	05	10	10

A10.205-2 ROCKET ASCENT

5577A BRIGHTNESS (KR)

TIME BEFORE DATA (SEC)	ROCKET AT 70 KM (T + 55 SEC) ALTITUDE ALONG CVF AXIS (L_V = 7°)							ROCKET AT 80 KM (T + 62 SEC) ALTITUDE ALONG CVF AXIS (L_V = 20°)							ROCKET AT 90 KM (T + 68 SEC) ALT ALONG CVF AXIS (L_V = 20°)						ROCKET AT 100 KM (T + 75 SEC) ALT ALONG CVF AXIS (L_V = 17°)					
	80	100	120	140	160	180	200	80	100	120	140	160	180	200	100	120	140	160	180	200	100	120	140	160	180	200
0 to -20	S070	S085	S095	S125	S150	S160	N155	S075	S080	S120	S150	S150	S155	S160	S080	S095	S140	S145	S145	S150	S095	S095	S100	S110	S130	S130
-40	N050	N075	N070	N075	N070	N095	70	N070	N085	N090	N115	N100	N110	N115	S090	N090	N140	N125	N115	N140	S085	S095	N125	N150	N150	N155
-60	20	25	20	20	20	25	15	25	30	40	30	20	20	25	N060	40	65	35	30	50	N095	N090	60	65	60	60
-80	20	30	15	10	05	10	10	15	15	15	10	15	15	10	25	15	15	15	15	15	30	25	30	25	20	20
-100	20	15	05	05	01	01	05	25	10	05	01	05	05	01	20	10	05	10	05	05	30	10	10	05	05	10
-120	05	05	05	01	01	01	01	10	05	05	01	01	01	01	05	05	01	01	01	01	10	05	05	01	01	05
-140	10	10	05	05	01	01	01	10	05	05	01	01	01	01	05	05	01	01	01	01	05	05	05	01	01	01
-160	15	15	10	10	05	01	01	15	10	05	01	01	01	01	10	05	05	01	01	01	05	05	05	01	01	01
-180	20	10	10	05	05	01	01	20	10	05	01	01	01	01	10	10	05	01	01	01	10	10	10	05	01	01
-200	10	05	15	10	05	05	01	15	10	05	01	01	01	01	10	05	05	01	01	01	10	10	10	05	01	01
-220	10	10	15	15	10	05	01	10	15	10	05	01	01	01	10	15	05	05	01	01	10	15	10	05	05	01
-240	35	20	10	10	05	05	01	25	10	15	05	01	01	01	15	20	10	05	01	01	10	15	15	10	05	01
-260	65	30	15	10	10	05	01	55	15	10	05	01	01	01	10	10	05	01	01	01	20	10	10	10	05	01
-280	50	15	15	10	10	05	01	50	10	10	05	01	01	01	10	15	05	01	01	01	25	15	10	10	05	01

TIME BEFORE DATA (SEC)	RKT @ 110 KM (T + 82 SEC) ALT ALONG CVF AXIS(L_V=8°)					RKT @ 120 KM (T + 90 SEC) ALT ALONG CVF AXIS(L_V=29°)					(L_V = 36°) RKT @ 130 KM(T+98 SEC) ALT ALONG CVF AXIS				(L_V = 11°) RKT @ 140 KM(T+106 SEC) ALT ALONG CVF AXIS				(L_V = 10°) RKT @ 150 KM(T+115 SEC) ALT ALONG CVF AXIS		
	120	140	160	180	200	120	140	160	180	200	140	160	180	200	140	160	180	200	160	180	200
0 to -20	S110	S125	S135	N135	N145	S130	S155	N165	N150	N140	S180	S190	N150	N110	S180	N190	N190	N190	N175	N175	N160
-40	S095	S125	S145	150	150	S095	S130	135	145	145	S125	S145	140	120	S140	S150	S155	S160	S175	S180	S180
-60	N075	N075	N110	110	100	S110	N145	120	155	150	S150	S150	165	150	S125	S145	S145	S145	S130	S130	S135
-80	30	35	45	30	20	N045	70	35	60	60	N105	N090	100	70	N100	N140	N115	N110	S155	S150	S150
-100	15	15	10	10	15	15	15	15	15	10	35	20	20	10	45	50	35	20	N095	N080	N060
-120	05	05	01	05	05	10	05	10	05	05	10	10	10	01	15	15	15	15	30	20	20
-140	05	05	01	01	01	05	01	05	01	01	05	05	01	01	10	05	05	05	10	10	10
-160	05	05	01	01	01	05	01	01	01	01	05	01	01	01	05	05	05	01	05	05	05
-180	10	05	05	01	01	05	05	01	01	01	05	01	01	01	05	01	01	01	01	01	01
-200	10	10	05	01	01	10	05	01	01	01	05	01	01	01	05	01	01	01	01	01	01
-220	10	05	05	01	01	10	05	01	01	01	05	01	01	01	05	01	01	01	01	01	01
-240	15	10	05	05	01	15	05	01	01	01	05	01	01	01	05	01	01	01	01	01	01
-260	10	15	10	05	01	15	10	01	01	01	10	01	01	01	10	05	01	01	05	01	01
-280	15	10	10	05	01	10	05	01	01	01	10	01	01	01	10	10	01	01	05	01	01

A18.219-1 ROCKET DESCENT

5577A BRIGHTNESS (KR)

L_v = 5.5° THROUGHOUT FLIGHT EXCEPT L_v = 1° AT 83 KM ALTITUDE

TIME BEFORE DATA (SEC)	RKT @ 138 KM(T+325 SEC) ALTITUDE ALONG CVF AXIS				RKT @ 127 KM(T+345 SEC) ALTITUDE ALONG CVF AXIS				RKT @ 117 KM(T+353 SEC) ALTITUDE ALONG CVF AXIS					RKT @ 108 KM(T+361 SEC) ALTITUDE ALONG CVF AXIS					RKT @ 103 KM(T+365 SEC) ALTITUDE ALONG CVF AXIS				
	140	160	180	200	140	160	180	200	120	140	160	180	200	120	140	160	180	200	120	140	160	180	200
0-20	S010	S015	S015	S015	S005	S010	S010	S010	S005	S005	S005	S005	S005	S001	S001	S001	S005	S001	S001	S001	S001	S001	S001
-40	45	55	55	60	25	25	30	35	10	15	15	15	20	10	10	10	10	10	05	05	05	10	10
-60	S115	S120	S135	S140	S095	S100	S100	S125	55	60	S070	S085	S075	35	40	35	45	50	25	25	30	40	40
-80	N090	N075	N075	N060	N125	N115	N120	N105	S125	S130	N135	N140	N155	S105	S105	S120	S130	S140	S090	S095	S100	S120	S120
-100	05	05	05	05	20	15	15	10	N065	N050	50	35	40	N105	N095	N095	N085	N075	N120	N130	N120	N120	N110
-120	01	01	01	01	01	01	01	01	05	05	05	05	01	10	10	10	05	05	20	25	20	10	05
-140	01	01	01	01	01	01	01	01	01	01	01	01	01	01	01	01	01	01	01	01	01	01	01
-160	01	01	01	01	01	01	01	01	01	01	01	01	01	01	01	01	01	01	01	01	01	01	01
-180	10	05	01	05	01	01	01	01	01	01	01	01	01	01	01	01	01	01	01	01	01	01	01
-200	95	65	30	25	35	25	15	10	15	10	05	05	05	01	01	01	01	01	01	01	01	01	01
-220	155	90	50	35	120	75	45	30	110	75	45	30	25	50	45	25	15	10	40	25	20	10	05
-240	125	75	45	25	95	55	35	20	150	95	55	30	20	145	95	45	35	15	140	95	45	30	10
-260	70	50	30	15	80	50	25	10	120	70	45	25	10	110	60	35	25	05	105	75	35	20	05
-280	50	25	20	05	40	15	10	01	55	45	30	10	05	80	55	30	20	05	80	65	25	10	05
-300	35	15	15	01	40	10	05	01	50	25	25	05	01	40	20	10	05	01	40	25	10	05	01
-320	15	05	01	01	20	05	01	01	35	20	10	01	01	35	20	10	05	01	35	20	05	01	01
-340	01	01	01	01	01	01	01	01	10	05	01	01	01	15	10	05	01	01	15	10	01	01	01
-360	01	01	01	01	01	01	01	01	01	01	01	01	01	01	01	01	01	01	01	01	01	01	01

TIME BEFORE DATA (SEC)	ROCKET @ 97 KM (T + 369 SEC) ALTITUDE ALONG CVF AXIS						ROCKET @ 93 KM (T + 372 SEC) ALTITUDE ALONG CVF AXIS						ROCKET @ 88 KM (T + 376 SEC) ALTITUDE ALONG CVF AXIS						ROCKET @ 83 KM (T + 380 SEC) ALTITUDE ALONG CVF AXIS					
	100	120	140	160	180	200	100	120	140	160	180	200	100	120	140	160	180	200	100	120	140	160	180	200
0-20	S001	S001	S001	S001	S001	S005	S001	S001	S001	S001	S001	S005	S001	S001	S001	S001	S001	S001	S001	S001	S001	S001	S010	S015
-40	05	05	05	05	05	10	01	01	05	05	05	10	01	05	05	05	05	10	01	01	05	10	15	20
-60	15	20	20	20	25	35	10	10	15	20	20	25	10	10	15	15	15	25	10	10	15	20	30	35
-80	75	S070	S085	S095	S090	S110	50	60	S055	65	S065	S080	40	45	50	55	55	65	35	40	40	50	70	85
-100	S130	N135	N135	N135	N140	N145	S125	S130	N140	S140	N155	N180	S115	S120	S135	S140	S155	S170	S110	S125	S135	S155	S195	S220
-120	N040	35	30	25	20	15	N055	N060	45	N035	30	20	N090	N080	N075	N070	N065	N060	N100	N115	N080	N075	N075	N100
-140	01	01	01	01	01	01	05	05	05	01	01	01	05	05	05	05	05	05	10	05	05	05	05	05
-160	01	01	01	01	01	01	01	01	01	01	01	01	01	01	01	01	01	01	01	01	01	01	01	01
-180	01	01	01	01	01	01	01	01	01	01	01	01	01	01	01	01	01	01	01	01	01	01	01	01
-200	01	01	01	01	01	01	01	01	01	01	01	01	01	01	01	01	01	01	01	01	01	01	01	01
-220	25	20	15	10	10	05	20	10	10	05	05	05	05	05	05	05	05	01	05	05	05	05	01	01
-240	150	105	70	40	25	15	130	95	45	30	25	15	90	60	30	25	20	10	50	30	15	10	10	10
-260	150	100	50	35	20	10	150	100	55	30	20	10	155	95	50	35	20	10	135	60	25	10	10	10
-280	135	85	50	30	10	05	125	90	45	25	10	05	120	125	40	25	10	05	100	50	10	05	05	05
-300	65	45	25	10	05	01	65	40	25	10	05	01	70	50	30	15	05	01	75	40	10	01	01	01
-320	55	40	20	05	01	01	50	30	20	01	01	01	50	25	20	05	01	01	30	10	05	01	01	01
-340	40	20	10	01	01	01	40	20	10	01	01	01	40	20	10	01	01	01	25	10	01	01	01	01
-360	10	01	01	01	01	01	10	05	01	01	01	01	10	05	05	01	01	01	15	05	01	01	01	01

A18.205-1 ROCKET ASCENT

5577A BRIGHTNESS (KR)

$L_v = 3^o$ THROUGHOUT FLIGHT

TIME BEFORE DATA (SEC)	ROCKET AT 70 KM (T + 61 SEC) ALTITUDE ALONG CVF AXIS							ROCKET AT 80 KM (T + 68 SEC) ALTITUDE ALONG CVF AXIS							ROCKET AT 90 KM (T + 76 SEC) ALTITUDE ALONG CVF AXIS						ROCKET AT 100 KM (T + 83 SEC) ALTITUDE ALONG CVF AXIS					
	80	100	120	140	160	180	200	80	100	120	140	160	180	200	100	120	140	160	180	200	100	120	140	160	180	200
0 to -20	S005	S005	S010	S010	S020	S015	S025	S010	S015	S015	S015	S020	S030	S030	S015	S020	S030	S050	S055	N075	S025	S050	S055	65	N065	N065
-40	01	01	05	10	15	20	25	05	05	10	15	15	25	40	15	15	20	35	40	S050	20	25	40	S050	S060	S065
-60	01	01	01	05	10	20	25	01	01	05	15	20	30	40	10	20	20	30	30	45	20	25	40	30	40	45
-80	01	01	01	05	05	15	20	01	01	05	10	15	20	40	05	15	15	25	35	50	20	25	35	35	45	60
-100	01	01	01	05	10	20	25	01	01	05	10	20	25	40	05	20	20	25	30	55	15	20	30	35	55	70
-120	01	01	05	10	15	25	30	01	01	10	15	25	40	40	10	20	25	30	35	55	20	25	35	40	55	70
-140	01	01	05	10	15	20	25	01	01	15	15	20	35	35	15	20	25	35	35	50	25	30	40	45	55	70
-160	01	01	01	05	15	15	20	01	01	10	10	15	25	30	15	15	20	30	30	40	20	25	35	35	50	60
-180	01	01	01	05	10	15	20	01	01	05	10	15	15	20	10	15	20	20	25	35	15	25	25	30	40	45
-200	01	01	01	10	05	15	20	01	01	05	10	15	15	15	10	10	15	15	20	25	15	20	20	20	30	40
-220	01	01	01	10	10	15	20	01	01	05	10	15	15	15	05	10	15	15	20	20	15	20	20	15	25	30
-240	01	05	05	10	15	15	?	01	01	05	10	15	15	20	05	15	20	?	?	?	15	15	?	?	?	?
-260	01	10	10	10	?	?	?	01	05	10	15	?	?	?	10	15	?	?	?	?	15	?	?	?	?	?
-280	05	?	?	?	?	?	?	05	10	15	15	?	?	?	?	?	?	?	?	?	?	?	?	?	?	?
-300	05	?	?	?	?	?	?	10	?	?	?	?	?	?	?	?	?	?	?	?	?	?	?	?	?	?
-320	?	?	?	?	?	?	?	?	?	?	?	?	?	?	?	?	?	?	?	?	?	?	?	?	?	?
-340	?	?	?	?	?	?	?	?	?	?	?	?	?	?	?	?	?	?	?	?	?	?	?	?	?	S040
-360	?	?	?	?	?	?	?	?	?	?	?	?	?	?	?	?	?	?	?	?	?	?	?	?	S045	045

TIME BEFORE DATA (SEC)	RKT @ 110 KM (T + 92 SEC) ALTITUDE ALONG CVF AXIS					RKT @ 120 KM(T + 101 SEC) ALTITUDE ALONG CVF AXIS					RKT @ 130 KM(T+110 SEC) ALTITUDE ALONG CVF AXIS				RKT @ 140 KM(T+121 SEC) ALTITUDE ALONG CVF AXIS				RKT @ 150 KM(T+133 SEC) ALTITUDE ALONG CVF AXIS		
	120	140	160	180	200	120	140	160	180	200	140	160	180	200	140	160	180	200	160	180	200
0 to -20	N060	N060	N060	N050	N035	N050	N050	N035	N020	N020	N020	N020	N015	N010	N020	N015	N015	N010	N015	N010	N010
-40	S050	S060	N070	N070	60	N075	N070	55	40	30	40	25	25	15	20	15	10	10	10	10	05
-60	35	40	S050	S065	70	S060	S065	65	55	45	55	40	35	30	30	25	20	15	15	10	10
-80	30	40	45	60	55	40	45	60	50	45	60	45	40	35	40	35	25	20	15	15	10
-100	35	45	60	70	45	50	60	50	45	40	50	40	35	25	35	35	25	15	15	15	10
-120	35	50	60	70	45	55	65	50	40	40	45	35	30	15	30	30	15	10	10	10	10
-140	40	50	65	75	50	60	60	50	40	40	45	35	30	15	30	25	10	05	10	05	05
-160	40	45	60	80	N065	60	70	N065	45	40	50	35	35	25	30	30	15	05	05	05	05
-180	30	40	50	60	S070	50	60	S075	N065	45	N065	40	40	35	35	35	25	10	10	05	05
-200	25	30	40	40	55	40	45	60	S065	N055	S070	N050	N045	45	45	40	35	25	15	10	?
-220	20	25	30	35	40	35	40	40	45	S050	50	S055	S055	45	N055	45	40	30	25	20	?
-240	?	?	?	35	40	?	35	40	40	40	35	35	45	50	S050	50	40	35	35	30	?
-260	?	?	?	35	40	?	35	40	35	40	35	35	50	50	45	N050	45	40	45	35	?
-280	?	?	?	35	45	?	40	40	40	45	35	40	50	50	45	S050	45	40	40	40	?
-300	?	?	?	30	40	?	35	35	45	45	35	45	60	55	50	55	60	45	40	40	?
-320	?	?	?	35	40	?	35	40	45	50	35	45	55	N060	50	60	70	55	50	45	?
-340	?	?	?	30	40	?	35	40	45	55	40	50	60	S055	50	55	70	50	55	50	?
-360	?	?	?	?	40	?	35	35	40	50	40	50	55	65	55	60	75	55	50	45	?

APPENDIX B

DATA ANOMALIES OF ROCKET 18.219-1 FLIGHT

APPENDIX B

DATA ANOMALIES OF ROCKET 18.219-1 FLIGHT

Black Brant 18.219-1 was successfully flown on February 25, 1974 from the Poker Flat Research Range. The bright arc associated with it was well documented by ground-based instruments (Figures B1 and B2) and the payload instruments provided some excellent data, particularly, of electron energy spectra. The payload included a forward-looking SWIR spectrometer (CVF) and a side-looking 2.7 μm radiometer. The data provided by these instruments is the subject of this appendix.

The planned in-flight sequence of events is shown in Figure B3. Everything occurred as planned with a few exceptions. The rocket was despun to almost exactly 2 rps instead of 3 rps, and the ACS aligned the payload about 5^{o} off vertical (Figure B4) so that on this alignment the axially-mounted instruments looked almost directly into the payload wake on descent.

First, let us consider the data from the side-looking radiometer. Figures B5 through B10 show data from the 2.7 μm radiometer. The system noise had just about quieted down when, at about 100 km, a source entered the field-of-view (Figure B7). This source is believed to be the rocket motor which had achieved a greater velocity than the payload. One explanation for this is that the rocket motor did not completely burn out until after separation. At any rate, the 2.7 μm signal continued to increase and saturated at about 115 km altitude (Figure B9). It began to drop with increasing altitude and was well below saturation at 127 km (Figure B10).

Meanwhile, the data from the axially-mounted CVF spectrometer (Figure B11) showed the usual SWIR bands at 4.3 and 5.3 μm, and a very low level band at 2.7 μm peaking at about 88 kilometers. Co-adding of this data near 2.7 μm yields the results shown in Figure B12. At an

altitude of about 115 km, the CVF spectrometer data also became afflicted with the intrusion of the rocket motor into the field-of-view. Figure B13 shows an early spectral scan which is typical of the measurements as the rocket motor enters the field-of-view. The NO band at 5.3 μm is still detectable at this altitude. By the time the payload had reached an altitude of 135 km, the signal had increased an order of magnitude (Figure B14) and the 5.5 emission was no longer apparent. The signal from the motor appears to be something like a combination of a blackbody at a temperature of about 700° K and an additional signal peaking at about 2.8 μm. It is presumed the latter is due to signal exhaust gases which appear hotter than 700° K because they more nearly fill the field-of-view of the instrument.

At an altitude of 147 km (Figure B15), the blackbody portion of the signal has decreased but a sharp signal appears at about 3 μm. On subsequent sweeps, the peak shifted to shorter wavelengths, rapidly increased in amplitude, and saturated the instrument (Figure B16) while another peak appears at 5 μm. This second peak also moved on subsequent sweeps to shorter wavelengths and its amplitude increased and saturated the instrument (Figure B17). This sequence was repeated many times with peaks appearing at the long wavelength end of the scan and subsequently shifting to shorter wavelengths (Figure B18). We suggest that these very intense signals which appear to shift in wavelength are due to a hot part of the rocket motor spinning in and out of the instrument FOV. The signals are modulated at a frequency slightly less than the filter scan frequency, which makes them move temporally through the spectral scan. The period of the spectral scan is .493 sec. Using Figure B19, which gives scan wavelength as a function of scan time, the modulation time is found to be equal to .499 seconds. This is just equal to the spin time of the payload so that if there were any misalignment of the CVF spectrometer axis and the payload axis, it would be the right modulation frequency. However,

the field-of-view of the instrument has been carefully mapped, as shown in Figures B20 and B21, and it is difficult to imagine how any axial misalignment could cause the multipeaked signals which appear in the data.

A much more likely candidate for causing the modulation is the rocket motor itself, which, as noted in Figure B3, was also despun before payload separation to a rate of 2 rps. The nozzle end of the motor was still very hot, and the complexity of its component parts could readily cause the type of observed modulation as the motor spins.

As the motor moved farther away from the payload, signal saturation ended and the general temporal shape of the modulation signal can be observed. This characteristic shape persisted for much of the payload trajectory, as can be seen in Figures B22 through B24, the time between the first and last Figure being over 80 seconds.

We measured the peak brightnesses of four of the more prominent modulation peaks as a function of wavelength with the results shown in Figures B25 through B28. Since the peaks move slowly through the spectral scan, the time to obtain one scan is very long and the rocket motor moves farther away and presumably cools down. This produces a significant decrease in signal from the long to the short wavelength end of the scan. The numbers indicate the rocket altitude at the beginning and end of each scan. The number of points plotted is far from the total number available, but even with the limited number used, there is an intriguing increase at about 2.7 μm which appears in a number of the scans. This may mean that hot gas is continuing to escape from the motor.

During the downleg portion of its trajectory, the peaks continued to be evident; the one plotted in Figure B25 being tracked down to an altitude of 115 km.

To summarize the preceding discussion, there is clear evidence on upleg and downleg that the rocket motor is within the field-of-view of infrared instruments. The motor is initially seen by the side-looking 2.7 μ

radiometer at 100 kilometers upleg. Subsequently, it is viewed by the vertical looking CVF starting at about 117 km upleg. On downleg below about 115 km, the motor associated signal is about equivalent to the instrument noise level.

As the payload descended to about 105 km, emission at 2.7 μm again increased above noise in the CVF data (Figure B11). It continued to increase down to 82 km when the rocket began to tip over. We consider this increase in emission to be an artifact produced in the rocket wake and not emission from the aurorally perturbed atmosphere. This is based on the following observations:

1. The rocket on downleg is tilted so that the axially mounted instrumentation is looking through the rocket wake (Figure B4).

2. The 2.7 μ emission increases monotonically until rocket starts to tip over (Figure B29). The dependence of intensity with elevation angle (Alpha in Figure B29) is not consistent with that which would be observed either from an optically thick or an optically thin emitter. Rather, the behavior is indicative of emission from a small region (e.g., the rocket wake).

3. The ratio of the 2.7 μm side looking radiometer signal to the vertical looking (CVF) is different on upleg and downleg. The side looking radiometer data in Figures B30 and B31 clearly do not show the enhancement on downleg shown by the vertical looking CVF spectrometer.

4. The behavior of the band center is qualitatively different on 18.219 downleg from 10.205 upleg and from that measured on 519.07 (Figure B32). At tip over, the band center of the 2.7 μm emission shifts rapidly to longer wavelengths indicating a change in the emitting mechanism and also indicating the emitting mechanism is a localized region.

5. If the mechanism producing the 2.7 μ emission is closely coupled to the 4.3 μ emission, the 2.7 μ emission should have been seen on upleg of 18.219 when the 4.3 emission exceeds 10 MR/μm at 100 kilometers. It was not (Figure B11).

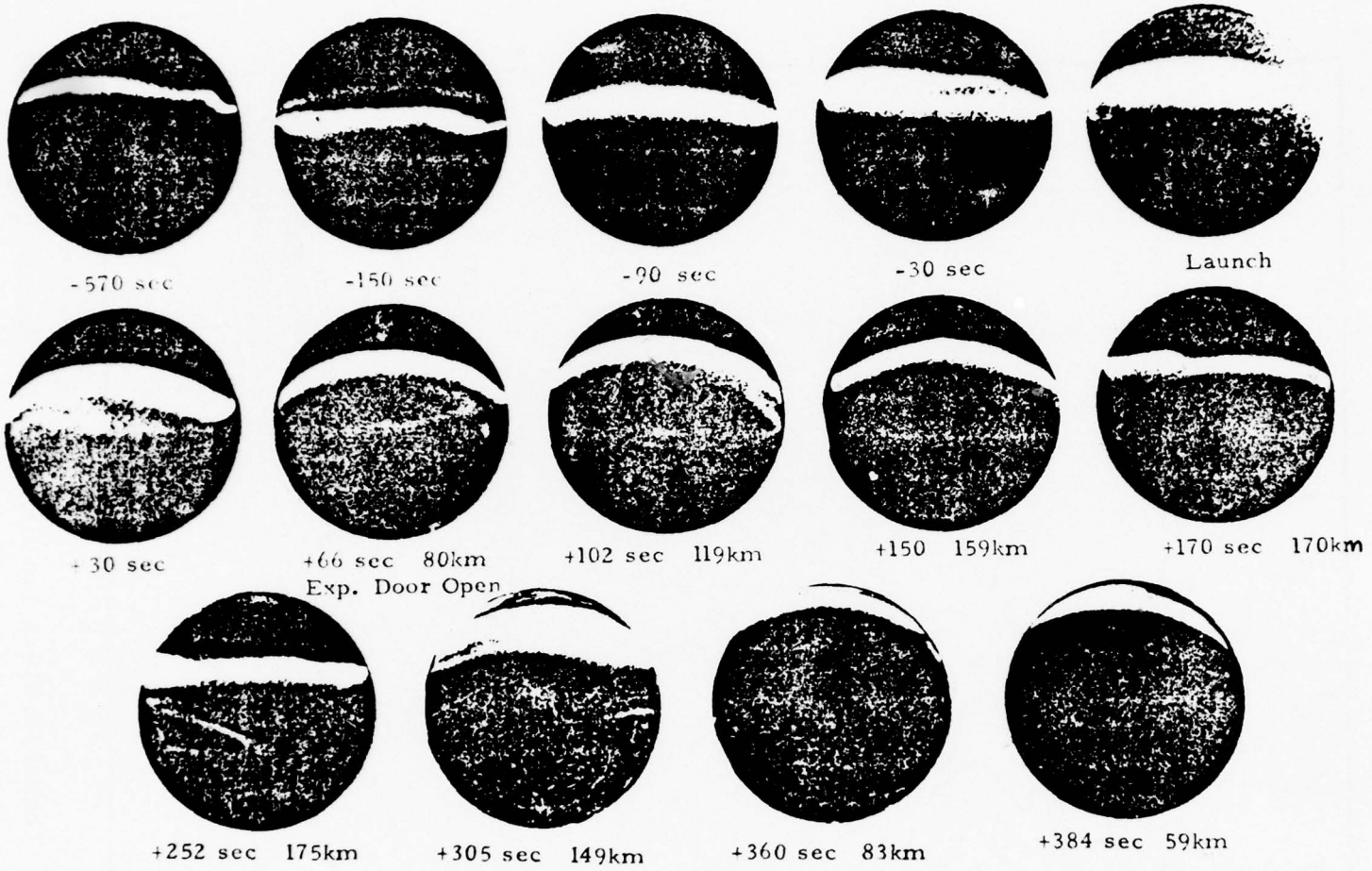

Figure B1. All-Sky Camera Photographs of Auroral Arc Associated With Rocket 18.219-1

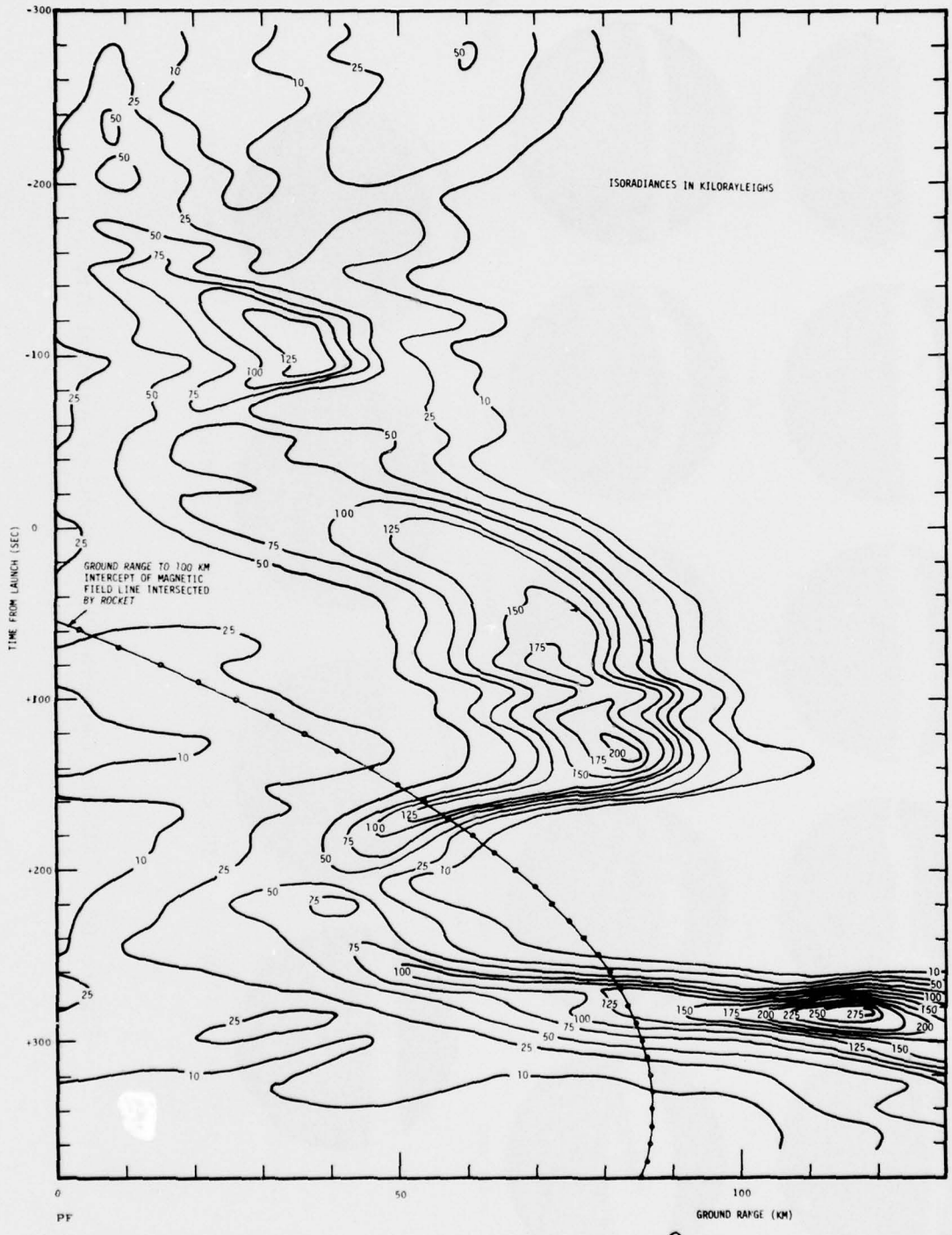

Figure B2. Rocket 18.219-1 Position of 5577Å Aurora vs. Time

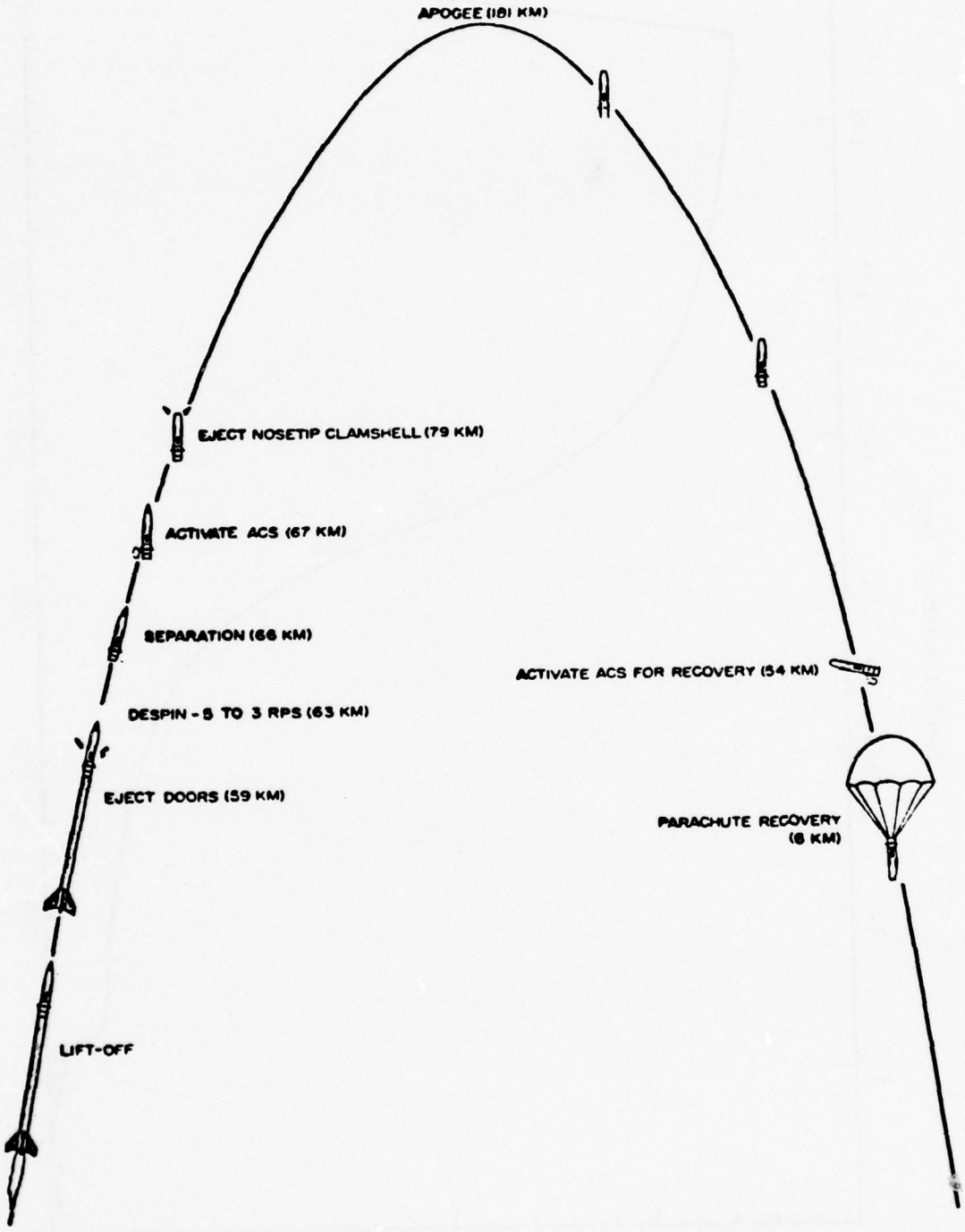

Figure B3. Illustration of the planned in-flight sequence of events of Black Brant 18.219-1

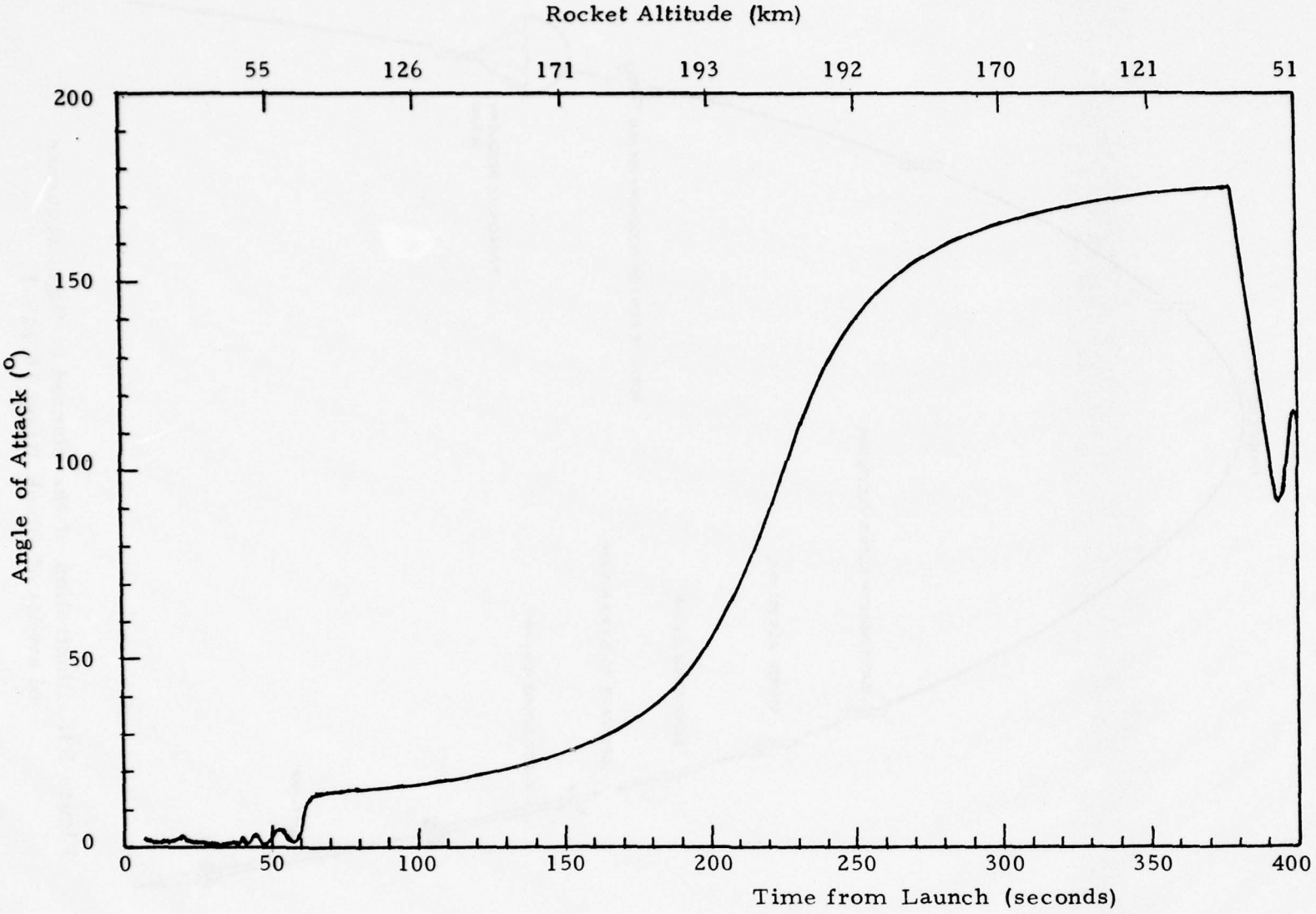

Figure B4. Rocket 18.219-1 Angle of Attack vs. Time from Launch

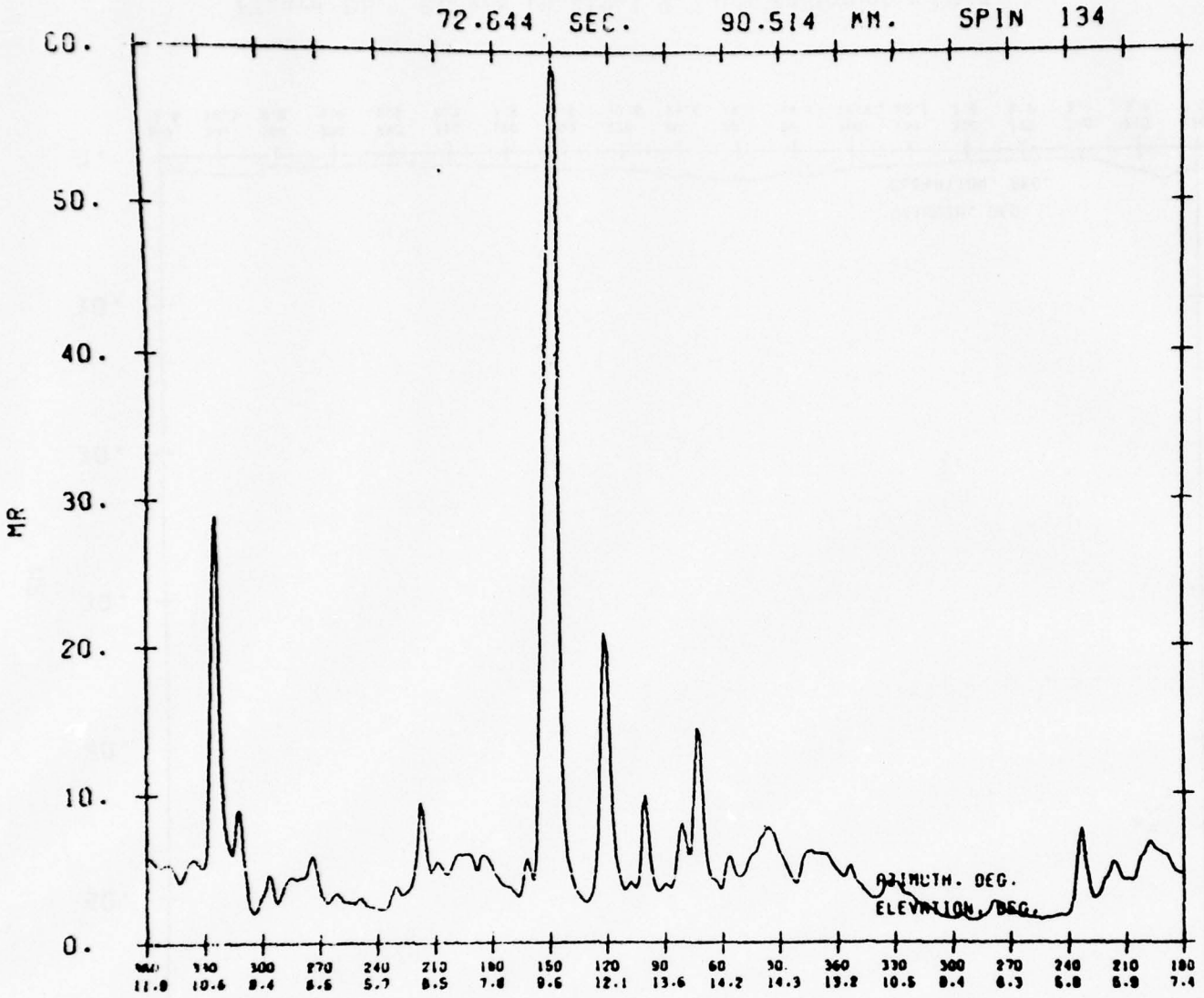

Figure B5. Rocket 18.219-1 2.7 μm Radiometer Data at 90 km, Ascent

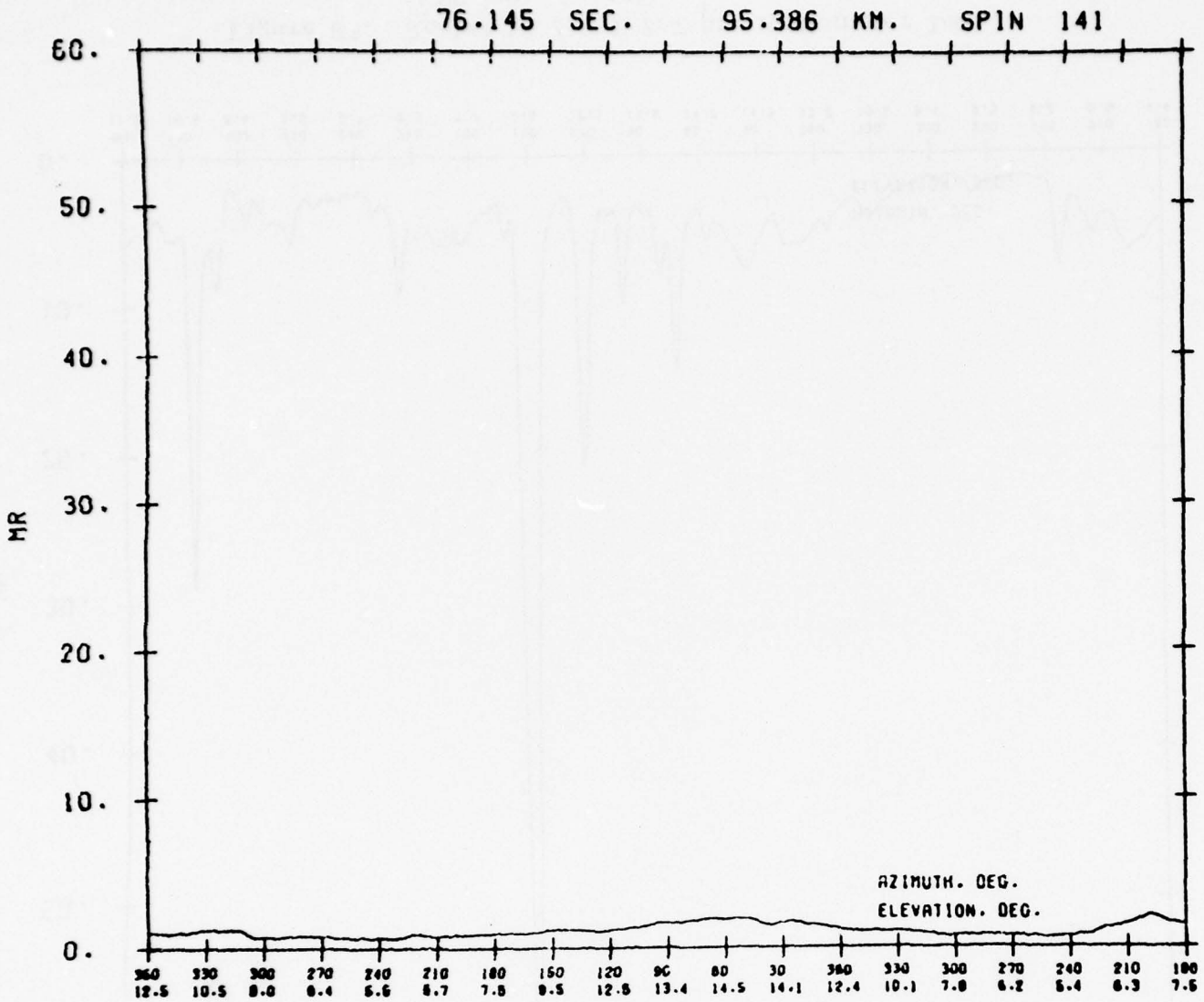

Figure B6. Rocket 18.219-1 2.7 μm Radiometer Data at 95 km, Ascent

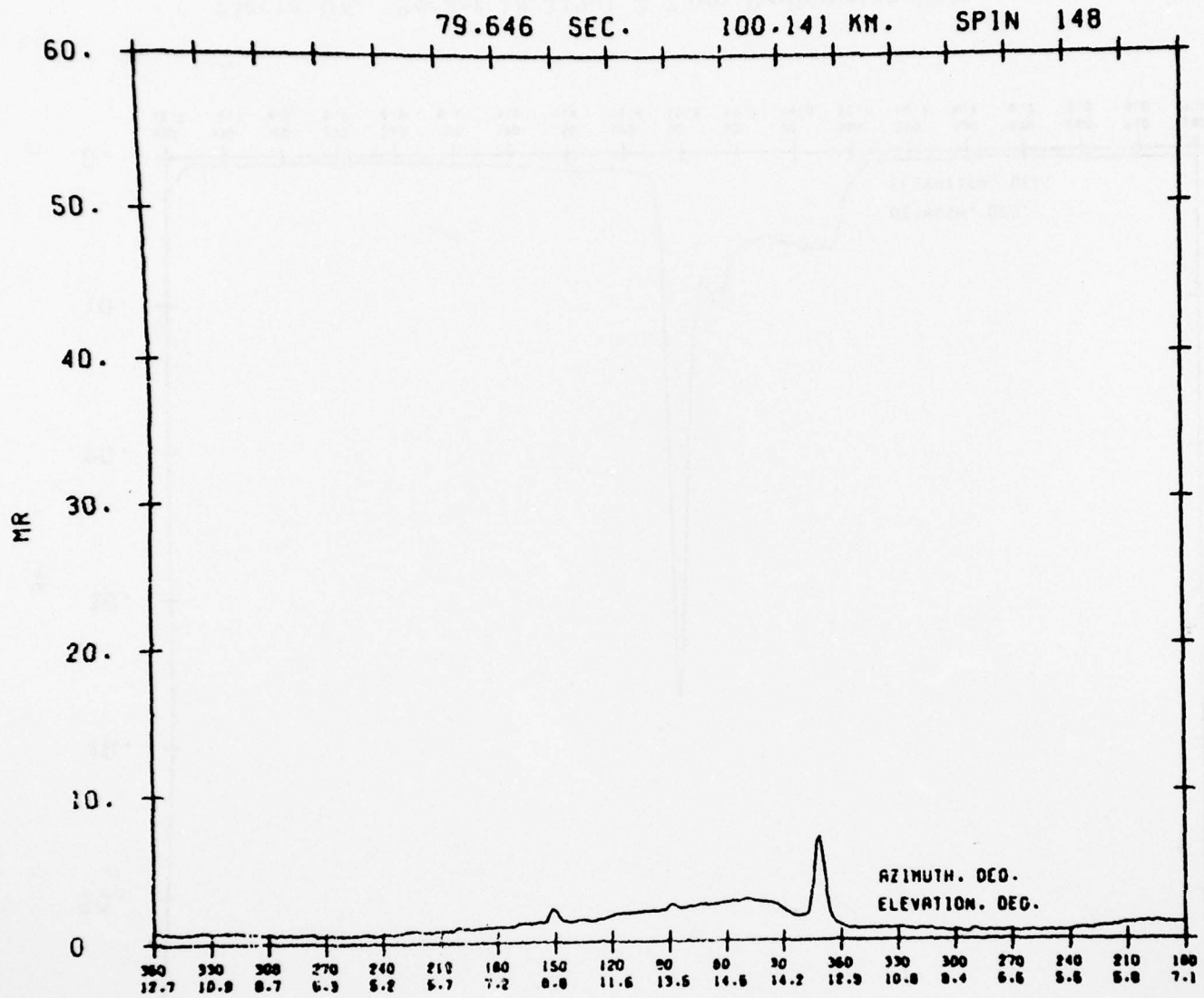

Figure B7. Rocket 18.219-1 2.7 μm Radiometer Data at 100 km, Ascent

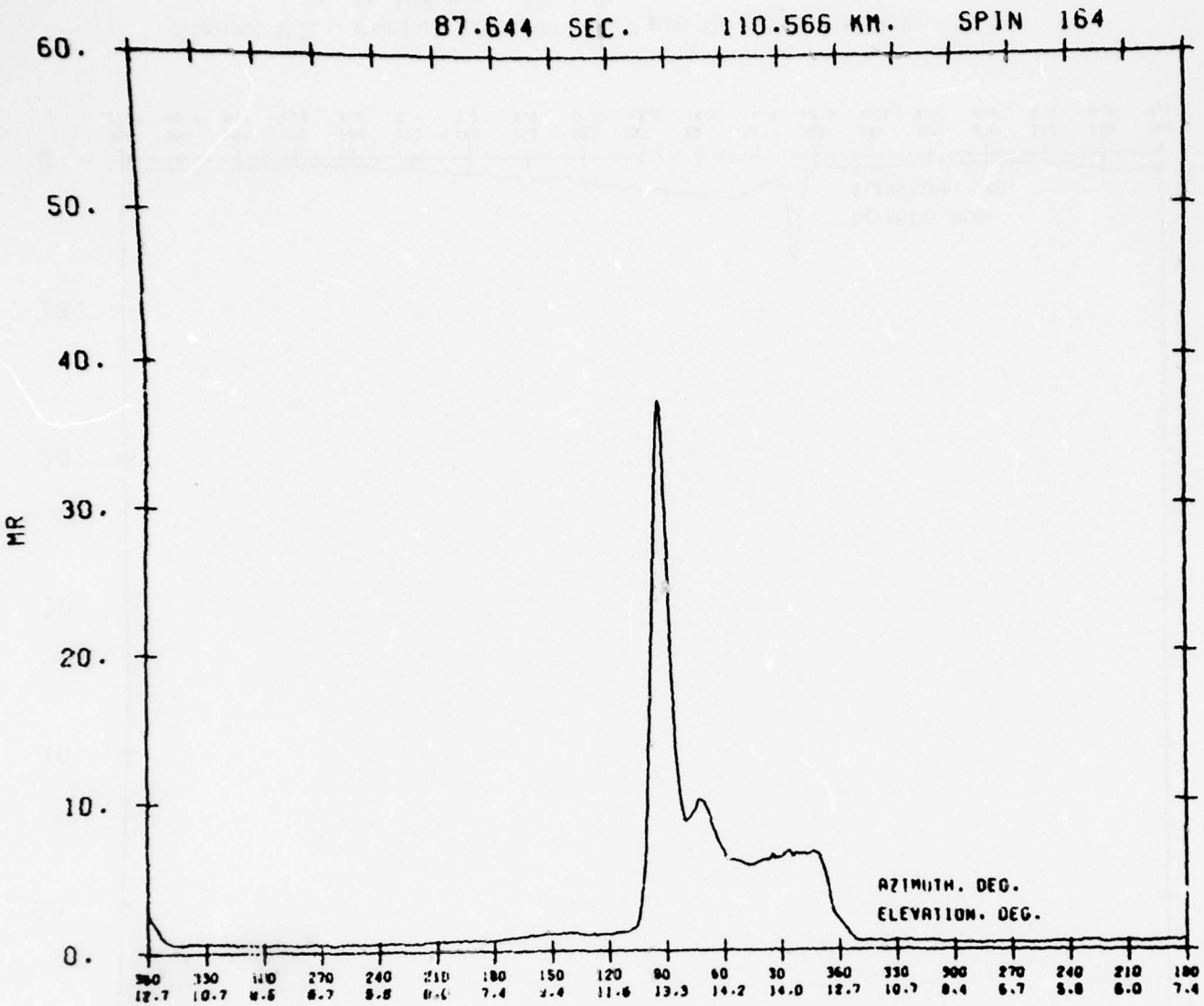

Figure B8. Rocket 18.219-1 2.7 μm Radiometer Data at 110 km, Ascent

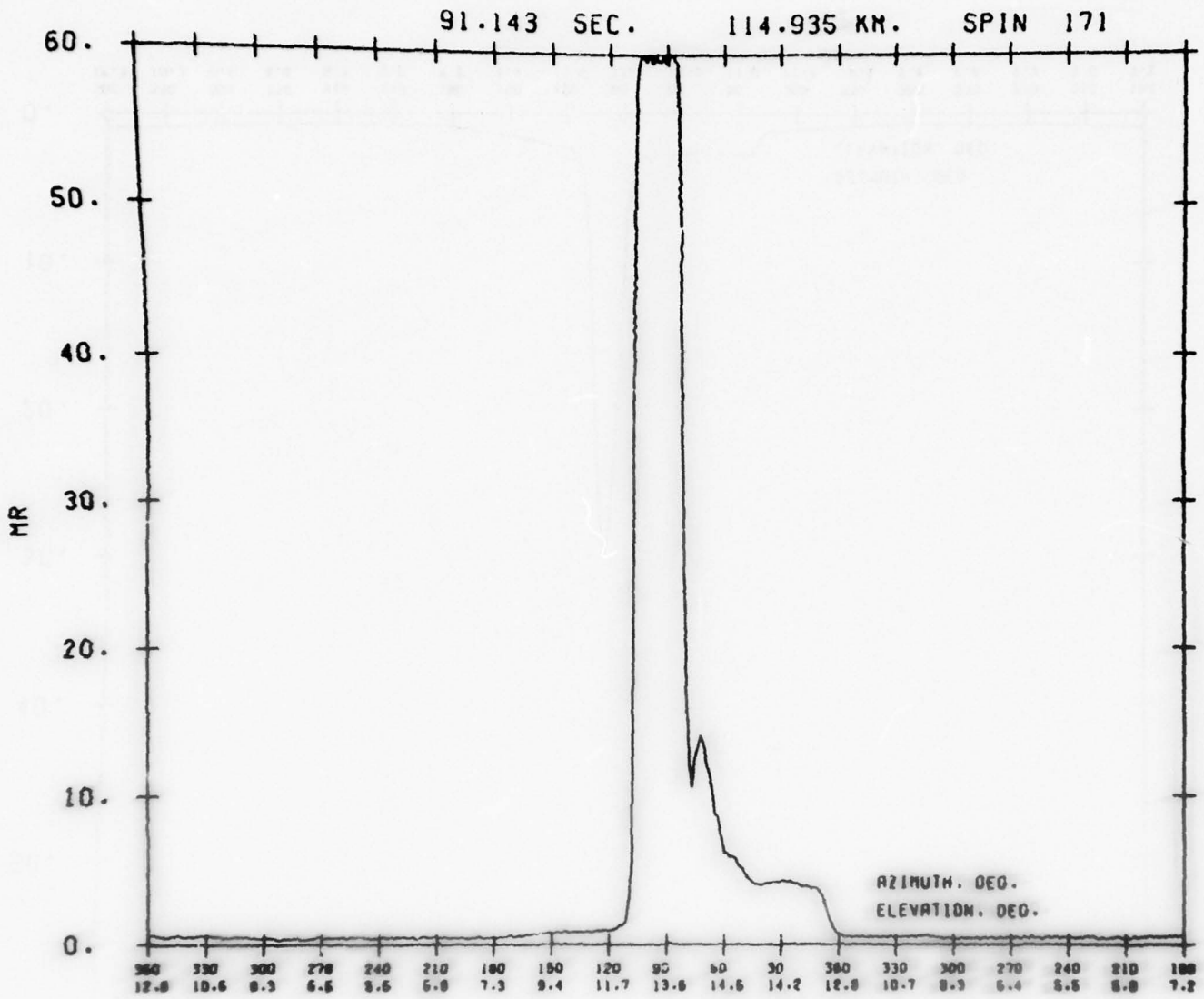

Figure B9. Rocket 18.219-1 2.7 μm Radiometer Data at 115 km, Ascent

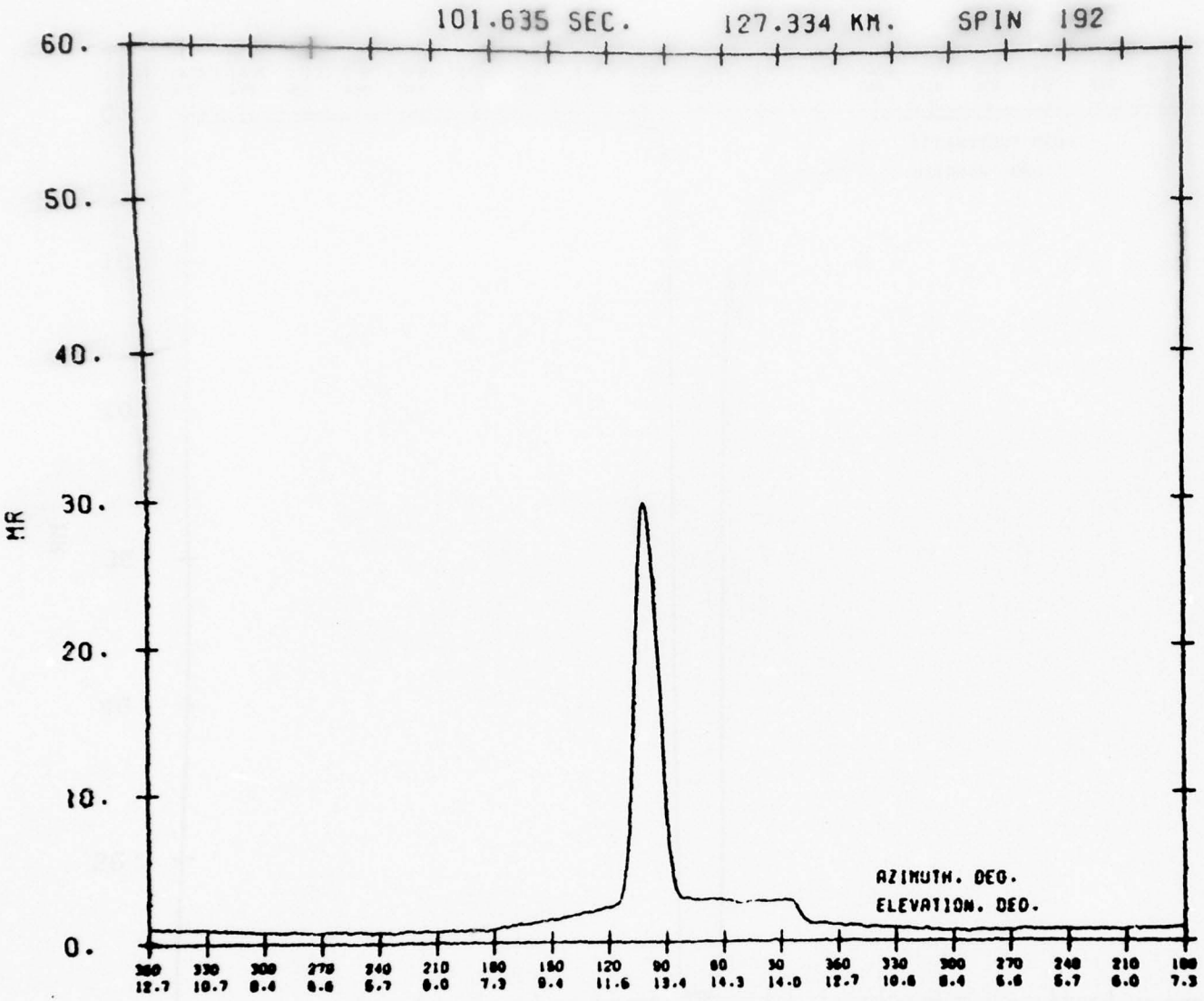

Figure B10. Rocket 18.219-1 2.7 μm Radiometer Data at 127 km, Ascent

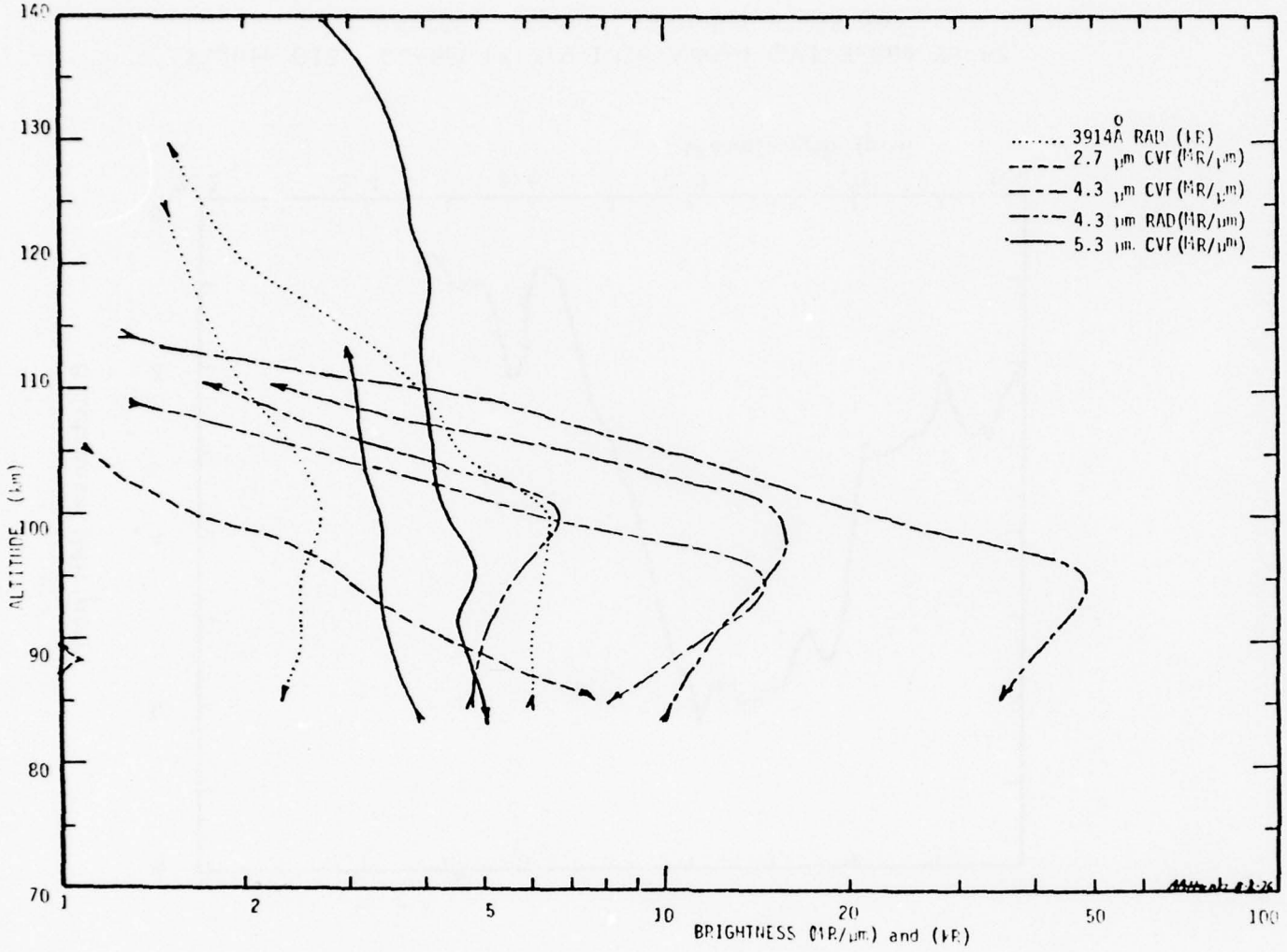

Figure B11. Rocket 18.219-1 Data From Axially-Mounted Instruments

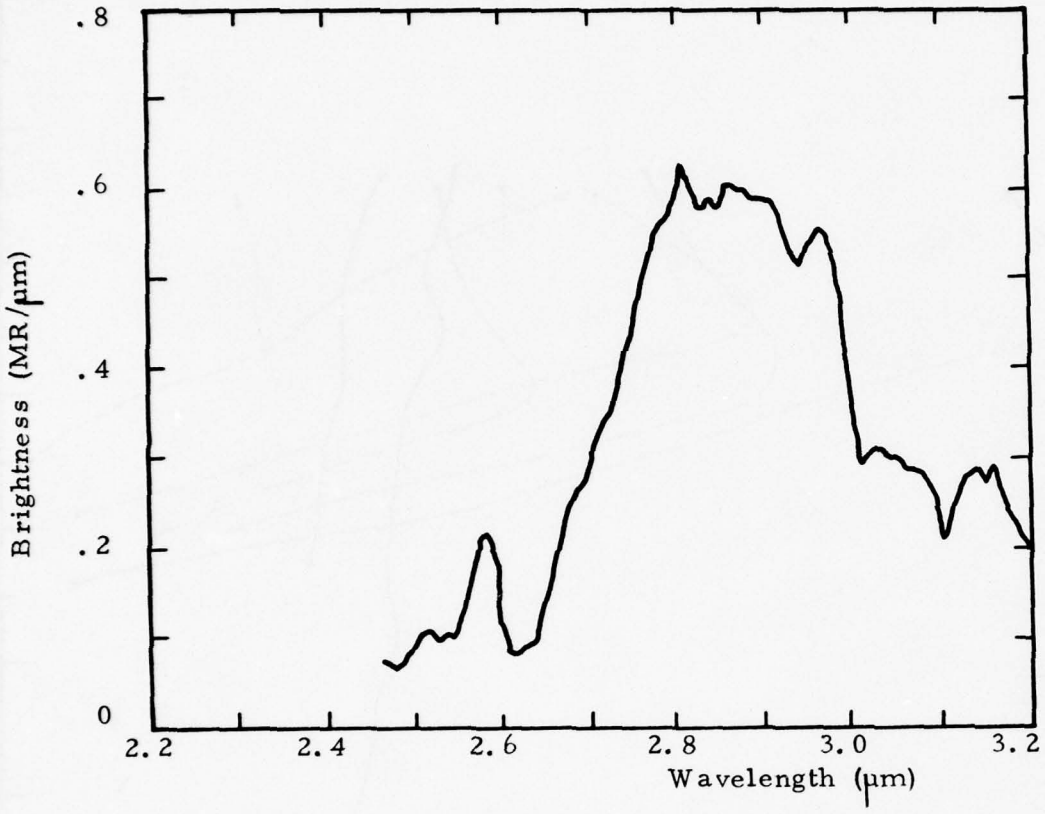

Figure B12. Rocket 18.219-1 Co-Added CVF Scans 76-92, 94-100, Ascent Altitudes 83-98 km

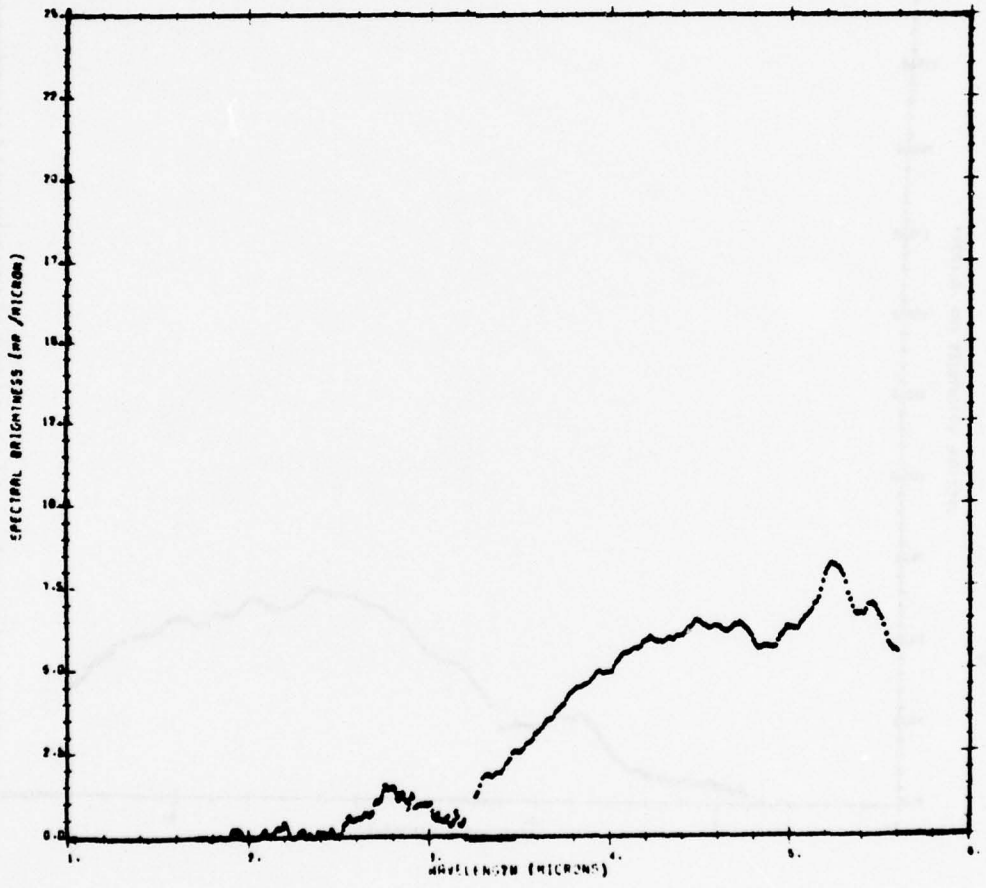

Figure B13. Rocket 18.219-1 CVF Data Scan, 117 km, Ascent

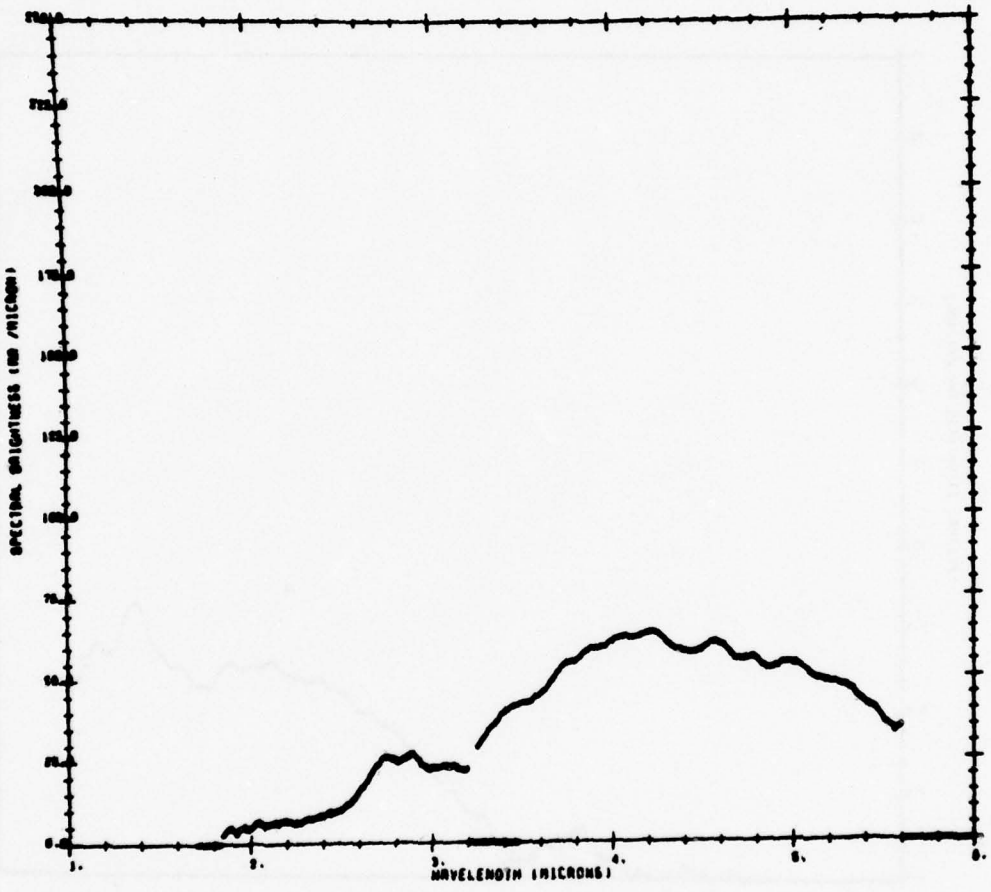

Figure B14. Rocket 18.219-1 CVF Data Scan, 135 km, Ascent

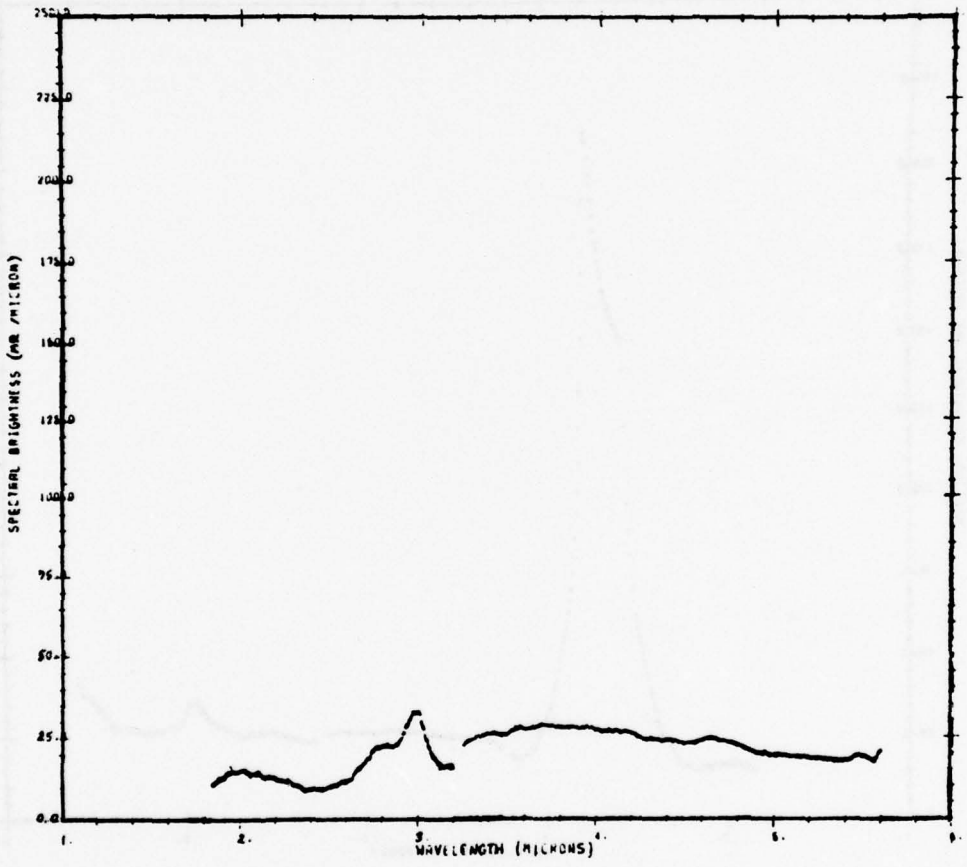

Figure B15. Rocket 18.219-1 CVF Data Scan, 147 km, Ascent

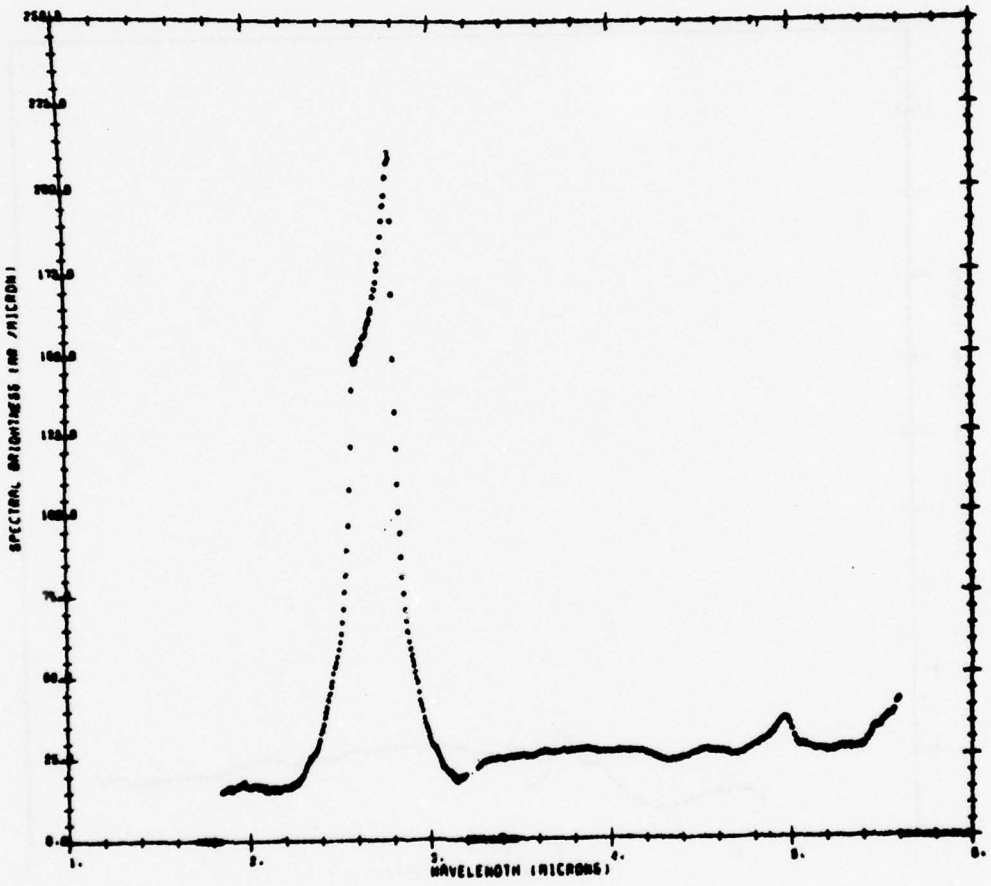

Figure B16. Rocket 18.219-1 CVF Data Scan, 150 km, Ascent

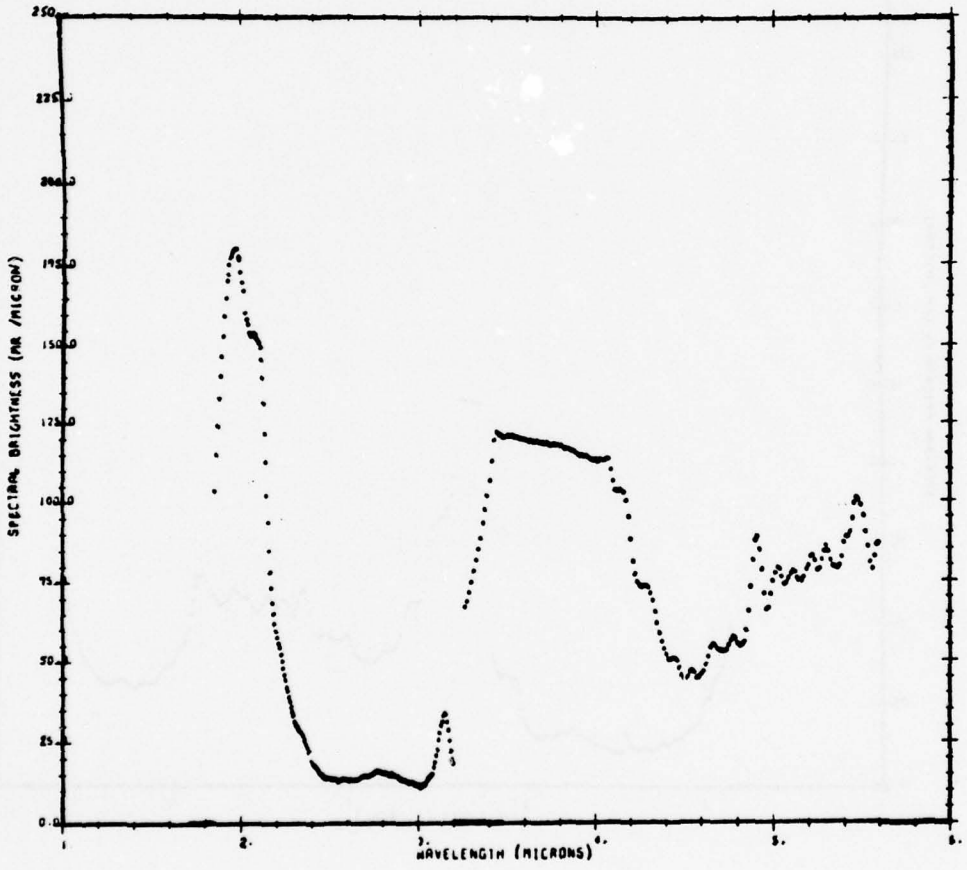

Figure B17. Rocket 18.219-1 CVF Data Scan, 157 km, Ascent

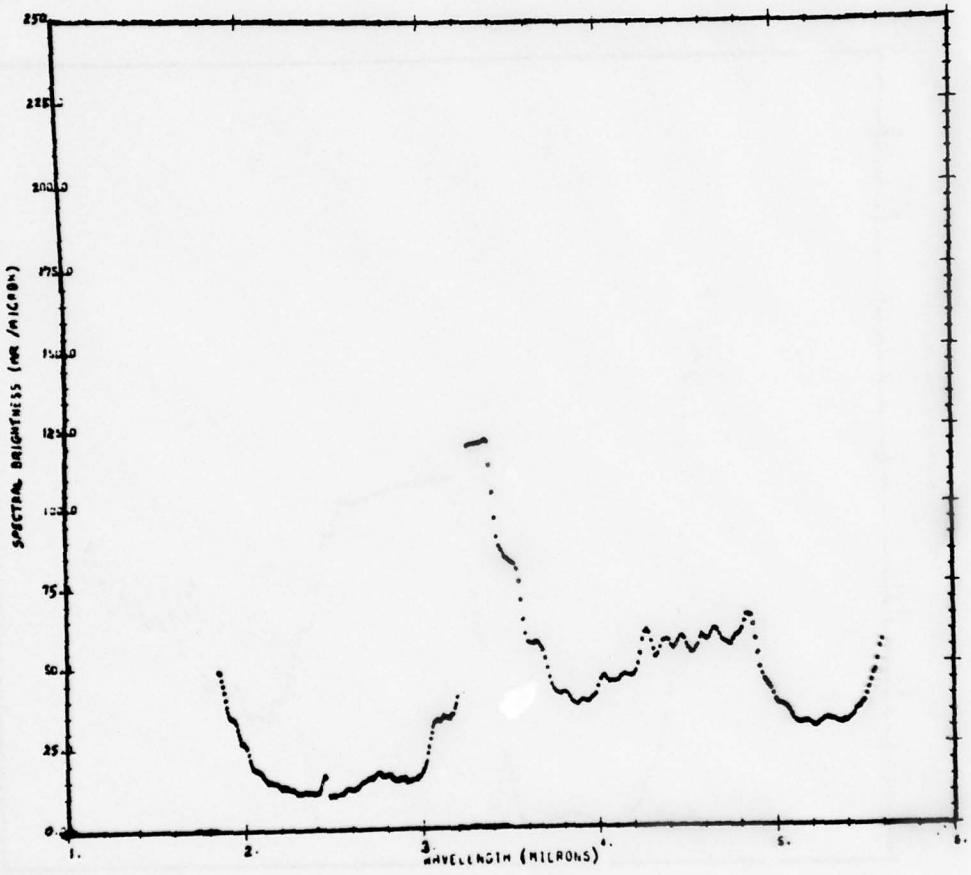

Figure B18. Rocket 18.219-1 CVF Data Scan, 160 km, Ascent

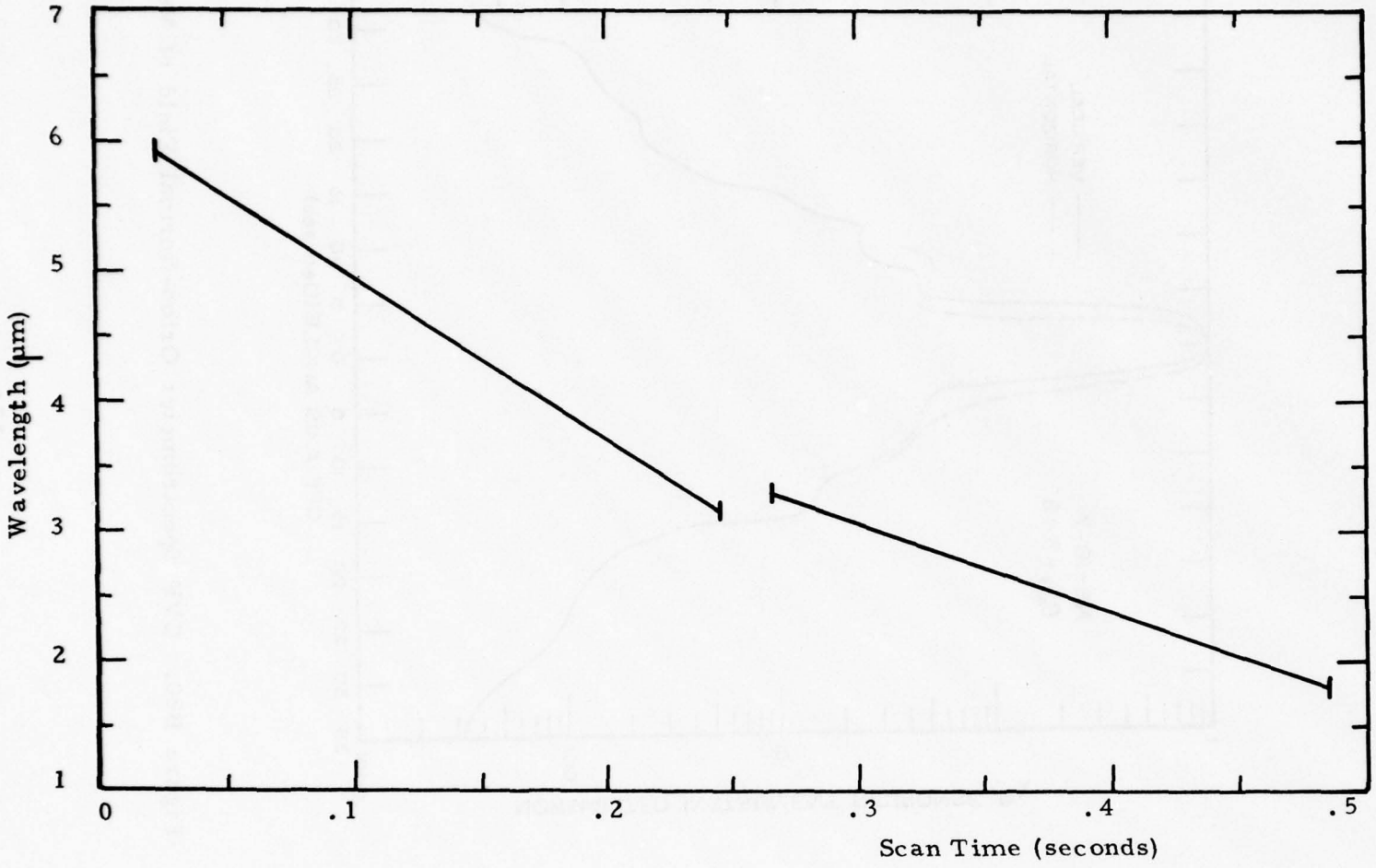

Figure B19. CVF Spectrometer Wavelength vs. Scan Time

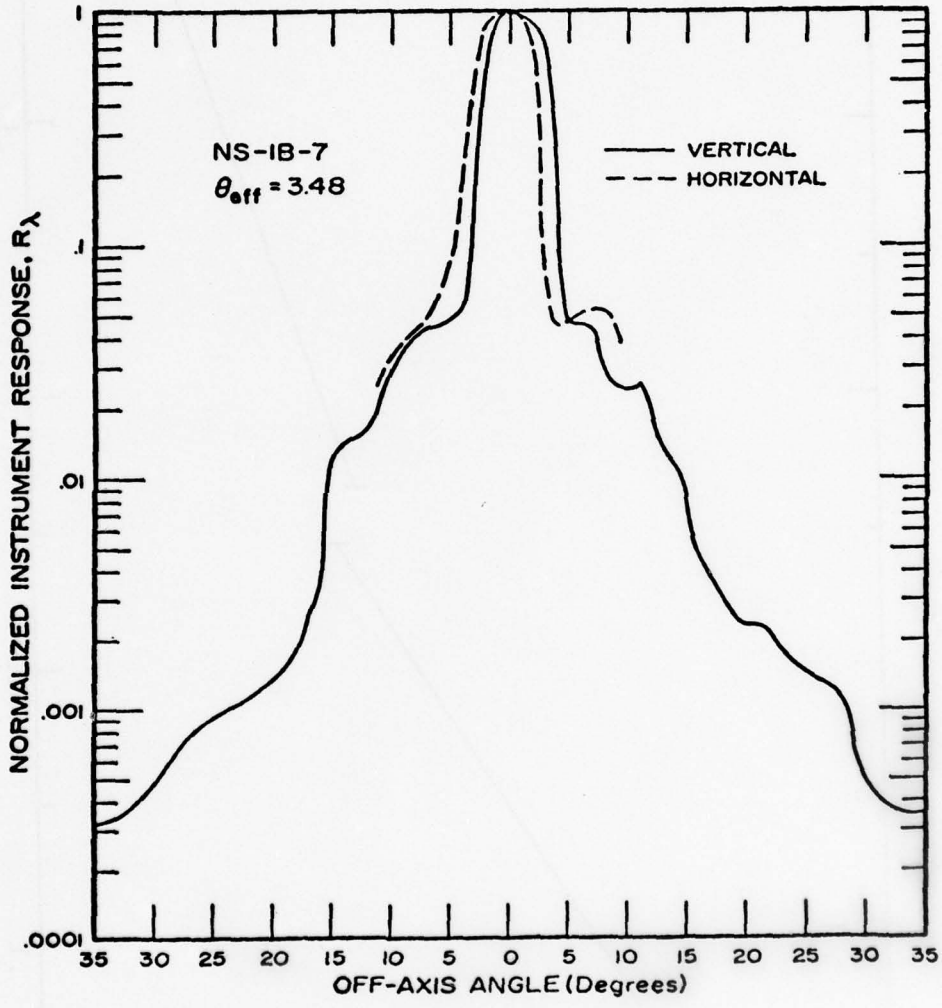

Figure B20. CVF Spectrometer Ortho-Normal Field of View

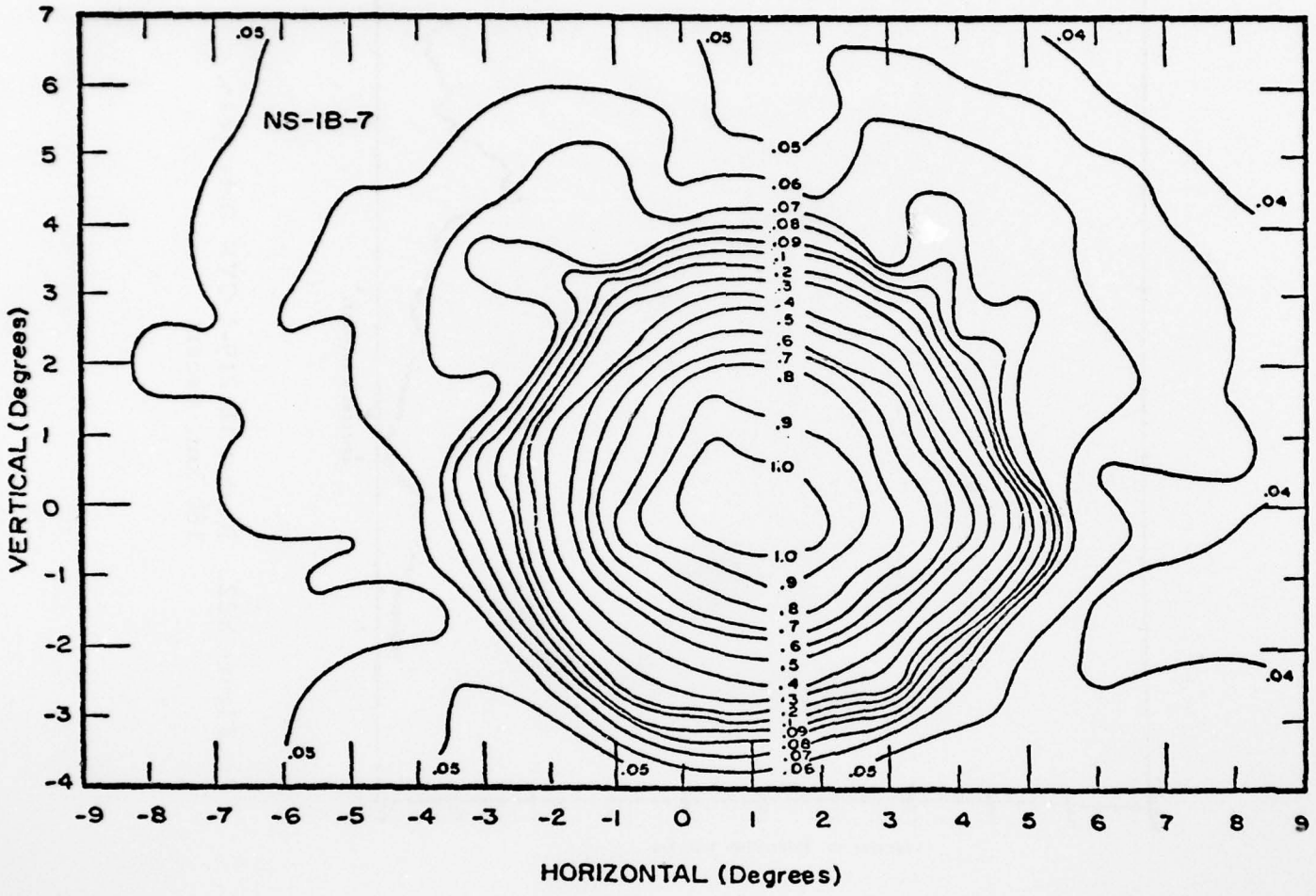

Figure B21. CVF Spectrometer Polar Field of View

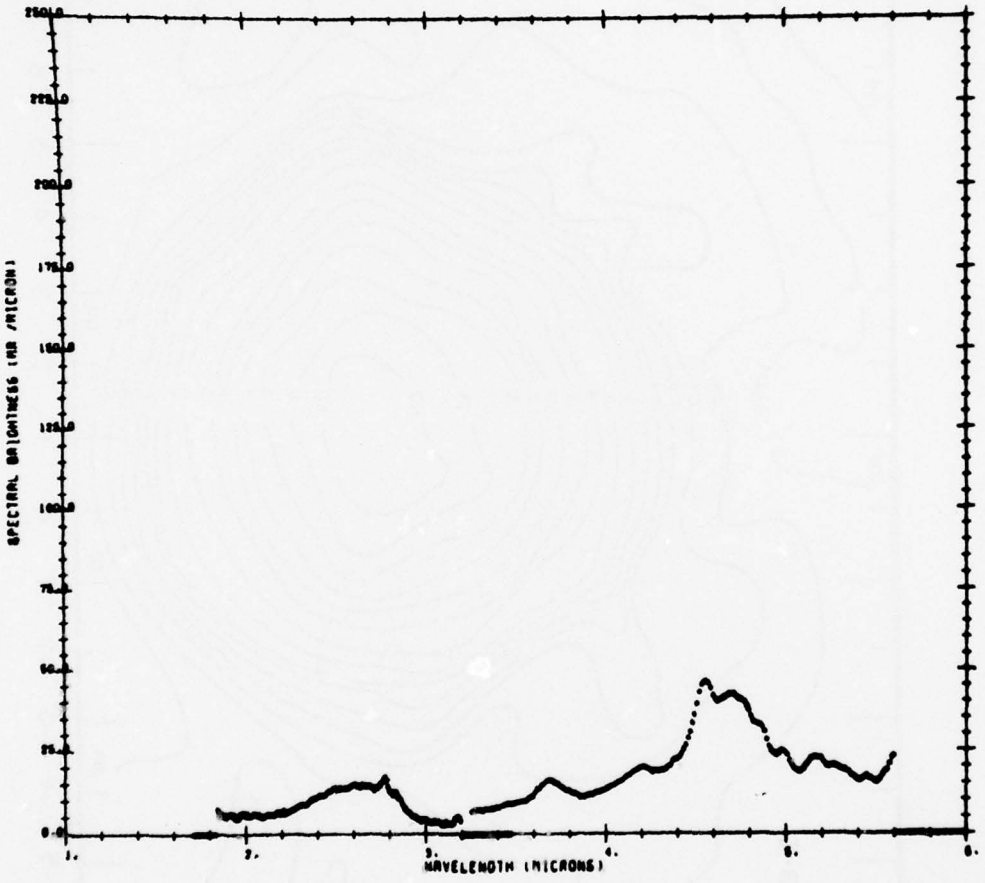

Figure B22. Rocket 18.219-1 CVF Data Scan, 180 km, Ascent

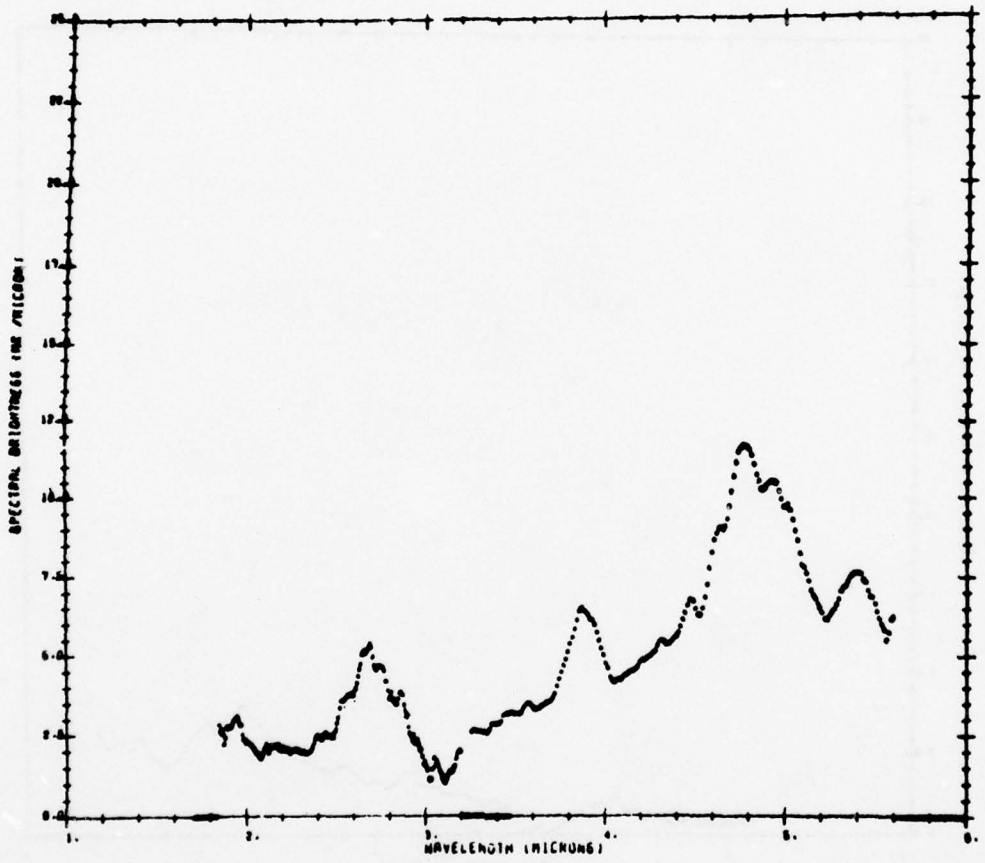

Figure B23. Rocket 18.219-1 CVF Data Scan, 194 km, Ascent

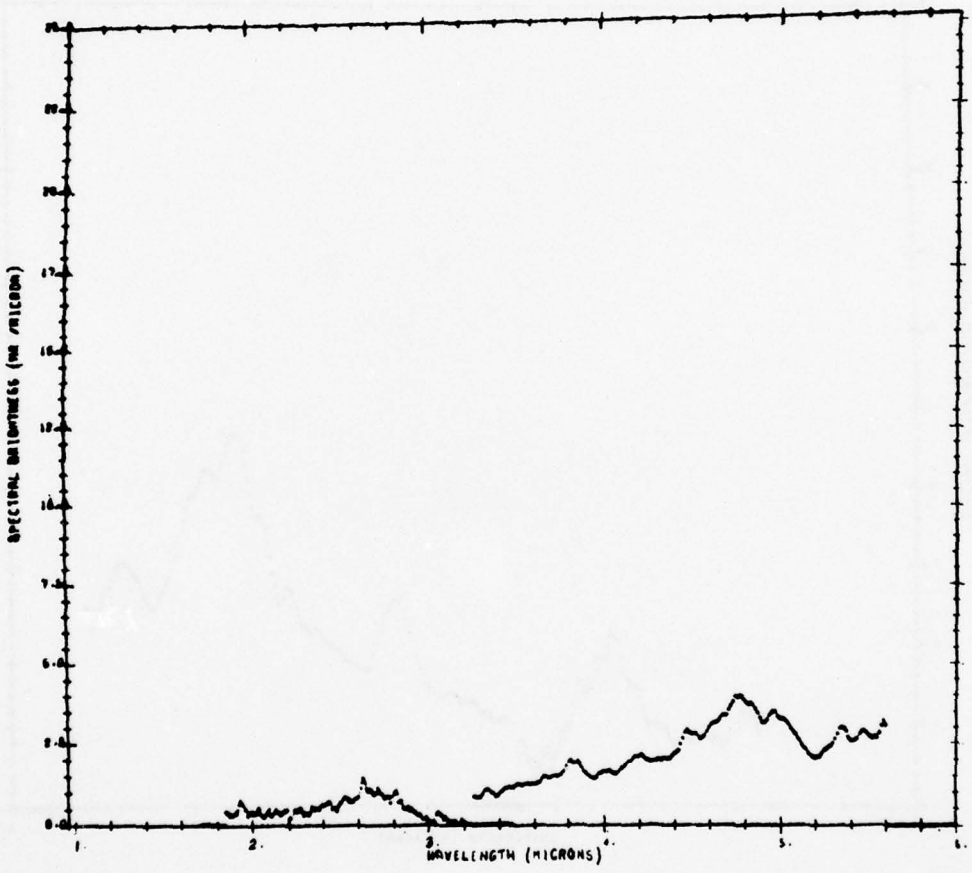

Figure B24. Rocket 18.219-1 CVF Data Scan, 193 km, Descent

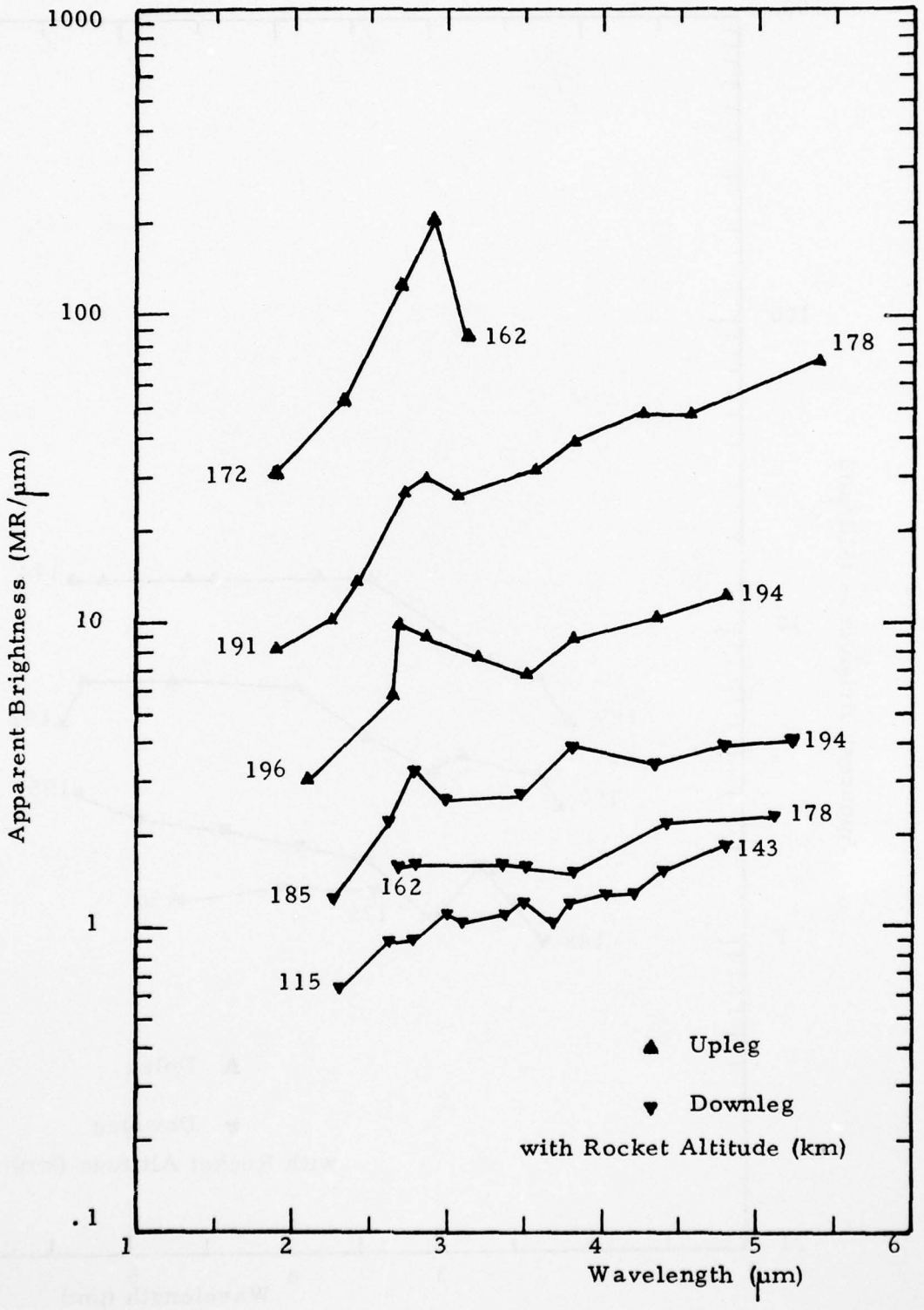

Figure B25. Rocket 18.219-1 Motor Signals, Peak No. 1

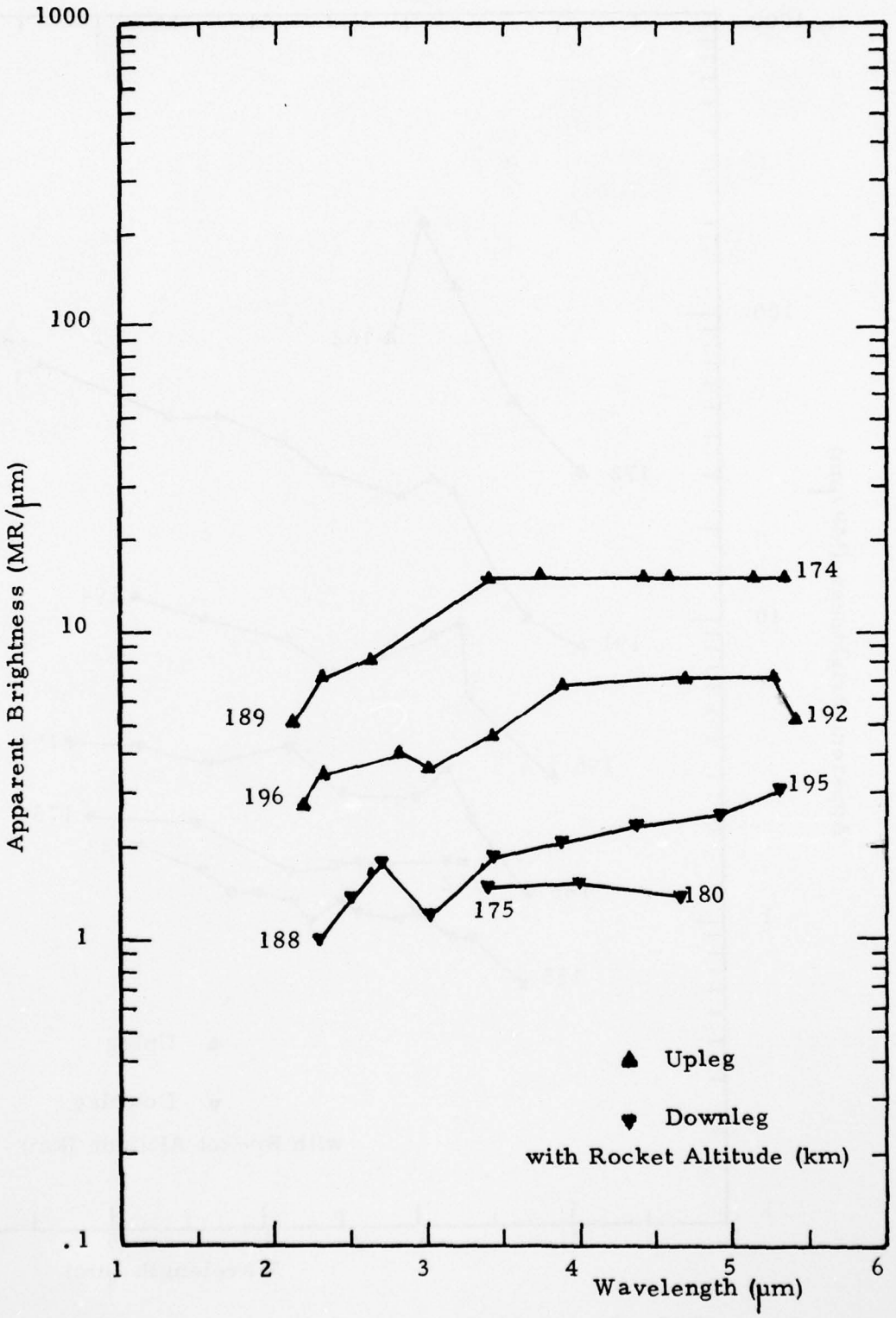

Figure B26. Rocket 18.219-1 Motor Signals, Peak No. 2

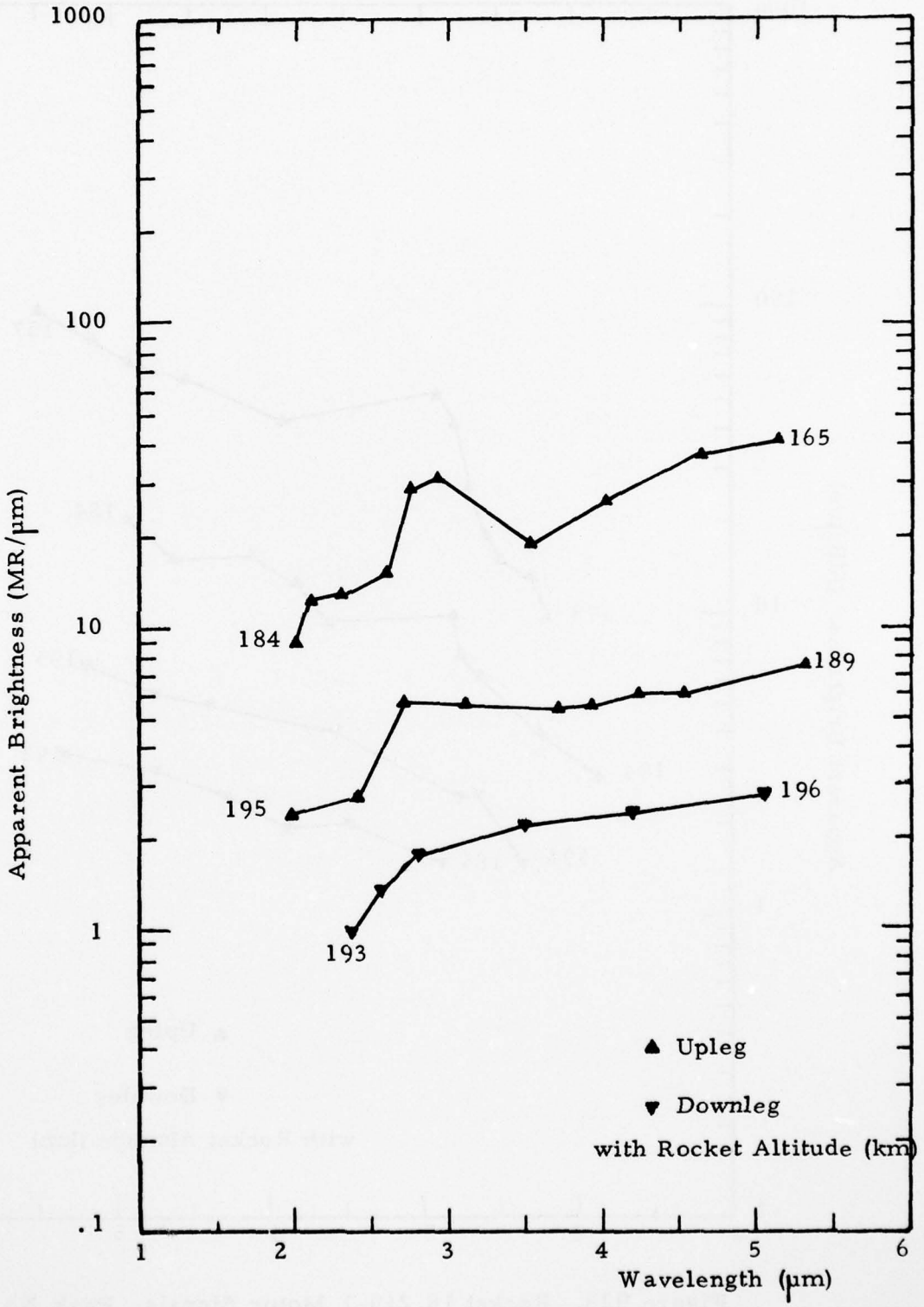

Figure B27. Rocket 18.219-1 Motor Signals, Peak No. 3

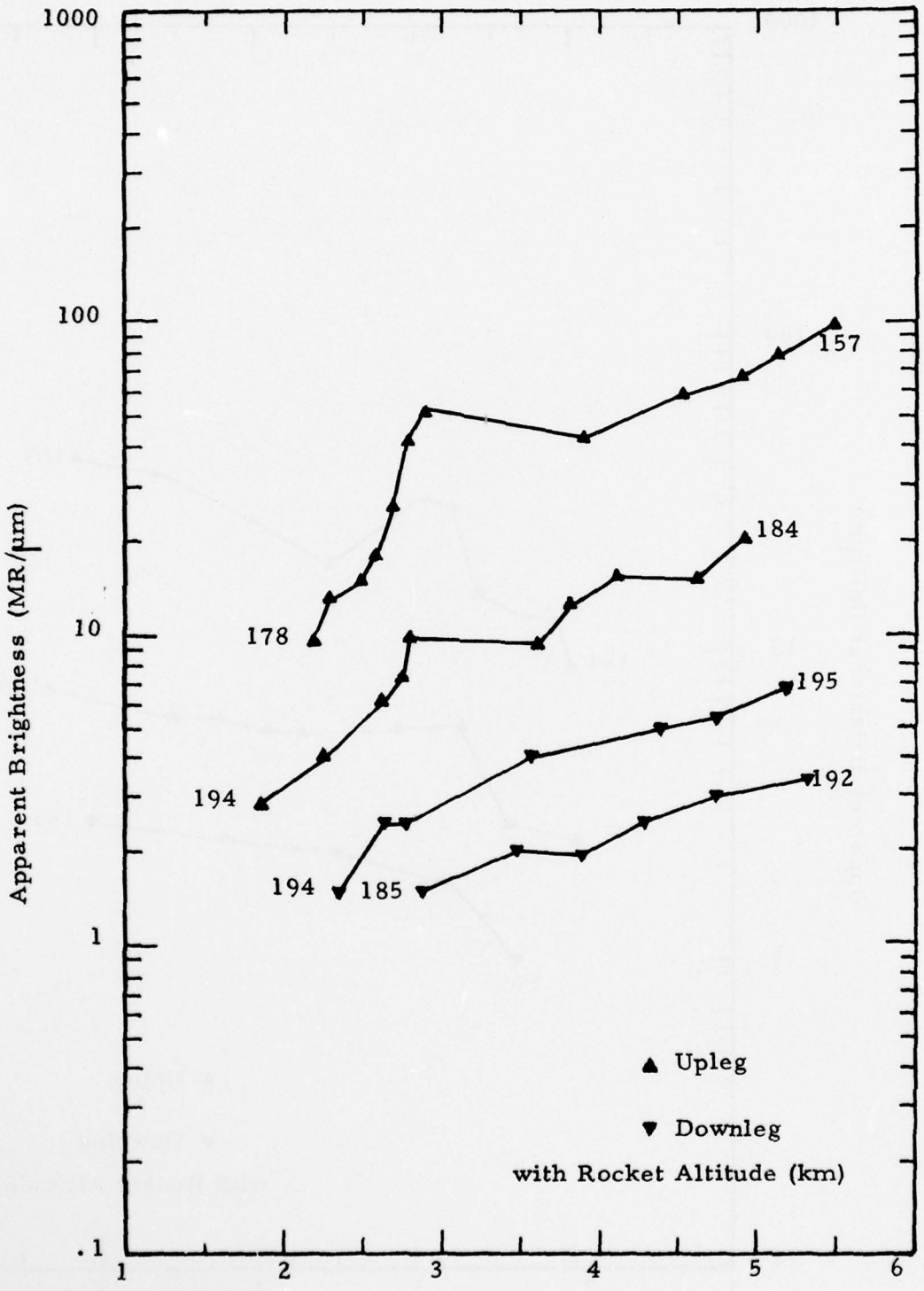

Figure B28. Rocket 18.219-1 Motor Signals, Peak No. 4

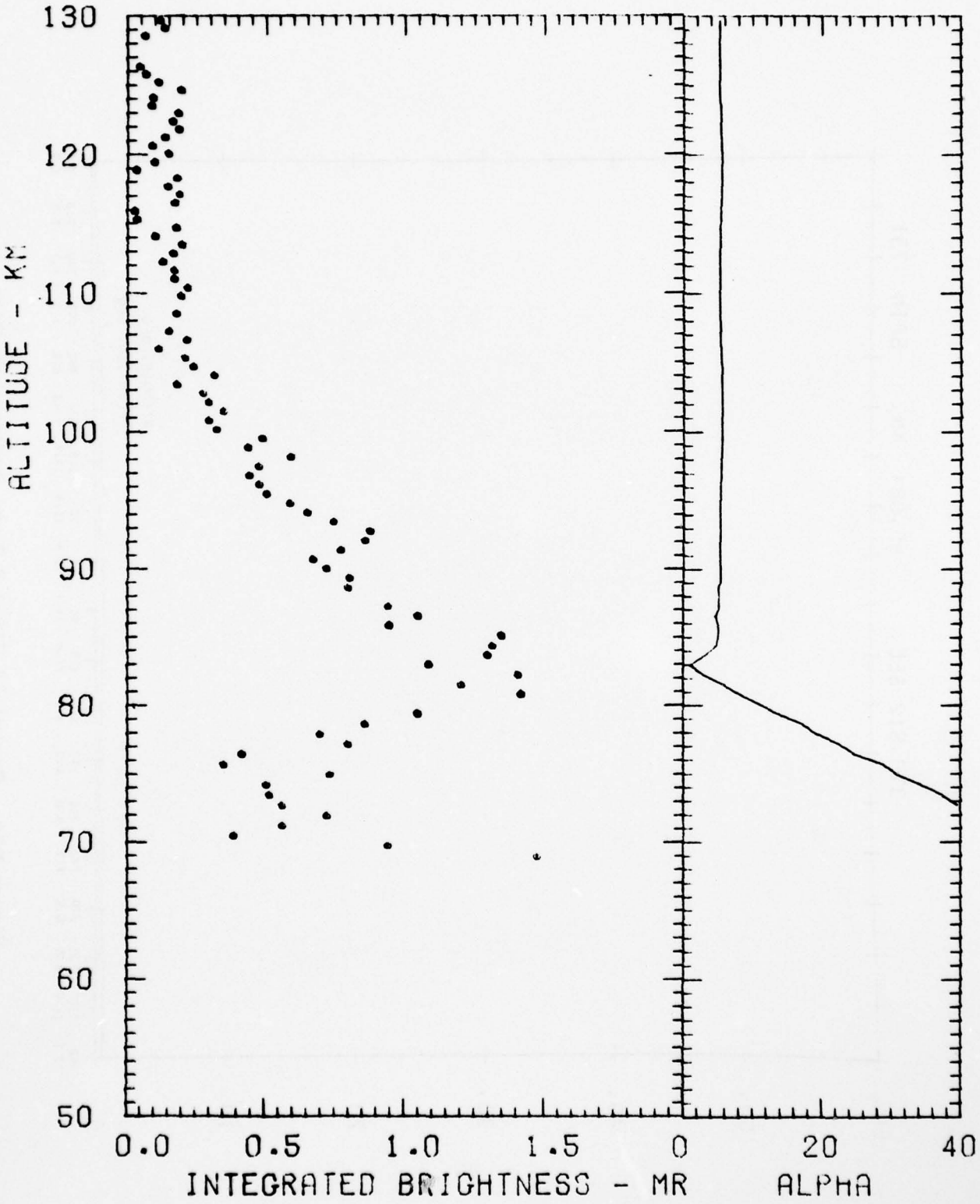

Figure B29. Rocket 18.219-1 2.7 μm Band Brightness and Rocket Axis Angle from Vertical vs. Altitude. Descent

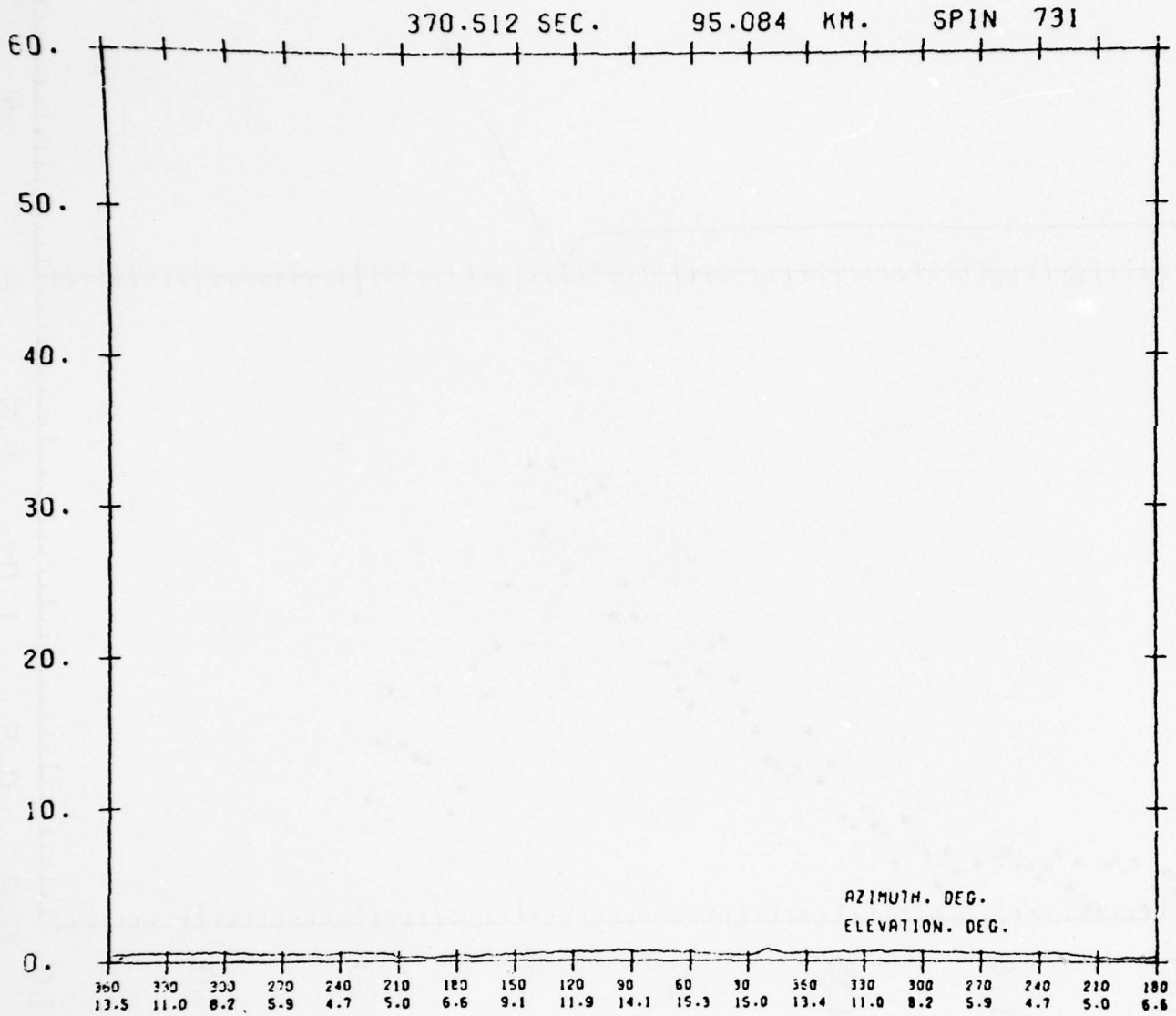

Figure B30. Rocket 18.219-1 2.7 μm Radiometer Data at 95 km, Descent

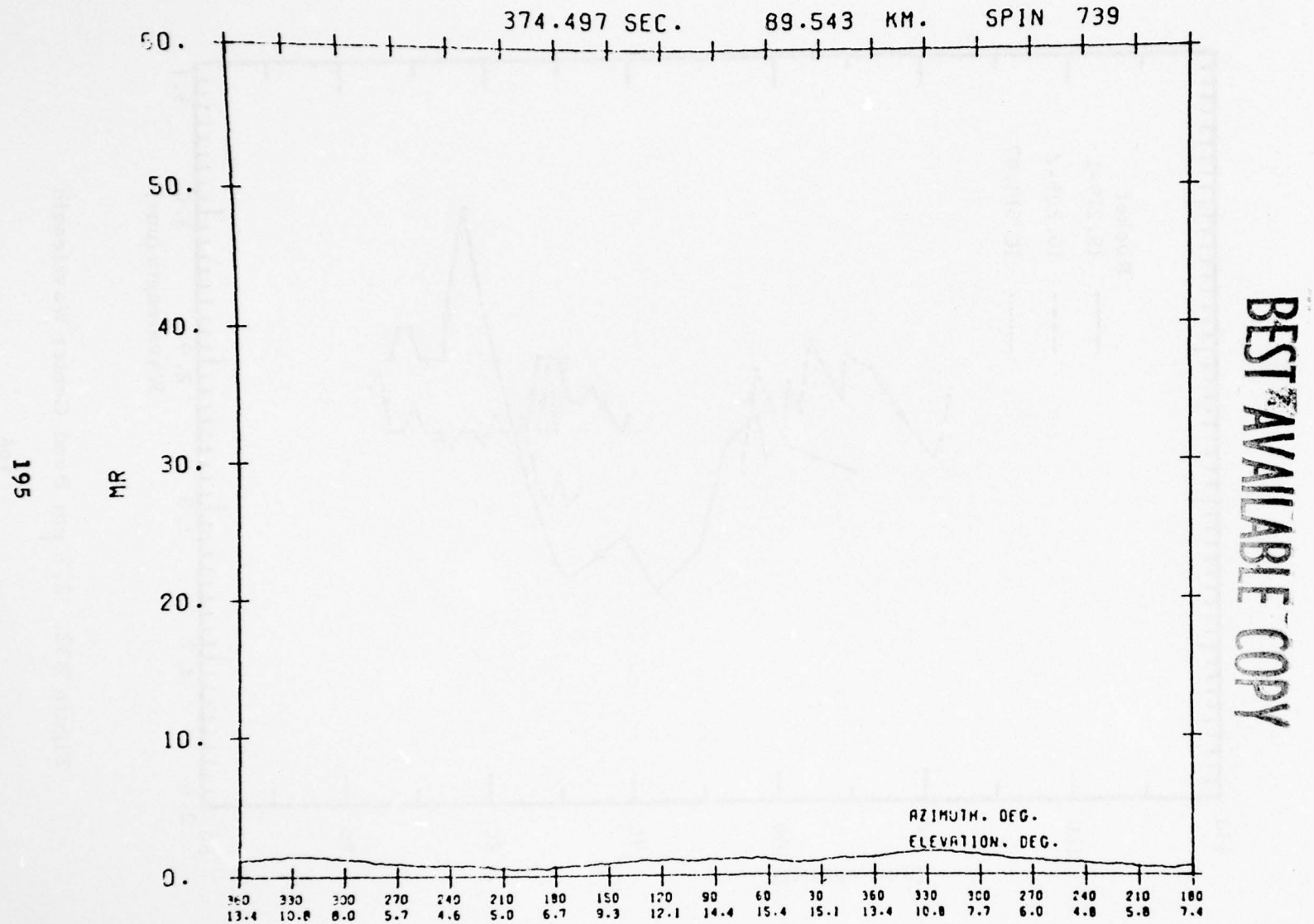

Figure B31. Rocket 18.219-1 2.7 μm Radiometer Data At 90 km, Descent

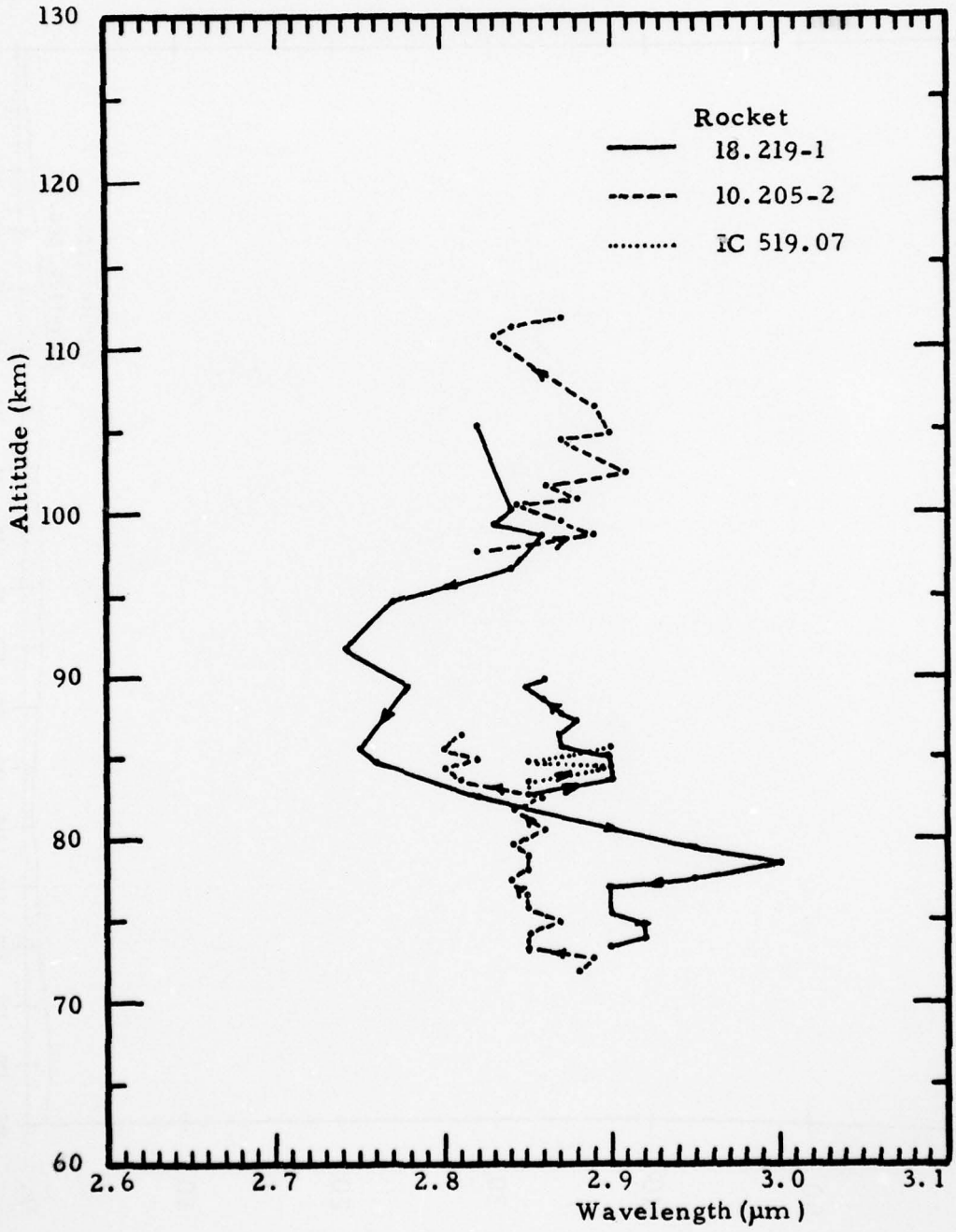

Figure B32. 2.7 μm Band Center Wavelength

APPENDIX C

ROCKET 18.219-1, ANALYSIS OF 4.3μm BAND CVF DATA

APPENDIX C

ROCKET 18.219-1 ANALYSIS OF 4.3 μm BAND CVF DATA

The analysis of the Circular Variable Filter (CVF) probe data on Rocket A18.219-1 has been completed even though the interpretation of the results is not. The CVF data on this rocket exhibited only three dominant emission features that were sufficiently above the instrument NESR ($\sim$125 KR at 4.3 μm) to warrant computer analyses. These were the 4.3 μm and the 2.7 μm bands and the enhanced emission feature at 5.3 μm. In the following discussion, the 4.3 μm data are examined in detail.

Three altitude-dependent characteristics of the 4.3 μm band emission (presumably due to CO_2) were considered - (1) peak emission intensity; (2) wavelength of the peak emission; and (3) half power value of the emission feature. In the first computer analysis of the peak emission a simple method of searching for the maximum radiance in a narrow band around 4.3 μm was used. Although this approach provided a reasonable altitude profile of the peak radiance, determination of the wavelength of the peak was poor because of noise superimposed on the emission signal. To improve the analysis, a curve fitting approach (Bevington 1969) was used. In this approach the equation

$$R_\lambda = a_1 e^{1/2 \left[\frac{\lambda - a_2}{a_3}\right]^2} + a_4\lambda^2 + a_5\lambda + a_6$$

where

R_λ = radiance at λ – (mR/μm)

λ = wavelength – (μm)

a_1 thru a_6 = coefficients to be determined

was fitted to the digitized data by optimizing χ^2 (maximizing likelihood). The exponential portion of the equation represents a Gaussian function descriptive of the 4.3 μm CVF data (but not necessarily descriptive of CO_2 emission), and the quadratic portion describes a variable background. The best fit constants for the equation were determined for each CVF scan between 3.8 μm and 5.0 μm. The constants represent the peak radiance (a_1), center wavelength (a_2) and half power optical bandwidth (a_3). An example of the fit to the data is shown in Figure C1. The empirical equation that represents CVF data at 4.3 μm with background removed $[a_4\lambda^2 + a_5\lambda + a_6]$ is thus simply

$$R_\lambda = R_p\, e^{1/2\left[\frac{\lambda - \lambda_o}{\Delta\lambda}\right]^2}$$

where

R_p = peak radiance in the 4.3 μm band (MR/μm)

λ_o = center wavelength of 4.3 μm band (μm)

$\Delta\lambda$ = half power optical bandwidth of the 4.3 μm band (μm)

The variation of the parameters R_p, λ_o, and $\Delta\lambda$ as a function of altitude as determined from the CVF data on A18.219-1 are shown in Figure C2 and C3. Note that the λ_o and $\Delta\lambda$ data have been further approximated by a least squares fit with the resulting linear equation given on the plots.

Thus at 100 km the empirical equation describing the CVF 4.3 μm data between 3.8 and 5.0 μm with background removed is

$$R_\lambda = 21\, e^{1/2\left[\frac{\lambda - 4.3}{0.072}\right]^2} \text{ MR/μm.}$$

AD-A047 526 VISIDYNE INC BURLINGTON MASS F/G 4/1
COMPARISON OF ICECAP AND EXCEDE ROCKET MEASUREMENTS WITH COMPUT--ETC(U)
FEB 77 A G HURD, J W CARPENTER, T C DEGGES F19628-74-C-0177
UNCLASSIFIED VI-381 AFGL-TR-77-0060 NL

3 OF 3
ADA047 526

END
DATE FILMED
1 - 78
DDC

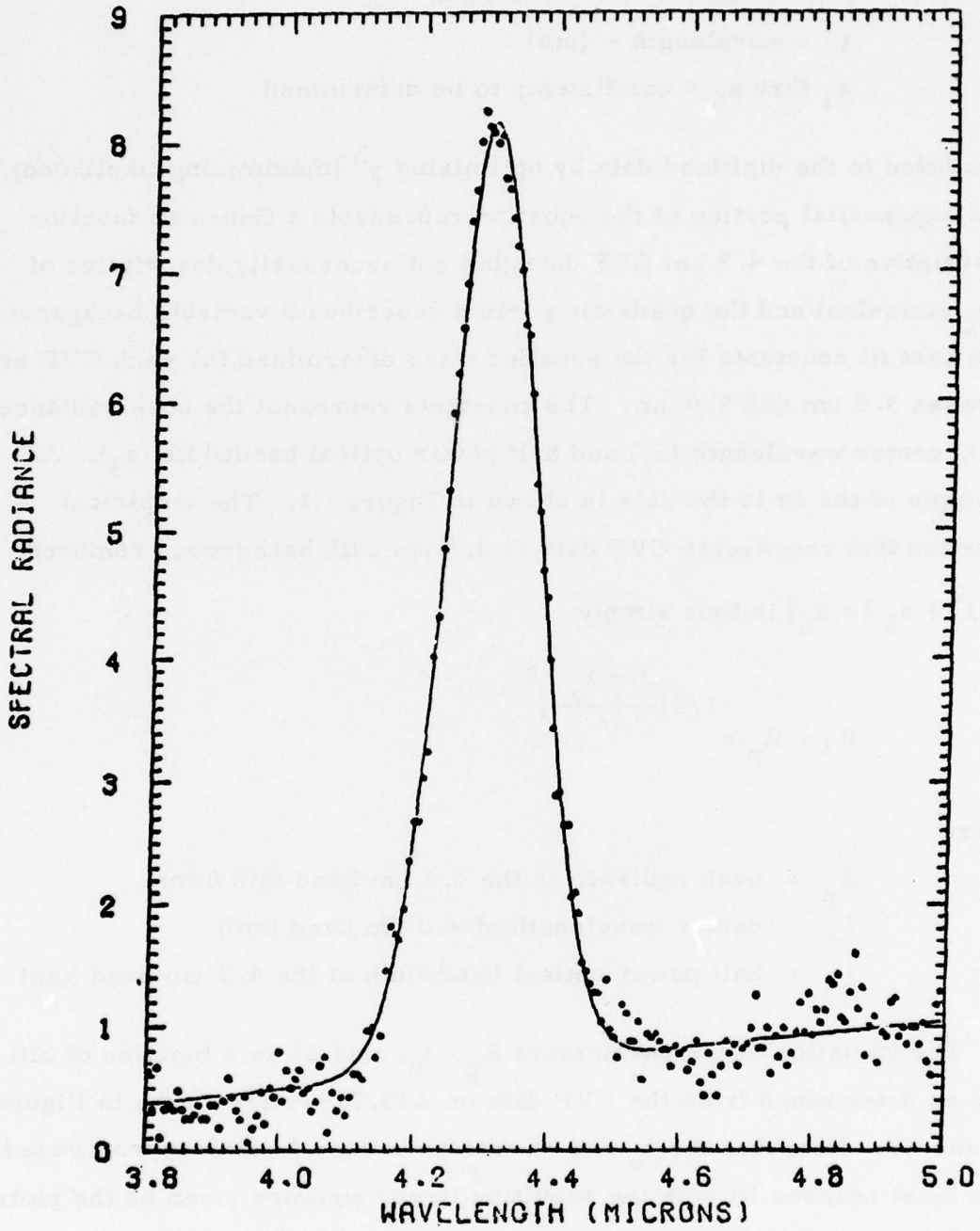

FIGURE C1: SAMPLE OF GAUSSIAN WITH POLYNOMIAL BACKGROUND FIT TO ACTUAL CVF DATA FOR ROCKET A18.219-1.

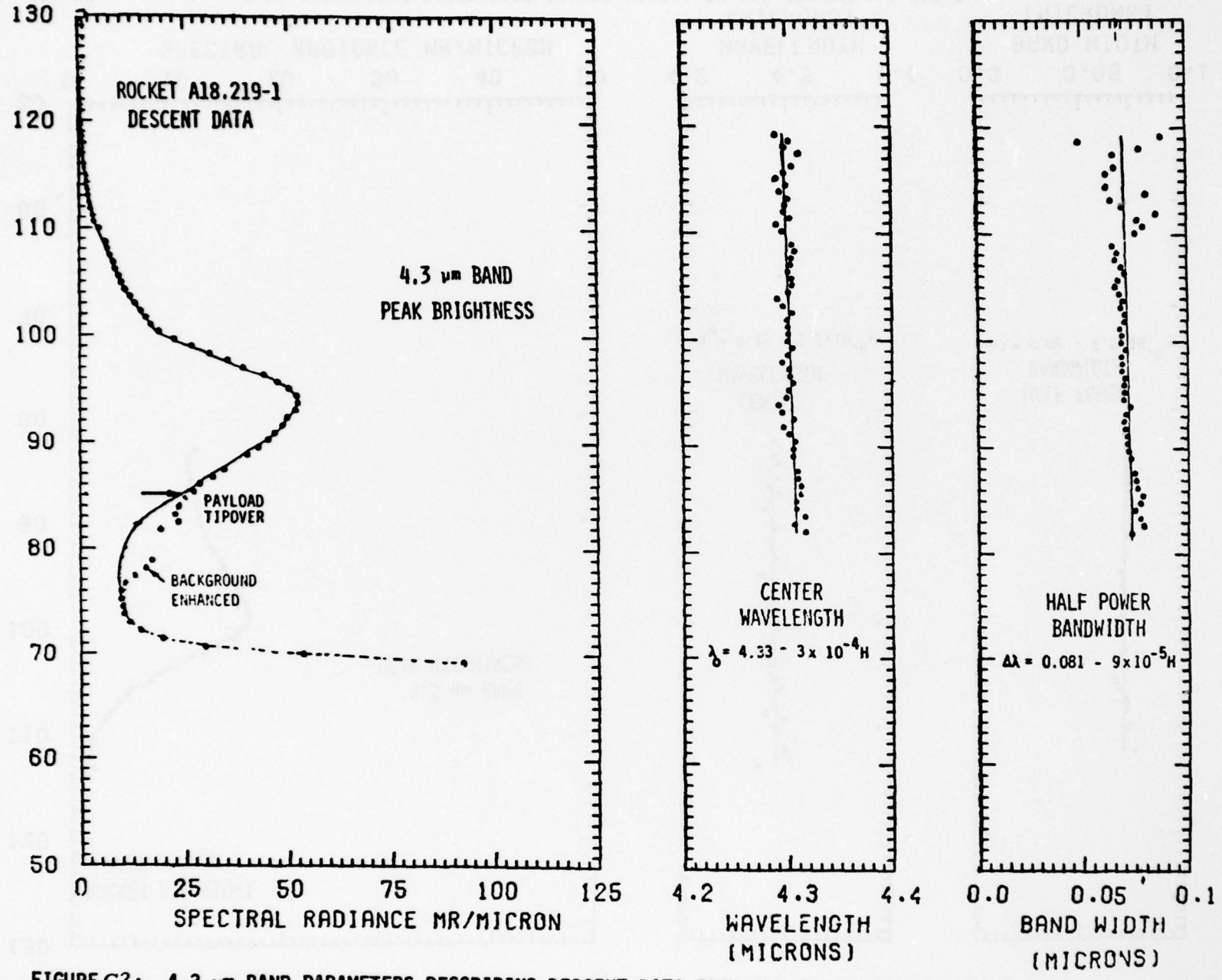

FIGURE C2: 4.3 μm BAND PARAMETERS DESCRIBING DESCENT DATA FROM CVF ON ROCKET A18.219-1.

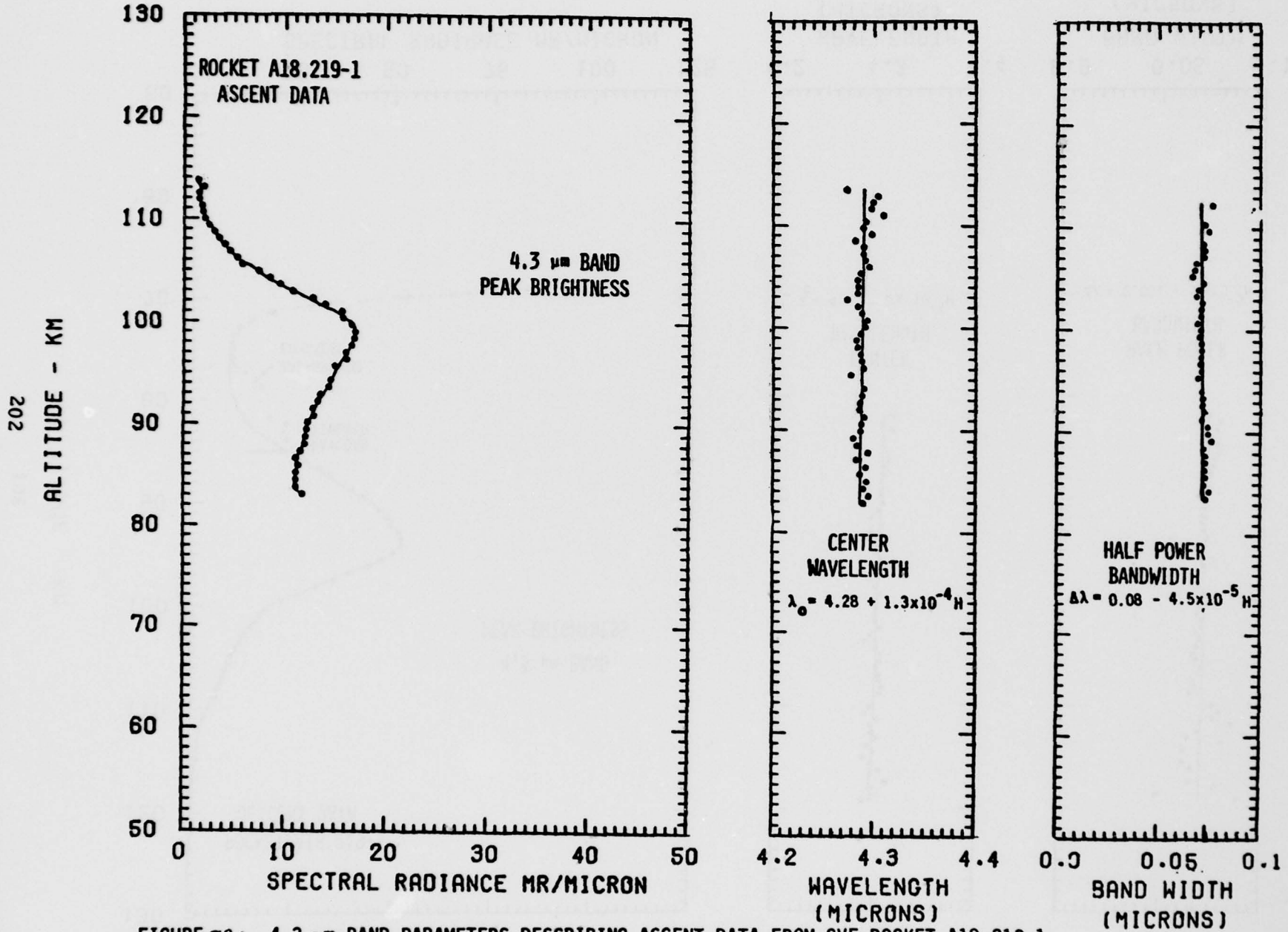

FIGURE C3: 4.3 μm BAND PARAMETERS DESCRIBING ASCENT DATA FROM CVF ROCKET A18.219-1.

APPENDIX D

THEORETICAL ESTIMATES OF 4.3μm BAND AURORAL EMISSIONS

APPENDIX D

THEORETICAL ESTIMATES OF 4.3 μm BAND AURORAL EMISSIONS

The results presented herein are initial qualitative estimates of the zenith brightness in the 4.3 micron band from regions outside, but adjacent to, an auroral arc.

In the case we have considered an auroral arc extending east-west moves from the north at a velocity of 100 kilometers per hour. The arc then stops and remains stationary for a time t. We then calculate the zenith brightness at various altitudes and various horizontal distances due to radiative transport from the arc.

The situation is sketched below.

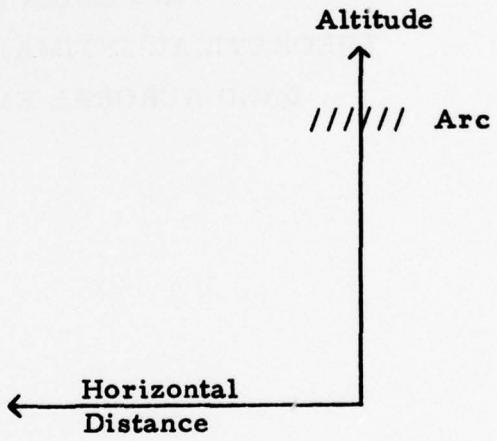

Four cases are considered;

1.	IBC III	t = 316 sec	(Figure D1)
2.	IBC III	t = 1000 sec	(Figure D2)
3.	IBC II	t = 316 sec	(Figure D3)
4.	IBC II	t = 1000 sec	(Figure D4)

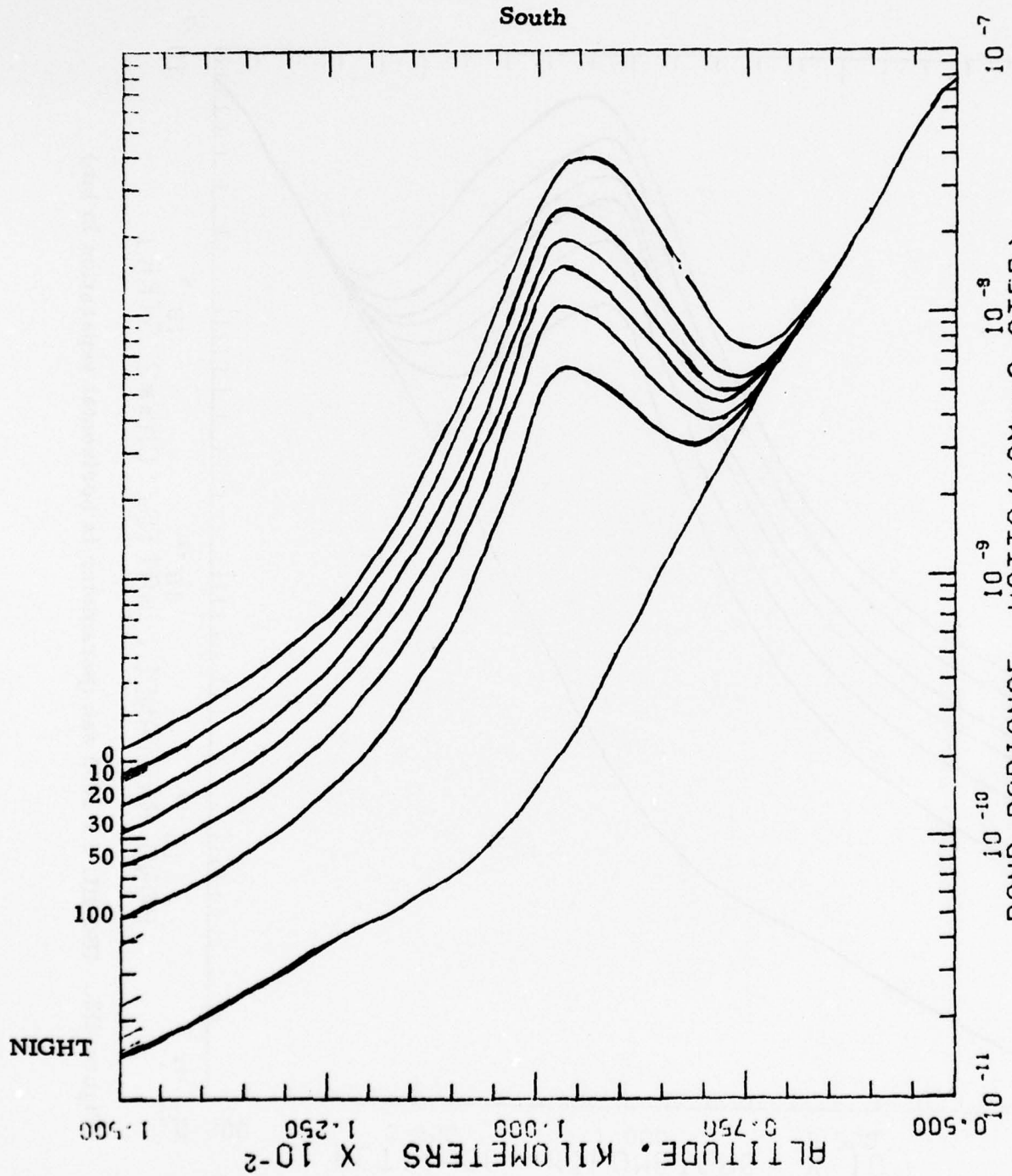

Figure D1. IBC III, t = 316 sec (parameter is horizontal separation in kms)

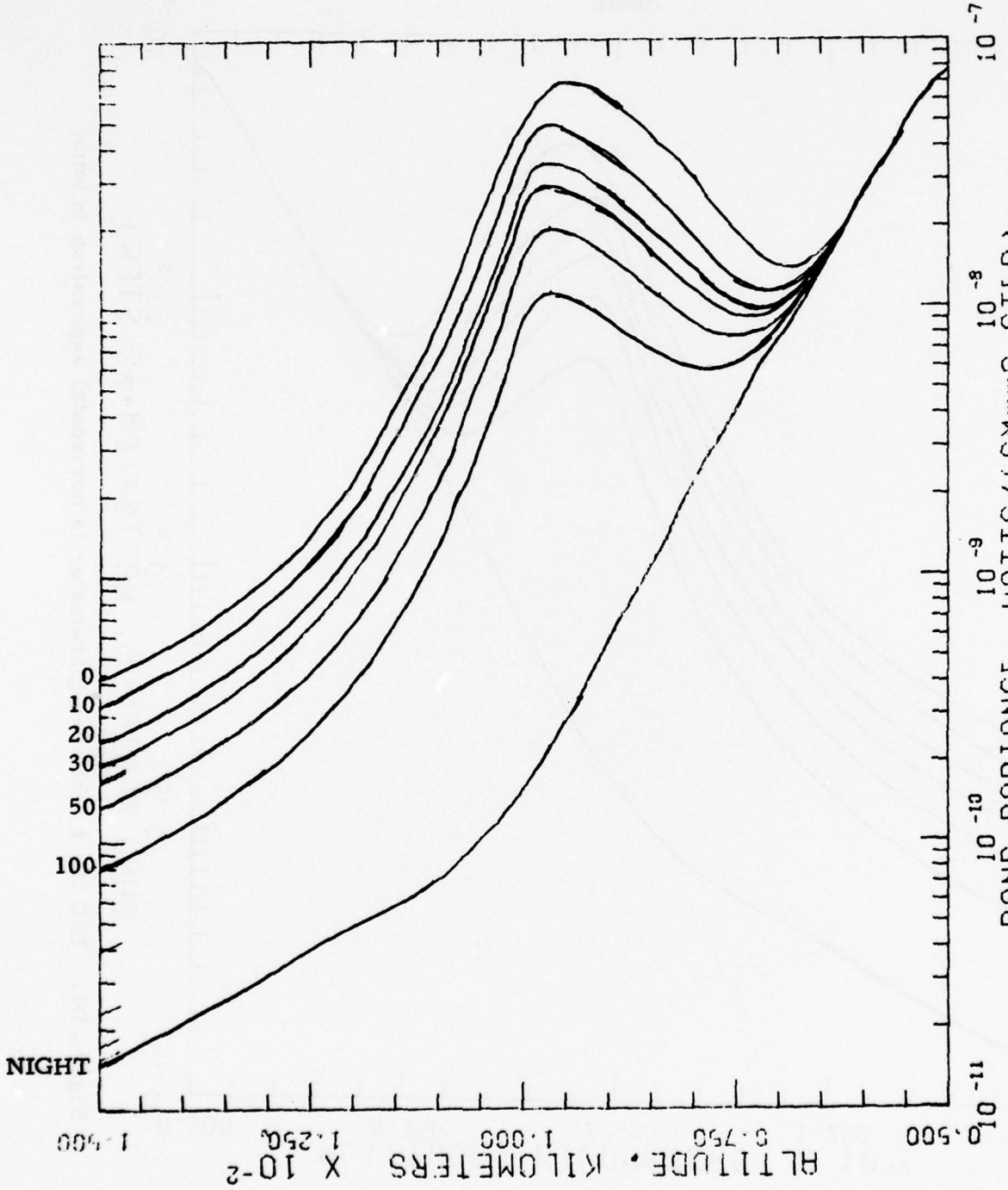

Figure D2. IBC III, t = 1000 sec (parameter is horizontal separation in km)

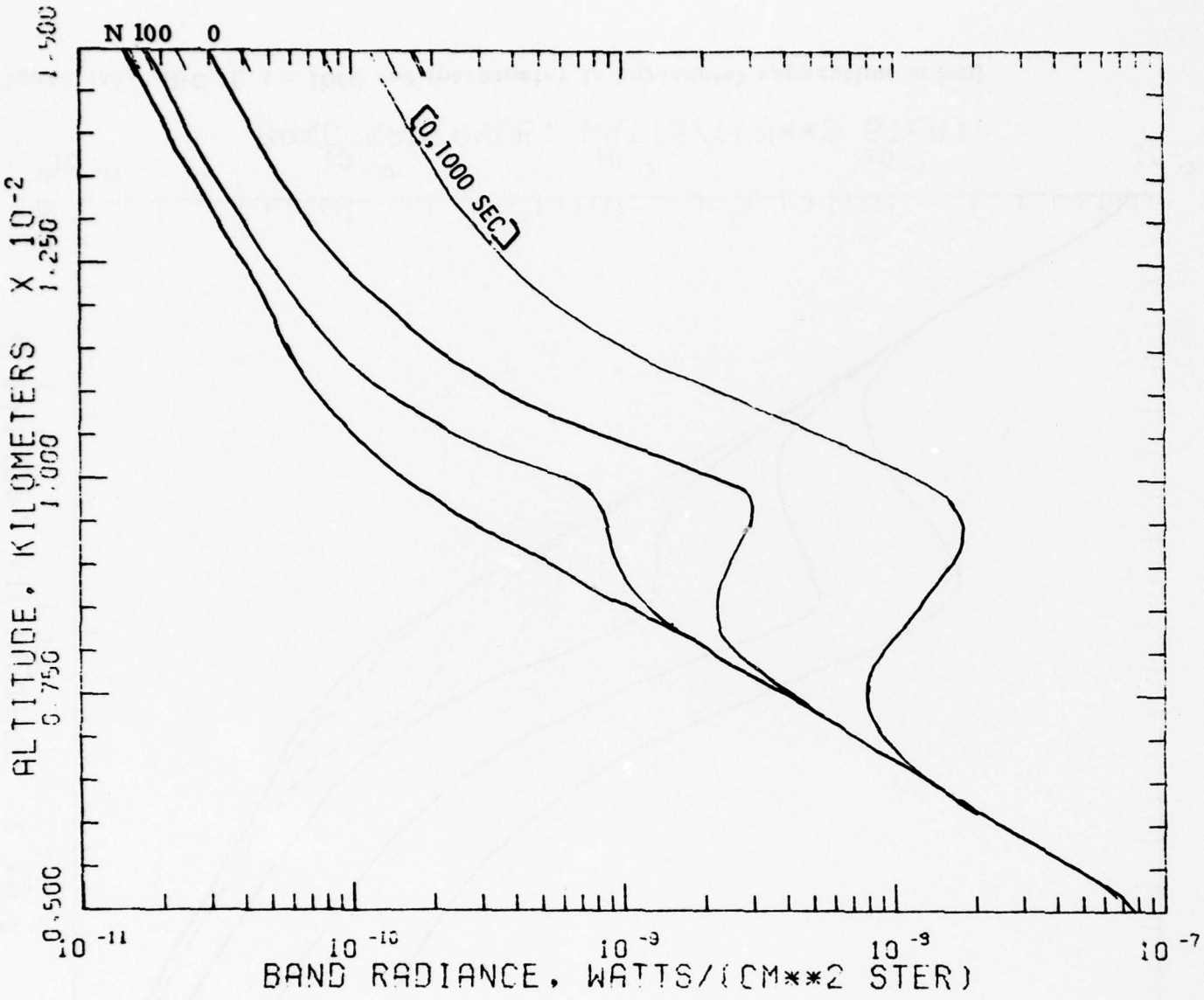

Figure D3. IBC II, t = 316 sec (parameter is horizontal separation in km)

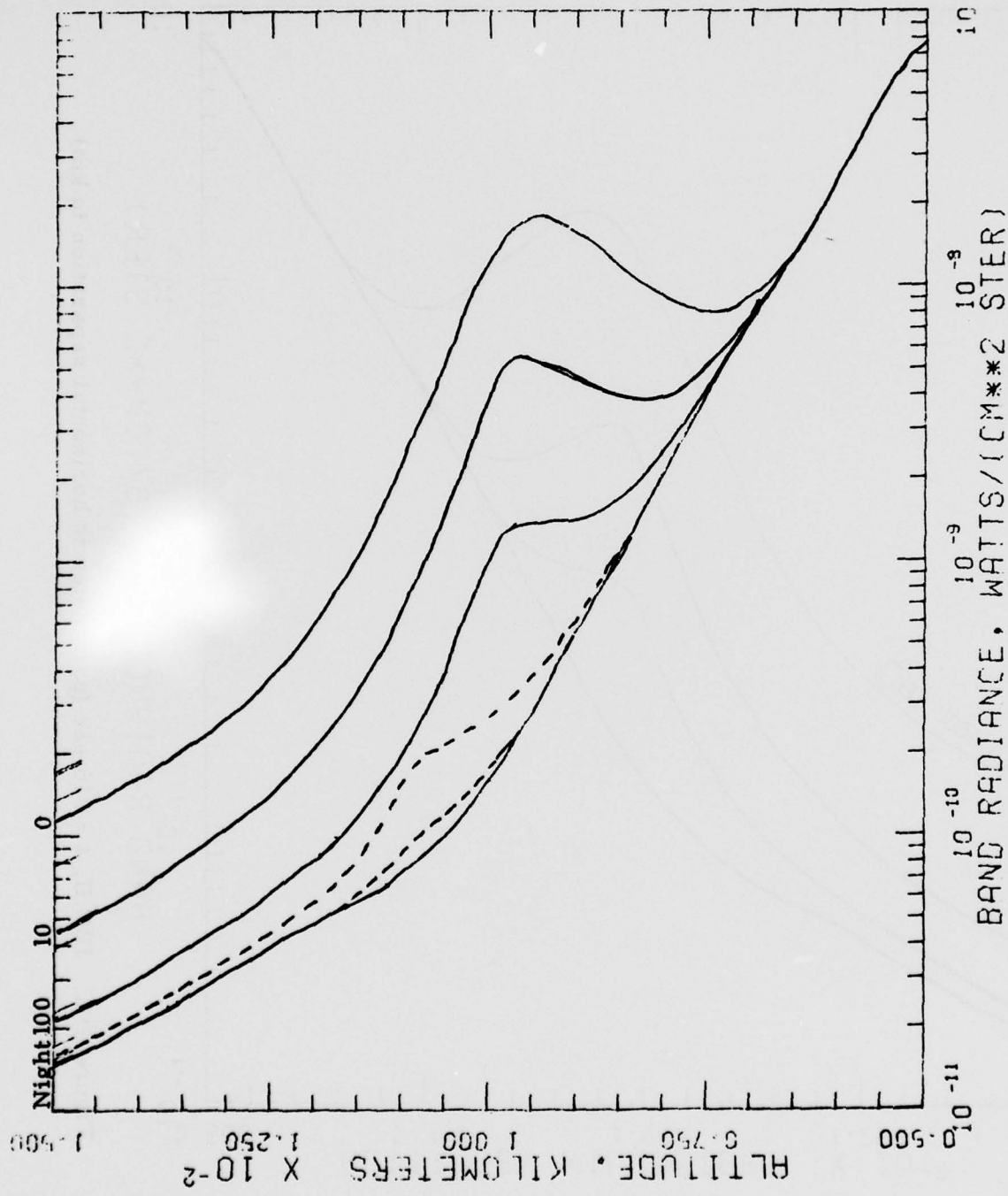

Figure D4. IBC II, t = 1000 sec (parameter is horizontal separation in km)

We have also estimated the zenith brightness after an auroral arc has passed through a region. Figure D5 shows the decay in zenith radiance after an IBC II aurora which has been stationary for 10^4 seconds (dashed line) moves away. Decaying brightness is shown for times of 316, 1000 and 3162 seconds. Also shown are the zenith radiance curves for an IBC III aurora at times of 316 and 1000 seconds from Figures D1 and D2.

The data in Figures D1 through D4 do not include attenuation in the horizontal direction by self-absorption of the 4.3 micron radiation by CO_2 molecules. The curves in Figure D6 have been obtained by using as a guide the horizontal attenuation factors below, and making a subjective evaluation of effects of radiative pumping from adjacent regions.

Horizontal Attenuation Factor

	Horizontal Distance	
Altitude	10	100
90	2/25	---
100	1/4	1/30
110	4/5	1/10

This figure shows the zenith radiance due to attenuated radiance transfer as a function of horizontal displacement from the auroral arc.

North of the auroral arc we have combined the effects of radiative transfer (Figure D1) and delayed emission of stored auroral energy (Figure D5) to obtain the data shown in Figure D7.

Figures D8 and D9 compare the band radiance values shown in Figures D6 and D7 at specific altitudes north and sourth of the arc (90 km, 100 km, 110 km, and 120 km).

The purpose of the results presented here is to provide a qualitative estimate of the zenith brightness profile due to radiation transfer from an auroral arc. The data presented are order of magnitude estimates, and the final results in Figures D6 - D9 apply to an aurora with brightness somewhere between IBC II and IBC III.

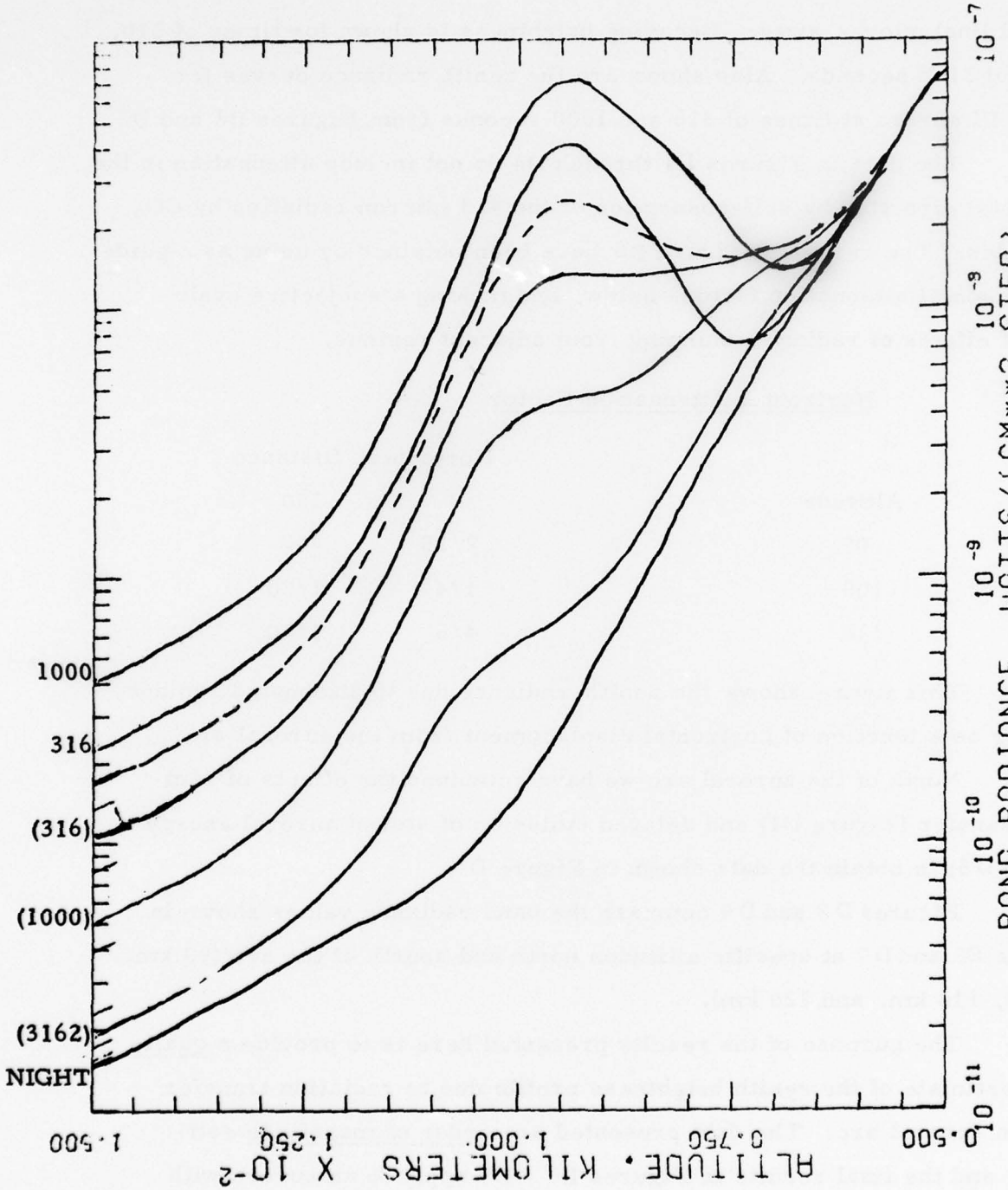

Figure D5. Delayed Emission [parameter is (time) in seconds after passage of arc and auroral class]

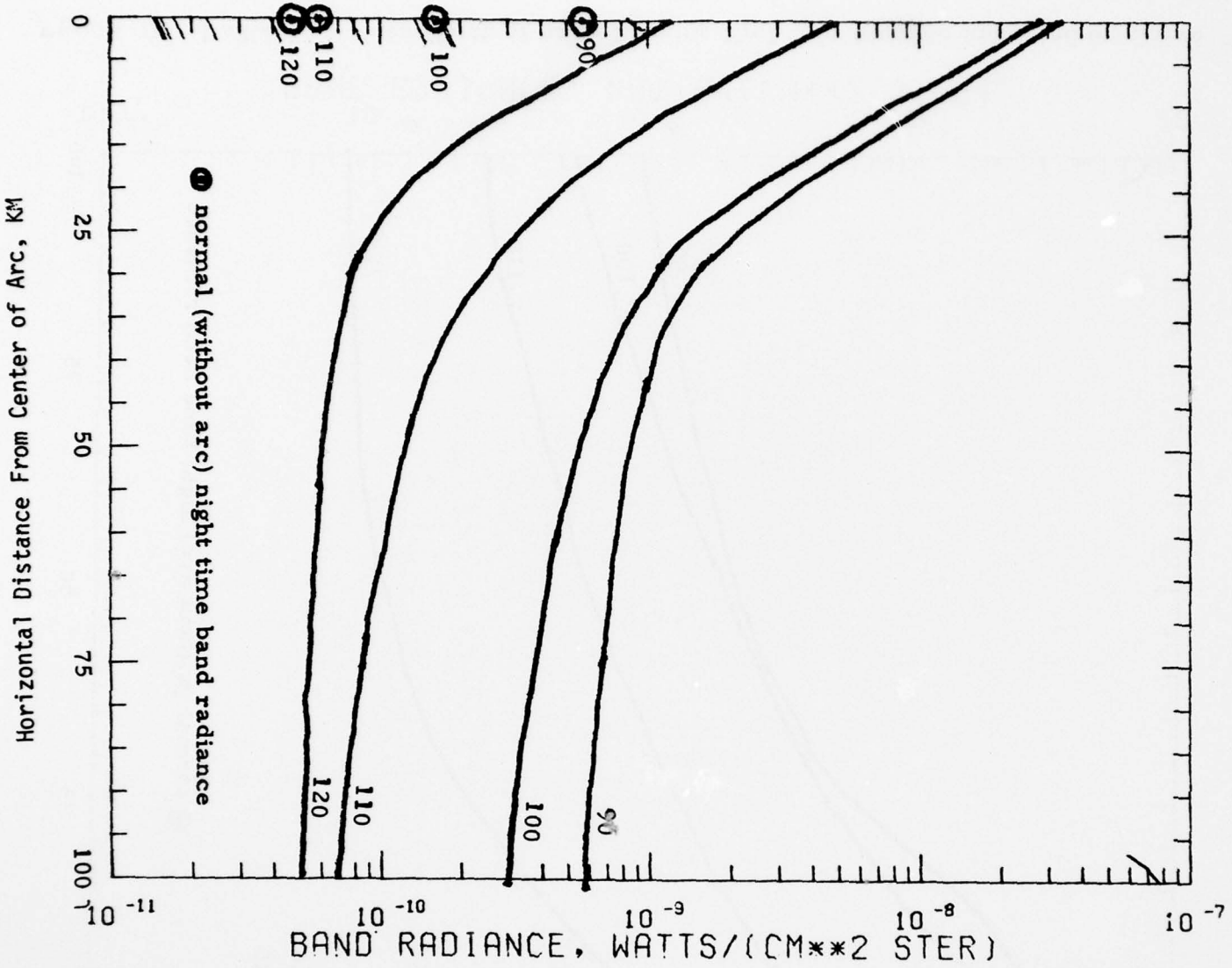

Figure D6. **Radiance Values South of Arc, Looking Up From Altitude Indicated on Curve**

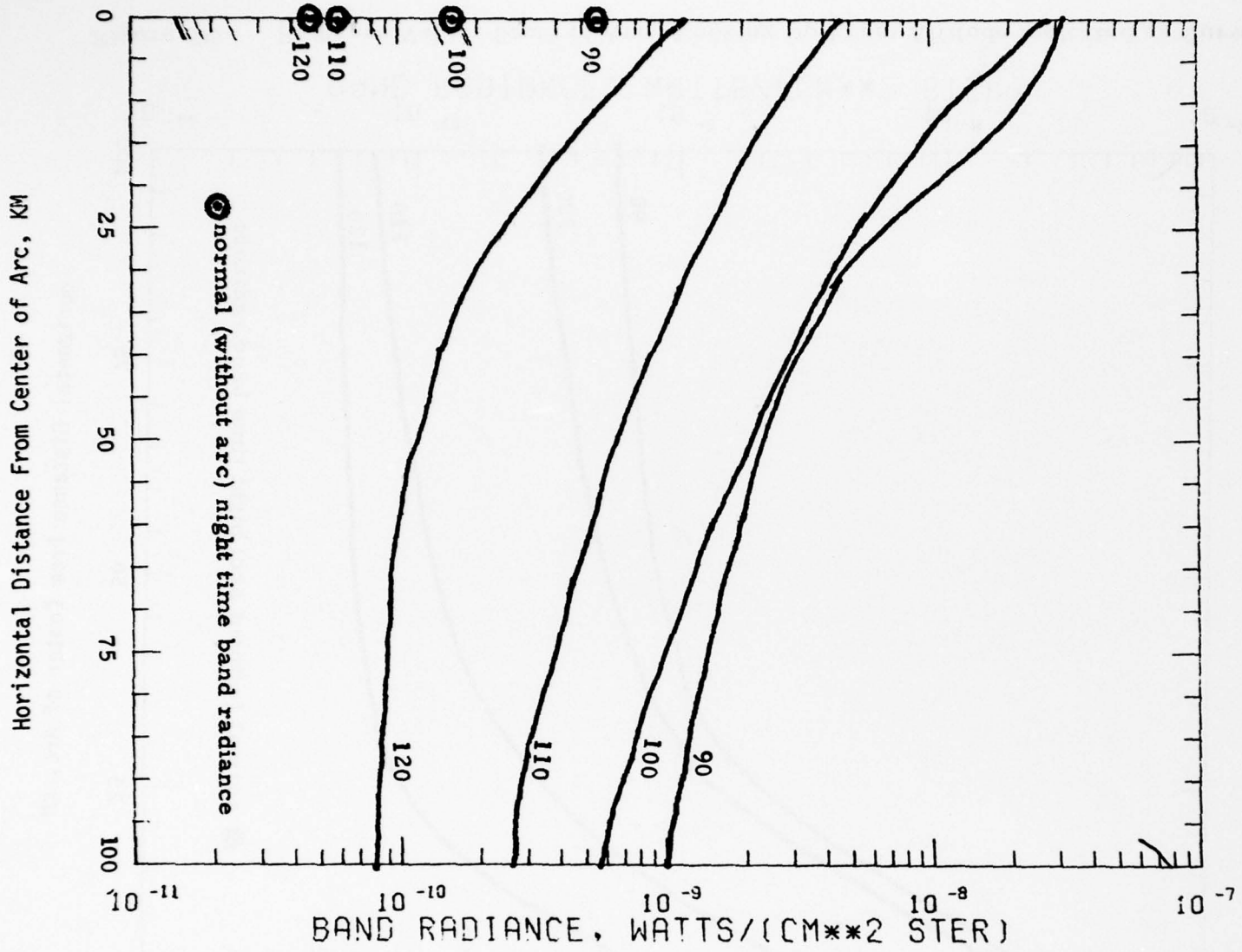

Figure D7. Radiance Values North of Arc, Looking Up From Altitude Indicated on Curve

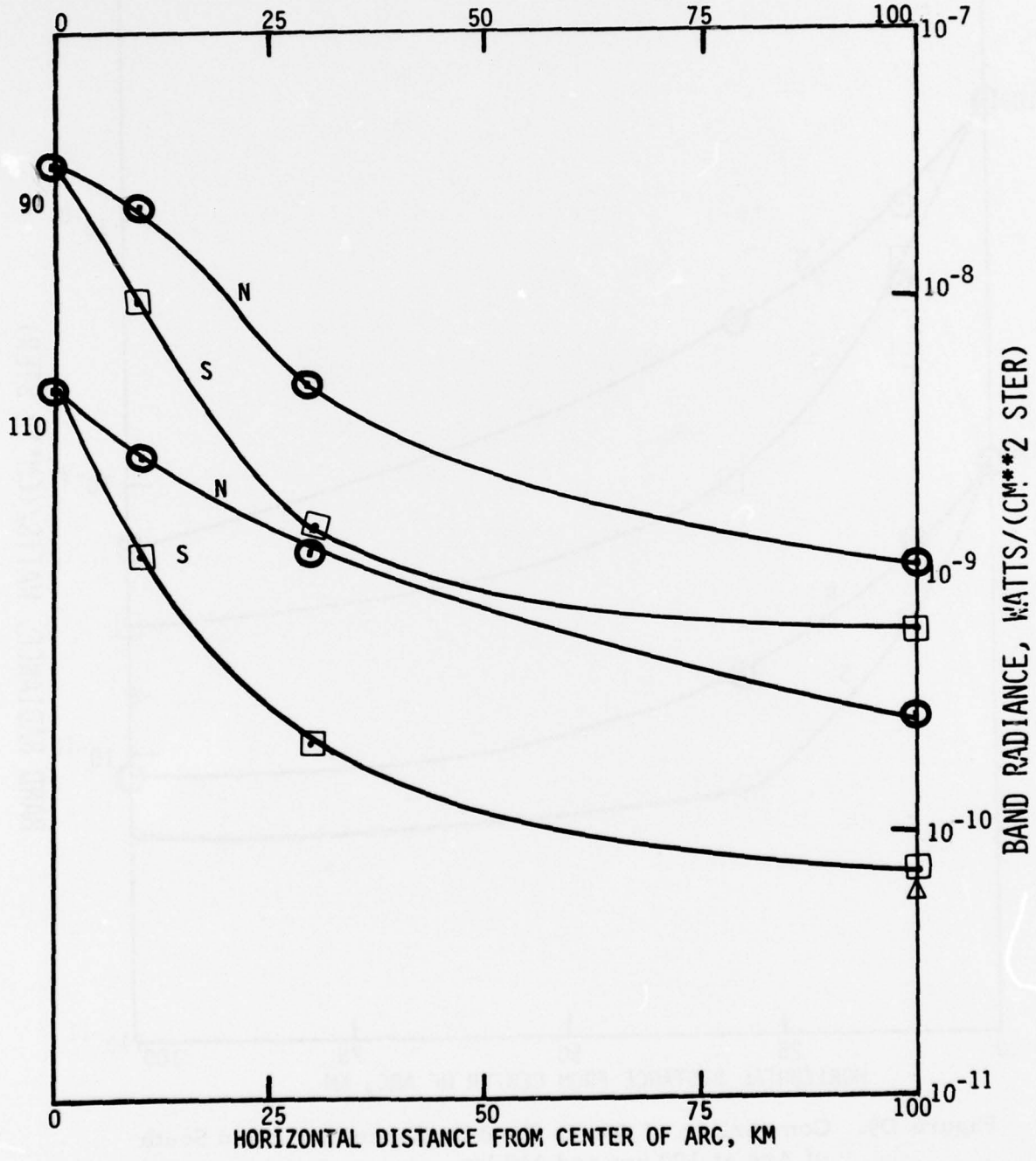

Figure D8: Comparison of Zenith Band Radiance North and South of Arc at 90 km and 110 km

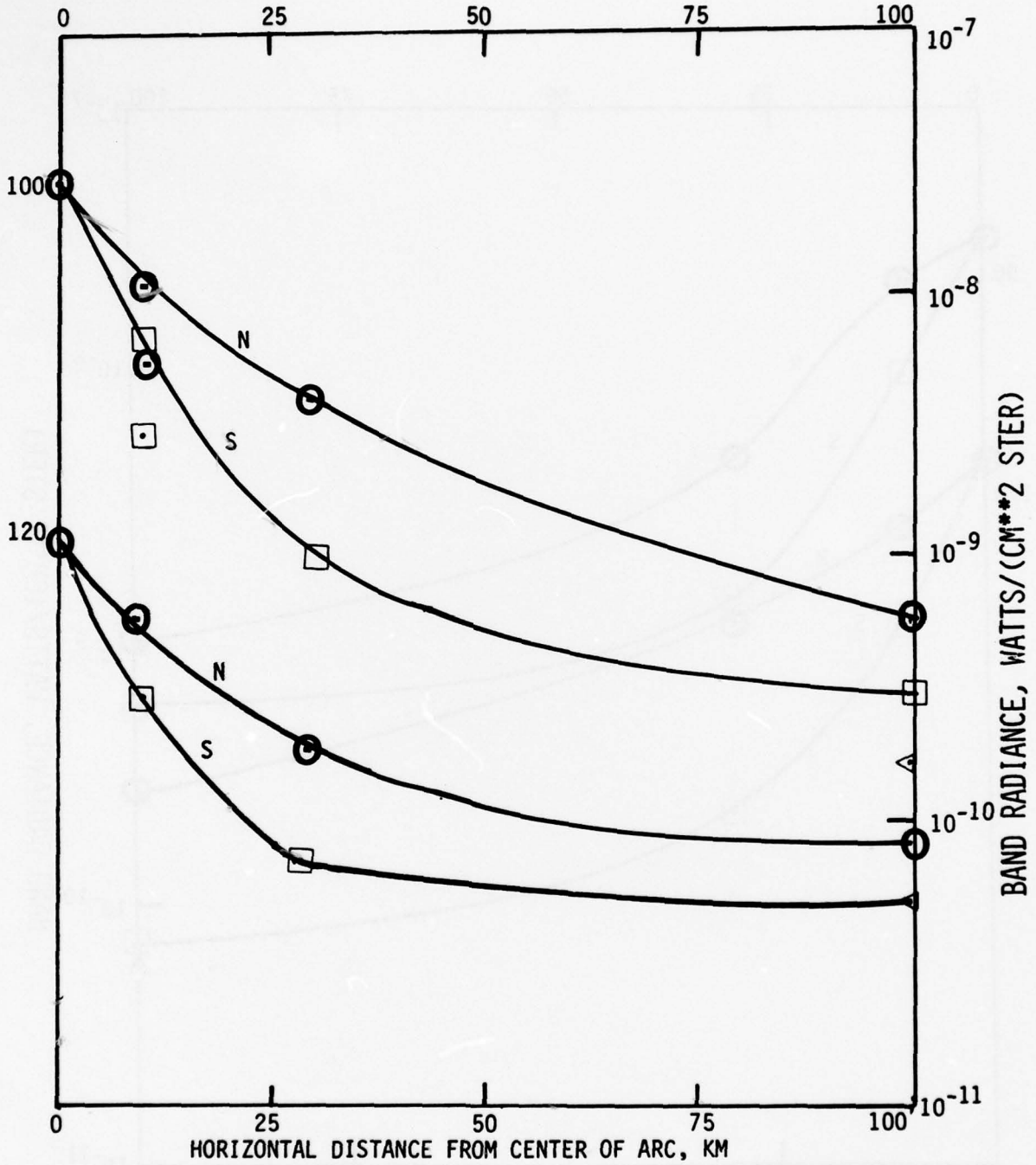

Figure D9. Comparison of Zenith Band Radiance North and South of Arc at 100 km and 110 km

APPENDIX E
PROPOSED USE OF EXCEDE TECHNOLOGY FOR SATELLITE COMMUNICATION STUDIES

Proposed Use of EXCEDE Technology for Satellite Communication Studies

EXCEDE is an experimental program to perturb the upper atmosphere in a controlled and predetermined manner and to make quantitative measurements of the effect of this perturbation. The initial EXCEDE experiments have used an electron accelerator as the energy source. Many of the parameters that control important phenomena are not well known or understood, (e.g., minor species concentration, electric field effects, development of structure) and therefore cannot be adequately simulated in the laboratory. In addition, the scale of some atmospheric phenomena is such that laboratory simulation is not feasible.

Since the ratification of the ban on nuclear testing, scientists have been limited to naturally occurring phenomena (e.g., aurora, PCA, solar flare etc.) and to such methods as chemical releases and high frequency heating as inputs for studies of perturbed atmospheres. These studies have proven the value of in-situ measurements but have some major limitations. Natural phenomena are variable and hard to predict and do not reach the energy deposition levels achievable with EXCEDE which are comparable with those experienced in the vicinity of high altitude nuclear detonations. Chemical releases introduce foreign substances into the upper atmosphere and the subsequent behavior may be influenced by the chemical or physical properties of that substance, especially when optical/infrared emissions are studied.

The advantages of the EXCEDE Program are several:

a. Energy deposition rates are orders of magnitude above that achieved by other means.

b. The effects of nuclear X-ray and Beta-ray deposition over very large areas can be studied.

c. Direct in situ measurements can be made of atmospheric conditions before and after energy deposition. The altitude, volume, time of deposition, and deposition structure can be selected and programmed in advance. The energy and current levels can be selected and programmed in advance.

d. EXCEDE electron deposition does not introduce contaminants or minor species which can alter the atmospheric chemistry.

To date there have been two rocket launches in the EXCEDE Program. The first launch, PRECEDE, was from White Sands Missile Range on 17 October 1974. The rocket was instrumented with a 2 kilowatt accelerator and diagnostic instrumentation to measure beam voltage and current, particle flux and vehicle potential. In addition, ground-based instrumentation measured the spatial, temporal, and spectral structure of the optical emissions. This launch successfully demonstrated the EXCEDE concept, provided an engineering test of the EXCEDE-SWIR accelerator, demonstrated that vehicle neutralization was not a significant problem, provided data on the deposition profile which was in agreement with prelaunch calculations, and provided measurements on the intensity and life time of various optical radiators excited by the electron deposition.

The second launch, EXCEDE II Test, took place on 13 April 1975. The launch site was Poker Flate Research Range, Alaska. The 30 kilowatt electron accelerator represented an order of magnitude increase in power over the PRECEDE rocket. On-board instrumentation included radiometers, photometers, and diagnostic instruments to measure vehicle potential, and the energy spectrum of the return beam. Transmitters at various frequencies were used to determine the electron density in the vicinity of the rocket. The flight was successful. Full beam power was attained (although the programmed modulation of one of the two accelerators failed, that accelerator operated in the d-c mode). Again, vehicle neutralization proved not to be a problem and the photometers and radiometers operated properly and were not affected by the accelerator or the return beam current. The local electron density was between 2×10^8 and 8×10^8 electrons cm^{-3}. Rocket apogee was 136 kilometers.

These two rocket flights have laid the groundwork for advanced studies of the optical, SWIR, MWIR and LWIR spectra and structure that can be

produced at high energy deposition rates in the upper atmosphere.

In our opinion the EXCEDE concept need not be limited to optical/IR studies. The concept of a controlled preprogrammable energy deposition should also be applicable to communications effects. Even at present power levels ionization screens can be produced which will have measurable effects at frequencies of interest. The remainder of this paper will be devoted to a discussion of a possible THIN SCREEN scintillation experiment. While such a THIN SCREEN would not degrade present communication systems, it does provide the opportunity to evaluate the effects of various electron density spatial frequencies on the propagation of electromagnetic waves.

Experimental Objectives

1. Produce a known, controllable pattern of ionospheric irregularities.
2. Measure the effects produced by this pattern on the transmission of data from present satellite systems and/or rocket-borne transmitters.
3. Use the known structure and the measured communication effects to evaluate present theories on ionospheric propagation and as a benchmark test for present communication codes.

Experimental Constraints

Ionization will be produced by one or several EXCEDE modules utilizing available technology. (For the calculations in this note, one module will be considered to be 10 amp at 3 keV (EXCEDE II test power level.)

Technical Approach

The electron deposition in the upper atmosphere will be roughly rectangular with the long axis along the magnetic field line when the

Larmor frequency is much greater than the collision frequency. The proposed approach is to produce a structured ionization enhancement by pulsing the EXCEDE module during the flight. This is shown conceptually in the sketch below.

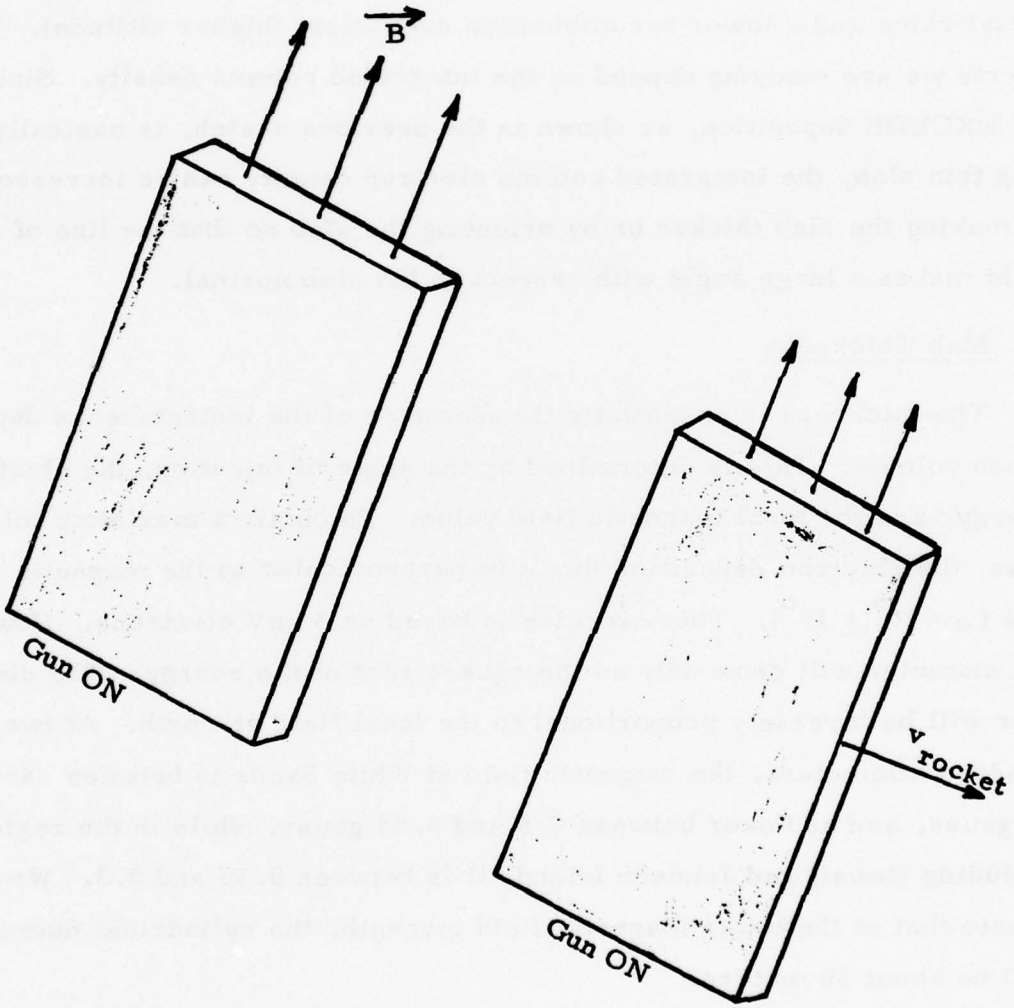

There are several trade-offs in an EXCEDE experiment design which depend upon the specific experiment to be performed.

In this experiment, we wish to produce an ionization structure that persists for tens of seconds and extends over a relatively large area. The persistence of an ionization enhancement depends on the initial ion density, N_o, and the recombination coefficient α. The initial electron-ion density will decrease 50% in a time $t = 1/N_o \alpha$ after the ionization source is turned off. Therefore, a longer persistence implies a lower initial value and a lower recombination coefficient (higher altitude). The effects we are studying depend on the integrated column density. Since the EXCEDE deposition, as shown in the previous sketch, is basically a long thin slab, the integrated column electron density can be increased by making the slab thicker or by orienting the slab so that the line of sight makes a large angle with respect to the slab normal.

Slab Thickness

The thickness is essentially the diameter of the instantaneous deposition volume. This is determined by the angle of injection, the electron energy, and the local magnetic field value. To obtain a maximum thickness, the electron deposition should be perpendicular to the magnetic field line ($\alpha = 90^o \pm 15^o$). This exercise is based on 3 keV electrons. However, the diameter will grow only as the square root of the energy. The diameter will be inversely proportional to the local field strength. At two hundred kilometers, the magnetic field at White Sands is between .45 and .5 gauss, and at Poker between 0.5 and 0.55 gauss, while in the region, including Hawaii and Johnson Island, it is between 0.35 and 0.3. We estimate that at the lower magnetic field strength, the cylindrical diameter will be about 50 meters.

Electron Density

For the purposes of these calculations, we will use an atmospheric density of 10^{-10} kgm m^{-3} (10^{-13} gm cm^{-3}) which is approximately 225

kilometers using the mean CIRA atmosphere and a recombination coefficient of 2×10^{-8} cm^3 sec^{-1}. The range of a 3 keV electron is 3.66×10^{-5} gm cm^{-2} and we assume a pitch angle of 75^o. The average deposition per unit length by one electron along the field line will be about 3×10^{-5} ev/cm. The average ion production rate is about 3×10^6 ion/cm^3-sec or 3×10^{12} ions/m^3-sec for a 10 ampere beam.

The total ion production will depend on the velocity of the accelerator. Assume the velocity across the field lines is 150 m sec^{-1}, then for a 50 m diameter, the region will be irradiated for 1/3 second, the initial average electron density will be 9.8×10^5 electrons cm^{-3}. The time for this to reduce to one-half the initial electron density is about 50 seconds.

In 50 seconds the deposition will be 7.5 kilometers wide, 50 meters thick, and the length, if the deposition were at constant altitude, would be about 1000 km.

Integrated Electron Column Density

The effective electron column density depends on the angle, β, between the line of sight from transmitter to receiver and the normal to the slab.

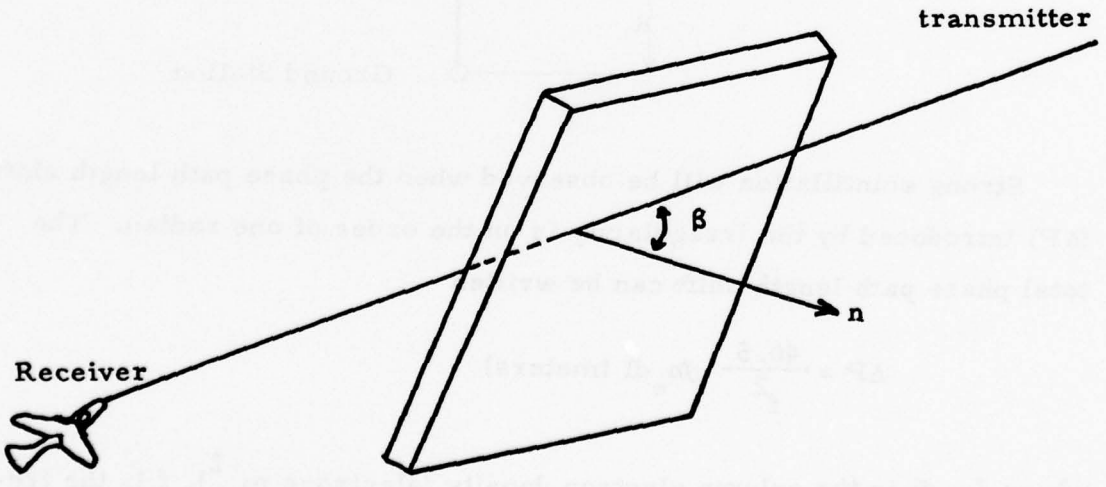

The effective integrated electron column density ($\int n_e dl$) is

$$\frac{5 \times 10^{13}}{\cos\beta} \text{ electrons m}^{-2}$$

Scintillations

Scintillations are a major cause of signal degradation. *Scintillations* are amplitude and phase variations introduced into electromagnetic waves by ionospheric irregularities. Consider the following simplified case. A satellite is located at a distance R above an ionospheric irregularity and a ground station is located at a distance R below it. The height of the irregularity is small compared to R. The effects of ionospheric irregularities are maximized when the irregularity occupies a horizontal size on the order of the first Fresnel zone radius (r). The situation is sketched below.

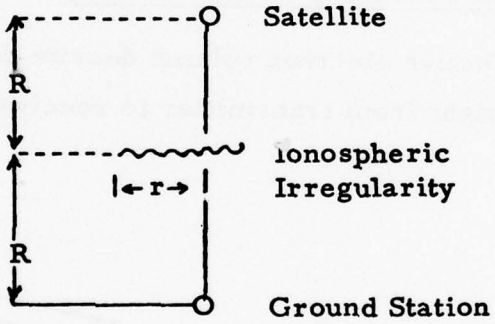

Strong scintillation will be observed when the phase path length shift (ΔP) introduced by the irregularity is on the order of one radian. The total phase path length shift can be written

$$\Delta P = \frac{40.5}{f^2} \int n_e dl \text{ (meters)}$$

where $\int n_e dl$ is the column electron density (electrons m^{-2}), f is the frequency in Hertz.

The effective integrated electron column density $\int n_e dl$ is $5 \times 10^{13}/\cos$ (electrons m^{-2}).

If we require ΔP to correspond to 1 radian (i.e., $\frac{\lambda}{2\pi}$) then

$$\int n_e dl \text{ (electron } m^{-2}) = \frac{cf}{2\pi 40.5} = 1.2 \times 10^6 f$$

The following table lists the integrated column density to produce a phase change of one radian and the scale size, r, (Frensnel zone radius) of the irregularity necessary to produce strong scintillations from satellite transmissions for frequencies of interest.

f (Hertz)	$\int n_e dl$ (electron meter^{-2})	r (meters)
3×10^7	3.6×10^{13}	10^3
3×10^8	3.6×10^{14}	3.2×10^2
3×10^9	3.6×10^{15}	10^2

The preceding discussion is based on a single EXCEDE module. A three-dimensional modulation can be obtained by using multiple EXCEDE modules separated from a single launch vehicle. This would not only increase $\int n_e dl$, but also provide the capability to study propagation through multiple known ionospheric structures. This capability does not exist today. Figure E1 shows schematically how such a structured region could be used for satellite-to-airplane, rocket-to-ground, or ground-to-ground measurements.

Table E1 illustrates the phase shift produced at three frequencies using three modules as illustrated in Figure E1. The phase shift is calculated for various values of the angle β discussed previously.

TABLE E1. PHASE SHIFT vs. ANGLE OF INCIDENCE

β	$\int n_e dl$	PHASE SHIFT		
		30 MHz (λ=10m)	300 MHz (λ=1m)	3000 MHz (λ=.1m)
Degrees	electrons m^{-2}	radians	radians	radians
0	1.5×10^{14}	4.2	.4	4.2×10^{-2}
45	2×10^{14}	6	.6	6×10^{-2}
60	3×10^{14}	8.4	.8	8.4×10^{-2}
75	6×10^{14}	16	1.6	1.6×10^{-1}

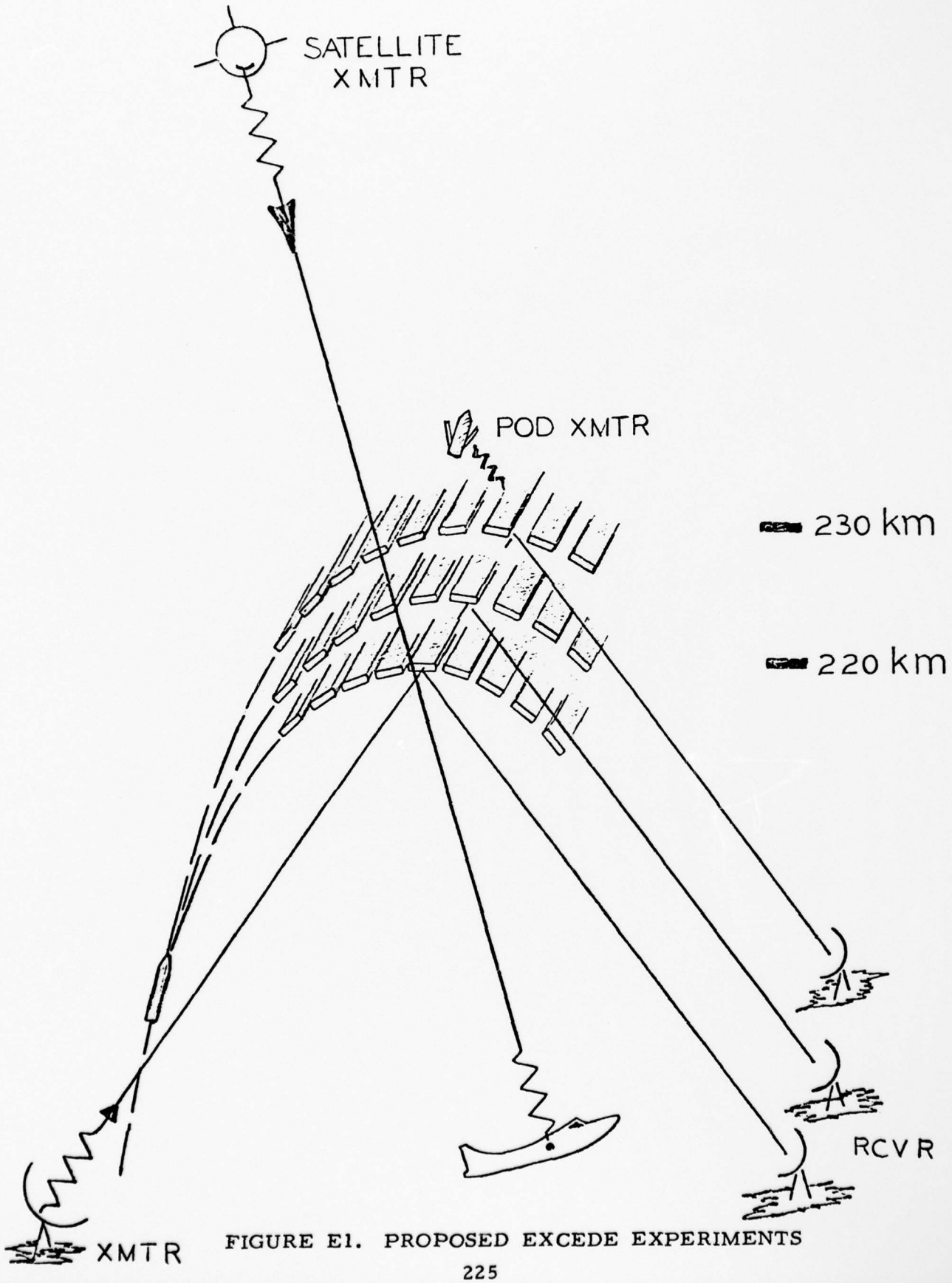

FIGURE E1. PROPOSED EXCEDE EXPERIMENTS

DIRECTOR
DEFENSE ADVANCED RSCH PROJ AGENCY
ARCHITECT BUILDING
1400 WILSON BLVD.
ARLINGTON,VA 22209
ATTN LTC W A WHITAKER

DIRECTOR
DEFENSE ADVANCED RSCH PROJ AGENCY
ARCHITECT BUILDING
1400 WILSON BLVD.
ARLINGTON,VA 22209
ATTN MAJOR GREGORY CANAVAN

DEFENSE DOCUMENTATION CENTER
CAMERON STATION
ALEXANDRIA,VA 22314
ATTN TC

DEFENSE DOCUMENTATION CENTER
CAMERON STATION
ALEXANDRIA,VA 22314
ATTN TC

DEFENSE NUCLEAR AGENCY
WASHINGTON, DC 20305
ATTN RAAE CHARLES A BLANK

DIRECTOR
DEFENSE NUCLEAR AGENCY
WASHINGTON, DC 20305
ATTN TITL TECH LIBRARY

DIRECTOR
DEFENSE NUCLEAR AGENCY
WASHINGTON, DC 20305
ATTN TITL TECH LIBRARY

DIRECTOR
DEFENSE NUCLEAR AGENCY
WASHINGTON, DC 20305
ATTN TISI ARCHIVES

DIRECTOR
DEFENSE NUCLEAR AGENCY
WASHINGTON, DC 20305
ATTN RAEV HAROLD C FITZ, JR

DIRECTOR
DEFENSE NUCLEAR AGENCY
WASHINGTON, DC 20305
ATTN RAAE MAJ. J. MAYO

DIRECTOR
DEFENSE NUCLEAR AGENCY
WASHINGTON, DC 20305
ATTN RAAE G. SOPER

DIRECTOR
DEFENSE NUCLEAR AGENCY
WASHINGTON, DC 20305
ATTN MAJOR R. BIGONI

DIR OF DEFENSE RSCH & ENGINEERING
DEPARTMENT OF DEFENSE
WASHINGTON DC 20301
ATTN DD/S&SS (OS) DANIEL BROCKWAY

DIR OF DEFENSE RSCH & ENGINEERING
DEPARTMENT OF DEFENSE
WASHINGTON, DC 20301
ATTN DD/S&SS DANIEL BROCKWAY

COMMANDER
FIELD COMMAND
DEFENSE NUCLEAR AGENCY
KIRTLAND AFB, NM 87115
ATTN FCPR

CHIEF LIVERMORE DIVISION
FLD COMMAND DNA
LAWRENCE LIVERMORE LABORATORY
P.O. BOX 808
LIVERMORE, CA 94550
ATTN FCPRL

COMMANDER/DIRECTOR
ATMOSPHERIC SCIENCES LABORATORY
U S ARMY ELECTRONICS COMMAND
WHITE SANDS MISSILE RANGE, NM 88002
ATTN DRSEL-BL-SY-A F. NILES 3 copies

COMMANDER/DIRECTOR
ATMOSPHERIC SCIENCES LABORATORY
U S ARMY ELECTRONICS COMMAND
WHITE SANDS MISSILE RANGE, NM 88002
ATT H. BALLARD 3 copies

COMMANDER
HARRY DIAMOND LABORATORIES
2800 POWDER MILL RD
ADELPHI MD 20783
ATTNDRXDO-NP, F.H. WIMINETZ

COMMANDER
U S ARMY NUCLEAR AGENCY
FORT BLISS,TX 79916
ATTN MONA-WE

DIRECTOR
BMD ADVANCED TECH CTR
HUNTSVILLE,AL 35807
ATTN ATC-T, M CAPPS

DIRECTOR
BMD ADVANCED TECH CTR
HUNTSVILLE,AL 35807
ATTN ATC-O,W.DAVIES

DEP.CHIEF OF STAFF FOR RSCH, DEV&ACQ
DEPARTMENT OF THE ARMY
WASHINGTON DC 20310
ATTN MCB DIVISION

DEP.CHIEF OF STAFF FOR RSCH,DEV&ACQ
DEPARTMENT OF THE ARMY
WASHINGTON,DC 20310
ATTN DAMA-CSZ-C

DEP.CHIEF OF STAFF FOR RSCH, DEV&ACQ
DEPARTMENT OF THE ARMY
WASHINGTON DC 20310
ATTN DAMA-WSZC

DIRECTOR
US ARMY BALLISTIC RESEARCH LABS
ABERDEEN PROVING GROUNDS,MD 21005
ATTN DRXBR-AM,G. KELLER

DIRECTOR

US ARMY BALLISTIC RESEARCH LABS
ABERDEEN PROVING GROUNDS,MD 21005
ATTN DRXRD-BSP,J.HEIMERL

DIRECTOR
US ARMY BALLISTIC RESEARCH LABS
ABERDEEN PROVING GROUNDS,MD 21005
ATTN JOHN MESTER

DIRECTOR
US ARMY BALLISTIC RESEARCH LABS
ABERDEEN PROVING GROUNDS,MD 21005
ATTN TECH LIBRARY

COMMANDER
US ARMY ELECTRONICS COMMAND
FORT MONMOUTH,N.J. 37703
ATTN INST FOR EXPL RESEARCH

COMMANDER
US ARMY ELECTRONICS COMMAND
FORT MONMOUTH,N.J. 37703
ATT DRSEL 5 copies

COMMANDER
US ARMY ELECTRONICS COMMAND
FORT MONMOUTH,N.J. 37703
ATN STANLEY KRONENBERGER

COMMANDER
US ARMY ELECTRONICS COMMAND
FORT MONMOUTH,N.J. 37703
ATN WEAPONS EFFECTS SECTION

COMMANDER
US ARMY FOREIGN SCIENCE & TECH CTR
220 7TH STREET,NE
CHARLOTTESVILLEVA 22901

ATTN ROBERT JONES

CHIEF
US ARMY RESEARCH OFFICE
P.O. BOX 12211
TRIANGLE PARK,N.C. 27709
ATT ROBERT MACE

COMMANDER
NAVAL OCEANS SYSTEMS CENTER
SAN DIEGO,CA 92152
ATTN CODE 2200 ILAN ROTHMULLER

COMMANDER
NAVAL OCEANS SYSTEMS CENTER
SAN DIEGO,CA 92152
ATTN CODE 2200 WILLIAM MOLER

COMMANDER
NAVAL OCEANS SYSTEMS CENTER
SAN DIEGO,CA 92152
ATTN CODE 2200 HERBERT HUGHES

COMMANDER
NAVAL OCEANS SYSTEMS CENTER
SAN DIEGO,CA 92152
ATTN CODE 2200 RICHARD PAPPERT

COMMANDER
NAVAL OCEANS SYSTEMS CENTER
SAN DIEGO,CA 92152
ATTN CODE 2200JURGEN R RICHTER

DIRECTOR
NAVAL RESEARCH LABORATORY
WASHINGTON,DC 20375
ATTN CODE 7712 DOUGLAS P MCNUTT

DIRECTOR
NAVAL RESEARCH LABORATORY
WASHINGTON, DC 20375
ATTN CODE 7701 JACK D BROWN

DIRECTOR
NAVAL RESEARCH LABORATORY
WASHINGTON, DC 20375
ATTN CODE 2600 TECH LIB

DIRECTOR
NAVAL RESEARCH LABORATORY
WASHINGTON, DC 20375
ATTN CODE 7127 CHARLES Y JOHNSON

DIRECTOR
NAVAL RESEARCH LABORATORY
WASHINGTON, DC 20375
ATTN CODE 7700 TIMOTHY P COFFEY

DIRECTOR
NAVAL RESEARCH LABORATORY
WASHINGTON, DC 20375
ATTN CODE 7709 WAHAB ALI

DIRECTOR
NAVAL RESEARCH LABORATORY
WASHINGTON, DC 20375
ATTN CODE 7750 DARRELL F STROBEL

DIRECTOR
NAVAL RESEARCH LABORATORY
WASHINGTON, DC 20375
ATTN CODE 7750 PAUL JULUENNE

DIRECTOR

NAVAL RESEARCH LABORATORY.
WASHINGTON,DC 20375
ATTN CODE 7750 J. FEDDER

DIRECTOR
NAVAL RESEARCH LABORATORY
WASHINGTON,DC 20375
ATTN CODE 7750 S. OSSAKOW

DIRECTOR
NAVAL RESEARCH LABORATORY
WASHINGTON,DC 20375
ATTN CODE 7750 J. DAVIS

COMMANDER
NAVAL SURFACE WEAPONS CENTER
WHITE OAK,SILVER SPRING,MD 20910
ATTN CODE WA501 NAVY NUC PRGMS OFF

COMMANDER
NAVAL SURFACE WEAPONS CENTER
WHITE OAKS,SILVER SPRING,MD 20910
ATTN TECHNICAL LIBRARY

SUPER INTENDENT
NAVAL POST GRADUATE SCHOOL
MONTEREY,CA 93940
ATTN TECH REPORTS LIBRARIAN

COMMANDER
NAVAL ELECTRONICS SYSTEMS COMMAND
NAVAL ELECTRONICS SYSTEMS COMMAND HQS
ATTN PME 117

COMMANDER
NAVAL INTELLIGENCE SUPPORT CTR
4301 SUITLAND RD. BLDG 5
WASHINGTON,DC20390

ATTN DOCUMENT CONTROL

AF GEOPHYSICS LABORATORY,AFSC
HANSCOM AFB, MA 01731
ATTN LKB KENNETH S W CHAMPION

AF GEOPHYSICS LABORATORY,AFSC
HANSCOM AFB, MA 01731
ATTN OPR ALVA T STAIR

AF GEOPHYSICS LABORATORY,AFSC
HANSCOM AFB, MA 01731
ATTN OPR-1 J. ULWICK

AF GEOPHYSICS LABORATORY,AFSC
HANSCOM AFB, MA 01731
ATTN OPR-1 R. MURPHY

AF GEOPHYSICS LABORATORY,AFSC
HANSCOM AFB, MA 01731
ATTN OPR-1J. KENNEALY

AF GEOPHYSICS LABORATORY,AFSC
HANSCOM AFB, MA 01731
ATTN PHG JC MCCLAY

AF GEOPHYSICS LABORATORY,AFSC
HANSCOM AFB, MA 01731
ATTN LKD ROCCO NARCIS

AF GEOPHYSICS LABORATORY,AFSC
HANSCOM AFB, MA 01731
ATTN LKO,R. HUFFMAN

AF WEAPONS LABORATORY,AFSC
KIRTLAND,AFB,NM 87117
ATTN MAJ.GARY GANONG,DYM

COMMANDER
ASD
WPAFB,OH 45433
ATTN ASD-YH-EX LTC ROBERT LEVERETTE

SAMSO/AW
POST OFFICE BOX 92960
WORLDWAY POSTAL CENTER
LOS ANGELES,CA 90009
ATTNSZJ MAJOR LAWRENCE DOAN

SAMSO/SW
P.O. BOX 92960
WORLDWAY POSTAL CENTER
LOS, ANGELES,CA 90009
ATTN AW

AFTAC
PATRICK AFB,FL 32925
ATTN TECH LIBRARY

AFTAC
PATRICK AFB,FL 32925
ATTN TD

HQ

AIR FORCE SYSTEMS COMMAND
ANDREWS AFB
WASHINGTON, DC 20331
ATTN DLS

HQ
AIR FORCE SYSTEMS COMMAND
ANDREWS AFB
WASHINGTON, DC 20331
ATTN TECH LIBRARY

HQ
AIR FORCE SYSTEMS COMMAND
ANDREWS AFB
WASHINGTON, DC 20331
ATTN DLCAE

HQ
AIR FORCE SYSTEMS COMMAND
ANDREWS AFB
WASHINGTON, DC 20331
ATTN DLTW

HQ
AIR FORCE SYSTEMS COMMAND
ANDREWS AFB
WASHINGTON, DC 20331
ATTN DLXP

HQ
AIR FORCE SYSTEMS COMMAND
ANDREWS AFB
WASHINGTON, DC 20331
ATTNSDR

HQ USAF/RD
WASHINGTON, DC 20330
ATTN RDQ

COMMANDER
ROME AIR DEVELOPMENT CTR
GRIFFISS AFB, NY 13440
ATTN JJ. SIMONS OCSC

DIVISION OF MILITARY APPLICATION
U S ENERGY RSCH & DEV ADMIN
WASHINGTON,DC 20545
ATTN DOC CON

LOS ALAMOS SCIENTIFIC LABORATORY
P.O. BOX 1663
LOS,ALAMOS, NM 87545
ATTN DOC CON FOR R A JEFFRIES

LOS ALAMOS SCIENTIFIC LABORATORY
P.O. BOX 1663
LOS,ALAMOS, NM 87545
ATTN DOC CON FOR CR MEHL ORG 5230

LOS ALAMOS SCIENTIFIC LABORATORY
P.O. BOX 1663
LOS,ALAMOS, NM 87545
ATTN DOC CON FOR H V ARGO

LOS ALAMOS SCIENTIFIC LABORATORY
P.O. BOX 1663
LOS,ALAMOS, NM 87545
ATTN DOC CON FOR M. TIERNEY J-10

LOS ALAMOS SCIENTIFIC LABORATORY
P.O. BOX 1663
LOS,ALAMOS, NM 87545
ATTN DOC CON FOR ROBERT BROWNLEE

LOS ALAMOS SCIENTIFIC LABORATORY
P.O. BOX 1663
LOS,ALAMOS, NM 87545
ATTN DOC CON FOR WILLIAM MAIER

LOS ALAMOS SCIENTIFIC LABORATORY
P.O. BOX 1663
LOS,ALAMOS, NM 87545
ATTN DOC CON FOR JOHN ZINN

LOS ALAMOS SCIENTIFIC LABORATORY
P.O. BOX 1663
LOS,ALAMOS, NM 87545
ATTN DOC CON FOR REFERENCE LIBRARY
ANN BEYER

SANDIA LABORATORIES
LIVERMORE LABORATORY
P.O. BOX 965
LIVERMORE,CA 94556
ATTN DOC CONTROL FOR
THOMAS COOK ORG 8000

SANDIA LABORATORIES
P.O. BOX 5800
ALBUQUERQUE,NM 87115
ATT DOC CONT. FOR
W.D. BROWN ORG 1353

SANDIA LABORATORIES
P.O. BOX 5800
ALBUQUERQUE,NM 87115
ATT DOC CONT. FOR
L. ANDERSON ORG 1247

SANDIA LABORATORIES
P.O. BOX 5800
ALBUQUERQUE,NM 87115
ATT DOC CONT.
FOR MORGAN KRAMMA ORG 5720

SANDIA LABORATORIES
P.O. BOX 5800
ALBUQUERQUE,NM 87115
ATT DOC CONT.
FOR FRANK HUDSON ORG 1722

SANDIA LABORATORIES

P.O. BOX 5800
ALBUQUERQUE,NM 87115
ATT DOC CONT.
FOR ORG 3422-1 SANDIA REPTS COLL.

ARGONNE NATIONAL LABORATORY
RECORDS CONTROL
9700 SOUTH CASS AVENUE
ARGONNE, IL 60439
ATTN DOC CON FOR A C WAHL

ARGONNE NATIONAL LABORATORY
RECORDS CONTROL
9700 SOUTH CASS AVENUE
ARGONNE, IL 60439
ATTN DOC CON FOR DAVID W GREEN

ARGONNE NATIONAL LABORATORY
RECORDS CONTROL
9700 SOUTH CASS AVENUE
ARGONNE, IL 60439
ATTN DOC CON FOR LIR SVCS RPTS SEC

ARGONNE NATIONAL LABORATORY
RECORDS CONTROL
9700 SOUTH CASS AVENUE
ARGONNE, IL 60439
ATTN DOC CON FOR S GARELNICK

ARGONNE NATIONAL LABORATORY
RECORDS CONTROL
9700 SOUTH CASS AVENUE
ARGONNE, IL 60439
ATTN DOC CON FOR GERALD T REEDY

UNIVERSITY OF CALIFORNIA
LAWRENCE LIVERMORE LABORATORY
P.O. BOX 808
LIVERMORE CA 94550
ATTN W.H. DUEWER GEN L-404

UNIVERSITY OF CALIFORNIA
LAWRENCE LIVERMORE LABORATORY
P.O. BOX 808
LIVERMORE CA 94550

ATTN JULIUS CHANG L-71

UNIVERSITY OF CALIFORNIA
LAWRENCE LIVERMORE LABORATORY
P.O. BOX 808
LIVERMORE CA 94500
G.R. HAUGEN L-404

UNIVERSITY OF CALIFORNIA
LAWRENCE LIVERMORE LABORATORY
P.O. BOX 808
LIVERMORE CA 94550
ATTN D.J. WUEBBLES L-142

CALIFORNIA, STATE OF
AIR RESOURCE BOARD
9528 TELSTA AVE
AL MONTE, CA 91731
ATTNLEO ZAFONTE

CALIFORNIA INSTITUTE OF TECHNOLOGY
JET PROPULSION LABORATORY
4800 OAK GROVE DRIVE
PASADENA,CA 91103
ATTN JOSEPH A JELLO

U S ENERGY RSCH & DEV ADMIN
DIVISION OF HEADQUARTERS SERVICES
LIBRARY BRANCH G-043
WASHINGTON,DC 20545
ATTN DOC CON FOR CLASS TECH LIB

DEPARTMENT OF TRANSPORTATION
OFFICE OF THE SECRETARY
TAD-44,1,ROOM 10402-R
400 7TH STREET S.W.
WASHINGTON,DC 20590
ATTN SAMJEL C CORONITI

NASA
GODDARD SPACE FLIGHT CENTER
GREENBELT,MD 20771
ATTN A C AIKEN

NASA
GODDARD SPACE FLIGHT CENTER
GREENBELT,MD 20771
ATTN A TEMPKIN

NASA
GODDARD SPACE FLIGHT CENTER
GREENBELT,MD 20771
ATTN A J BAUER

NASA
GODDARD SPACE FLIGHT CENTER
GREENBELT,MD 20771
ATTN TECHNICAL LIBRARY

NASA
GODDARD SPACE FLIGHT CENTER
GREENBELT,MD 20771
ATTN J. SIRY

NASA
600 INDEPENDENCE AVENUE S W
WASHINGTON,DC 20546
ATTN A GESSOW

NASA
600 INDEPENDENCE AVENUE S W
WASHINGTON,DC 20546
ATTN D P CAUFFMAN

NASA
600 INDEPENDENCE AVENUE S W
WASHINGTON,DC 20546
ATTN LTC D R HALLENBECK CODE SG

NASA

600 INDEPENDENCE AVENUE S W
WASHINGTON,DC 20546
ATTN R FELLOWS

NASA
600 INDEPENDENCE AVENUE S W
WASHINGTON,DC 20546
ATTN A SCHARDT

NASA
600 INDEPENDENCE AVENUE S W
WASHINGTON,DC 20546
ATTN M TEPPER

NASA
LANGLEY RESEARCH CENTER
LANGLEY STATION
HAMPTON,VA 23365
ATTN CHARLES SCHEXNAYDER MS-168

NASA
AMES RESCH CENTER
MOFFETT FIELD,CA 90435
ATTN N-254-4 WALTER L. STARR

NASA
AMES RESEARCH CENTER
MOFFETT FIELD,CA 94035
ATTN N-254-4 R WHITTEN

NASA
AMES RESEARCH CENTER
MOFFETT FIELD,CA 94035
ATTN N-254-4 ILIA G POPPOFF

NASA
AMES RESEARCH CENTER
MOFFETT FIELD,CA 94036
ATTN N-254-3 NEIL H FARLOW

NASA
GEORGE C MARSHALL SPACE FLIGHT CENTER
HUNTSVILLE, AL 35812
ATTN C R BALCHER

NASA
GEORGE C MARSHALL SPACE FLIGHT CENTER
HUNTSVILLE, AL 35812
ATT N H STONE

NASA
GEORGE C MARSHALL SPACE FLIGHT CENTER
HUNTSVILLE, AL 35812
ATT W A ORAN

NASA
GEORGE C MARSHALL SPACE FLIGHT CENTER
HUNTSVILLE, AL 35812
ATT CODE ES22JOHN WATTS

NASA
GEORGE C MARSHALL SPACE FLIGHT CENTER
HUNTSVILLE,AL 35812
ATTN W T ROBERTS

NASA
GEORGE C MARSHALL SPACE FLIGHT CENTER
HUNTSVILLE,AL 35812
ATTN R D HUDSON

NASA
GEORGE C MARSHALL SPACE FLIGHT CENTER
HUNTSVILLE,AL 35812
ATTN R CHAPPELL

ALBANY METALLURGY RESEARCH CENTER
U S BUREAU OF MINES
P.O. BOX 70
ALBANY,OR 97321
ATTN ELEANOR ARSHIRE

CENTRAL INTELLIGENCE AGENCY
ATTN RD/SI RM 5G48 HQ BLDG
WASHINGTON DC 20505
ATTN NED/OSI-2G4R HQS

DEPARTMENT OF COMMERCE
NATIONAL BUREAU OF STANDARDS
WASHINGTON,DC 20234
ATTN SEC OFFICER FOR ATTN JAMESS DEVOE

DEPARTMENT OF COMMERCE
NATIONAL BUREAU OF STANDARDS
WASHINGTON,DC 20234
ATTN SEC OFFICER
STANLEY ARRAMOWITZ

DEPARTMENT OF COMMERCE
NATIONAL BUREAU OF STANDARDS
WASHINGTON,DC 20234
ATTN SEC OFFICER FOR ATTN J COOPER

DEPARTMENT OF COMMERCE
NATIONAL BUREAU OF STANDARDS
WASHINGTON,DC 20234
ATTN SEC OFFICER FOR ATTN GEORGE A SINNATT

DEPARTMENT OF COMMERCE
NATIONAL BUREAU OF STANDARDS
WASHINGTON,DC 20234
ATTN SEC OFFICER FOR ATTN K KESSLER

DEPARTMENT OF COMMERCE

NATIONAL BUREAU OF STANDARDS
WASHINGTON,DC 20234
ATTN SEC OFFICER FOR ATTN M KRAUSS

DEPARTMENT OF COMMERCE
NATIONAL BUREAU OF STANDARDS
WASHINGTON,DC 20234
ATTN SEC OFFICER FOR
ATTN LEWIS H GEVANTMAN

DEPARTMENT OF COMMERCE
NATIONAL BUREAU OF STANDARDS
WASHINGTON,DC 20234
ATTN SEC OFFICER FOR ATTN JAMES DEVOE

NATIONAL OCEANIC & ATMOSPHERIC ADMIN
ENVIRONMENTAL RESEARCH LABORATORIES
DEPARTMENT OF COMMERCE
BOULDER,CO 80302
ATTN GEORGE C REID AERONOMY LAB

NATIONAL OCEANIC & ATMOSPHERIC ADMIN
ENVIRONMENTAL RESEARCH LABORATORIES
DEPARTMENT OF COMMERCE
BOULDER,CO 80302
ATTN ELDON FERGUSON

NATIONAL OCEANIC & ATMOSPHERIC ADMIN
ENVIRONMENTAL RESEARCH LABORATORIES
DEPARTMENT OF COMMERCE
BOULDER,CO 80302
ATTN FRED FEHSENFELD

AERO-CHEM RESEARCH LABORATORIES,INC
P.O. BOX 12
PRINCETON,NJ 08540
ATTN A FONTIJN

AERO-CHEM RESEARCH LABORATORIES,INC
P.O. BOX 12
PRINCETON,NJ 08540
ATTN H PERGAMENT

AERODYNE RESEARCH, INC.
BEDFORD RESEARCH PARK
CROSBY DRIVE
BEDFORD,MA 01731 ATTN F BIEN

AERODYNE RESEARCH, INC.
BEDFORD RESEARCH PARK
CROSBY DRIVE
BEDFORD,MA 01731 ATTN M CAMAC

AERONOMY CORPORATION
217 S NEIL STREET
CHAMPAIGN, IL 61820
ATTN A BOWHILL

AEROSPACE CORPORATION
P.O. BOX 92957
LOS ANGELES,CA 90009
ATTN N COHEN

AEROSPACE CORPORATION
P.O. BOX 92957
LOS ANGELES,CA 90009
ATTN HARRIS MAYER

AEROSPACE CORPORATION
P.O. BOX 92957
LOS ANGELES,CA 90009
ATTN SIDNEY W KASH

AEROSPACE CORPORATION
P.O. BOX 92957
LOS ANGELES,CA 90009
ATTN T WIDHOPH

AEROSPACE CORPORATION
P.O. BOX 92957
LOS ANGELES,CA 90009
ATTN R J MCNEAL

AEROSPACE CORPORATION
P.O. BOX 92957
LOS ANGELES,CA 90009
ATTN R GROVE

AEROSPACE CORPORATION
P.O. BOX 92957
LOS ANGELES,CA 90009
ATTN IRVING M GARFUNKEL

AEROSPACE CORPORATION
P.O. BOX 92957
LOS, ANGLELS, CA 90009
ATTN THOMAS D TAYLOR

AEROSPACE CORPORATION
P.O. BOX 92957
LOS, ANGELES,CA 90009
ATTN V JOSEPHSON

AEROSPACE CORPORATION
P.O. BOX 92957
LOS,ANGELES,CA 90009
ATTN JULIAN REINHEIMER

AEROSPACE CORPORATION
P.O. BOX 92957
LOS, ANGELES,CA 90009
ATTN R D RAWCLIFFE

AVCO-EVERETT RESEARCH LABORATORY INC

2385 REVERE BEACH PARKWAY
EVERETT,MA 02149
ATTN TECHNICAL LIBRARY

AVCO-EVERETT RESEARCH LABORATORY INC
2385 REVERE BEACH PARKWAY
EVERETT,MA 02149
ATTN GEORGE SUTTON

AVCO-EVERETT RESEARCH LABORATORY INC
2385 REVERE BEACH PARKWAY
EVERETT,MA 02149
ATTN C W VON ROSENBERG JR

BATTELLE MEMORIAL INSTITUTE
505 KING AVENUE
COLUMBUS, OH 43201
ATTN DONALD J HAMMAN

BATTELLE MEMORIAL INSTITUTE
505 KING AVENUE
COLUMBUS, OH 43201
ATTN DONALD J HAM

BATTELLE MEMORIAL INSTITUTE
505 KING AVENUE
COLUMBUS,OH 43201
ATTN STOIAC

BATTELLE MEMORIAL INSTITUTE
505 KING AVENUE
COLUMBUS,OH 43201
ATTN RICHARD K THATCHER

BROWN ENGINEERING COMPANY,INC
CUMMINGS RESEARCH PARK
HUNTSVILLE,AL 35807
ATTN N PASSINO

THE TRUSTEES OF BOSTON COLLEGE
CHESTNUT HILL CAMPUS
CHESTNUT HILL, MA 02167
ATTN CHAIRMAN DEPT OF CHEM

BROWN ENGINEERING COMPANY,INC
CUMMINGS RESEARCH PARK
HUNTSVILLE,AL 35807
ATTN RONALD PATRICK

CALIFORNIA AT RIVERSIDE, UNIV OF
RIVERSIDE, CA 92502
ATTN ALAN C LLOYD

CALIFORNIA AT RIVERSIDE, UNIV OF
RIVERSIDE, CA 92502
ATTN JAMES N PITTS JR

CALIFORNIA AT SAN DIEGO, UNIV OF
3175 MIRAMAR ROAD
LA JOLLA, CA 92037
ATTN S C LIN

CALIFORNIA UNIVERSITY OF
BERKELEY CAMPUS ROOM 318
SPROUL HALL
BERKELEY,CA 94720
ATTN SEC OFFICER FOR HAROLD JOHNSTON

CALIFORNIA UNIVERSITY OF
BERKELEY CAMPUS ROOM 318
SPROUL HALL
BERKELEY,CA 94720
ATTN SEC OFFICER FOR F MOZER

CALIFORNIA UNIVERSITY OF
BERKELEY CAMPUS ROOM 318
SPROUL HALL
BERKELEY,CA 94720
ATTN SEC OFFICER FOR DEPT OF CHAM
W H MILLER

CALIFORNIA, STATE OF
AIR RESOURCES BOARD
9528 TELSTAR AVENUE
EL MONTE, CA 91731
ATTN LEO ZAFONTE

CALSPAN CORPORATION
P.O. BOX 235
BUFFALO, NY 14224
ATTN C E TREANOR

CALSPAN CORPORATION
P.O. BOX 235
BUFFALO,NY 14221
ATTN G C VALLEY

CALSPAN CORPORATION
P.O. BOX 235
BUFFALO,NY 14221
ATTN M G DUNN

CALSPAN CORPORATION
P.O. BOX 235
BUFFALO,NY 14221
ATTN W WJRSTER

COLORADO,UNIVERSITY OF
OFFICE OF CONTRACTS AND GRANTS
380 ADMINISTRATIVE ANNEX BOULDER,CO 80302
ATTN A PHELPS JILA

COLORADO,UNIVERSITY OF

OFFICE OF CONTRACTS AND GRANTS
380 ADMINISTRATIVE ANNEX
BOULDER, CO 80302
ATTN JEFFREY B PEARCE LASP

COLORADO,UNIVERSITY OF
OFFICE OF CONTRACTS AND GRANTS
380 ADMINISTRATIVE ANNEX
BOULDER,CO 80302
ATTN C BEATY JILA

COLORADO,UNIVERSITY OF
OFFICE OF CONTRACTS AND GRANTS
380 ADMINISTRATIVE ANNEX
BOULDER,CO 80302
ATTN C LINEBERGER JILA

COLORADO,UNIVERSITY OF
OFFICE OF CONTRACTS AND GRANTS
380 ADMINISTRATIVE ANNEX
BOULDER,CO 80302
ATTN CHARLES A BARTH LASP

COLUMBIA UNIVERSITY,THE TRUSTEES
IN THE CITY OF NEW YORK
LA MONT DOHERTY GEOLOGICAL
OBSERVATORY-TORREY CLIFF
PALISADES,NY 19064
ATTN B PHELAN

COLUMBIA UNIVERSITY,THE TRUSTEES OF
CITY OF NEW YORK
116TH STREET & BROADWAY
NEW YORK, NY 10027
ATTN RICHARD N ZARE

COLUMBIA UNIVERSITY, THE TRUSTEES OF
CITY OF NEW YORK
116TH & BROADWAY
NEW YORKNY 10027
ATTN SEC OFFICER H M FOLEY

CONCORD SCIENCES
P.O. BOX 119
CONCORD,MA 01742
ATTN EMMETT A SUTTON

DENVER,UNIVERSITY OF
COLORADO SEMINARY
DENVER RESEARCH INSTITUTE
P.O. BOX 10127DENVER, CO 80210
ATTN SEC OFFICER FOR MR VAN ZYL

DENVER,UNIVERSITY OF
COLORADO SEMINARY
DENVER RESEARCH INSTITUTE
P.O. BOX 10127DENVER,CO 80210
ATTN SEC OFFICER FOR DAVID MURCRAY

GENERAL ELECTRIC COMPANY
TEMPO-CENTER FOR ADVANCED STUDIES
816 STATE STREET (P.O DRAWER QQ)
SANTA BARBARA,CA 93102
ATTN DASAIC

GENERAL ELECTRIC COMPANY
TEMPO-CENTER FOR ADVANCED STUDIES
816 STATE STREET (P.O. DRAWER QQ)
SANTA BARBARA,CA 93102
ATTN WARREN S KNAPP

GENERAL ELECTRIC COMPANY
TEMPO-CENTER FOR ADVANCED STUDIES
816 STATE STREET (P.O DRAWER)
SANTA BARBARA,CA 93102
ATTN TIM STEPHENS

GENERAL ELECTRIC COMPANY
TEMPO-CENTER FOR ADVANCED STUDIES
816 STATE STREET (P.O. DRAWER QQ)
SANTA BARBARA,CA 93102
ATTN DON CHANDLER

GENERAL ELECTRIC COMPANY
TEMPO-CENTER FOR ADVANCED STUDIES
816 STATE STREET (P.O. DRAWER QQ)
SANTA BARBARA,CA 93102
ATTN B CAMBILL

GENERAL ELEC. CO.
SPACE DIVISION
VALLEY FORGE SPACE CTR
GODDARD BLVD
KING OF PRUSSIA
P.O. BOX 8555
PHILADELPHIA,PA 19101
ATTN M H BORTNER, SPACE SCIENCE LAB

GENERAL ELECTRIC COMPANY
SPACE DIVISION
VALLEY FORGE SPACE CENTER
GODDARD BLVD KING OF PRUSSIA
P.O. BOX 8555
PHILADELPHIA,PA 19101
ATTN J BURNS

GENERAL ELECTRIC COMPANY
SPACE DIVISION
VALLEY FORGE SPACE CENTER
GODDARD BLVD KING OF PRUSSIA
P.O. BOX 8555
PHILADELPHIA,PA 19101
ATTN F ALYEA

GENERAL ELECTRIC COMPANY
SPACE DIVISION
VALLEY FORGE SPACE CENTER
GODDARD BLVD KING OF PRUSSIA
P.O. BOX 8555
PHILADELPHIA,PA 19101
ATTN P ZAVITSANOS

GENERAL ELECTRIC COMPANY
SPACE DIVISION
VALLEY FORGE SPACE CENTER
GODDARD BLVD KING OF PRUSSIA
P.O. BOX 8555
PHILADELPHIA,PA 19101
ATTN R H EDSALL

GENERAL ELECTRIC COMPANY
SPACE DIVISION
VALLEY FORGE SPACE CENTER
GODDARD BLVD KING OF PRUSSIA
P.O. BOX 8555
PHILADELPHIA,PA 19101
ATTN T BAURER

GENERAL RESEARCH CORPORATION
P.O. BOX 3587
SANTA BARBARA,CA93105
ATTN JOHN ISE JR

GEOPHYSICAL INSTITUTE

UNIVERSITY OF ALASKA
FAIRBANKS,AK 99701
ATTN D HENDERSON

GEOPHYSICAL INSTITUTE
UNIVERSITY OF ALASKA
FAIRBANKS,AK 99701
ATTN J S WAGNER PHYSICS DEPT

GEOPHYSICAL INSTITUTE
UNIVERSITY OF ALASKA
FAIRBANKS,AK 99701
ATTN B J WATKINS

GEOPHYSICAL INSTITUTE
UNIVERSITY OF ALASKA
FAIRBANKS,AK 99701
ATTN T N DAVIS

GEOPHYSICAL INSTITUTE
UNIVERSITY OF ALASKA
FAIRBANKS,AK 99701
ATTN R PARTHASARATHY

GEOPHYSICAL INSTITUTE
UNIVERSITY OF ALASKA
FAIRBANKS,AK 99701
ATTN NEAL BROWN

LOWELL, UNIVERSITY OF
CENTER FOR ATMOSPHERIC RESEARCH
450 AIKEN STREET
LOWELL,MA 01854
ATTN G T BEST

LOCKHEED MISSILES AND SPACE COMPANY
3251 HANOVER STREET
PALO ALTO, CA 94394
ATTN JOHN KUMER DEPT 52-54

LOCKHEED MISSILES AND SPACE COMPANY
3251 HANOVER STREET
PALO,ALTO,CA 94304
ATTNJOHN KIMER DEPT 52-54

LOCKHEED MISSILES AND SPACE COMPANY
3251 HANOVER STREET
PALO,ALTO,CA 94304
ATTNJOHN B CLADIS DEPT 52-12

LOCKHEED MISSILES AND SPACE COMPANY
3251 HANOVER STREET
PALO,ALTO,CA 94304
ATTNBILLY M MCCORMAC DEPT 52-54

LOCKHEED MISSILES AND SPACE COMPANY
3251 HANOVER STREET
PALO,ALTO,CA 94304
ATTNTOM JAMES DEPT 52-54

LOCKHEED MISSILES AND SPACE COMPANY
3251 HANOVER STREET
PALO,ALTO,CA 94304
ATTNJ B REAGAN D/52-12

LOCKHEED MISSILES AND SPACE COMPANY
3251 HANOVER STREET
PALO,ALTO,CA 94304
ATTNMARTIN WALT DEPT 52-10

LOCKHEED MISSILES AND SPACE COMPANY
3251 HANOVER STREET
PALO,ALTO,CA 94304
ATTNRICHARD G JOHNSON DEPT 52-12

LOCKHEED MISSILES AND SPACE COMPANY
3251 HANOVER STREET
PALO,ALTO,CA 94304
ATTNROBERT D SEARS DEPT 52-14

LOCKHEED MISSILES AND SPACE COMPANY
3251 HANOVER STREET
PALO,ALTO,CA 94304
ATTNJ R WINKLER

INSTITUTE FOR DEFENSE ANALYSE
400 ARMY-NAVY DRIVE
ARLINGTON,VA 22202
ATTN ERNEST BAUER

INSTITUTE FOR DEFENSE ANALYSE
400 ARMY-NAVY DRIVE
ARLINGTON VA 22202
ATTN HANS WOLFHARD

MISSION RESEARCH CORPORATION
735 STATE STREET
SANTA BARBARA,CA 93101
ATTN D ARCHER

MISSION RESEARCH CORPORATION
735 STATE STREET
SANTA BARBARA,CA 93101
ATTN D FISCHER

MISSION RESEARCH CORPORATION
735 STATE STREET
SANTA BARBARA,CA 93101
ATTN M SCHEIBE

MISSION RESEARCH CORPORATION

735 STATE STREET
SANTA BARBARA,CA 93101
ATTN D SAPPENFIELD

MISSION RESEARCH CORPORATION
735 STATE STREET
SANTA BARBARA,CA 93101
ATTN D SOWLE

PHOTOMETRIC, INC.
442 MARRETT ROAD
LEXINGTON,MA 02173
ATTN IRVING L KOFSKY

PHYSICAL DYNAMICS INC.
P.O. BOX 1069
BERKELEY,CA 94701
ATTN J B WORKMAN

PHYSICAL DYNAMICS INC.
P.O. BOX 1069
BERKELEY,CA 94701
ATTN A THOMPSON

PHYSICAL SCIENCES,INC.
30 COMMERCE WAY
WOBURN,MA 01801
ATTN KURT WRAY

PHYSICAL SCIENCES,INC.
30 COMMERCE WAY
WOBURN,MA 01801
ATTN R L TAYLOR

PHYSICAL SCIENCES,INC.
30 COMMERCE WAY
WOBURN,MA 01801
ATTN G CALEDONIA

PHYSICS INTERNATIONAL COMPANY
2700 MERCED STREET
SAN LEANDRO,CA 94577
ATTN DOC CON FOR TECH LIB

PITTSBURGH, UNIVERSITY OF
OF THE COMWLTH SYS OF HIGHER EDUC
CATHEDRAL OF LEARNING
PITTSBURGH,PA 15213
ATTN WADE L FITE

PITTSBURGH, UNIVERSITY OF
OF THE COMWLTH SYS OF HIGHER EDUC
CATHEDRAL OF LEARNING
PITTSBURGH,PA 15213
ATTN MANFRED A BIONDI

PITTSBURGH, UNIVERSITY OF
OF THE COMWLTH SYS OF HIGHER EDUC
CATHEDRAL OF LEARNING
PITTSBURGH,PA 15213
ATTN FREDERICK KAUFMAN

PITTSBURGH, UNIVERSITY OF
OF THE COMWLTH SYS OF HIGHER EDUC
CATHEDRAL OF LEARNING
PITTSBURGH,PA 15213
ATTN EDWARD GERJUOY

PRINCETON UNIV, THE TRUSTEES OF
FORRESTAL CAMPUS LIBRARY
BOX 710
PRINCETON UNIVERSITY
PRINCETON,NJ 08540
ATTN ARNOLD J KELLY

R & D ASSOCIATES
P.O. BOX 9695
MARINA DEL REY,CA 90291
ATTN RICHARD LATTER

R & D ASSOCIATES
P.O. BOX 9695
MARINA DEL REY,CA 90291
ATTN R G LINDGREN

R & D ASSOCIATES
P.O. BOX 9695
MARINA DEL REY,CA 90291
ATTN BRYAN GABBARD

R & D ASSOCIATES
P.O. BOX 9695
MARINA DEL REY,CA 90291
ATTN H A DRY

R & D ASSOCIATES
P.O. BOX 9695
MARINA DEL REY,CA 90291
ATTN ROBERT E LELEVIER

R & D ASSOCIATES
P.O. BOX 9695
MARINA DEL REY,CA 90291
ATTN R P TURCO

R & D ASSOCIATES
P.O. BOX 9695
MARINA DEL REY,CA 90291
ATTN ALBERT L LATTER

R & D ASSOCIATES
P.O. BOX 9695
MARINA DEL REY,CA 90291
ATTN FORREST GILMORE

R & D ASSOCIATES

P.O. BOX 9695
MARINA DEL REY,CA 90291
ATTN D DEE

R & D ASSOCIATES
1815 N. FT. MYER DRIVE
11TH FLOOR
ARLINGTON,VA 22209
ATTN HERBERT J MITCHELL

R & D ASSOCIATES
1815 N. FT. MYER DRIVE
11TH FLOOR
ARLINGTON,VA 22209
ATTN J W ROSENGREN

RAND CORPORATION
1700 MAIN STREET
SANTA MONICA,CA 90406
ATTN CULLEN CRAIN

SCIENCE APPLICATIONS, INC.
P.O. BOX 2351
LA JOLLA,CA 92038
ATTN DANIEL A HAMLIN

SCIENCE APPLICATIONS, INC.
P.O. BOX 2351
LA JOLLA, CA 92038
ATTN DAVID SACHS

SPACE DATA CORPORATION
1331 SOUTH 26TH STREET
PHOENIX,AZ 85034
ATTN EDWARD F ALLEN

STANFORD RSCH INSTITUTE INTERNATIONAL
333 RAVENSWOOD AVENUE
MENLO PARK, CA 94025
ATTN M BAPON

STANFORD RSCH INSTITUTE INTERNATIONAL
333 RAVENSWOOD AVENUE
MENLO PARK, CA 94025
ATTN L LEADABRAND

STANFORD RSCH INSTITUTE INTERNATIONAL
333 RAVENSWOOD AVENUE
MENLO PARK, CA 94025
ATTN WALTER G CHESTNUT

STANFORD RSCH INSTITUTE INTERNATIONAL
1611 NORTH KENT STREET
ARLINGTON,VA 22209
ATTN WARREN W BERNING

STANFORD RSCH INSTITUTE INTERNATIONAL
1611 NORTH KENT STREET
ARLINGTON,VA 22209
ATTN CHARLES HULBERT

TECHNOLOGY INTERNATIONAL CORPORATION
75 WIGGINS AVENUE
BEDFORD,MA 01730
ATTN W P BOQUIST

UNITED TECHNOLOGIES CORPORATION
755 MAIN STREET
HARTFORD,CT 06103
ATTN H MICHELS

UNITED TECHNOLOGIES CORPORATION
755 MAIN STREET
HARTFORD,CT 06103
ATTN ROBERT HBULLIS

UTAH STATE UNIVERSITY
LOGAN, UT 84321
ATTN DORAN BAKER

UTAH STATE UNIVERSITY
LOGAN, UT 84321
ATTN KAY BAKER

UTAH STATE UNIVERSITY
LOGAN, UT 84321
ATTN C WYATT

UTAH STATE UNIVERSITY
LOGAN, UT 84321
ATTN D BURT

VISIDYNE, INC.
19 THIRD AVENUE
NORTHWEST INDUSTRIAL PARK
BURLINGTON, MA 01803
ATTN HENRY J SMITH

VISIDYNE, INC.
19 THIRD AVENUE
NORTHWEST INDUSTRIAL PARK
BURLINGTON, MA 01803
ATTN J W CARPENTER

VISIDYNE, INC.
19 THIRD AVENUE
NORTHWEST INDUSTRIAL PARK
BURLINGTON, MA 01803
ATTN WILLIAM REIDY

19 THIRD AVENUE
NORTHWEST INDUSTRIAL PARK
BURLINGTON, MA 01803
ATTN T C DEGGES

VISIDYNE, INC.
19 THIRD AVENUE
NORTHWEST INDUSTRIAL PARK
BURLINGTON, MA 01803
ATTN CHARLES HUMPHREY

WAYNE STATE UNIVERSITY
1064 MACKENZIE HALL
DETROIT, MI 48202
ATTN PIETER K ROL CHAM ENGRG & MAT SCI

WAYNE STATE UNIVERSITY
1064 MACKENZIE HALL
DETROIT, MI 48202
ATTN R H KUMMLER

WAYNE STATE UNIVERSITY
~~DEPT. OF PHYSICS~~
DETROIT, MI 48202
ATTN WALTER E KAUPPILA

YALE UNIVERSITY
NEW HAVEN, CT 06520
ATTN ENGINEERING DEPARTMENT

☆ U. S. GOVERNMENT PRINTING OFFICE: 1977--700-031--132